Interacting quantum systems in one dimension at arbitrary energy

Habilitationsschrift von
Oleksandr Tsyplyatyev
aus Charkow

Vorgelegt beim Fachbereich Physik
der Goethe Universität
zu Frankfurt am Main

Januar 2018

Contents

Chapter 1

Introduction

The first theory of interactions in quantum many-body systems (presently known as the Landau's Fermi liquid theory) was proposed by L. D. Landau in 1950s [1–3] and is the starting point for the whole field of many-body physics. This seminal work was the first example of a before unimaginative solution to the exponential complexity of an interacting system consisting of many quantum particles that was actually found in a robust way creating a basis for the modern understanding of the effect of Coulomb interactions between electrons in conductors. Since then a great deal of progress has been made in this field: J. Bardeen, L. N. Cooper, and J. R. Schrieffer have created a microscopic theory of the pairing effect between electrons [4] as an effort to identify the microscopic mechanism behind superconductivity in the same decade of 1950s and two decades later in the 1970s new theoretical tools were developed[1] [5–8] culminating in the theory of interactions in one dimension (commonly referred to as Luttinger liquid as opposite to Fermi liquid) where both the Fermi liquid and the BCS theory do not apply.

All of these three theories describe the low energy excitations of a many-body system above its ground state, or above the gap energy in the case of a superconductor. At higher energy they become uncontrollable, e.g. the lifetime of the quasiparticles of Fermi liquid becomes shorter and shorter when the excitation energy is increased away from the Fermi energy due to the effect of the non-linearity of the single particle spectrum that eventually reduces the quasiparticle's lifetime to zero. This common limit of applicability raises the contemporary question: "what is/are the many-body theory/ies at high energy?". A part of the answer was given only very recently (in 2000s) in one dimension by L. Glazman and his co-workers in the form of the mobile impurity model [10, 11]. And this will be the point of departure for the present work.

Although, the domain of this work is one dimension, it is instructive to recall first the Landau's Fermi liquid, since it was historically the first theory of interactions and is a convenient way of introducing basic many-body concepts and notations and

[1] This list is by no means complete, for a systematic review of the literature on this topic see for example [9].

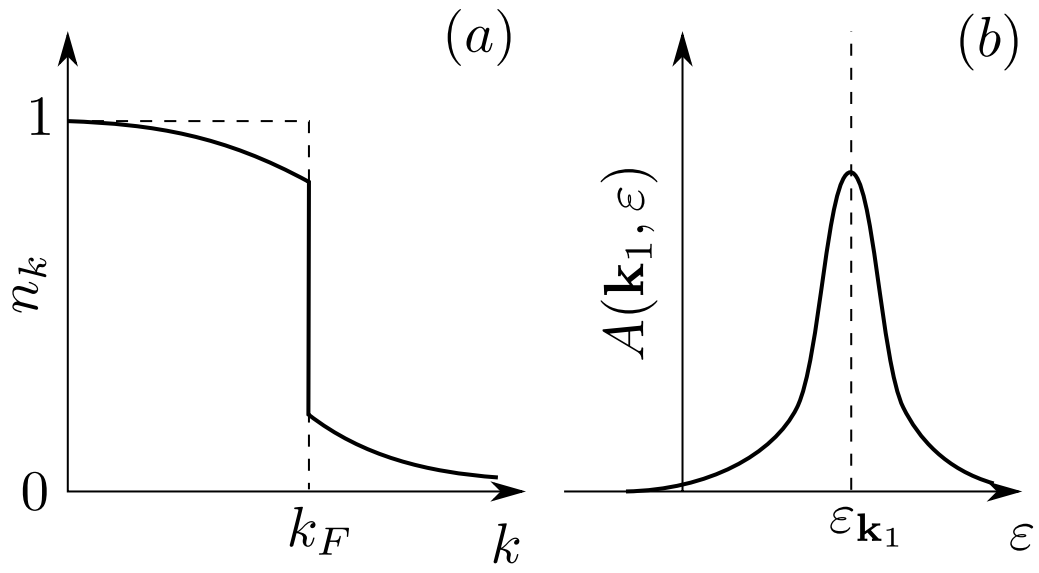

Figure 1.1: (a) Occupation numbers n_k of a system consisting of many fermions as a function of the modulus of the momentum $k = |\mathbf{k}|$: the dashed line is the free electron system at zero temperature in which all the states up to the Fermi momentum k_F are filled and the full line is an interacting system in two or three dimensions described by the Landau's Fermi liquid theory. (b) Spectral function $A(\mathbf{k}, \varepsilon)$ for a fixed value of $\mathbf{k}_1$ as a function energy ε: the dashed line is the position of a delta function of a non-interacting system and the full line is a Lorentzian with a finite width that corresponds to a quasiparticle in the Fermi liquid theory.

sketching the overall framework[2]. At zero temperature ($T = 0$) a system consisting of N free fermions forms a Fermi-Dirac condensate, e.g. electrons fill single particle states with the lowest energy up a given threshold—Fermi energy E_F. The corresponding occupation number $n_{\mathbf{k}}$, where k is the single particle momentum, of the Fermi sea is a step function that is one for all momenta which modulus $|\mathbf{k}| \leq k_F$, where k_F is the Fermi momentum, and is zero for $|\mathbf{k}| > k_F$, see the dashed line in Fig. 1.1(a). Excitations of the free system with respect to its ground state, correspond to adding an extra particle above the Fermi energy (or removing a particle below it) with a well-defined momentum $\mathbf{k}$. These excitations also have a well-defined energy $\varepsilon_{\mathbf{k}}$ and the infinite lifetime since they are the eigenstates of the Hamiltonian. A common way of characterising these many-body excitations is the spectral function $A(\mathbf{k}, \varepsilon)$, which is defined as the probability density of finding an excitation with energy ε and momentum $\mathbf{k}$. For free electrons it is $A(\mathbf{k}, \varepsilon) = \delta(\varepsilon - \varepsilon_{\mathbf{k}} + E_F)$, see the dashed line in the cut of the spectral function along the energy axis for a fixed momentum $k_1 > k_F$ in Fig. 1.1(b).

[2]The BCS theory will not be introduced here at all since we are dealing with repulsive interactions only and also since interactions of any sign do not open a gap in one dimension making the theoretical approach the same for repulsion as for attraction, unlike higher dimensions where the pairing instability opens a gap leading to a completely different physics.

When interactions are turned on, the properties of the system essentially do not change, i.e. they remain almost the same as that of the free electrons—and this is the main result of the Fermi liquid theory. The free particles are not individual excitations anymore, they are dressed by density fluctuations of the existing Fermi sea, constructed out of the excitations of the electron-hole pairs type that do not change the total number of particles but they are coupled to the single particle states via the interaction. These collective objects are called quasiparticles now since they are formed by many individual electrons, however these quasiparticles still retain most of the fermionic properties of the undressed single particle excitations within the Fermi liquid theory. The whole effect of the interactions is manifested only in renormalisation of the single particle properties by so-called Landau parameters.

Occupation numbers n_k in the Fermi liquid theory still have a discontinuity at the Fermi surface, see the full line in Fig. 1.1(a). However the amplitude of this discontinuity is not one anymore but is a number Z smaller than one $Z < 1$, which represents the fraction of electrons which still keeps the original fermionic property of a free electron after it has been smeared by the interactions with other electrons. The bigger is the smearing the less of the original single particle properties remain and the smaller is Z. Any finite $Z > 0$ means that quasiparticles are still defined through a single-particle-like dispersion relation $\varepsilon_{\mathbf{k}}$. Although, $\varepsilon_{\mathbf{k}}$ is not the bare energy of a single electron. Nevertheless, close to the Fermi surface the dispersion can be linearised in the powers of $k - k_F$ as

$$\varepsilon_{\mathbf{k}} = E_F + \frac{k_F}{m^*}\left(k - k_F\right), \tag{1.1}$$

where $k = |\mathbf{k}|$ is the modulus of the momentum and m^* is a parameter that is usually called effective mass, for free electrons $m* = m$ is the mass of the electron itself. Here we assumed rotational symmetry in two and three dimensions, therefore the Fermi surface is circular (spherical) and the above expansion is the same in all directions. Thus, close to the Fermi surface we can use the same free electron dispersion changing only the mass of the particles from m to m^*, and no extra parameters are needed. The Fermi momentum is not changed by interactions due to Luttinger theorem [12]. The theorem states that for the translationally invariant systems, though the shape of the Fermi surface can be changed by interactions, the volume enclosed by it is proportional only to the electron density irrespective of the interactions. For also rotationally invariant systems it directly implies that k_F is also independent of interactions (it is an invariant of the interaction strength).

Since the quasiparticles are not completely free particles, their lifetime τ is finite. The corresponding spectral function in Fig. 1.1(b) is not a delta function anymore, like for a free particle (dashed line), but is a Lorentzian with a finite width $1/\tau$ (solid line), which position for a fixed $\mathbf{k}_1$ is centred at the energy given by Eq. (1.1). When the lifetime τ is shorter than the characteristic timescale defined by the dispersion, $1/\left(\varepsilon_{\mathbf{k}} - E_F\right)$, the notion of a quasiparticle disappears altogether, i.e. it is not possible anymore to define a single-particle-like dispersion in Eq. (1.1). In the proximity to the Fermi surface $k \to k_F$, the timescale $1/\left(\varepsilon_{\mathbf{k}} - E_F\right)$ becomes

bigger and bigger, but fortunately the lifetime τ also diverges since electrons have less and less phase space to scatter close to the Fermi surface leading to a smaller degree of smeariness of the quasiparticles that is reflected in the energy dependence of the lifetime τ_ε. For instance, simple phase-space arguments [13] show that $\tau_\varepsilon \sim 1/\left(\varepsilon - E_F\right)^2$ close to the Fermi energy in three dimension. Thus, the width of the Lorentzian $1/\tau_\varepsilon$ is always narrower than the energy scale $(\varepsilon - E_F)$ making the quasiparticles always well-defined and, therefore, making the Fermi liquid theory better and better when the energy is closer and closer to the Fermi level. For most of the low energy properties a big but finite lifetime can be just ignored.

It has to be noted that the quasiparticle states are not the exact eigenstates of the quantum model. The Fock space of a many-body system is exponentially large. For example for a system of spinless fermions on a lattice in D dimensions the total number of states is 2^N, where $N = L^D$ is the number of sites, L is the linear dimension of the lattice in the units of the lattice spacing, and D is its spatial dimension. Therefore, the average distance between the many-body eigenenergies is exponentially small, $\sim \exp(-L)$. For a free system however the excitation energy for is given by Eq. (1.1) with $m^* = m$, thus the distance between the states in the energy domain is much larger, $\sim 1/L$, than the level spacing of the interacting system. This is caused by a huge degeneracy of the many-body states of the free system, which is lifted by the interactions. The existence of quasiparticles in a Fermi liquid is a result of clustering of the exact eigenstates from the exponentially large continuum around certain points in the energy domain, given by the quasiparticle dispersion in Eq. (1.1). An ensemble of many states from the exponentially large continuum forms a quasiparticle with its finite lifetime, a Lorentzian with a finite width given by the full dashed line in Fig. 1.1(b).

Essentially a free Fermi gas description of interacting electrons, the interactions only renormalise parameters of the free system, is what makes Fermi liquid so successful. For instance, it forms the basis of the modern theory of transport in conductors: metals and semiconductors. Even in semiconductors the Fermi energy is at least 5000K (for Silicon or GaAs) and is even higher for metals. In a typical range from low 1K to room 300K temperatures the relevant quasiparticles are always close to the Fermi energy and thus the almost free particle approximation of Fermi liquid is generally robust. It is routinely confirmed by a plethora of solid-state experiments, including electrical, thermo-electrical, classical Hall, spintronics, thermo-spin, and so on experiments[3]. Another realisation of Fermi liquid is He_3, which obeys the Fermi statistics at low temperatures since it has total spin 1/2. The Fermi energy is quite small $\simeq$ 5K that requires the temperatures to be in the milli-Kelvins range in order to keep excitations only close to the Fermi surface. This temperature range is still accessible via the currently available cryogenic techniques, where experiments do observe a renormalisation of the free Fermi gas parameters, e.g. in Ref. [14, 15]. Also in industry the field of electronics uses the transport theory of semiconductors

[3]The applications of the Fermi liquid theory in the field of solid-state are so many and are so diverse that reviewing them with any reasonable degree of comprehension is just not possible. Only a few highlights are given here.

based on the Fermi liquid theory as a fundamental building block of a countless number of modern consumer devices.

Landau has originally constructed the Fermi liquid theory [1, 2] in a phenomenological way by expanding the free energy of an interacting Fermi gas up to the second order in small deviations from the free particle distribution function. Then, all of the observable properties can derived starting from this postulated form of free energy. Later, the same picture was reproduced microscopically by the many-body perturbation theory in interactions in diagrammatic form [16, 17] (a good review is given in the book [13]) and by renormalisation group [18, 19]. Although the Landau's phenomenological approach still keeps its value due to its technical simplicity and physical transparency. Both, microscopically and phenomenologically, the lifetime of the excitations shortens away from the Fermi energy. Eventually quasiparticles become undefined. This breakdown point happens not at a large energy scale, like the Fermi energy, but at a much lower energy. It can be visualised as an increasing contribution of the parabolic correction to Eq. (1.1). When it becomes of the same order as the linear term the quasiparticles are no longer defined, making the Fermi liquid theory valid only at low energy. The non-linear theory—for excitations with non-linear dispersion—still remains an open problem.

While the Fermi liquid theory works well in two and three dimensions, it fails completely in one dimension, even at low energy. The lowest order perturbative correction in the interaction potential to the free electron self-energy in one dimension is proportional to $1/\left(\varepsilon - \varepsilon_{\mathbf{k}}\right)$ close to the Fermi level [20]. This divergence signals that the many-body eigenstates are very different from free particle excitations, and require a new solution to the many-body problem. Fortunately, at low energy the one dimensional problem was completely solved at the microscopic level by bosonisation. Under linearisation of the single particle dispersion at low energy $\varepsilon_k = E_F + v_F k$, the electron-hole excitations of the free particle spectrum becomes equidistant and very degenerate, like for bosons, that allows to map all of the free Fermi states onto pure bosonic excitations consisting of many electron-hole pairs [21]. Moreover the density-density interaction between the fermions, quartic in the field operators, becomes only quadratic in bosonic operators under this mapping. Thus, this procedure of bosonisation makes the interacting Hamiltonian quadratic in the bosonic degrees of freedom, which is just a harmonic oscillator that is solved immediately, and the same procedure remains valid for arbitrary strength of the interactions between the original fermionic particles.

The usual way of performing calculations using the result of this bosonisation procedure is to start from the so-called Tomonaga-Luttinger model [21, 22]

$$H_{TL} = \frac{v}{2\pi} \int dx \left[K \left(\nabla\theta\right)^2 + \frac{1}{K} \left(\nabla\varphi\right)^2 \right], \tag{1.2}$$

where the bosonic degrees of freedom are represented by a pair of fields, $\nabla\theta$ and $\nabla\varphi$, that have the meaning of the current and the density operators respectively, with the following boson-like commutation relation between them $\left[\varphi\left(x\right), \nabla\theta\left(x'\right)\right] = i\pi\delta\left(x - x'\right)$. Here we use the notations of the Giamarchi's book [23]. The only two

effective parameters that describe a generic interacting system in one dimension are v and K: v is the sound velocity and K is Luttinger parameter, which together encode the original interaction strength.

Since the Tomonaga-Luttinger model is quadratic in bosonic operators, the corresponding conformal field theory can be constructed straightforwardly by writing down the action for the Hamiltonian in Eq. (1.2). Then, observables are calculated as Gaussian averages of the operators over the free fields θ and φ producing the hallmark of the Luttiger liquid physics, power-law dependencies in various quantities, where the exponents depends on v and K. For the dynamical structure factor, $S(k,\varepsilon) = \int dtdxe^{i(\varepsilon t-kx)}\langle\rho(x,t)\rho(0,0)\rangle$ where the density ρ has to be expressed through $\nabla\varphi$ and its time evolution $\rho(x,t)$ and the zero temperature average $\langle\dots\rangle$ are given by the model in Eq. (1.2), this procedure gives the zero delta-functional width of the excitations $S(k,\varepsilon) \sim |k-k_F|\,\delta(\varepsilon - v|k-k_F|)$. However, these excitations are Bose-like hydrodynamic modes consisting of many electron-hole excitations of the original fermions (the so-called charge density wave or CDW) instead of the Fermi-like quasiparticles of the Landau's Fermi liquid theory. The occupation numbers $n_k = \int dxe^{-ikx}\left\langle\psi^\dagger(x)\psi(0)\right\rangle \sim 1/2 + \text{const}\cdot\text{sign}(k-k_F)|k-k_F|^{\left(K+K^{-1}\right)/2-1}$, where the original fermionic field operator is bosonised as $\psi \sim e^{i\theta+i\varphi}$, has no discontinuity at the Fermi momentum unlike Fermi liquid, see Fig. 1.1(a), but rather has a smooth power-law behaviour with the exponent $\left(K+K^{-1}\right)/2-1 > 0$ given by Luttinger parameter K, which is a clear manifestation of a non-Fermi liquid nature of the interacting systems in one dimension.

The systems with spin behave in even stranger way in one dimension—their spin degeneracy is lifted by interaction producing two different velocities, unlike higher dimensions where the double degeneracy of electron spin-1/2 enters only as a factor in the density of states. The up and the down spin states produce two sets of bosonic fields in the Tomonaga-Luttinger model. The density-density interaction couples two species since fermions with the same spin cannot be at the same point in space but different spins can, hybridising the two independent liquids. Application of the bosonisation technique to the model of spinful fermions gives two independent Tomonaga-Luttinger models for the charge degree of freedom ρ (CDW) and for the spin degree of freedom σ (spin density wave or SDW) [23]. Each of the two models has the form of Eq. (1.2) but the sound velocities $v_{\rho,\sigma}$ and Luttinger parameters $K_{\rho,\sigma}$ are different for any finite interaction strength between the original fermions. Thus, the degeneracy with respect to the spin degree of freedom is not present, which is manifested, for example, in a extra branch of dispersion with $v_\sigma \neq v_\rho$ in the excitation spectrum in one dimension [23].

Realisations of one dimensional system are quite uncommon in nature. But the big theoretical advancements in 1970s motivated strongly the experimental community to manufacture artificial systems that behave essentially one-dimensional inside a three-dimensional system. One class of such designs are strongly anisotropic magnetic insulators or organic materials, which three-dimensional crystals consist of bundles of magnetic chains with a weak magnetic exchange between them that can be neglected, e.g. $KCuF_3$ [24] and $(TNTSF)_2PF_6$ [25]. Another system

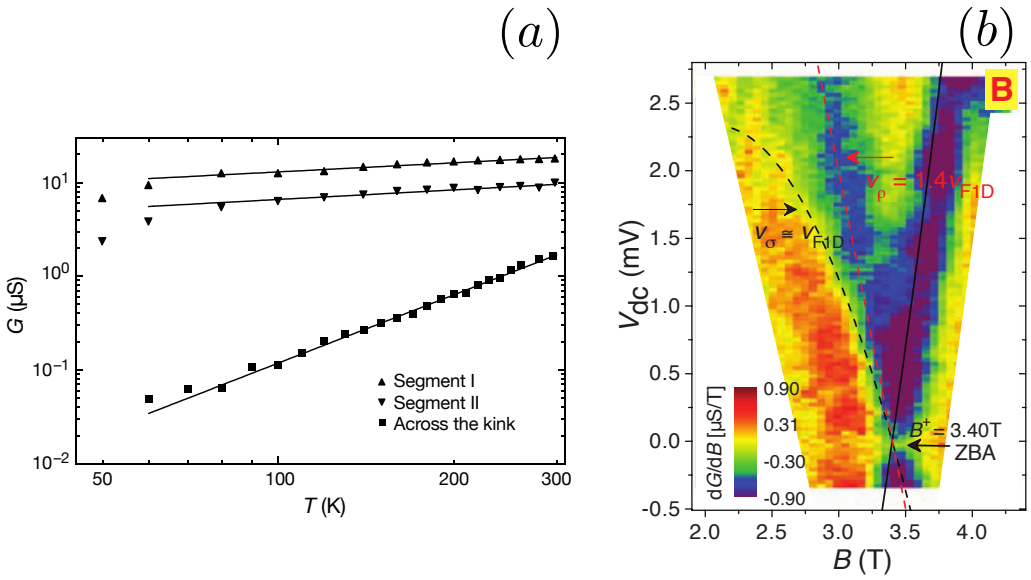

Figure 1.2: (a) Linear-response two-terminal conductances G of single-wall carbon nanotubes as functions of temperature at a double-logarithmic scale. The triangles are a pair of straight nanotubes and squares are a nanotube with a kink. The solid lines are power-law functions $G \sim T^{\alpha}$ with the real exponents α ($\alpha = 0.35$ for the straight nanotubes and $\alpha = 2.2$ for the nanotube with a kink) generally predicted by the Tomonaga-Luttinger model for an interacting one-dimensional conductor. The figure is taken from Ref. [26]. (b) Differential conductance measured through a double-well GaAs heterostructure where quantum wires are formed in the upper layer by potential gates. The magnetic field B applied perpendicular to the wires and the bias between the two layers V_{dc} provide the momentum and the energy resolution in the measured spectral function. Two branches with linear dispersions, marked by $v_\rho \neq v_\sigma$, extend from the Fermi point at $B = 3.4$ T and $V_{dc} = 0$. The figure is taken from Ref. [28].

is carbon nanotubes that self-assemble themselves under certain conditions and are one-dimensional conductors. Electrical conductance of a nanotube can be measured straightforwardly by attaching it to a pair of electrodes. The temperature dependence of the conductance [26] shows a power-law function predicted by the Tomonaga-Luttinger model, we reproduce them in Fig. 1.2(a). A quantum wire can also be made using the currently available techniques of nano-lithography in semiconductors. Starting from the GaAs double-well heterostructures this design allows to measure a more detailed quantity, spectral function $A(k, \varepsilon)$, with both momentum and energy resolutions, where the separation of the free electronic excitations into the spin and the charge modes with different velocities, also predicted by the Tomonaga-Luttinger model, was observed [27, 28], which we reproduce in Fig. 1.2(b).

Away from low energy the curvature of the original parabolic dispersion at the

Fermi energy becomes progressively more important. It, for instance, broadens the sharp dynamical structure factor that is strictly delta-functional, $S(k,\varepsilon) \sim \delta(\varepsilon - v|k-k_F|)$, for the linearised spectrum, reflecting the infinite lifetime of the hydrodynamic modes of the Tomonaga-Luttinger model. Addition of a quadratic term, $k^2/(2m^*)$, to the linearised dispersion $\varepsilon_k = E_F + v_F k$ should on a simple level introduces a finite width to the delta function. Close to the Fermi energy the momentum can be expressed though energy as $k = (\varepsilon - E_F)/v_F$ giving the broadening $1/\tau_\varepsilon \sim (\varepsilon - E_F)^2/(mv_F^2)$ that increases from zero at $\varepsilon = E_F$ to bigger and bigger values away from it, like the quasiparticle lifetime of the Fermi liquid in higher dimensions. However, unlike in the Fermi liquid perturbation theory in the $k^2/(2m^*)$ correction on top of the Tomonaga-Luttiger model fails due to many divergencies, and there is no clear way how to deal with them [29, 30]. This is not totally surprising since linearisation of the dispersion imposes an additional symmetry (Lorentz invariance) on the system. Thus, the eigenstates become additionally degenerate, the energy and the momentum conservation laws of the linear model become the same. When, a finite curvature (the parabolic $1/m^*$ term) reduces the Lorentz invariance to Galilean, the energy and momentum conservation laws become different, making the corresponding perturbation theory degenerate and producing various divergencies.

These singularities occur not only at the special (Fermi) points but also at arbitrary momenta, analogously to another problem, the Fermi edge singularity effect in x-ray absorption or emission in three dimensional metals. The solution to the latter problem was given by Nozieres and De Dominicis in the form of the heavy impurity model [31] that is an effective one-body problem of a single impurity (representing a hole-like excitation deep under the Fermi level) coupled to many Fermi liquid quasiparticles at the Fermi level. The connection between the nonlinearity problem in one dimension and the edge singularity in a Fermi liquid was first spotted on the microscopic level for weakly interacting fermions in [32, 33].

The field theoretical methods, which were based only on this analogy, further led L. Glazman and his co-workers to the phenomenological construction of the nonlinear Luttiger liquid theory [34]. In one dimension the continuum of the many-body excitations does not cover the whole energy-momentum plane due to a kinematic constraint, see the white regions in Fig. 1.3(a). For example, creation of an excitation of the electron-hole pair type at a fixed momentum $k \neq k_F$ requires at least a finite energy of removing at least a single particle at some finite distance from the Fermi level and putting in the lowest available state just above the Fermi level since there are only two Fermi points $\pm k_F$. In two dimension such a constraint already does not exists since it is always possible to connect two different points on the Fermi circle with a vector $\mathbf{k}$ of an arbitrary length, creating an excitation with zero energy at arbitrary finite momentum $|\mathbf{k}| < 2k_F$. Therefore, a threshold in the energy-momentum plane that separates the region with a finite density of states from the zero density is yet another peculiarity of the one-dimensional physics.

This spectral threshold is an analog of the Fermi edge in the x-ray scattering problem in three dimension. The nonlinear Luttinger liquid model was constructed

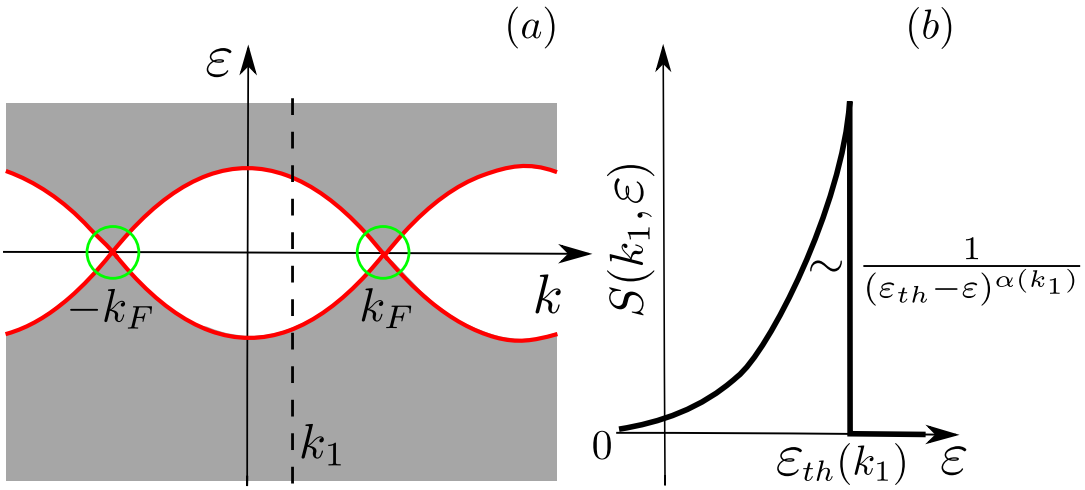

Figure 1.3: (a) Density of the many-body excitations of a one-dimensional system on the energy-momentum plane: finite in the grey areas and zero in the white areas. The red line marks the border between the two defining the dispersion of the spectral edge $\varepsilon_{th}(k)$, it is generally a multi-valued function. The low energy regions around the $\pm k_F$ points, where the linear Luttinger liquid theory is valid, are marked with green circles (b) Dynamical structure factor $S(k,\varepsilon)$ along the vertical cut at a fixed k_1 in the non-linear region marked by the dashed line in (a) as a function of ε (only its bottom half for $\varepsilon < 0$ is plotted). Above the threshold, $\varepsilon > \varepsilon_{th}(k_1)$, it is zero and below, $\varepsilon < \varepsilon_{th}(k)$, it is a power-law singularity close to the threshold with the exponent $\alpha(k_1)$ that generally depends on the position of the cut k_1.

phenomenologically [34] as a heavy impurity at a fixed momentum, which takes the excitations along the edge with arbitrary curvature up to higher energy—see the red line in Fig. 1.3(a), coupled to the Luttinger liquid modes at low energy, which describe the excitations just above (in the particle sector) or below (in the hole sector) the spectral edge. The coupling is of the density-density type conserving the occupation number of the heavy impurity that restricts the validity of this model to higher energy, where the process of absorption or emission of the heavy impurity by the Luttinger liquid modes is forbidden by a large energy barrier[4].

The two unknown coupling constant between the mobile impurity and the pair of the canonically conjugated variables of the Tomonaga-Luttinger model in Eq. (1.2) can be fixed phenomenologically considering physical properties of the hybrid system. One is the translation invariance of the couple model and the other is an observable that corresponds to the change of the total energy with respect long-range variations of the density. Thus, only one addition parameter in the nonlinear Luttinger liquid theory, on top of v and K of the linear theory in one dimension, is the dispersion of the spectral threshold $\varepsilon_{th}(k)$, represented by the red line in Fig.

[4]Unlike in the x-ray problem, heavy impurity in the non-linear Luttinger theory has to be mobile (so-called mobile impurity model) since the spectral threshold extends long all momenta.

1.3(a), that enters as the single particles dispersion of the mobile impurity

$$H_{nLL} = H_{TL} + \int dx \left[\left(V_\theta \nabla\theta + V_\varphi \nabla\varphi \right) d^\dagger d + d^\dagger \left(\varepsilon_{th}\left(k\right) - i \frac{\partial \varepsilon_{th}\left(k\right)}{\partial k} \partial_x \right) d \right], \quad (1.3)$$

where d is the fermionic operator of the mobile impurity that depends on the spatial coordinate $d \equiv d\left(x\right)$, the coupling constants are $V_\theta = \partial_k \varepsilon_{th}\left(k\right) - k/m$ and $V_\varphi = \partial_\rho \varepsilon\left(k\right) + \pi v/K$, ρ is the particle density, and H_{TL} is the Tomonaga-Luttinger model in Eq. (1.2). Then, owing to the quadratic in the bosonic operators structure of H_{TL}, the observables in the nonlinear Luttinger theory given by the model in Eq. (1.3) can be calculated using again the conformal field theory, after the coupling between the mobile impurity and the hydrodynamic modes eliminated via a unitary rotation, relating expectation value to the dispersion of the spectral threshold and the Luttinger parameters. For instance, this gives power-law singularities around the threshold in the dynamic response function in a wide energy range, see Fig. 1.3(b), and relates the corresponding exponents to the derivatives of $\varepsilon_{th}\left(k\right)$, v, and K. This behaviour is very different from just gradually disappearing quasiparticle lifetime in the Fermi liquid theory in higher dimensions in Fig. 1.1(b).

Being constructed phenomenologically, the nonlinear Luttinger liquid theory is universal in the sense that it is applicable to all types of interacting models in one dimension: fermionic, bosonic, and spin. It also breaks the low energy restriction of the Tomonaga-Luttinger model, strictly imposed by the linearisation condition around the Fermi point. At the same time the nonlinear Luttinger liquid theory leaves the problem of calculating the dispersion of the spectral edges in an interacting system $\varepsilon_{th}\left(k\right)$ open. It is also only the first example of an interacting theory beyond the low energy limit in one dimension, which is however still restricted to the proximity of the spectral edges. A broader question remains open: what is the general theory of interacting systems at high energy that is not restricted to a particular class of many-body excitations in one-dimension?

In this introduction to six papers [35–40], reprinted in the appendix, the answers to both of these questions are discussed in the form of explicit calculation of the dispersion for the spectral threshold and a new theory at high energy–hierarchy of modes–that is not restricted to the proximity of the spectral edges, as well as a few experiments confirming these theoretical predictions. Here we will also discuss an application of the new high energy theory to the problem of magnetoelasticity in one dimension.

The fundamental models of Fermi and Bose particles with short-range interaction (with and without spin) in one dimension can be analysed using the available exact diagonalisation method of Bethe ansatz [41]. While this approach is completely free of approximations and it does provide the full microscopic information about the exponentially large continuum of the many-body states at all energy scales, it makes calculation of observables very difficult in practice, especially the ones that still involve the many-body matrix elements, due to a huge mathematical complexity. The problem of evaluating energy of the lowest (in the particle sector) and the highest (in the hole sector) energy states for a fixed momentum, which form the

dispersion of the spectral edge modes $\varepsilon_{th}(k)$ and require solving only the eigenvalue problem for a polynomial number of states, is still feasible in the thermodynamic limit [35, 36]. It gives an empirical model for the dispersion with only one free parameter–effective mass m^*,

$$\varepsilon_{th}(k) = \mu + \frac{k_F^2}{2m^*} \pm \frac{(k-k_0)^2}{2m^*}, \tag{1.4}$$

where $\pm$ refers to the particle/hole sector, see Fig. 1.3(a), $k_0 = 0\,(k_F)$ for fermions (bosons), and μ is the chemical potential. Here the concept of effective mass is introduced at all energy scales that reduces to the renormalised velocity $v = k_F/m^*$ of the Tomonaga-Luttinger model at low energy. Thus, m^* can be defined using only the already existing low energy Luttinger parameter v in addition to the original mass of the free particles as $m^* = Km$ for spinless particles and $m^* = K_\sigma m$ in the spinful case. This result is exact for spinless particles and non-parabolic deviations are small but still finite for particles with spin [36]. In combination with Eq. (1.4) the nonlinear Luttinger theory gives full description of the high energy modes around the spectral edges in terms of only two Luttinger parameters v and K defined at low energy, e.g. it gives an explicit dependence of the threshold exponent α on k, see Fig. 1.3(b), in term of only v and K.

Away from the spectral edges the nonlinear Luttinger liquid theory becomes inapplicable. However, also away from low energy, a different structure emerges–the exponentially huge continuum of the many-body excitations splits itself into a hierarchy of levels formed by only polynomial number of excitations, separated by powers of the small parameter $\mathcal{R}^2/L^2$ in their spectral power, where $\mathcal{R}$ is the interaction radius and L is the length of the system [37, 38]. Thus, only small numbers of excitations in a representative region on the energy-momentum plane accumulate the principle amplitude of a particular observable. This allows analytical calculations in the thermodynamic limit that are not restricted to the proximity of the spectral edges. For instance, for spinless fermions the two strongest excitations, with $\mathcal{R}^2/L^2$ to the zeroth power, form a single particles-like (parabolic) dispersion with a renormalised mass in the spectral function and the second-level, with $\mathcal{R}^2/L^2$ to the first power, produce an inverse power-law line shape to the principle parabola. In the hole sector, where the strongest excitations are on the spectral edge, see the red line between the points $\pm k_F$ in Fig. 1.3(a), the low energy side of this line shape is the threshold singularity calculated by the nonlinear Luttinger theory and the exponent $\alpha(k)$ is the same as predicted by the model in Eq. (1.3).

At low energy the hierarchy of modes crosses over into the linear Luttinger liquid that can be illustrated using the local density of states $n(\varepsilon)$. At high energy the main contribution is accumulated by the principal parabola (the strongest level for this observable) giving the inverse square root functional behaviour, $n(\varepsilon) \sim 1/\sqrt{\varepsilon}$, like for a free system, where the interactions only renormalise the prefactor. At low energy the Tomonaga-Luttinger model predicts that $n(\varepsilon)$ is suppressed at the Fermi energy as a power-law, $n(\varepsilon) \sim |\varepsilon - E_F|^\beta$ where the exponent β depends on the Luttinger parameter K [23]. This signals a breakdown of the hierarchy of

modes, which predicts a finite $n(\varepsilon) \sim 1/\sqrt{E_F}$, at low energy. Thus, the Tomonaga-Luttinger model becomes the relevant theory, in which all of the many-body modes form hydrodynamic excitations in the linear regime, marked by green circles in Fig. 1.3(a), in which Lorentz invariance is dominant. However, the further we go into the non-linear region the more important becomes the nonlinearity, reducing Lorentz invariance to Galilean and making the hierarchy of modes the relevant theory at high energy. The border between the two regimes is of the crossover type that can be established via the Bethe ansatz approach, which is valid at all energy scales—see [38] for details.

Hierarchy of interacting modes has already been applied to the many-body theory of magnetoelasticity in one dimension. In a spin chain, the atoms that hosts the spins can move around their equilibrium positions changing the exchange energy between the neighbours. This is the microscopic mechanism for coupling magnetic excitations of the Heisenberg model with the phonons that are formed by motion of the atoms in the chain. The magnetic energy scale characterised by the exchange energy is usually much smaller than the phononic energy scale characterised by the Debye's energy, making the interaction between the two subsystems perturbative. The renormalisation of the mechanical properties, e.g. change of the velocity of the acoustic mode, is given by the next-neighbour correlation function of the spins, which can be related only to the ground states energy of the Heisenberg model in one dimension, which is a well-established quantity [41].

There is also another process in the microscopic theory—attenuation of the phonons, which is a bit more complicated. The resonance decay into the many-body excitations of the spin chain is always possible due to a continuum of their excitations, see the grey area in Fig. 1.3(a), but is very slow since the relevant high-energy excitations belong to the second level of the hierarchy so that the transition amplitude, $\sim 1/L^4$, vanishes in the thermodynamic limit. The main mechanism is then hybridisation of a single phonon with a continuum of the many-body magnetic excitations. While the degree of hybridisation with one many-body state is tiny, the sum over a polynomial number of these second-level excitations compensates for this smallness remaining finite in the thermodynamic limit. And the contribution of the third- and higher-level excitations become already small, i.e. their contribution also vanishes in the thermodynamic limit, which is a manifestation of the hierarchy of modes in this theory [40]. The magnetic field dependence of the phononic attenuation is an observable that can be probed directly, e.g. in ultrasound experiments in anisotropic magnetic insulators.

Experiments on probing the high energy regime are already ongoing in fermionic realisations of interacting one-dimensional systems [38, 39]. In a double-well heterostructure, the two-dimensional electron gas in the bottom layer has a well defined Fermi energy (a Fermi liquid) that serves as a good probe of the quantum wires formed in the top layer by potential gates, see the sketch in the top-left inset in Fig. 1.4(a). A current through such a system adds or removes an electron from the wire, depending on the sign of the bias applied between the two layers V_{dc}, measuring the spectral function of the one-dimensional electronic system. A variable in amplitude

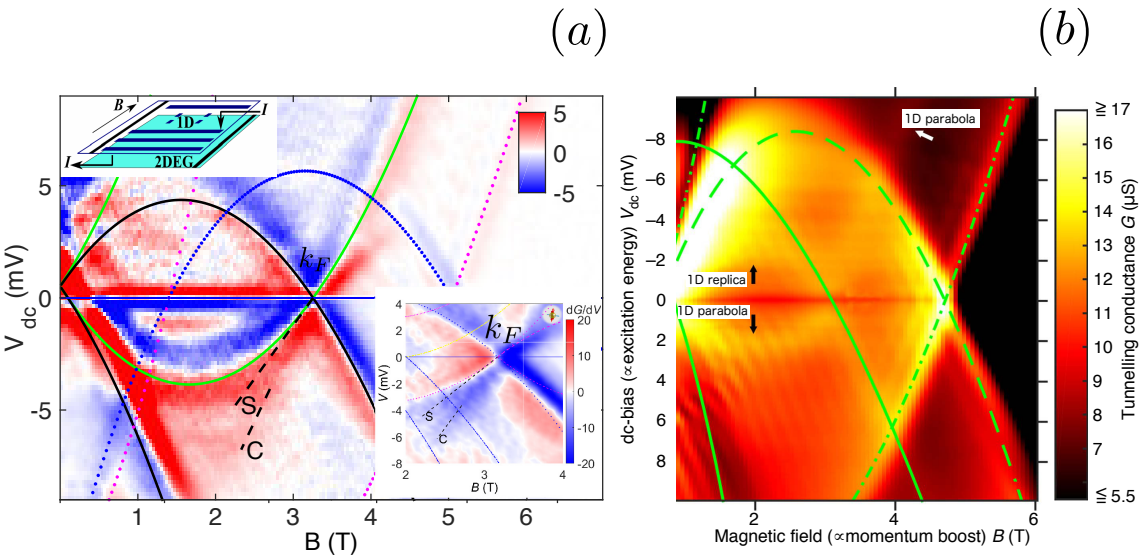

Figure 1.4: (a) Conductance through a double-well heterostructure with quantum wires of length $L = 10\mu$m, see details in the text. In the linear regime around k_F it shows two different velocities, spin-charge separation—see a zoom-in in the bottom-right inset. The solid green parabola marks the strongest excitations of the one-dimensional system. All other lines mark parasitic signals coming from different parts of the sample and from two-dimensional dispersion probed by the one-dimensional system. The figure is taken from Ref. [38]. (b) The same experiment as in (a) but the wires are shorter, $L = 1\mu$m. All lines mark parasitic signals. In addition to the principal one-dimensional parabola, a one-dimensional replica formed by subleading excitation is observed; marked by arrows. The figure is taken from Ref. [39].

magnetic field applied perpendicular to the wires (B) gives a momentum resolution by changing the projection of the electron momentum parallel to the wire in a controllable way. A transport measurement through such a structure as a function of B and V_{dc} probes directly the spectral function as a function of momentum and energy $A(k, \varepsilon)$, see details in [28].

At low energy the already known spin-charge separation—a Luttinger liquid effect—is observed, see the bottom-left inset in Fig. 1.4(a). Fitting of the charge and the spin velocities gives the ration $v_\rho/v_\sigma = 1.4 \div 1.8$. The existence of two objects with different linear dispersions (that is absent in the Fermi liquid theory but is predicted for Luttinger liquids) confirms that the interactions in the one-dimension electronic system are appreciable and this ration between the velocities gives the ration between the interaction and the kinetic energies of the order of one. At high energy there is only a single parabola—formed by the leading order excitations—in long wire (of length about $L = 10\mu$m), see the main figure in Fig. 1.4(a). An estimate of the amplitude of the first subleading modes gives four orders of magnitude ($\lambda_F^2/L^2 \sim 10^4$ where λ_F was used as an estimate for the screening

radius $\mathcal{R}$) suppression with respect to the amplitude of the observable leading mode, reducing the amplitude of the subleading modes at least an order of magnitude below the noise floor of this experiment. In shorter wires (of length about $L = 1\mu$m) the suppression $\lambda_F^2/L^2 \sim 10^2$ becomes two order of magnitude weaker making the first subleading mode (a replica of the principal parabola in the particle sector) observable, see Fig. 1.4(b), thus, experimentally confirming the existence of the small parameter $\mathcal{R}^2/L^2$ at high energy in a one-dimensional interacting system.

The remainder of the introduction is organised as follows. Chapter 2 contains a derivation of the Tomonaga-Luttinger model and a brief account of the observables evaluated within this model. This low energy theory of interactions is well-developed in the literature and is confirmed quite comprehensively in experiments. Thus, it can serve as a good reference point to any further developments in one dimension. Section 2.1 describes the bosonisation technique in one dimension that will be used in Sections 2.2 and 2.3 and will be needed in Chapter 3 in the non-linear Luttinger liquid theory. A derivation of the local density of states within the Tomonaga-Luttinger model is given in Section 2.2. This quantity is used to demonstrate the crossover from the hierarchy of modes at high energy to the Luttinger liquid behaviour at low energy in papers [37, 38]. In Section 2.3, the spin-charge separation effect is derived for the spinful model with short range interactions using the bosonisation approach. The ratio of the velocities of the charge to the spin modes is used as a gauge of the interaction strength in the experiment on transport spectroscopy that measures a one dimensional spectral function at all energy scales [39].

A summary of the mobile impurity model and its main prediction—power-law singularities at the spectral threshold—is presented in Chapter 3. In Section 3.1, a phenomenological construction of the model is given by extending the notion of Luttinger liquids beyond the linear region and low energy. This only new quantity needed for the non-linear model is dispersion of the spectral edge at high energies. A calculation of the power-laws around the spectral edges is given in terms of the curvature of this dispersion and the low energy parameters v and K. This dispersion is evaluated microscopically in the papers [35, 36] for the all principal models with short range interactions in one dimension in terms of only the Luttinger parameter K and the free particle mass. In conjunction with the mobile impurity model result, it reduces the dependencies of the threshold exponents to only the momentum in the non-linear region and the Luttinger parameters from low energy. These expressions for the spinless and spinful fermion cases are obtained in Section 3.2.

Details of the microscopic Bethe ansatz technique are given in Chapter 4. This is an exact diagonalisation tools that is applicable to a wide range of systems with short range interactions in one dimension. In Section 4.1, a derivation of the Bethe ansatz equations is given, using the XXZ model as an example, which reduces the exponential complexity of diagonalising a many-body Hamiltonian to solving only a system of N non-linear equation, where N is the number of particles. A construction of the algebraic representation of Bethe ansatz is given in Section 4.2. This approach is an essential tool enabling evaluation of the matrix elements, generally needed for the observables, for a large number of particles. Both technique are used as a work

horse in the papers [35, 36] for evaluating the dispersion of the spectral threshold, for identifying the hierarchy of modes at high energy and for studying its crossover to the Luttinger liquid physics in low energy in the papers [37, 38], and for constructing the many-body theory of magnetoelasticity in the paper [40].

An introduction to magnetoelasticity is given in Chapter 5. The microscopic origin of the magneto-elastic coupling is discussed in Section 5.1 and experimentally accessible observables in this class of systems in one dimension are summarised in Section 5.2. This chapter also serves as an extended introduction to the paper [40]. Finally, concluding remarks are given in Chapter 6.

Chapter 2

Low energies

This chapter contains a review of the Luttiger liquid theory. It starts from the linear approximation to the interacting model of spinless fermions. Then, the bosonic degrees of freedom are introduced via a rotation in Fock space and it is shown that in these variables the interacting model is diagonal. The usual form of the Tomonaga-Luttiger model is finally given in term of the canonically conjugated fields θ and φ that are superpositions of the bosonic operators. A more convenient tool for calculating the expectation values is the conformal field theory since the model is quadratic in bosons. In Section 2.2 we will present a calculation of the correlation function and the local density of states. Finally, we will bosonise the model of spinful fermions with density-density interaction and show that the resulting pair of Tomonaga-Luttinger models for the spin and charge degrees of freedom have different velocities explicitly in Section 2.3. In this chapter we will use the notations of the book [23].

Let us start from the model of interacting spinless fermions,

$$H = \sum_k \varepsilon_k c_k^\dagger c_k + \sum_q \frac{V_q}{2L} \rho(q)\, \rho(-q)\,, \tag{2.1}$$

where

$$\varepsilon_k = \frac{k^2}{2m} \tag{2.2}$$

is the parabolic dispersion, the c_k operators obey the Fermi commutation relations

$$\left\{ c_k, c_{k'}^\dagger \right\} = \delta_{kk'}, \tag{2.3}$$

the Fourier transform of the density operator is

$$\rho(q) = \sum_k c_{k+q}^\dagger c_k, \tag{2.4}$$

V_q is the Fourier transform of the two-body interaction potential, and we assume $\hbar = 1$.

Close to the Fermi energy the spectrum is almost linear so it can be linearised

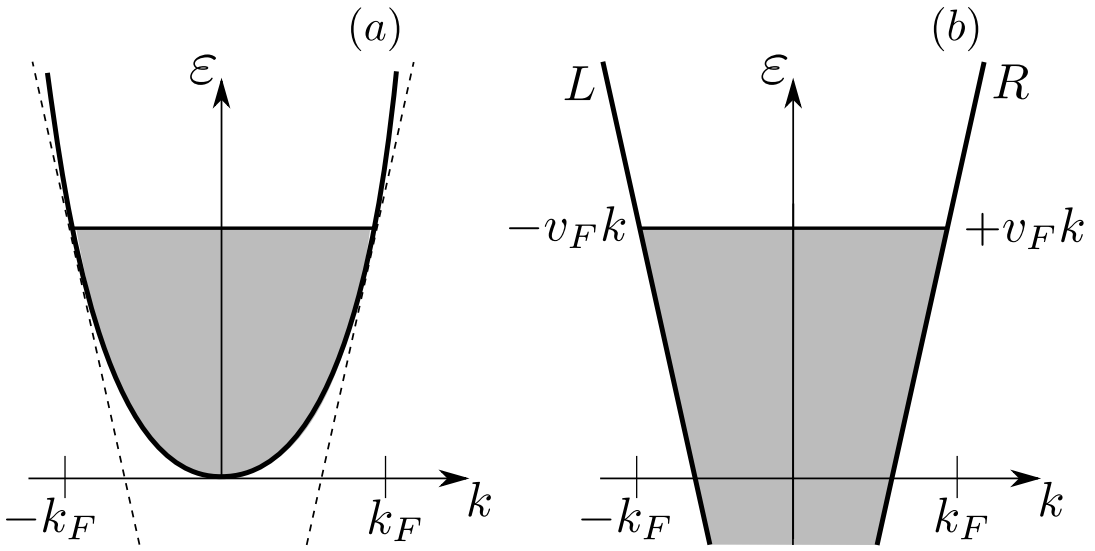

Figure 2.1: (a) The model of fermions with a parabolic dispersion in one dimension in free space. The single particles states up to a Fermi energy are filled (grey region) and the states above the Fermi energy are empty (white region). The dashed lines are the linearised dispersion at the two Fermi points $\pm k_F$. (b) The model with linearised dispersion that splits the electrons into two subbands: the left (L) and the right (R) movers with the velocities $\pm v_F$. Each subband is extended to infinite number of negative states.

explicitly in the model in Eq. (2.1). Since there are only two Fermi point ($\pm k_F$) in one dimension this procedure introduces two subbands,

$$\varepsilon_k \approx \epsilon_{L,R} v_F k \tag{2.5}$$

where $v_F = p_F/m$, that represent the left movers (L) with $\epsilon_L = -1$ and the right movers (R) with $\epsilon_R = 1$, see Fig. 2.1(b). Substitution of Eq. (2.5) into Eq. (2.1) gives

$$H = \sum_{k,r=L,R} v_F \left(\epsilon_r k - k_F\right) c_k^\dagger c_k + \sum_q \frac{V_q}{2L} \rho\left(q\right) \rho\left(-q\right), \tag{2.6}$$

where the Fermi energy was already subtracted from the Hamiltonian.

Although, at high energy the models in Eq. (2.1) and Eq. (2.6) are very different, see Fig. 2.1, at low energy they are almost the same making their observable at low energy also almost the same. The models in Eq. (2.6) however is much easier to analyse due to purely linear spectrum of the single particle excitations that increases the symmetry from Galelian to Lorentzian, making the energy and the momentum conservation laws the same. In the following section we review the analysis of model in Eq. (2.6) extending k to $\pm\infty$ and forgetting about the curvature of the original dispersion completely.

E	0	1	2	3	
Fermions	$\|110000\dots\rangle_F$	$\|101000\dots\rangle_F$	$\|011000\dots\rangle_F$ $\|100100\dots\rangle_F$	$\|010100\dots\rangle_F$ $\|100010\dots\rangle_F$	
Bosons	$\|00\rangle_B$	$\|10\rangle_B$	$\|01\rangle_B$ $\|20\rangle_B$	$\|11\rangle_B$ $\|30\rangle_B$	

Table 2.1: The correspondence between the electron-hole pair excitations in a fermionic system with a linear dispersion and bosonic excitations with the same dispersion for $N = 2$ fermionic particles and up to the energy $E = 3$.

2.1 Bosonisation

Before mapping the fermionic degrees of freedom in Eq. (2.6) onto bosons, it is convenient to split the linear Hamiltonian into the free part

$$H_0 = \sum_{k,r=L,R} v_F \left(\epsilon_r k - k_F\right) c_{kr}^\dagger c_{kr} \tag{2.7}$$

and the interaction part

$$H_{int} = \sum_q \frac{V_q}{2L} \rho\left(q\right) \rho\left(-q\right). \tag{2.8}$$

Then, let us deal with H_0 first.

The linear spectrum in Eq. (2.7) has equidistant level spacing reminding of a single bosonic level, which can be populated with one, two, three, and so on excitations producing the same spectrum. At a more detailed level, it is not a single fermion that can be represented as a bosonic excitation in a many-particle system but an electron-hole pair on top of the Fermi sea; its total spin is even (zero) like that of a boson. In order to visualise the structure of the many-body spectrum of free particles, let us consider a simple example of a Fermi sea consisting of only $N = 1$ fermion, see Fig. 2.2(a). There is only one electron-hole pair with possible momentum $k = 1, 2, 3, \dots$, see an illustration in Fig. 2.2(b). This spectrum corresponds to the spectrum of the bosonic Hamiltonian[1] $H = \sum_{k=0}^{\infty} k b_k^\dagger b_k$ under the constraint that the total number of bosons is $N = 1$. Starting from the Fermi sea with $N = 2$ fermions, there is only one electron-hole pair excitation at the lowest energy $E = 1$ with $k = 1$. There are two excitations with $E = 2$, two excitations with $E = 3$, and so on. The correspondence between the fermionic $|1_1, 1_2, 0_3, \dots\rangle_F = c_1^\dagger c_2^\dagger \cdots |0\rangle$ and the bosonic $|n_1, n_2, \dots\rangle_B = \left(b_1^\dagger\right)^{n_1} \left(b_2^\dagger\right)^{n_2} \cdots |0\rangle$ states (where $|0\rangle$ is the vacuum state) up to the energy $E = 3$ is given in Table. 2.1. The degeneracies coincide as well thus this is also the spectrum of the same bosonic

[1] We consider only one branch ($\epsilon_R = 1$) in the model in Eq. (2.7) and assume that $v_F = 1$ and $k = 0, 1, 2, \dots$ for illustrative purposes here.

Hamiltonian $H = \sum_{k=0}^{\infty} k b_k^\dagger b_k$ for $N = 2$ bosons. A rigorous proof of completeness of the Fock space under the Bose-Fermi mapping for arbitrary N is given in [42].

A formal change of variables can be introduced by constructing bosonic operators out of the fermionic density operator in the momentum space in Eq. (2.4), which creates electron-hole pairs, in the following way

$$\begin{aligned} b_{pr}^\dagger &= i\sqrt{\frac{2\pi}{L\,|p|}}\rho_{pr}^\dagger \\ &= i\sqrt{\frac{2\pi}{L\,|p|}}\sum_k c_{k+p,r}^\dagger c_{kr}, \qquad (2.9) \\ b_{pr} &= -i\sqrt{\frac{2\pi}{L\,|p|}}\rho_{pr} \\ &= -i\sqrt{\frac{2\pi}{L\,|p|}}\sum_k c_{k-p,r}^\dagger c_{kr}. \qquad (2.10) \end{aligned}$$

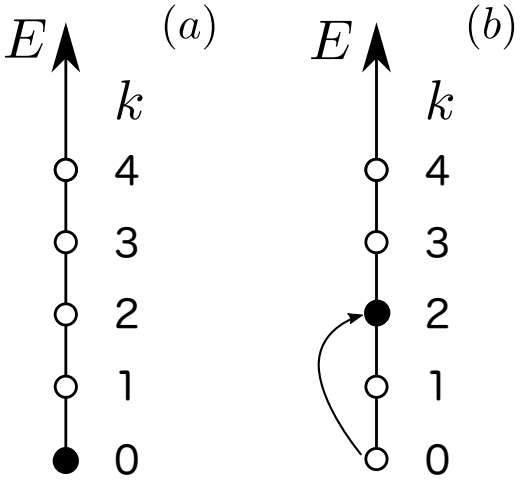

Figure 2.2: States of a fermionic system with a linear spectrum for $N = 1$: (a) the ground state $|10000\ldots\rangle_F$ and (b) an electron-hole pair $|00100\ldots\rangle_F$.

These bosonic operators immediately commute when the band index r is different, $\left[b_{pR}, b_{pL}^\dagger\right] = 0$. Within the same subband commutation relations encounter a divergence that needs to regularised first. It is caused by extension of the linearised spectrum to $-\infty$, see Fig. 2.1(b), that creates formally an infinite number of occupied states at negative energies. The common way of handling this problem is by introducing normal ordering,

$$: AB := AB - \langle 0\,|AB|\,0\rangle\,, \qquad (2.11)$$

where the average of over the ground state, $\langle 0\,|\ldots|\,0\rangle$, is subtracted from the operators. This is the only property of the normal ordering that is needed in the present context. For instance, application of the rule in Eq. (2.11) to the fermionic operators Eqs. (2.9,2.10) gives

$$: c_{k\pm p,r}^\dagger c_{pr} := \begin{cases} c_{k\pm p,r}^\dagger c_{kr}, & p \neq 0, \\ c_{kr}^\dagger c_{kr} - \left\langle 0 \left| c_{kr}^\dagger c_{kr} \right| 0 \right\rangle, & p = 0. \end{cases} \qquad (2.12)$$

The commutator between the bosonic operators within the same subband eval-

uates as

$$\begin{aligned}\left[b_{pr}, b^{\dagger}_{p'r}\right] &= \frac{2\pi}{L\sqrt{|p|\,|p'|}}\sum_{k}\left(c^{\dagger}_{k+p-p',r}c_{kr} - c^{\dagger}_{k+p,r}c_{k+p',r}\right)\\ &= \frac{2\pi}{L\,|p|}\delta_{pp'}\sum_{k}\Bigg(:c^{\dagger}_{kr}c_{kr} - c^{\dagger}_{k+p,r}c_{k+p,r}:\\ &\quad + \left\langle 0\left|c^{\dagger}_{kr}c_{kr} - c^{\dagger}_{k+p,r}c_{k+p,r}\right|0\right\rangle\Bigg)\\ &= \delta_{pp'}. \end{aligned} \tag{2.13}$$

When $p \neq p'$ in the first line of the above expression, the momentum k in the first term under the sum can be shifted as $k \to k-p$ and is canceled by the second term, resulting in zero for the whole sum, i.e. in $\delta_{pp'}$ in the second line. When $p = p'$, the shift in k becomes trickier. A way to clarify it is by introducing the normal ordering in the second line of the above expression using Eq. (2.12). Then, the two parts of the normal ordered term cancel each other under the shift of $k \to k+p$ in the first part. And the second term with the expectation values evaluates as

$$\frac{2\pi}{Lp}\left(\sum_{k=-\infty}^{0} 1 - \sum_{k=-\infty}^{-p} 1\right) = \frac{2\pi}{Lp}\frac{Lp}{2\pi} = 1, \tag{2.14}$$

where 1 is the expectation value of the filled fermionic states, producing the bosonic commutation relation between the operators defined in Eqs. (2.9,2.10)

$$\left[b_{pr}, b^{\dagger}_{p'r'}\right] = \delta_{pp'}\delta_{rr'}. \tag{2.15}$$

Now, the free model in terms of the original fermionic degrees of freedom in Eq. (2.7) has to be mapped to the bosonic representation in Eqs. (2.9,2.10). Instead of solving the inverse problem of expressing the fermionic operators through the bosonic operators explicitly, it is more convenient to commute the b_{pr} with H_0 using the fermionic commutation rules,

$$\begin{aligned}[b_{pr}, H_0] &= -i\sqrt{\frac{2\pi}{L\,|p|}}\sum_{r'kk'}\left[c^{\dagger}_{k-p,r}c_{kr}, v_F\left(\epsilon_{r'}k' - k_F\right)c^{\dagger}_{k'r'}c_{k'r'}\right]\\ &= -i\sqrt{\frac{2\pi}{L\,|p|}}v_F\epsilon_r\,|p|\sum_{k} c^{\dagger}_{k-p,r}c_{kr}\\ &= v_F\epsilon_r\,|p|\,b_{pr}. \end{aligned} \tag{2.16}$$

The commutator of the bosonic creation operators is done in the same way giving $\left[b^{\dagger}_{pr}, H_0\right] = v_F\epsilon_r\,|p|\,b^{\dagger}_{pr}$.

The number of electron hole-pairs operator can be introduced as follows,

$$N_r = \sum_k \left(c_{kr}^\dagger c_{kr} - \left\langle 0 \left| c_{kr}^\dagger c_{kr} \right| 0 \right\rangle \right), \tag{2.17}$$

where the average $\langle 0 | \ldots | 0 \rangle$ is again taken with respect to the ground state. Since this operator commutes with the Hamiltonian, $[H_0, N_r] = 0$, we can evaluate an expectation value of H_0 with respect to a state with a fixed value of $\langle N_r \rangle = n_r$,

$$\langle n_r | H_0 | n_r \rangle = \frac{2\pi v_F}{L} \sum_{q=1}^{n_r} q = \frac{\pi v_F}{L} n_r \left(n_r + 1 \right). \tag{2.18}$$

Here the electron-hole pairs are created around the Fermi energy. The only form that obeys Eq. (2.16) and Eq. (2.18) is

$$H_0 = \sum_{r,p\neq 0} \left(v_F |p| \, b_{pr}^\dagger b_{pr} + \frac{\pi v_F}{L} N_r^2 \right), \tag{2.19}$$

where we have already substructed the linear in N_r term since it is a conserved quantity of the model.

It is more convenient to use the bosonic model in terms of canonically conjugated variables rather than in the form of second quantisation in Eq. (2.19). The usual way of introducing coordinate-momentum variables is via a pair of fields in real space in terms of the bosonic operators,

$$\varphi(x) = -\left(N_R + N_L \right) \frac{\pi x}{L} - \frac{i\pi}{L} \sum_{p\neq 0} \sqrt{\frac{L|p|}{2\pi}} \frac{e^{-\alpha|p|/2 - ipx}}{p} \left[b_{pR}^\dagger + b_{-p,L}^\dagger \right] \tag{2.20}$$

and

$$\theta(x) = \left(N_R - N_L \right) \frac{\pi x}{L} - \frac{i\pi}{L} \sum_{p\neq 0} \sqrt{\frac{L|p|}{2\pi}} \frac{e^{-\alpha|p|/2 - ipx}}{|p|} \left[b_{pR}^\dagger - b_{-p,L}^\dagger \right], \tag{2.21}$$

where $Y(x) = 1$ for $x \geq 0$ and $Y(x) = 0$ for $x < 0$ is a step function and α is an arbitrary small parameter that is needed for regularisation. Strictly speaking the $\alpha \to 0$ limit has to be taken, but it is simpler for calculations to keep it finite that corresponds to having a finite bandwidth, $\omega_0 \sim 1/\alpha$, for the model. The commutation relation between these two fields can be evaluated using Eq. (2.15) as

$$\begin{aligned} \left[\varphi(x), \theta(x') \right] &= \sum_{p\neq 0} \frac{\pi}{Lp} e^{ip(x'-x) + \alpha|p|} \\ &= i \int_0^\infty \frac{dp}{p} \sin\left(p\left(x' - x \right) \right) e^{-\alpha|p|} \\ &= \frac{i\pi}{2} \mathrm{sign}\left(x' - x \right), \end{aligned} \tag{2.22}$$

where in the second line the continuum, $\sum_p 2\pi/L \to \int dp$, and the $\alpha \to 0$ limit were taken. Here $\mathrm{sign}(x) = 1$ for $x > 0$, $\mathrm{sign}(x) = -1$ for $x < 0$, and $\mathrm{sign}(0) = 1/2$ is the sign function. The derivative of the above equation with respect to x' gives almost the canonical commutation relation,

$$[\varphi(x), \nabla\theta(x')] = i\pi\delta(x' - x), \tag{2.23}$$

for φ and $\nabla\theta$. Thus, $\nabla\theta/\pi$ can be identified as the momentum and φ as the coordinate variable.

Gradients of φ and θ can be evaluated in terms of the density operators of the left and the right movers in the continuum limit as

$$\nabla\varphi(x) = -\pi(\rho_R(x) + \rho_L(x)), \tag{2.24}$$
$$\nabla\theta(x) = \pi(\rho_R(x) - \rho_L(x)), \tag{2.25}$$

where the real space densities are the Fourier transforms of Eqs. (2.9,2.10)

$$\rho_r(x) = \frac{1}{2\pi}\int dp e^{ipx}\rho_{pr}. \tag{2.26}$$

It gives $\nabla\varphi(x)$ as a sum of the densities of both subbands that can be interpreted as a total density fluctuation at point x and $\nabla\theta(x)$ is a difference in the number of the left and the right movers. Thus, it can be interpreted as the current operator. Finally, the free model in Eq. (2.19) can be written using Eqs. (2.20,2.21) as

$$H_0 = \frac{v_F}{2\pi}\int dx \left[(\nabla\theta)^2 + (\nabla\varphi)^2\right]. \tag{2.27}$$

The last step is mapping of the interaction part of the linear Hamiltonian in Eq. (2.8) onto the bosonic variables. The bosonic operators in Eqs. (2.9,2.10) are linear in densities. Therefore, the resulting form of H_{int} will also be a quadratic form in bosonic variables. This is a huge advantage of the bosonisation procedure that maps the whole interacting Hamiltonian that is quartic in the original fermionic operators onto a quadratic form in a bosonic operators that can be diagonalised trivially. This mapping holds for any interaction strength V, including the regions of intermediate and large values of V where there is no hope to apply the perturbation theory to free fermion in any form.[2] Instead of the momentum representation of H_{int} in Eq. (2.8), we will start from the real space representation,

$$H_{int} = \int dx dx' V(x - x')\rho(x)\rho(x'), \tag{2.28}$$

and consider only a short range interaction potential, $V(x - x') \approx V_0\delta(x - x')$. Finite range interactions potential can also be taken in account by a similar procedure but we restrict ourselves to the delta function for illustration purposes here.

[2] In one dimension perturbation theory in interactions produces logarithmic divergencies, unlike in two and three dimensions, so strictly speaking it is inapplicable even at small V.

The fermionic field operator in the real space can be split into a sum over two subbands consisting the left and right the movers, see visual representation of the bands in Fig. 2.2(b), as

$$\begin{aligned} \psi(x) &= \frac{1}{\sqrt{L}}\left[\sum_{-\Lambda<k-k_F<\Lambda} e^{ikx}c_k + \sum_{-\Lambda<k+k_F<\Lambda} e^{ikx}c_k\right] && (2.29)\\ &= \psi_L(x) + \psi_R(x)\,. && (2.30)\end{aligned}$$

where Λ is a momentum cutoff. The total density operator, $\rho(x) = \psi^\dagger(x)\,\psi(x)$, becomes

$$\rho(x) = \psi_L^\dagger(x)\,\psi_L(x) + \psi_R^\dagger(x)\,\psi_R(x) + \left[\psi_R^\dagger(x)\,\psi_L(x) + \psi_L^\dagger(x)\,\psi_R(x)\right]. \quad (2.31)$$

The first two terms here correspond to the scattering processes within the same subband that are responding to the density fluctuation at $q \sim 0$ and the last two terms are the scattering process between the two subbands at $q \sim 2k_F$. In a continuum model with a short range interaction only the first pair is responsible for the low energy excitations [43, 44]. Thus we keep only their contributions to the density fluctuations,

$$\rho(x) = \rho_L(x) + \rho_R(x)\,, \quad (2.32)$$

where the density operators for each subband can, in turn, be expressed in terms of the bosonic variables using Eqs. (2.9,2.10).

For the delta-functional interaction profile the interaction Hamiltonian depends only on one parameter, the interaction strength V_0,

$$H_{int} = V_0 \int dx \rho^2(x)\,, \quad (2.33)$$

where the density squared operator is split into the left and the right movers using Eq. (2.32) as

$$\rho(x)^2 = \rho_R^2(x) + \rho_L^2(x) + 2\rho_R(x)\,\rho_L(x)\,, \quad (2.34)$$

where the densities of different subbands commute with each other. Expressing the $\rho_r(x)$ operator in the bosonic language of φ and θ by means of the relations in Eqs. (2.24, 2.25) the contribution of the first two terms become

$$V_0 \int dx \rho_R(x)\,\rho_R(x) = \frac{V_0}{(2\pi)^2}\int dx\,(\nabla\varphi - \nabla\theta)^2 \quad (2.35)$$

and

$$V_0 \int dx \rho_L(x)\,\rho_L(x) = \frac{V_0}{(2\pi)^2}\int dx\,(\nabla\varphi + \nabla\theta)^2\,. \quad (2.36)$$

The contribution of the third term is obtained via the same procedure as

$$2V_0 \int dx \rho_L(x) \rho_R(x) = \frac{2V_0}{(2\pi)^2} \int dx \left[(\nabla\varphi)^2 - (\nabla\theta)^2 \right]. \tag{2.37}$$

Then, the interaction part of the Hamiltonian is the sum of all three contributions in Eqs. (2.35,2.36,2.37),

$$H_{int} = \frac{4V_0}{(2\pi)^2} \int dx (\nabla\varphi)^2. \tag{2.38}$$

The total Hamiltonian in terms of φ and θ is a sum of H_0 in Eq. (2.27) and H_{int} in Eq. (2.38),

$$H = \frac{v_F}{2\pi} \int dx (\nabla\theta)^2 + \left(\frac{v_F}{2\pi} + \frac{4V_0}{(2\pi)^2} \right) \int dx (\nabla\varphi)^2. \tag{2.39}$$

It is usually parameterised in terms of the Luttinger parameters v and K that are defined via the factors in front of the two terms above as

$$vK = v_F, \tag{2.40}$$

$$\frac{v}{K} = v_F \left(1 + \frac{2V_0}{\pi v_F} \right), \tag{2.41}$$

which can be solved immediately for v and K as

$$v = v_F \sqrt{1 + \frac{2V_0}{\pi v_F}}, \tag{2.42}$$

$$K = \frac{1}{\sqrt{1 + \frac{2V_0}{\pi v_F}}}. \tag{2.43}$$

Note that for a finite-range interaction, $V(x)$, the explicit expressions of Luttinger parameters in terms of microscopic interaction parameters will be different but the form of H in terms of φ and θ will stay the same. It is also instructive to note that Eq. (2.40) holds generally for all microscopic systems with Galilean invariance [45]. In terms of these parameters Eq. (2.39) reads as

$$H_{TL} = \frac{v}{2\pi} \int dx \left[K (\nabla\theta)^2 + \frac{1}{K} (\nabla\varphi)^2 \right]. \tag{2.44}$$

This is the celebrated Tomonaga-Luttiger model written in the commonly used form that was stated in the introduction in Eq. (1.2).

While the derivation here was performed starting from a specific microscopic model, the resulting Hamiltonian is generic for linear spectrum and arbitrary interactions, e.g. see the book in [23]. It is usual in the literature to start already from the Tomonaga-Luttinger model in Eq. (2.44), where v and K are arbitrary

parameters that contain all the relevant information about microscopic details of the specific underlaying model, without rederiving it every time. For fermionic systems $K < 1$ ($v > v_F$) for repulsive and $K > 1$ ($v < v_F$) for attractive interactions.

2.2 Correlation functions

The bosonised model in Eq. (2.19) in the second quantisation representation or in Eq. (2.44) in the representation of canonically conjugated variables is already diagonal in the bosonic degrees of freedom: its eigenvectors are single bosonic excitations. In terms of the original fermions, see Eq. (2.9), each bosonic excitation consists of many electron-hole pairs created at a given momentum that form (charge) density waves (CDW) on top of the Fermi ground state. Thus, it is also easier to evaluate observables as expectation values with respect to the effective free bosonic model, since the bosonic path integrals are easer to construct than the fermionic ones, in which anti-commuticity of the fermions complicate matters considerably [46]. Then, the well developed machinery of path integral can be used for practical calculations of the correlation functions. The only non-trivial task in this approach is expressing the original fermionic operators of the physical observables in terms of the bosonic degrees of freedom.

The form of the fermionic field operator for a single subband $\psi_r(x)$ can be assessed by means of a similar procedure to what has been used for establishing the form of the free Hamiltonian H_0, see in Eqs. (2.16,2.19). For $\psi_r(x)$, the density operator $\rho_r(x)$ needs to be commuting with the field operator for the same subband using their representations in terms of the fermionic operators in Eqs. (2.9,2.29) and the fermionic commutation rules,

$$\begin{aligned}\left[\rho_{pr}^{\dagger}, \psi_r\right] &= \frac{1}{\sqrt{L}} \sum_{kk'} e^{ik'x} \left[c_{k+p,r}^{\dagger} c_{kr}, c_{k',r}\right] \\ &= -e^{ipx} \psi_r(x) . \end{aligned} \tag{2.45}$$

The bosonic representation of the field operator then can be guessed as

$$\psi_r(x) \sim e^{\sum_p \frac{2\pi\epsilon_r}{pL} e^{ipx} \rho_{pr}} \tag{2.46}$$

that satisfy the same commutation rule in Eq. (2.45), which can be straightforwardly checked by using the bosonic commutation relation for ρ_{pr} and $\rho_{pr}^{\dagger}$ in Eq. (2.13).

The form in Eq. (2.45) is correct but, unfortunately, it still misses an essential part. It can be seen almost immediately since the field operator $\psi_r(x)$ changes the total number of particles in the system by destroying one. On the other hand the form in Eq. (2.45) conserves the number of particles since the density operator ρ_{pr} creates only electron-hole pairs. Therefore, the missing factor in the bosonic representation has to change the total number of fermions. These additional operators are the so-called 'Klein factors'. They commute with the bosonic operators and are introduced for each fermion species r as U_r. The full expression for the field operator

reads

$$\psi_r(x) = U_r e^{\sum_p \frac{2\pi\epsilon_r}{pL} e^{ipx} \rho_{pr}} \tag{2.47}$$

In the above expression, the operator U_r destroys the density uniformly, i.e. U_r is independent of x, and the exponential factor is responsible for the spatial dependence. Due to this factorisation only the exponential part is needed for calculating the correlation functions. Although the U_r operators are needed for the rigorous mapping between the fermions and the bosons [42, 47], they will not be introduced here since they will not be needed for the calculations in what follows. A detailed but a bit tedious construction of the Klein factors U_r and the exact fermionic to bosonic mapping is given, for example, in a good review in [9]. The usual form of the $\psi_r(x)$ operator in terms of the bosonic fields $\varphi(x)$ and $\theta(x)$ can be recovered by employing the definitions in Eqs. (2.24,2.25,2.26) from Eq. (2.47) as

$$\psi_r(x) = \frac{U_r}{\sqrt{2\pi\alpha}} e^{i\epsilon_r k_F x} e^{-i(\epsilon_r \varphi(x) - \theta(x))}, \tag{2.48}$$

where α is a small auxiliary variable that should be understood as a cutoff representing a finite bandwidth, like in the definitions of $\varphi(x)$ and $\theta(x)$ in Eqs. (2.20,2.21), and the $\alpha \to 0$ limit has to be taken in the final results.

Correlation function can be evaluated in a convenient way using the formalism of the functional integral. Here a detailed information to the technique will be omit and the reader is referred to the book in [48]. The notations of this book in the bosonic case will be followed below.

Let us start with Tomonaga-Luttinger model H_{TL} in Eq. (2.44) represented in terms of two canonically conjugated fields $\varphi(x)$ and $\Pi = \nabla\theta/\pi$ that satisfy the canonical commutation relation

$$[\psi(x), \Pi(x')] = i\delta(x - x'), \tag{2.49}$$

which is equivalent to Eq. (2.23). The partition function can be expressed via the following functional integral,

$$Z = \int D\varphi D\Pi e^{\int d\tau dx (i\Pi\partial_\tau\varphi - H_{TL})}, \tag{2.50}$$

where $\varphi \equiv \varphi(x,\tau)$ and $\Pi \equiv \Pi(x,\tau)$ and the function of coordinate x and imaginary time τ, $\int D\varphi$ means integration over all possible functions $\varphi(x,\tau)$, finite temperatures are considered thus the integral over τ is taken over a finite range $\int_0^\beta d\tau$, and β is the inverse temperature. Bosonic statistics of H_{TL} allows only the periodic boundary condition, $\varphi(x,\tau+\beta) = \varphi(x,\tau)$ [48]. The time-ordered correlation functions, involving a product of two operators $A(x,\tau)$ and $B(0,0)$, where the time evolution of an operator is given by the Hamiltonian,

$$A(\tau) = e^{\tau H} A(0) e^{-\tau H}, \tag{2.51}$$

can also be expressed via functional integral as

$$\langle TA(x,\tau)\,B(0,0)\rangle = \frac{1}{Z}\int D\varphi D\Pi A(x,\tau)\,B(0,0)\,e^{\int d\tau dx(i\Pi\partial_\tau\varphi - H_{TL})}, \tag{2.52}$$

where T is the time ordering operator and $A(x,\tau)$ and $B(0,0)$ depend on x and τ through the bosonic fields as $A(\varphi(x,\tau),\theta(x,\tau))$ and $B(\varphi(0,0),\theta(0,0))$. The functional integral representation automatically takes care of the time order in the right hand side of the above expression [48].

The common observable that describes dynamical properties of the system is the single-particle Green function. For the right movers subband it reads

$$\begin{aligned} G_R(x,\tau) &= -\left\langle T\psi_R(x,\tau)\,\psi_R^\dagger(0,0)\right\rangle \\ &= -\frac{e^{ik_Fx}}{2\pi\alpha}\left\langle Te^{i(\varphi(x,\tau)-\theta(x,\tau))}e^{-i(\varphi(0,0)-\theta(0,0))}\right\rangle \\ &= -\frac{e^{ik_Fx}}{2\pi\alpha}e^{-\frac{1}{2}\left\langle T[(\varphi(x,\tau)-\theta(x,\tau))-(\varphi(0,0)-\theta(0,0))]^2\right\rangle} \end{aligned} \tag{2.53}$$

where Eq. (2.48) was used to express $\psi_R(x)$ in terms of the field operators φ and θ. The third line was obtained from the second by means of the Debye-Waller relationship, which can be proved directly in the operator form [49]. Now the function integral in Eq. (2.52) can be used in order to evaluate the following correlation functions,

$$\begin{gathered} \left\langle T(\varphi(\mathbf{r})-\varphi(0))^2\right\rangle, \\ \left\langle T(\theta(\mathbf{r})-\theta(0))^2\right\rangle, \\ \langle T\theta(\mathbf{r})\,\varphi(0)\rangle, \end{gathered} \tag{2.54}$$

of the bosonic fields, where the short hand notations $\mathbf{r}=(x,\tau)$ in the real and $\mathbf{q}=(k,\omega)$ in the Fourier space for the calculations below were introduced.

Let us first evaluate the first line in Eq. (2.54) in the Fourier domain of the bosonic field. Introducing Fourier reprentation of the field $\varphi(\mathbf{r})$ as

$$\varphi(\mathbf{r}) = \frac{1}{\beta L}\sum_{\mathbf{q}}\varphi(\mathbf{q})\,e^{i\mathbf{q}\cdot\mathbf{r}}, \tag{2.55}$$

where $\varphi(\mathbf{q})$ is its Fourier component, the needed correlation function can be written as

$$\left\langle T(\varphi(\mathbf{r})-\varphi(0))^2\right\rangle = \frac{1}{(\beta L)^2}\sum_{\mathbf{q}_1\mathbf{q}_2}\langle T\varphi(\mathbf{q}_1)\,\varphi(\mathbf{q}_2)\rangle\left(e^{i\mathbf{q}_1\cdot\mathbf{r}}-1\right)\left(e^{i\mathbf{q}_2\cdot\mathbf{r}}-1\right), \tag{2.56}$$

where $e^{i\mathbf{q}\cdot\mathbf{r}} = e^{i(kx-\omega\tau)}$. The average in the momentum space has to be evaluated

using the function integral in Eq. (2.52) as

$$\langle T\varphi(\mathbf{q}_1)\,\varphi(\mathbf{q}_2)\rangle = \frac{1}{Z}\int D\varphi D\theta\varphi(\mathbf{q}_1)\,\varphi(\mathbf{q}_2)\,e^{-S}, \tag{2.57}$$

where the action given by Hamiltonian in Eq. (2.44) in the real space,

$$S = -\int d^2r\left[\frac{i}{\pi}\nabla\theta(\mathbf{r})\,\partial_\tau\varphi(\mathbf{r}) - \frac{1}{2\pi}\left(vK\left(\nabla\theta(\mathbf{r})\right)^2 + \frac{v}{K}\left(\nabla\varphi(\mathbf{r})\right)^2\right)\right], \tag{2.58}$$

has to be expressed in the momentum space as well. Using Eq. (2.55) and the corresponding expression for the other field $\theta(\mathbf{r})$, which is written in the absolutely the same way in terms of its Fourier components $\theta(\mathbf{q})$, the action reads

$$S = -\frac{1}{\beta L}\sum_{\mathbf{q}}\left[-\frac{ik\omega}{\pi}\varphi(\mathbf{q})\,\theta(-\mathbf{q}) - \frac{vK}{2\pi}k^2\theta(\mathbf{q})\,\theta(-\mathbf{q}) - \frac{vk^2}{2\pi K}\varphi(\mathbf{q})\,\varphi(-\mathbf{q})\right], \tag{2.59}$$

Note that Fourier components of the real fields φ and θ have the following property $\varphi(-\mathbf{q}) = \varphi^*(\mathbf{q})$ and $\theta(-\mathbf{q}) = \theta^*(\mathbf{q})$. Since the expression under the average does not depend on θ, the integration over θ is easier to do first. By completing the square of the θ part in the action,

$$S = -\frac{1}{\beta L}\sum_{\mathbf{q}}\left[-\frac{vK}{2\pi}k^2\left(\theta(\mathbf{q}) + \frac{i\omega\varphi(\mathbf{q})}{uKk}\right)\left(\theta(-\mathbf{q}) + \frac{i\omega\varphi(-\mathbf{q})}{uKk}\right) - \frac{\omega}{2\pi vK}\varphi(\mathbf{q})\,\varphi(-\mathbf{q}) - \frac{vk^2}{2\pi K}\varphi(\mathbf{q})\,\varphi(-\mathbf{q})\right], \tag{2.60}$$

the shifted field $\tilde{\theta}(\mathbf{q}) = \theta(\mathbf{q}) + \frac{i\omega\varphi(\mathbf{q})}{uKk}$ can be integrated as a Gaussian integral. The resulting factor cancels with the same in the denominator reducing Eq. (2.57) to an integral over only one field φ,

$$\langle T\varphi(\mathbf{q}_1)\,\varphi(\mathbf{q}_2)\rangle = \frac{1}{Z_\varphi}\int D\varphi\varphi(\mathbf{q}_1)\,\varphi(\mathbf{q}_2)\,e^{-S_\varphi}, \tag{2.61}$$

where the partition function, $Z_\varphi = \int D\varphi e^{-S_\varphi}$, and the reduced action is a function of φ field only,

$$S_\varphi = \frac{1}{\beta L}\sum_{\mathbf{q}}\frac{1}{2\pi K}\left[\frac{\omega}{v} + vk^2\right]\varphi^*(\mathbf{q})\,\varphi(\mathbf{q}). \tag{2.62}$$

The second Gaussian integral over φ finally gives

$$\langle T\varphi(\mathbf{q}_1)\,\varphi(\mathbf{q}_2)\rangle = \frac{\pi K\delta_{\mathbf{q}_1,\mathbf{q}_2}\beta L}{\frac{\omega^2}{v} + vk^2}. \tag{2.63}$$

Substitution of the above result into Eq. (2.56) gives the following real space

correlation function,

$$\begin{aligned}\left\langle T\left(\varphi\left(\mathbf{r}\right)-\varphi\left(0\right)\right)^{2}\right\rangle &= \frac{1}{\beta L}\sum_{\mathbf{q}}\frac{\pi K}{\frac{\omega^{2}}{v}+vk^{2}}\left(2-2\cos\left(\mathbf{q}\cdot\mathbf{r}\right)\right)\\ &= \frac{1}{\beta}\sum_{\omega}\int_{0}^{\infty}\frac{dk}{2\pi}\frac{\pi K}{\frac{\omega^{2}}{v}+vk^{2}}\left(1-\cos\left(kx+\omega\tau\right)\right)\end{aligned}$$

The thermodynamic limit of $L\to\infty$ was taken producing an integral over k in the second line of the above expression. In the zero temperature limit the summation over the bosonic Matsubara frequencies turns into an integral over the imaginary axis, $\sum_{\omega}/\beta\to\int d\omega/\left(2\pi\right)$ and the sum over energies can be evaluated explicitly, see [13] for details of the finite temperature technique, producing

$$\left\langle T\left(\varphi\left(\mathbf{r}\right)-\varphi\left(0\right)\right)^{2}\right\rangle = K\int_{0}^{\infty}\frac{dk}{k}\left(1-e^{-v|\tau|k}\cos\left(kx\right)\right). \tag{2.64}$$

This integral is diverged for large k demanding a regularisation. It can be done by inserting a factor of $e^{-\alpha k}$, where $\alpha>0$ is a small parameter, emulating a finite bandwidth. This results in a finite integral,

$$\begin{aligned}\left\langle T\left(\varphi\left(\mathbf{r}\right)-\varphi\left(0\right)\right)^{2}\right\rangle &= K\int_{0}^{\infty}\frac{dk}{k}e^{-\alpha k}\left(1-e^{-v|\tau|k}\cos\left(kx\right)\right)\\ &= \frac{K}{2}\ln\left(\frac{x^{2}+\left(v\left|\tau\right|+\alpha\right)^{2}}{\alpha^{2}}\right).\end{aligned} \tag{2.65}$$

The second correlation function in Eq. (2.54) can be obtained immediately from Eq. (2.65) using a symmetry of the model. The model in Eq. (2.44) is invariant under the change of $\varphi\to\theta$ and $K\to 1/K$. Performing this substitution in Eq. (2.65), we get

$$\left\langle T\left(\theta\left(\mathbf{r}\right)-\theta\left(0\right)\right)^{2}\right\rangle = \frac{1}{2K}\ln\left(\frac{x^{2}+\left(v\left|\tau\right|+\alpha\right)^{2}}{\alpha^{2}}\right). \tag{2.66}$$

Note that a finite α is still needed in order to have a finite expression here.

The third correlation function in Eq. (2.54) is calculated in a similar way in the Fourier domain. Analogously to Eq. (2.56) we write

$$\begin{aligned}\left\langle T\theta\left(\mathbf{r}\right)\varphi\left(0\right)\right\rangle &= \frac{1}{\left(\beta L\right)^{2}}\sum_{\mathbf{q}_{1}\mathbf{q}_{2}}\left\langle\varphi\left(\mathbf{q}_{1}\right)\theta\left(\mathbf{q}_{2}\right)\right\rangle e^{i\mathbf{q}_{1}\cdot\mathbf{r}}\\ &= -\frac{1}{\beta L}\sum_{\mathbf{q}}\frac{i\pi\omega k}{v^{2}+\omega^{2}/k^{2}}e^{i\mathbf{q}\cdot\mathbf{r}},\end{aligned} \tag{2.67}$$

where the expectation value was calculation following the same procedure as between Eq. (2.57) and Eq. (2.63). The summation over $\mathbf{q}$ turns into two integrals: one is a

result of the continuum limit for k and another is a result of the zero temperature limit for ω. It has to be noted before calculating of the remaining integrals that we have used the bosonic time-ordering in evaluation of the averages in Eqs. (2.54), which is defined as

$$\left\langle T\psi\left(x,\tau\right)\psi^{\dagger}\left(0,0\right)\right\rangle = Y\left(\tau\right)\left\langle \psi\left(x,\tau\right)\psi^{\dagger}\left(0,0\right)\right\rangle + Y\left(-\tau\right)\left\langle \psi^{\dagger}\left(0,0\right)\psi\left(x,\tau\right)\right\rangle , \quad (2.68)$$

where $Y\left(x\right)=1$ for $x\geq 0$ and $Y\left(x\right)=0$ for $x<0$ is a step function. However the original Green function in the first line in Eq. (2.53) is fermionic, which is defined by as

$$\left\langle T\psi\left(x,\tau\right)\psi^{\dagger}\left(0,0\right)\right\rangle = Y\left(\tau\right)\psi\left(x,\tau\right)\psi^{\dagger}\left(0,0\right) - Y\left(-\tau\right)\psi^{\dagger}\left(0,0\right)\psi\left(x,\tau\right). \quad (2.69)$$

The different sign in front of the second term in Eqs. (2.68,2.69) can be accounted for by multiplying the whole Green function by a factor of

$$e^{-i\pi Y(-\tau)\mathrm{sign}(x)}. \quad (2.70)$$

It will be absorbed third line in Eq. (2.54) as a shift of $-iY\left(-\tau\right)\mathrm{sign}\left(x\right)$ in Eq. (2.67), see also the whole exponent of the Green function in Eq. (2.53),

$$\begin{aligned}\left\langle T\theta\left(\mathbf{r}\right)\varphi\left(0\right)\right\rangle &= -i\int_{0}^{\infty}\frac{dk}{k}e^{-\alpha k-v\tau k\mathrm{sign}(\tau)-i\pi Y(-\tau)\mathrm{sign}(x)}\sin\left(kx\mathrm{sign}(\tau)\right)\\ &= -i\arg\left(v\tau+ix+\alpha\mathrm{sign}(\tau)\right), \quad (2.71)\end{aligned}$$

where in the first line the integral over the imaginary axis was already evaluated and the bandwidth cutoff α was already introduced in the same way as in Eq. (2.65). In the second line the last integral over k was evaluated.

Now, substitution of Eqs. (2.65,2.66,2.71) into Eq. (2.53) gives the zero temperature Green function of the right movers as

$$G_{R}\left(x,\tau\right) = -\frac{e^{ik_{F}x}}{2\pi\alpha}\left(\frac{\alpha^{2}}{x^{2}+\left(v\left|\tau\right|+\alpha\right)^{2}}\right)^{\frac{K+K^{-1}}{4}}e^{i\arg(v\tau+ix+\alpha\mathrm{sign}(\tau))}, \quad (2.72)$$

where the contribution of $\left\langle\theta\left(r\right)\varphi\left(r\right)\right\rangle$ and $\left\langle\theta\left(0\right)\varphi\left(0\right)\right\rangle$ to the exponent in Eq. (2.53) is zero. For a non-zero interaction strength $V_{0}\neq 0$ in Eq. (2.72) the Luttinger parameter $K\neq 1$ and the exponent in the two-point correlation function is a non-universal real number that depends on the interactions instead of the a universal exponent, which is a hallmark of the Luttinger liquid physics. The $K=1$ limit of Eq. (2.72) recovers the free Green function for fermionic particles with linear dispersion,

$$G_{R}\left(x,\tau\right) = -\frac{ie^{ik_{F}x}}{2\pi}\frac{1}{x+iv_{F}\tau+i\alpha\mathrm{sign}\left(\tau\right)}, \quad (2.73)$$

where for the free system $v=v_{F}$ according to Eq. (2.72), that can be calculated straightaway in the fermionic language starting from the model in Eq. (2.7). The

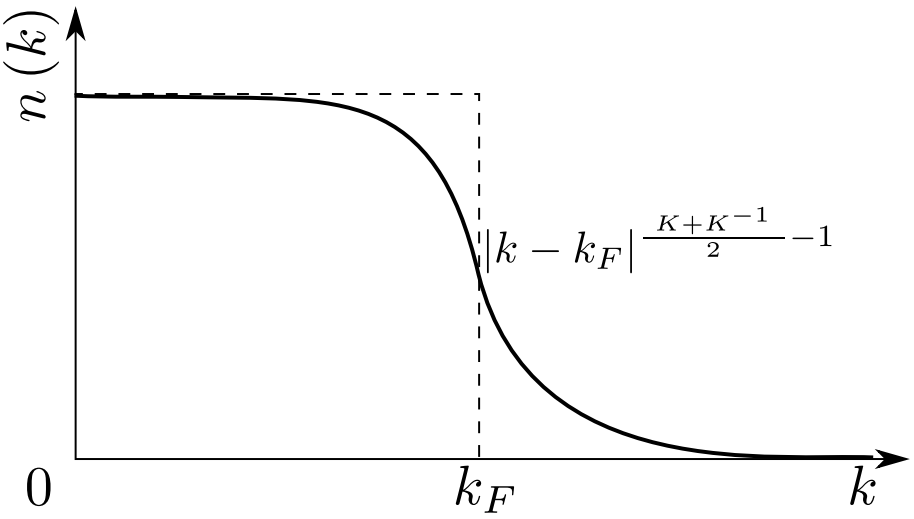

Figure 2.3: The occupation numbers $n(k)$from Eq. (2.74) as a function of the momentum k. At the Fermi momentum k_F it is continuous within the Luttinger liquid theory, being a power-law around k_F with the exponent $(K+K^{-1})/2-1$. This behaviour is qualitatively different from a discontinuity in two and three dimensions given by the Fermi liquid theory, see Fig. 1.1(a).

real-time Green function can be recovered by Wick rotation $\tau \to it$ in both Eqs. (2.72,2.73). At finite temperatures, the Green function can be evaluated in the same way but without taking the $\beta \to \infty$ limit in Eqs. (2.72,2.73).

Another correlation function that can be calculated using the bosonisation described in this Section is the occupation numbers n_k, an analog of the Fermi step in the Fermi liquid theory. Within the strongly-correlated theory it can be expressed directly using the two-point correlation function, see [13] for details of the definitions within the Green function language, that is already evaluated in this Section,

$$\begin{aligned} n(k) &= \int dx e^{-ikx} G_R(x, \tau = -0) \\ &= -\frac{1}{2\pi\alpha} \int dx e^{i(k_F-k)x} \left(\frac{\alpha^2}{x^2+\alpha^2}\right)^{\frac{K+K^{-1}}{4}} e^{i \arg(ix-\alpha)} \\ &\sim |k-k_F|^{\frac{K+K^{-1}}{2}-1}, \end{aligned} \tag{2.74}$$

where the zero temperature Green function from Eq. (2.72) is substituted in the second line and the third line is expanded in a Taylor series in a small $|k-k_F|$. Instead of a discontinuity at the k_F in two and three dimension, see Fig. 1.1(a) for the Fermi liquid result, in one dimension the height of the step is zero even at zero temperature signalling that, indeed, the individual Fermi-like quasiparticles do not survive. The occupation numbers in one dimension is a smooth function of k,

which behaves as a finite power-law around the k_F point, see Fig. 2.3. However, the position of k_F is not changed by the interactions even in one dimension due to the Luttinger's theorem.

The local density of states (LDOS) describes the tunnelling rate that is measured by a tip, that is brought in contact with the one dimensional system. This observable can be expressed again in terms of the two-point correlation function, see [13] for details, as

$$\begin{aligned} \rho\left(\varepsilon - E_F\right) &= -\frac{1}{\pi}\int dt e^{i(\varepsilon - E_F)t}\mathrm{Im}G_R\left(x=0,it\right) \\ &\sim \left|\varepsilon - E_F\right|^{\left(K+K^{-1}\right)/2-1}, \end{aligned} \tag{2.75}$$

where again the zero temperature Green function from Eq. (2.72) is substituted and the second line is expanded in a Taylor series in a small $|\varepsilon - E_F|$. Close to the Fermi energy the LDOS vanishes in a power-law fashion with a non-universal exponent $\left(K + K^{-1}\right)/2 - 1$ that depends on interaction strength V_0 through K given by Eq. (2.43). Note that $\rho\left(E_F\right) = 0$ does not mean that there are no states at the Fermi energy—the ground state of a Luttinger liquid is still gapless—but it means that the excitations around the Fermi energy are absolutely not single-particle like. The other dynamical correlation functions as well as static observables of Luttinger liquids can be evaluated in a similar way of doing bosonisation and integrating over the bosonic fields as described in this Section, see [23] for a good overview of the results.

2.3 Spin-charge separation

So far the spin degree of freedom of the fermionic particles was completely neglected. But fermions do have a non-zero (half-integer) spin, with the most important example being electrons—fermions with spin one-half. Since the wide relevance of this case for practical applications, it is instructive to consider it in detail. Instead of only one type of fermions on each subband of the left and the right movers, c_{kr} in Eq. (2.6), now there are two, c_{ksr}, where $s =\uparrow$ corresponds to electrons with spin up and $s =\downarrow$ to electrons with spin down. The fermion-to-boson mapping of the spinful model works in an almost identical way to the spinless case in the Section 2.1 with only doubled number of the bosonic field, $\varphi_{\uparrow,\downarrow}$ and $\theta_{\uparrow,\downarrow}$.

We reproduce this procedure briefly. The free particle part of the Hamiltonian in Eq. (2.7) gains additional summation over the spin index s within each of the left and the right movers subbands, see Fig. 2.1(b),

$$H_0 = \sum_{\substack{k,\, r = L,R \\ s =\uparrow,\downarrow}} v_F\left(\epsilon_r k - k_F\right) c^\dagger_{ksr} c_{ksr}. \tag{2.76}$$

Without interactions the two spin species are independent of each other. Thus, for

each value of s the bosonisation procedure can be performed in exactly the same way, like in Section 2.1, giving

$$H_0 = \frac{v_F}{2\pi} \sum_{s=\uparrow,\downarrow} \int dx \left[(\nabla\theta_s)^2 + (\nabla\varphi_s)^2 \right], \tag{2.77}$$

where θ_s and φ_s are two pairs of the bosonic fields that satisfy the commutation relation in Eq. (2.23) for the same s and just commute with each other for different s.

Like in the previous subsection we consider only the delta-functional potential profile, $V(x) = V_0\delta(x)$, for illustration purposes. The total density in Eq. (2.33) is the sum of the densities of the two spin species, $\rho(x) = \rho_\downarrow(x) + \rho_\uparrow(x)$, giving the interaction part of the Hamiltonian as

$$H_{int} = V_0 \int dx \left[2\rho_\downarrow(x)\rho_\uparrow(x) + \rho_\uparrow^2(x) + \rho_\downarrow^2(x) \right]. \tag{2.78}$$

For the $\rho_\uparrow^2(x)$ and $\rho_\downarrow^2(x)$ terms describing interactions within the same species the bosonisation procedure works exactly like in Section 2.1. Each density squared operators splits into the left and the right movers part, $\rho_s(x) = \rho_{sL}(x) + \rho_{sR}(x)$, giving the same contributions as in the spinless case,

$$\frac{4V_0}{(2\pi)^2} \int dx \left(\nabla\varphi_s\right)^2, \tag{2.79}$$

for each species in terms of the field φ_s that now has the spin index s. The first terms in Eq. (2.78) describing interactions between the different spin species is bit different. Using Eqs. (2.24,2.25) to express the density operators as $\rho_s(x) = -\nabla\varphi_s/\pi$ its contribution,

$$\frac{8V_0}{(2\pi)^2} \int dx \nabla\varphi_\uparrow \nabla\varphi_\downarrow, \tag{2.80}$$

makes the whole Hamiltonian, $H = H_0 + H_{int}$, non-diagonal,

$$H = \int dx \sum_{s=\uparrow,\downarrow} \left[\frac{v_F}{2\pi} (\nabla\theta_s)^2 + \frac{v_F}{2\pi} (\nabla\varphi_s)^2 + \frac{4V_0}{(2\pi)^2} (\nabla\varphi_s)^2 \right] + \frac{8V_0}{(2\pi)^2} \int dx \nabla\varphi_\uparrow \nabla\varphi_\downarrow. \tag{2.81}$$

The last hybridising term can be eliminated by a unitary rotation that introduces the new mixed degrees of freedom for the charge

$$\theta_\rho = \frac{1}{\sqrt{2}}\left(\theta_\uparrow + \theta_\downarrow\right), \tag{2.82}$$

$$\varphi_\rho = \frac{1}{\sqrt{2}}\left(\varphi_\uparrow + \varphi_\downarrow\right) \tag{2.83}$$

and for the spin

$$\theta_\sigma = \frac{1}{\sqrt{2}}\left(\theta_\uparrow - \theta_\downarrow\right), \tag{2.84}$$

$$\varphi_\sigma = \frac{1}{\sqrt{2}}\left(\varphi_\uparrow - \varphi_\downarrow\right) \tag{2.85}$$

fields. The resulting Hamiltonian is a sum of two copies of Eq. (2.44) in terms of these variables

$$H_{TL} = \frac{v_\rho}{2\pi}\int dx\left[K_\rho\left(\nabla\theta_\rho\right)^2 + \frac{1}{K_\rho}\left(\nabla\varphi_\rho\right)^2\right] + \frac{v_\sigma}{2\pi}\int dx\left[K_\sigma\left(\nabla\theta_\sigma\right)^2 + \frac{1}{K_\sigma}\left(\nabla\varphi_\sigma\right)^2\right], \tag{2.86}$$

where the number of the Luttinger parameters $K_{\rho,\sigma}$ and $v_{\rho,\sigma}$ also doubles. They are identified from the prefactors in Eq. (2.81) by mean of the same definitions as in Eqs. (2.40,2.41),

$$v_\rho = v_F\sqrt{1+\frac{4V_0}{\pi v_F}}, \tag{2.87}$$

$$K_\rho = \frac{1}{\sqrt{1+\frac{4V_0}{\pi v_F}}}, \tag{2.88}$$

$$v_\sigma = v_F\sqrt{1-\frac{4V_0}{\pi v_F}}, \tag{2.89}$$

$$K_\sigma = \frac{1}{\sqrt{1-\frac{4V_0}{\pi v_F}}}. \tag{2.90}$$

In the spinful case, the scattering between the branches of the left and the right movers is a bit more delicate. Keeping the cross terms in Eq. (2.31) for both species leads to an additional $\sim \int dx \cos\left(2\sqrt{2}\varphi_\sigma\right)$ term in Eq. (2.86) that generally is not negligible. However, for the most relevant case of fermions with repulsive interactions, i.e. electrons, this term flows to zero in the scaling analysis, see details in [23], leading only to a renormalisation of the Luttinger parameters in Eqs. (2.87-2.90), but does not result in any qualitative change of the ground state, i.e. it does not open any gap.

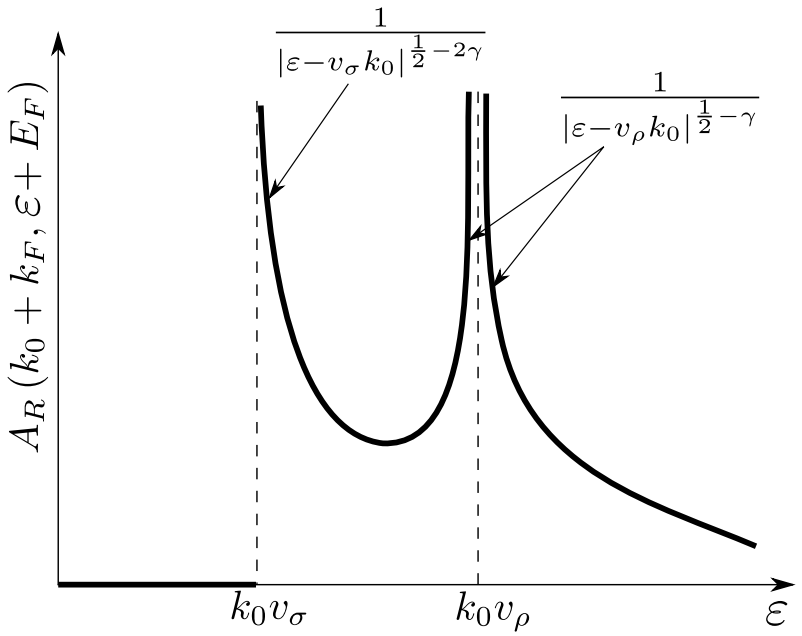

Figure 2.4: Spectral function of the right movers in a spinful Luttinger liquid for a fixed $k_0 > 0$ as a function of energy ε. Velocities of the spin v_σ and charge v_ρ modes are different for a finite interaction strength. The points of both linear dispersion are marked with the dashed lines. The divergent power-laws around this point are given by Eq. (2.91). For energies $\varepsilon < k_0 v_\sigma$ the spectral function is zero due the kinematic constraint.

A remarkable consequence of the result in Eq. (2.86) is the complete separation of the originally interacting particles with different spins into a decoupled pair of bosonic modes. Each of these modes consists of both of the original particles with both spin orientations but their charge (charge density waves or CDW) and their spin (spin density waves or SDW) degrees of freedom are disconnected into completely orthogonal collective excitations. Even more remarkably, the velocities of the CDW and SDW modes are different, see Eqs. (2.87,2.89), when the interaction strength is finite, which is entirely alien to the Fermi liquids in higher dimensions. This effect is called spin-charge separation. Different velocities make it easily observable in spectral properties, e.g. there will be two linear dispersions with different slopes in the spectral function of one dimensional fermions at low energy.

The correlation function in the spinful case can be evaluate by the same means of functional integral as described in Section 2.2. For the bosonised model in Eq. (2.86) the functional integral has to be take over the two pairs of the bosonic fields. The result for the two-point correlation function is analogous to Eq. (2.72) for each of the spin and the charge degrees of freedom. Then, the spectral function of, for instance, the right movers can be evaluated directly using the Green function via a

general relation

$$A_R\left(k+k_F,\varepsilon+E_F\right)=-\frac{1}{\pi}\int dxdte^{i(kx-\varepsilon t)}\mathrm{Im}G_R\left(x,it\right), \tag{2.91}$$

see [13] for the definition. This calculation is done in the spinful case in detail in [50, 51] giving

$$A_R\left(k+k_F,\varepsilon+E_F\right) \sim \frac{Y\left(\varepsilon-v_\sigma k\right)}{\left|\varepsilon-v_\rho k\right|^{\frac{1}{2}-\gamma}\left|\varepsilon-v_\sigma k\right|^{\frac{1}{2}-2\gamma}}, \tag{2.92}$$

which is specified for the vicinity of the $+k_F$ point for the $k>0$ and $\varepsilon>0$ sector here and where $\gamma=\left(K_\rho+K_\rho^{-1}-2\right)/8+\left(K_\sigma+K_\sigma^{-1}-2\right)/8$. The two non-equal velocities $v_\rho\neq v_\sigma$ result in two divergencies along these dispersions, see a plot of the spectral function Eq. (2.92) in Fig. 2.4, where it is visualised as a function of ε for a fixed value of $q>0$. The shape of these peaks is a power-law instead of the usual Lorentzian manifesting a completely different nature of the spin and density wave excitations in the Luttinger liquid theory from the quasiparticles of the Fermi liquid in Fig. 1.1(b). Two different velocities of the Luttinger liquid were directly observed in transport measurements of the electronic spectral function in [27, 28].

Chapter 3

Nonlinear Luttinger liquids

The rigorous fermion to boson mapping described in the previous chapter, on which the bosonisation technique and the resulting Tomonaga-Luttinger model are based, assumes strictly linearity of the spectrum at the Fermi points in Eq. (2.6). Any finite curvature in the original fermionic spectrum lifts the Lorentz invariance making the bosons in form of the charge density waves not the the exact eigenstates, e.g. see Fig. 2.2 where the fermionic spectrum will become non-equidistant and thus not Bose like. At least close to the Fermi points it is tempting to treat a weak non-linear term as a perturbation in hope that the exact eigenstates in this regime are not very different from the CDW of the exactly linear model in Eq. (2.6). This route gives rise to an additional three-body interaction terms that is proportional to a finite curvature $1/m$ [42]. The perturbative analysis of this $1/m$ term in the basis of the linear CDWs fails already in the leading order producing a divergent bosonic self-energy on the mass shell [30]. No robust methods of resuming these singularities has been developed so far.

It is instructive to take a step back at this point and to consider the original model of interacting fermions. Any two-body interaction changes the delta-functional excitation spectrum of the free particles (centred at the single particle parabola) into a continuum since removal of a single particle from the system affects all other particles involving many degrees of freedom and producing the continuum. In two and three dimensions this continuum covers the whole energy-momentum space since it is always possible to create an excitation at an infinitesimally small energy at all finite momenta by connecting two points on a circle or on a sphere by a finite vector of the length $|\mathbf{k}| < k_F$. One dimension is special due to only two Fermi points. Thus, there is a minimal energy of removing a single particle at a finite k corresponding to taking out just this one particle without touching the rest, see the hole in Fig. 3.1(a). This leads to a forbidden regions on the energy-momentum plane, see white regions in Fig. 3.1(a), which are separated from the many-body continuum of the excitations by the dispersion of this single hole with the minimal energy, see thick red line in Fig. 3.1(a).

A hole state deep under the Fermi surface reminds of another problem—x-ray scattering in metals, where the hole is created by adsorption of a high energy x-

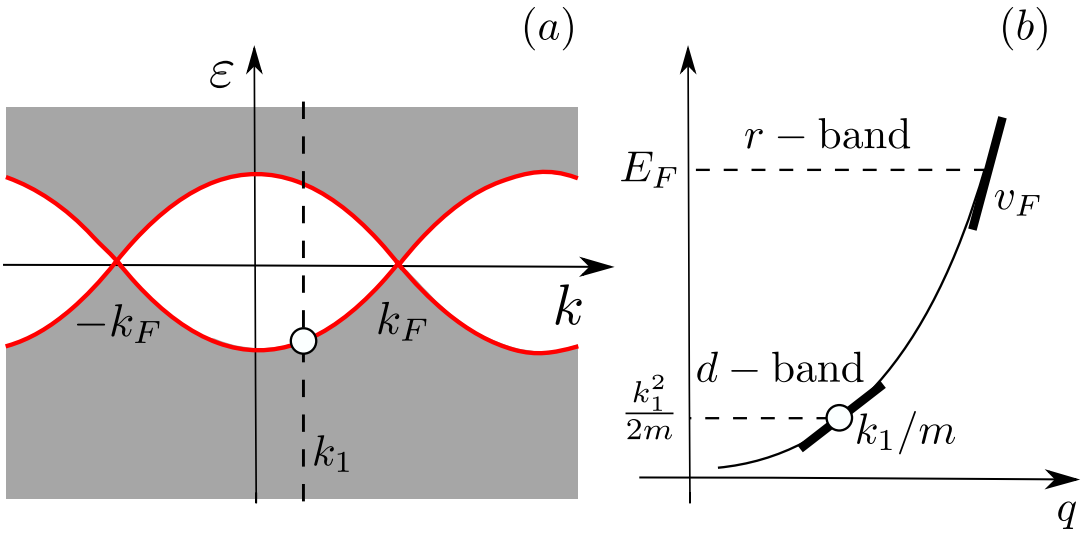

Figure 3.1: (a) Dispersion of an interacting one-dimensional system. White is the kinematically forbidden region (see explanation in the text) and grey is continuum of the many-body excitations. The thick red line separates the border between the two, the states on the border corresponds to removing a single particle (a hole at k_1) from the many-particle state. (b) Splitting of the fermionic dispersion into two subbands: for the heavy hole with the velocity k_1/m and for the excitations around the Fermi energy with the velocity v_F, see the Hamiltonian in Eq. (3.4) and explanation in the text.

ray photon. This problem is known to have a power-law singularity close to the Fermi level that originates from the interactions between the deep hole and the quasiparticles around the Fermi energy. The direct perturbation theory in the interaction in the x-ray problem is also known to be divergent [52, 53] and for which the way of handling these divergencies was proposed by Nozieres and De Dominicis in [31, 54] in the form of the heavy impurity model consisting of the Fermi liquid quasiparticles interacting with a localised state deep under the Fermi level; this model can be digonalised exactly. An analogous construction in one dimension can be done [10, 32, 33] by starting from the fermionic model[1]

$$H = \int dx \left[-\frac{1}{2m} \psi^\dagger \partial_x^2 \psi + V_0 \rho^2 (x) \right], \tag{3.1}$$

which corresponds to the model in Eq. (2.1) with $V(x) = V_0 \delta(x)$ in the real space and where the fermionic field operator is

$$\psi(x) = \frac{1}{\sqrt{L}} \sum_k c_k e^{ikx}. \tag{3.2}$$

[1]Here we follow the construction in [32] and the notations there.

Then, it can be projected into two subbands: one for the deep hole and another for the excitations around the Fermi point, say for positive total momenta around $+k_F$, see a sketch of the bands in Fig. 3.1(b). Correspondingly the field operators in Eq. (3.1) splits into

$$\psi_r(x) = \frac{1}{\sqrt{L}} \sum_{|q|<k_0} e^{iqx} c_{qR}; \quad \psi_d(x) = \frac{1}{\sqrt{L}} \sum_{|k-q|<k_0} e^{i(q-k)x} c_{qR}, \tag{3.3}$$

where k_0 is the size of both of the subbands, each of them is much smaller than the Fermi energy, $k_0 \ll k_F$.

Then, the spectrum of the both subbands can be linearised in order to obtain a linear model,

$$H_R = \int dx \Bigg[\psi_r^\dagger(x) \left(-iv_F \partial_x\right) \psi_r(x) + V_0 \rho_r^2(x) + \psi_d^\dagger(x) \left(\frac{k^2}{2m} - i\frac{k}{m}\partial_x\right) \psi_d(x) + V_0 \rho_d(x) \rho_r(x) \Bigg] \tag{3.4}$$

where the dispersion of the threshold is the free particle dispersion, $k^2/2m$, the velocity of the impurity band is k/m, the velocity at the Fermi energy is v_F, and the density operators are $\rho_r(x) = \psi_r^\dagger(r)\psi_r(r)$ and $\rho_d(x) = \psi_d^\dagger(x)\psi_d(x)$. There is no $V_0\rho_d^2$ term since there is no second impurity that can interact with the first one.

Unlike the x-ray model, the impurity in Eq. (3.4) has to be mobile since the total momentum of the both subbands still has to conserved when excitations are created in proximity to the edge. The other difference is a one-dimensional spectral threshold which is a line on the momentum-energy plane characterised by a dispersion instead of just the Fermi energy in the x-ray problem requiring a extra input parameter the momentum k in the Hamiltonian. The construction in Eq. (3.4) is also strictly speaking valid only in the weak interaction regime, in which the dispersion of the threshold is close to that of the free particles.

This linearised model in Eq. (3.4) can be solved without further approximations. The ψ_r operator in the first and the second term of Eq. (3.4) can be bosonised using the technique described in Section 2.1 producing a Tomonaga-Luttinger model—a free bosonic model. The coupling in the fourth term of Eq. (3.4) can be eliminated by a unitary rotation in the two-by-two space of the two subbands leaving the third term as a free model for a single fermion. The expectation value for the observables, then, can be evaluated as a pair of Gaussian integrals over the two free fields, similarly to the procedure described in Section 2.2. This already provides a way of accounting for the non-linear spectrum away from the Fermi energy in a non-perturbative way that resolves the problem of a finite mass in the Tomonaga-Luttinger model. The parabolicity of the original fermionic spectrum is incorporated in the third term in Eq. (3.4) as the dispersion of the spectral threshold, $k^2/2m$, while the dispersion of the dynamical variables is linearised in order to account for the fluctuations around

the edge. We, however, will not follow this microscopic analysis here but will consider a more general model that can be defined phenomenologically, motivated by this microscopic approach, in the next section.

3.1 Mobile impurity model

Instead of starting from the fermionic model in Eq. (2.1) the mobile impurity model can be constructed starting from the Tomonaga-Luttinger model in Eq. (2.44). Here we will follow the review [34]. A deep hole state can be added to H_{TL} assuming that the hole state is sufficiently far in the energy domain from the Fermi level so it is a distinct from the low-energy excitations, similarly to the construction in Fig. 3.1. The dispersion of this hole is now an arbitrary input parameter of the model, $\varepsilon_{th}(k)$. The coupling to the CDW of Luttinger liquid is of the density-density type exchange processes are forbidden by a larger energy difference between the hole band and the Fermi energy. The density operators can be expressed through the bosonisation expressions in Eqs. (2.24,2.25) in terms of the gradients of the θ and φ fields and there is an arbitrary coupling constants of these field to the mobile impurity density $\rho_d(x)$.

Adding up of these three terms the phenomenologically defined mobile impurity model reads [11, 55],

$$H_{nLL} = H_{TL} + \int dx\, d^{\dagger}(x) \left(\varepsilon_{th}(k) - i \frac{\partial \varepsilon_{th}(k)}{\partial k} \partial_x \right) d(x) + \int dx \left(V_\theta \nabla\theta + V_\varphi \nabla\varphi \right) \rho_d(x), \quad (3.5)$$

where the spinless Tomonaga-Luttinger model is given by H_{TL} in Eq. (2.44), $d(x)$ is the Fermi operator of a single fermion, $\left\{ d(x), d^{\dagger}(x') \right\} = \delta(x - x')$, the density operator of the impurity is $\rho_d(x) = d^{\dagger}(x) d(x)$, the bosonic fields θ and φ satisfy $[\varphi(x), \nabla\theta(x')] = i\pi\delta(x - x')$, $\partial_k \varepsilon_{th}(k)$ is the velocity of the deep hole band, analogously to Fig. 3.1, and V_θ and V_φ are two arbitrary couplings originating from the unknown interaction strengths of the deep hole with the left and the right movers of the Luttinger liquid—they will be fixed in a moment.

The two coupling constants V_θ and V_φ are not free parameters but are related to other parameters of the model. They can be derived from considering at least two different physical properties. One is the translation invariance of the system. The velocity of the bosonic excitations is given by $\langle \nabla\theta \rangle / \pi$, see discussion after Eq.(2.47), and it has to be compensated by the velocity within the d-band, see Fig. 3.1, since the total velocity of the whole system still has to be k/m, protected by the Galilean invariance. This fixes the interaction strength in front of $\nabla\theta$ as

$$V_\theta = \frac{k}{m} - \frac{\partial \varepsilon_{th}(k)}{\partial k}. \quad (3.6)$$

Another property is change of the energy of the whole system with a small change of its density, $\delta\rho = \nabla\theta/\pi$, see again the discussion after Eq. (2.47). Such a variation adds the term $V_\varphi \pi \delta\rho$ to the model in Eq. (3.5) that should be equal to $\partial\varepsilon_{th}(k)/\partial\rho + \partial\mu/\partial\rho$, where the last term can be expressed through the Luttinger parameters[2] using the bosonisation technique described in Section 2.1. This procedure gives

$$V_\varphi = \frac{1}{\pi}\frac{\partial\varepsilon_{th}(k)}{\delta\rho} + \frac{v}{K}, \tag{3.7}$$

where $\partial\varepsilon_{th}(k)/\partial\rho$ is derivative of the dispersion of the spectral edge with respect to the density of the particles.

The structure of the model in Eq. (3.5), together with Eqs. (3.6,3.7), is thus a generic way of accommodating a spectral non-linearity for arbitrary interactions and for arbitrary dispersion of the spectral threshold. This way of defining the non-linear model has the advantage of being valid for arbitrary non-linear parameters, unlike the derivation before Eq. (3.4). The input parameters, the pair of the linear Luttinger liquid v and K and the dispersion of the spectral threshold $\varepsilon_{th}(k)$, can have arbitrary values within the non-linear Luttinger liquid model. For a given microscopic model the low energy parameters v and K can be evaluated (or measured) in the usual way, see [23]. The additional parameter—the dispersion of the spectral edge—can be obtained similarly, see a sketch of a generic situation in Fig. 3.2. It consists of the electron and the hole parts for a given momentum between the $\pm k_F$ points and is $2k_F$ periodic due to the translation invariance of the model.

Although, the model is Eq. (3.5) is not restricted by the linear constraint of the Tomonaga-Luttinger model it is still valid only in the proximity of the spectral edges, see green regions in Fig. 3.2, since the spectrum of the mobile impurity was linearised; increasing the energy away from the edges means exploring larger and larger deviations in the position of the deep hole away from the point of the linearisation, rendering the linear approximation invalid. The input parameter k also has to be sufficiently different from the Fermi points $k = \pm k_F$. Otherwise the processes of emitting and absorbing the mobile impurity by the CDW around the Fermi energy become active, and the density-density interaction in Eq. (3.5) has to be extended by adding the exchange terms making the whole model in Eq. (3.5) inapplicable.

In the case of electrons with spin-1/2, phenomenological construction of the mobile impurity model can be done in a similar way [56, 57]. There will be two types of the bosonic fields, for the charge and the spin degrees of freedom—see their introduction for the linear Tomonaga-Luttinger model in Section 2.3. In the absence of the external magnetic field the mobile impurity couples only to the charge fields

[2]See more details on definition of the chemical potential within the Luttinger liquid theory in [23].

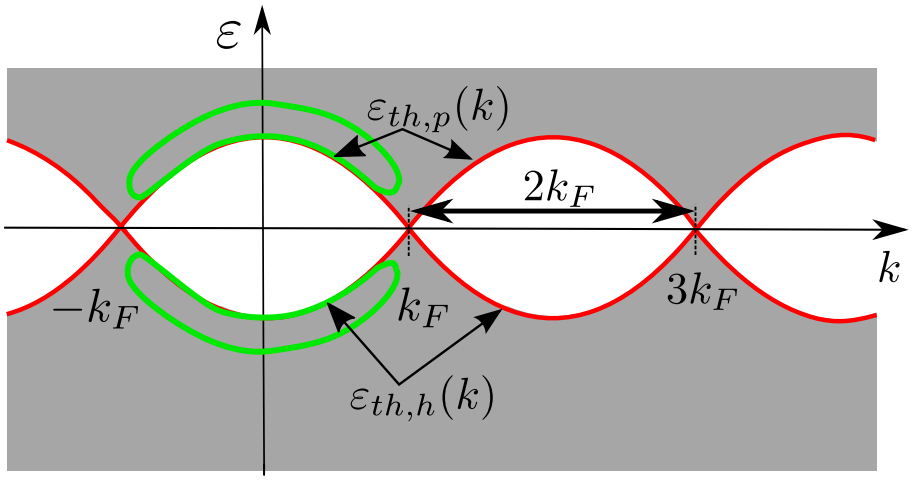

Figure 3.2: Applicability region of the mobile impurity model in Eq. (3.5) encircled with the green lines. They are in proximity of the spectral edges and are away from the Fermi points. There are two spectral threshold for a given k: $\varepsilon_{th,p}(k)$ in the particle sector and $\varepsilon_{th,h}(k)$ in the hole sector. They are symmetrical with respect to the $\varepsilon = E_F$ line and are $2k_F$ periodic along the momentum axis due to the translation invariance.

due to the symmetry of the two spin orientations,

$$H_{nLL} = H_{TL} + \int dx\, d^{\dagger}(x) \left(\varepsilon_{th}(k) - i\frac{\partial \varepsilon_{th}(k)}{\partial k}\partial_x \right) d(x) + \int dx \left(V_\theta \nabla\theta_\rho + V_\varphi \nabla\varphi_\rho \right) \rho_d(x), \quad (3.8)$$

where the spinful Tomonaga-Luttinger model is given by H_{TL} in Eq. (2.86), $\theta_{\rho(\sigma)}$ and $\varphi_{\rho(\sigma)}$ are the bosonic field of the CDW (SDW) satisfying $[\varphi_\alpha(x), \nabla\theta_\beta(x')] = i\pi\delta_{\alpha\beta}\delta(x-x')$, and the other parameters are the same as in the spinless non-linear model in Eq. (3.5). The coupling constants V_θ and V_φ are also not independent parameters. They can be related to the linear Luttinger parameter and the dispersion of the spectral edge by considering the velocity of the whole system and the variation of the total energy with the density, as in the spinless case, giving

$$V_\theta = \frac{k}{\sqrt{2}m} - \frac{\partial \varepsilon_{th}(k)}{\sqrt{2}\partial k}, \quad (3.9)$$

$$V_\varphi = \frac{\partial \varepsilon_{th}(k)}{\sqrt{2}\partial \rho} + \frac{v_\sigma}{\sqrt{2}K_\sigma}, \quad (3.10)$$

where v_σ and K_σ are the Luttinger parameters of the spin density mode. The mobile impurity model is not restricted only to fermions but it can be constructed for other one-dimensional systems, e.g. spin chains [58] and bosonic models [59]. A general

overview and corresponding references are given in the review in [34].

3.2 Power-law singularities around spectral edges

The model in Eq. (3.5) can be diagonalised using a unitary rotation in the two-by-two space of the Tomonaga-Luttinger model and the mobile impurity. Then, the expectation values for the observables can be evaluated using the Gaussian integrals over the free fields, like for the linear Luttinger liquid case in Section 2.2. The diagonalisation is performed via the $e^{-iU}H_{nLL}e^{iU}$ rotation, where the rotation matrix can be found in the perturbation theory analysis from the condition $[H,U]=0$ as

$$U=\int dx\left[C_{+}\left(\sqrt{K}\theta+\varphi/\sqrt{K}\right)+C_{-}\left(\sqrt{K}\theta-\varphi/\sqrt{K}\right)\right]\rho_{d}, \tag{3.11}$$

where the coefficients are

$$C_{\pm}=\frac{1}{2\sqrt{K}}\left(K\left(\frac{k}{m}-\frac{\partial\varepsilon_{th}\left(k\right)}{\partial k}\right)\pm\frac{1}{K}\left(\frac{1}{\pi}\frac{\partial\varepsilon_{th}\left(k\right)}{\delta\rho}+\frac{v}{K}\right)\right), \tag{3.12}$$

where the coupling constant from Eqs. (3.6,3.7) were already substituted.

The averages with respect to the free model after the rotation can be evaluated as Gaussian integrals in two types of the fields. We will consider only the spectral function here. It can be defined using the Green function as [13]

$$A\left(k,\varepsilon\right)=-\frac{1}{\pi}\mathrm{Im}G\left(k,\varepsilon\right)\mathrm{sign}\varepsilon, \tag{3.13}$$

where the real-frequency Green function is a Fourier transform of the time-ordered two-point correlation function, $G\left(k,\varepsilon\right)=-i\int dxdt\exp\left(i\varepsilon t-ikx\right)\left\langle T\psi\left(x,t\right)\psi\left(0,0\right)\right\rangle$. The fermionic excitation gives the dominant contribution to the spectral function close to the spectral threshold [11, 32, 33]. Thus, its most singular part can be expressed through the correlation function of the mobile impurity operator as

$$A\left(k,\varepsilon\right)\sim\int dtdxe^{i(\varepsilon t-kx)}\left\langle d^{\dagger}\left(x,t\right)d\left(0,0\right)\right\rangle \tag{3.14}$$

where the time evolution of the mobile impurity hole operator is given by the model in Eq. (3.5), $d\left(x,t\right)=\exp\left(-iH_{nLL}t\right)d\left(x\right)\exp\left(iH_{nLL}t\right)$, and the expectation value has to be taken also with respect to the whole model in Eq. (3.5).

The same procedure as was already described in Section 2.2 gives a power-law function in energy,

$$A\left(k,\varepsilon\right)\sim\frac{1}{\left|\varepsilon\pm\varepsilon_{th}\left(k\right)\right|^{\alpha_{\pm}}}, \tag{3.15}$$

where the exponent is

$$\alpha_{\pm} = 1 - \frac{1}{2}\left(2n\sqrt{K} - C_{+} - C_{-}\right)^{2} - \frac{1}{2}\left(\frac{1 \pm 1}{\sqrt{K}} + C_{+} - C_{-}\right)^{2}, \tag{3.16}$$

$\pm$ refer to the particle (hole) sector on the energy-momentum plane, n is the integer number of translations of principal region in the momentum variable from $-k_F$ to k_F, see Fig 3.2, and $C_{\pm}$ are given in Eq. (3.12).

The spectral function of the spinful fermionic model in Eq. (3.8) can be evaluated in the same way [56, 57]. Due the spin-charge separation the spectral function for spin-up and -down electrons is the same. For repulsive interactions $V_0 > 0$ the velocity of the SDW is slower, see Eqs. (2.87,2.89). Thus, the spectral threshold $\varepsilon_{th}(k)$ is given by the spin modes in this case and the spectral function[3] is

$$A_s(k, \varepsilon) \sim \frac{1}{|\varepsilon \pm \varepsilon_{th}(k)|^{\alpha_{\pm}}}, \tag{3.17}$$

where the right hand side is independent of the spin index $s = \uparrow, \downarrow$ and the exponent is

$$\alpha_{\pm} = \frac{1 \mp 1}{2} - \frac{1}{2}\left(\frac{(2n+1)\sqrt{K_c}}{\sqrt{2}} - C_{+} - C_{-}\right)^{2} - \frac{1}{2}\left(\frac{1}{\sqrt{2K_c}} - C_{+} - C_{-}\right). \tag{3.18}$$

Here the coefficient of the rotation matrix, which diagonalises the spinful model in Eq. (3.8) in the two-by-two space of the mobile impurity and the charge density modes, are given in term of curvature of the spectral edge as

$$C_{\pm} = \frac{\frac{k-k_F}{m\sqrt{K_c}} \pm \sqrt{K_c}\left(\frac{2}{\pi}\frac{\varepsilon_{th}(k)}{\partial\rho} + \frac{\partial\varepsilon_{th}(k)}{\partial k}\right)}{2\sqrt{2}\left(\frac{\partial\varepsilon_{th}(k)}{\partial k} \mp \frac{k_F}{mK_c}\right)}, \tag{3.19}$$

where the coupling constants from Eqs. (3.9,3.10) were already substituted.

Both exponents, in the spinless case in Eq. (3.16) and in the spinful case in Eq. (3.18), depend on momentum k through a finite curvature of the spectral edge in addition to the interaction strength through the Luttinger parameters in the usual linear Tomonaga-Luttinger model. For the both of the fermionic model the dispersions of the spectral edges can be calculated microscopically and is close to a parabola with a good accuracy [35, 36],

$$\varepsilon_{th}(k) = \mu + \frac{k_F^2}{2m^*} \pm \frac{(k - k_F)^2}{2m^*}, \tag{3.20}$$

where the effective mass is $m^* = mK$ and $m^* = mK_\sigma$ in the spinless and in the spinful case respectively and $\pm$ refer to the particle and to the hole branch of the spectral edge. Substitution of Eq. (3.20) in Eqs. (3.16,3.18) gives the explicit

[3] See details of this calculation in [57].

	spinless	spinful
particle (α_+)	$1-\frac{K}{2}\left(1-\frac{1}{K}\right)^2$	$-\frac{K_\rho}{4}\left(1-D_-\left(k\right)\right)^2-\frac{K_\rho}{4}\left(\frac{1}{K_\rho}+D_+\left(k\right)\right)^2$
hole (α_-)	$1-\frac{K}{2}\left(1-\frac{1}{K}\right)^2$	$1-\frac{K_\rho}{4}\left(1-D_-\left(k\right)\right)^2-\frac{K_\rho}{4}\left(\frac{1}{K_\rho}-D_+\left(k\right)\right)^2$

Table 3.1: Explicit momentum dependence of threshold exponents in the non-linear Luttinger models for fermions with repulsive interaction in the principal range $n = 0$: the left column is the spinless and the right column is the spinful case. The upper raw is for the particle edge and the bottom raw is for the hole edge. The explicit momentum function in the spinful case are $D_-\left(k\right) = \left(k-k_F\right)\left(k_F/K_\rho^2+k/K_\sigma^2\right)/\left(k^2/K_\sigma^2-k_F^2/K_\rho^2\right)$ and $D_+\left(k\right) = \left(k-k_F\right)\left(k_F/\left(K_\rho K_\sigma\right)+k/\left(K_\sigma K_\rho\right)\right)/\left(k^2/K_\sigma^2-k_F^2/K_\rho^2\right)$.

dependencies of the exponents on the momentum, see Table. 3.1. In the spinless case the momentum dependence cancels out but in the spinful case it remains. The latter can be measured directly using the already available technique of tunnelling spectroscopy in quantum wires defined electrostatically on top of a semiconductor heterostructure, like in experiments in [28, 38].

Chapter 4

Bethe ansatz

This chapter contains a brief introduction into the Bethe ansatz technique. In this approach many-body Hamiltonians in one dimension are diagonalised directly without any approximations, like linearisation of the dispersion or separation of the whole many-body spectrum into subbands. Thus, all energy regimes of the model can be analysed using the same method and on the same footing. However, since all microscopic details about the many-body excitations are retained, the practical calculations of physically measurable observables require quite a complicated mathematical machinery that took a rather long time to develop. The first complication is the exponentially large Hamiltonian that need to be diagonalised, the size of the Fock space is $\sim 2^N$ where N is the number of particles. It was resolved by reducing the diagonalisation problem to a system of only N non-linear equations for N parameters [60] that allows to take the thermodynamic limit. Another big complication is a non-factorised form of the N-particle wave functions in real space. This problem was resolved by construction of the algebraic Bethe ansatz [61] permitting evaluation of the many-body matrix elements.

A peculiarity of Bethe ansatz is in the first step of its construction, on which the form of the many-body functions has to be guessed. The fact that they are the eigenfunction of the Hamiltonian, orthogonality between them, and completeness of the basis that they form is proven only *post priori*, complicating generalisation of this method to other systems. Although, after the original discovery for the Heisenberg spin chains [60], the Bethe ansatz wave functions were constructed for bosons with contact interactions in the form of the Lieb-Liniger model [62, 63], fermions with the next-neighbour interactions [41], and for the Hubbard model in one dimension by nesting two Bethe wave functions [64]. These cover all principal systems with short range interactions in one dimension providing a way—though a somewhat complicated one—to check rigorously any more universal theory that still contains an approximation, like the Tomonaga-Luttinger model or the mobile impurity model described in Chapters 2 and 3, and to search for new still undiscovered many-body theories.

In the following two sections, a construction of the Bethe wave is described for a spin system, using the XXZ model as an example, and introduction in the algebraic

Bethe ansatz is given for the same system.

4.1 Set of non-linear equations as eigenvalue problem

The XXZ model is a generalisation of the Heisenberg model for a chain of spins, where an asymmetry $\Delta = 0 \dots \infty$ between the couplings in the $xy-$plane and in z-direction is introduced. For an external magnetic field B that is also parallel to the z-axis it reads [41]

$$H = J \sum_{j=1}^{L} \left(\frac{S_j^- S_{j+1}^+ + S_j^+ S_{j+1}^-}{2} + \Delta S_j^z S_{j+1}^z \right) + B \sum_{j=1}^{L} S_j^z, \tag{4.1}$$

where $\boldsymbol{S}_j$ are the spin-1/2 operators that obey the angular momentum commutation relation $\left[S_j^\alpha, S_{j'}^\beta \right] = i\delta_{jj'} e^{\alpha\beta\gamma} S_j^\gamma$, $S_j^\pm = S_j^x \pm i S_j^y$, J is the exchange coupling constant, and L is the number of spins in the chain. Here we assume the periodic boundary condition, $\boldsymbol{S}_{j+L} = \boldsymbol{S}_j$.

The model in Eq. (4.1) has z-project of the total spin, $S^z = \sum_{j=1}^{L} S_j^z$, as a conserved quantity $[H, S^z] = 0$, and therefore its expectation value $\langle S^z \rangle$ is a good quantum number. Thus, its eigenfunctions can be written in each sector with the given total number of spin flips with respect to reference state, say with all spins pointing down, that corresponds to the values of $\langle S^z \rangle = -L/2, \dots, L/2$ as

$$\Psi = \sum_{j_1 < \dots < j_N} a_{j_1 \dots j_N} S_{j_1}^+ \cdots S_{j_N}^+ \left| \Downarrow \right\rangle, \tag{4.2}$$

where N is the number of flips (or "particles") and the summation runs over an order set of coordinates of N particles, $j_1 < \dots < j_N$, since the S_j^+ operators commute for different spins and the product of two or more S_j^z operators for the same spin gives zero. The amplitudes $a_{j_1 \dots j_N}$ describe a wave function in a given sector.

For a single spin flip, $\langle S^z \rangle = -L/2 + 1$, the third term in Eq. (4.1) gives a constant since only one spin cannot interact with itself. Thus, the first two terms give just a free hopping model, see the sketch in Fig. 4.1(a), which eigenstates are the plain waves—magnons,

$$a_j = e^{iqj}. \tag{4.3}$$

The eigenenergy of the state above can be found from the eigenvalue problem, $H\Psi = E\Psi$. Acting of H in Eq. (4.1) on Ψ in Eq. (4.2) with $N = 1$ and projecting the result on each individual spin, $\left\langle \Downarrow | S_j^- H | \Psi \right\rangle$, gives the same expression for all j,

$$\frac{J}{2} \left(a_{j-1} + a_{j+1} \right) + \left(B \left(-\frac{L}{2} + 1 \right) + \frac{J\Delta L}{4} \right) a_j = E a_j. \tag{4.4}$$

Substitution of a_j from Eq. (4.3) in the above equation confirms that Eq. (4.3)

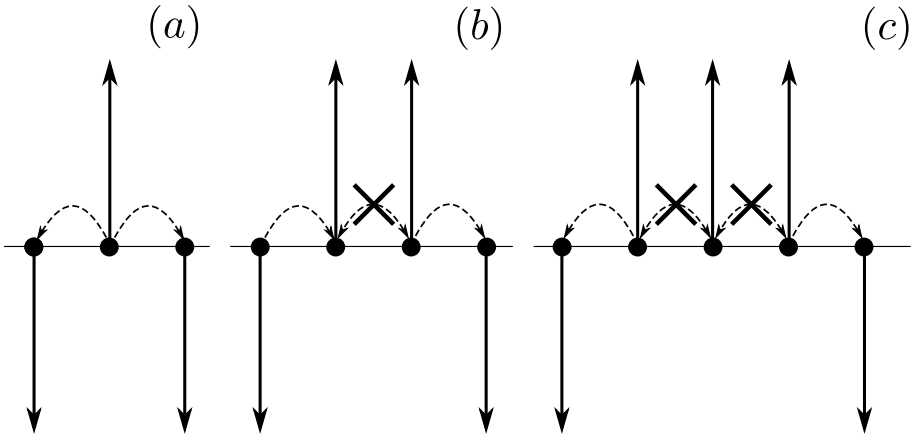

Figure 4.1: Sketches of representative spin configurations for the eigenvalue problem: (a) a single spin on with no neighbours for $N = 1$, (b) there is one neighbour for $N = 2$ and two-body scattering matrix, and (c) there are two neighbours for $N = 3$ and three-body scattering matrix. The dashed lines mark allowed jump and the crossed lines mark forbidden jump.

is an eigenstate and gives the corresponding eigenenergy as

$$E = J\left(\cos q - \Delta\right) + B + \left(\frac{J\Delta}{2} - B\right)\frac{L}{2}. \tag{4.5}$$

At the moment q is an arbitrary parameter. It can be fixed using the periodic boundary condition that implies $a_{j+L} = a_j$ and gives the usual quantisation condition for free particles,

$$q = \frac{2\pi I}{L}, \tag{4.6}$$

where I is an integer number from 0 to $L - 1$.

For two spin flips, $\langle S^z\rangle = -L/2+2$, the third term in Eq. (4.1) already becomes relevant since it describes an interaction between two magnons. When two spins are away from each other, i.e. $j_2 - j_1 > 1$, the eigenvalue problem still can be satisfied by a product of two plain waves, $e^{iq_1j_1}e^{iq_2j_2}$, suggesting the following ansatz for the eigenfunctions,

$$a_{j_1j_2} = A_1e^{i(q_1j_1+q_2j_2)} + A_2e^{i(q_2j_1+q_1j_2)}, \tag{4.7}$$

where the two coefficients $A_{1,2}$ are free parameters since the statistics of the two-magnon wavefunctions is not fixed yet. The eigenvalue equation for this wave function for $j_2 - j_1 > 1$,

$$\frac{J}{2}\left(a_{j_1-1,j_2} + a_{j_1+1,j_2}\right) + \left(B\left(-\frac{L}{2}+2\right) + \frac{J\Delta L}{4}\right)a_{j_1j_2} = Ea_{j_1j_2}, \tag{4.8}$$

$$\frac{J}{2}\left(a_{j_1,j_2-1} + a_{j_1,j_2+1}\right) + \left(B\left(-\frac{L}{2}+2\right) + \frac{J\Delta L}{4}\right)a_{j_1j_2} = Ea_{j_1j_2}, \tag{4.9}$$

is satisfied by Eq. (4.7) giving the following eigenenergy,

$$E = J\sum_{j=1}^{2}(\cos q_j - \Delta) + 2B + \left(\frac{J\Delta}{2} - B\right)\frac{L}{2}. \tag{4.10}$$

For the $j_2 = j_1 + 1$ case the eigenvalue problem reads, see the sketch in Fig. 4.1(b), as

$$\frac{J}{2}\left(a_{j_1-1,j_2} + a_{j_1,j_2+1}\right) + \left(B\left(-\frac{L}{2}+1\right) + \frac{J\Delta L}{4}\right)a_{j_1 j_2} = E a_{j_1 j_2}. \tag{4.11}$$

Luckily, there are still available free parameters $A_{1,2}$ in the ansatz in Eq. (4.7), which can be selected so that Eq. (4.11) is satisfied,

$$\frac{A_1}{A_2} = -\frac{e^{i(q_1+q_2)} + 1 - 2\Delta e^{iq_1}}{e^{i(q_1+q_2)} + 1 - 2\Delta e^{iq_2}}, \tag{4.12}$$

and so that the diagonalisation problem is solved for all j_1, j_2. Reparametring these coefficients $A_{1,2}$ in a symmetrical way

$$A_1 = e^{i\varphi/2}, \quad A_2 = e^{-i\varphi/2}, \tag{4.13}$$

where the phase $A_1/A_2 = \exp(i\varphi)$ is given by the r.h.s. of Eq. (4.12), we identify the so-called two-body scattering phase φ.

The periodic boundary condition, $a_{j,L+1} = a_{1,j}$, becomes a bit more complicated due to the ordered sum of coordinates in the wavefunction in Eq. (4.2). Application of it in the two-flip case admixes the scattering phases into the quantisation condition as

$$q_1 L - 2\varphi = 2\pi I_1, \tag{4.14}$$
$$q_2 L + 2\varphi = 2\pi I_2, \tag{4.15}$$

where I_1 and I_2 are two non-equal integer numbers and φ is the scattering phase in Eq. (4.12) that depends on q_1 and q_2 in a non-linear way making the system of two equations non-linear. Although, the sum of Eqs. (4.14,4.15) gives the free quantisation condition for the total momentum $Q = q_1 + q_2$ as $QL = 2\pi(I_1 + I_2)$, protected by the total translation invariance of the model in Eq. (4.1) that is not broken by the interactions.

In the three-flip case, $\langle S^z\rangle = -L/2 + 3$, the extra complication is represented by the configuration of three spins next to each other, see the sketch in Fig. 4.1(c). However, in one dimension the coordination number is two. Thus, one spin can have maximum two neighbours and the three-body scattering matrix factorises into a product of only two-body scattering matrices, i.e. it satisfies the Yang-Baxter equation [65]. Then, generalisation of the eigenfunctions for arbitrary N follows the

two-body case in Eqs. (4.7,4.12),

$$a_{j_1\ldots j_N} = \sum_{\mathcal{P}} \exp\left(i \sum_l q_{\mathcal{P}_l} j_l + i \sum_{l<l'} \frac{\varphi_{\mathcal{P}_l,\mathcal{P}_{l'}}}{2} \right), \tag{4.16}$$

where $\sum_{\mathcal{P}}$ is the sum over all permutations of N quasimomenta q_l and the two-body scattering phases between every pair of magnons l and l' are

$$e^{i\varphi_{ij}} = -\frac{e^{i(q_i+q_j)} + 1 - 2\Delta e^{iq_i}}{e^{i(q_i+q_j)} + 1 - 2\Delta e^{iq_j}}. \tag{4.17}$$

The eigenenergy is found from the eigenvalue problem as

$$E = J \sum_{j=1}^{N} (\cos q_j - \Delta) + NB + \left(\frac{J\Delta}{2} - B \right) \frac{L}{2}. \tag{4.18}$$

The periodic boundary condition gives the following set of N non-linear quantisation equations,

$$q_j L - \sum_{l\neq j} \varphi_{jl} = 2\pi I_j, \tag{4.19}$$

due to the scattering phases in Eq. (4.18), where I_j is a set of N non-equal integer numbers. The total momentum of all magnons, $Q = \sum_{j=1}^{N} q_j$, is a conserved quantity satisfying the free quantisation condition that can be checked by adding up all lines in Eq. (4.18).

The quantisation equations in Eqs. (4.18) are commonly called the coordinate Bethe ansatz. They reduce the original exponential complexity of diagonalisation of the Hamiltonian matrix to solving only a linear number of equations, for the price of non-linearity in this system of equations. Nevertheless, methods of taking the continuum limit for Eq. (4.18) are available, see the book in [41], allowing explicit calculations of the thermodynamic quantities.

4.2 Many-body matrix elements: Algebraic Bethe ansatz

The many-body states Ψ in the coordinate representation in Eq. (4.2,4.16) are not factorisable into a product for different particles like free Bose or Fermi wavefunction in the second quantisation representation, making calculations of the expectation values for the observables in this representation almost intractable. Even numerical evaluation of an N-fold integral becomes quickly unfeasible as N grows. However, evaluation of the matrix element becomes manageable using the algebraic form of Bethe ansatz [61], in which Bethe states do factorise in terms of operators with given commutation relations. Then, these commutation relations can be used for explicit

calculations, almost like in the usual second quantisation formalism. In this section we will follow the book in [61].

The many-body wave functions can be written down using operators that satisfy a Yang-Baxter algebra as

$$|\mathbf{u}\rangle = \prod_{j=1}^{N} C(u_j) |\Downarrow\rangle , \tag{4.20}$$

where u_j are N auxiliary parameters and $C(u)$ is one of the four matrix elements of the transition matrix

$$T(u) = \begin{pmatrix} A(u) & B(u) \\ C(u) & D(u) \end{pmatrix}, \tag{4.21}$$

which is defined in an auxiliary two-by-two space. This T-matrix satisfies the Yang-Baxter equation

$$R(u-v)\,(T(u) \otimes T(v)) = (T(v) \otimes T(u))\,R(u-v) . \tag{4.22}$$

Here we use the following R-matrix that corresponds to the spin Hamiltonian in Eq.(4.1),

$$R(u) = \begin{pmatrix} 1 & & & \\ & b(u) & c(u) & \\ & c(u) & b(u) & \\ & & & 1 \end{pmatrix}, \tag{4.23}$$

where $b(u) = \sinh(u) / \sinh(u+2\eta)$ and $c(u) = \sinh(2\eta) / \sinh(u+2\eta)$.

The entries of Eq. (4.22) give commutation relations between the matrix elements of T. Here we write down four of them that will be used later,

$$[B_u, C_v] = \frac{c(u-v)}{b(u-v)} (A_u D_v - A_v D_u) , \tag{4.24}$$

$$A_u C_v = \frac{1}{b(u-v)} C_v A_u - \frac{c(u-v)}{b(u-v)} C_u A_v, \tag{4.25}$$

$$D_u C_v = \frac{1}{b(v-u)} C_v D_u - \frac{c(v-u)}{b(v-u)} C_u D_v, \tag{4.26}$$

$$[A_u, D_v] = \frac{c(u-v)}{b(u-v)} (C_v B_u - C_u B_v) . \tag{4.27}$$

We have introduced the subscript u and v as a shorthand of the argument, e.g. $A_u \equiv A(u)$, above.

The transfer matrix $\tau(u) = \mathrm{Tr} T(u) = A(u) + D(u)$ contains all of the conserved quantities of the model in Eq. (4.1) including the Hamiltonian. Thus if $|\mathbf{u}\rangle$ is a eigenstate of $\tau(u)$ then it is an eigenstate of the Hamiltonian. The eigenvalue equation, $\tau(u)|\mathbf{u}\rangle = \mathcal{T}_u |\mathbf{u}\rangle$ where $\mathcal{T}_u$ is a scalar quantity – the corresponding eigenvalue,

can be solved using the commutation relations in Eqs. (4.24-4.27). The results of acting with the A_u and D_u operators on the state $|\mathbf{u}\rangle$ in Eq. (4.20) are obtained by commuting them from left to right through the product of $C(u_j)$ operators,

$$A_u \prod_{j=1}^{N} C(u_j)|0\rangle = a_u \prod_{j=1}^{N} \frac{1}{b_{uj}} C(u_j)|0\rangle - \sum_{j=1}^{N} a_j \frac{c_{uj}}{b_{uj}} C(u) \prod_{l=1\neq j}^{N} \frac{1}{b_{jl}} C(u_l)|\Downarrow\rangle, \quad (4.28)$$

$$D_u \prod_{j=1}^{N} C(u_j)|0\rangle = d_u \prod_{j=1}^{N} \frac{1}{b_{ju}} C(u_j)|0\rangle + \sum_{j=1}^{N} d_j \frac{c_{uj}}{b_{uj}} C(u) \prod_{l=1\neq j}^{N} \frac{1}{b_{lj}} C(u_l)|\Downarrow\rangle, \quad (4.29)$$

where the vacuum eigenvalues of the operators, $A_u|\Downarrow\rangle = a_u|\Downarrow\rangle$ and $D_u|\Downarrow\rangle = d_u|\Downarrow\rangle$, are

$$a_u = \frac{\cosh^L(u-\eta)}{\cosh^L(u+\eta)} \quad \text{and} \quad d_u = 1. \quad (4.30)$$

Since the right hand side of Eqs. (4.28,4.29) contains terms that are not proportional to the original state multiplied by a scalar, an arbitrary Bethe state is not an eigenstate of the transfer matrix τ for an arbitrary set of the auxiliary parameters u_j. However, the second terms in Eqs. (4.28,4.29) can be made zero by selecting specific sets of u_j that are solutions of the following set of non-linear equations,

$$\frac{a_j}{d_j} = \prod_{l=1\neq j}^{N} \frac{b_{jl}}{b_{lj}}, \quad (4.31)$$

where we have used the shorthand with the subscripts, i.e. $a_j \equiv a(u_j)$ and $b_{jl} \equiv b(u_j - u_l)$. Substitution of the expressions for a_j and d_j from Eq. (4.30) and for b_{jl} from Eq. (4.23) gives the following Bethe equation and the eigenvalue of the transfer matrix τ,

$$\frac{\cosh(u_j-\eta)^L}{\cosh(u_j+\eta)^L} = \prod_{l=1\neq j}^{N} \frac{\sinh(u_j-u_l-2\eta)}{\sinh(u_j-u_l+2\eta)}, \quad (4.32)$$

$$\mathcal{T}_u = a_u \prod_{j=1}^{N} \frac{1}{b_{uj}} + d_u \prod_{j=1}^{N} \frac{1}{b_{ju}}. \quad (4.33)$$

The Bethe ansatz equations—in the coordinate representation in Eq. (4.1)—are obtained under substitution of

$$u_j = \ln\left[\sqrt{\frac{1-e^{iq_j-2\eta}}{1-e^{-iq_j-2\eta}}}\right] - \frac{iq_j}{2} \quad (4.34)$$

and

$$\eta = \frac{\text{acosh}\Delta}{2} \tag{4.35}$$

into Eq. (4.32).

The scalar product between two Bethe states $\langle \mathbf{v}|$ and $|\mathbf{u}\rangle$ can be calculated using the commutation relations in Eqs. (4.24-4.27). The multiplication of the bra and ket states in the form of Eq. (4.20) is evaluated by commuting each operator $B(v_j)$ from left to right through the product of $C(u_j)$ operators and then by using the vacuum eigenvalues of the generated A and D operators from Eq. (4.30). When u_j is a solution of Eq. (4.32) and v_j is an arbitrary set of auxiliary parameters the result can be written in a compact form as a determinant of an $N \times N$ matrix – the so-called Slavnov's formula, [66]

$$\langle \mathbf{v}|\mathbf{u}\rangle = \frac{\prod_{i,j=1}^{N} \sinh(v_j - u_i)}{\prod_{j<i} \sinh(v_j - v_i) \prod_{j<i} \sinh(u_j - u_i)} \det \hat{T}, \tag{4.36}$$

where matrix elements are $T_{ab} = \partial_{u_a} \mathcal{T}(v_b)$. Under substitution of $\mathcal{T}(u)$ from Eq. (4.23) these matrix elements read

$$T_{ab} = \frac{\cosh^L(v_b - \eta)}{\cosh^L(v_b + \eta)} \frac{\sinh(2\eta)}{\sinh^2(v_b - u_a)} \prod_{j=1\neq a}^{N} \frac{\sinh(v_b - u_j + 2\eta)}{\sinh(v_b - u_j)} - \frac{\sinh(2\eta)}{\sinh^2(u_a - v_b)} \prod_{j=1\neq a}^{N} \frac{\sinh(u_j - v_b + 2\eta)}{\sinh(u_j - v_b)}. \tag{4.37}$$

The normalisation factor of Bethe states in Eq. (4.20) can be evaluated by taking the $\mathbf{v} \to \mathbf{u}$ limit of Eq. (4.36), [41, 61]

$$\langle \mathbf{u}|\mathbf{u}\rangle = \sinh^N(2\eta) \prod_{i\neq j=1}^{N} \frac{\sinh(u_j - u_i + 2\eta)}{\sinh(u_j - u_i)} \det \hat{M}, \tag{4.38}$$

where the matrix elements are

$$M_{ab} = \begin{cases} -L\frac{\sinh 2\eta}{\cosh(u_a+\eta)\cosh(u_a-\eta)} - \sum_{j\neq a} \frac{\sinh 4\eta}{\sinh(u_a-u_j-2\eta)\sinh(u_a-u_j+2\eta)} & , a = b, \\ \frac{\sinh 4\eta}{\sinh(u_b-u_a+2\eta)\sinh(u_b-u_a-2\eta)} & , a \neq b. \end{cases} \tag{4.39}$$

The local spin operators S_j^α can be expressed in the non-local operators of the algebraic Bethe ansatz A, B, C, and D in Eq. (4.21) by means of the so-called F-matrix [67], which is a representation of a Drinfeld twist [68]. This procedure gives the following explicit relations for all of the three spin operators [69, 70]

$$S_j^+ = \tau_\xi^{j-1} C_\xi \tau_\xi^{L-j}, \tag{4.40}$$

$$S_j^- = \tau_\xi^{j-1} B_\xi \tau_\xi^{L-j}, \tag{4.41}$$

$$S_j^z = \tau_\xi^{j-1} \frac{A_\xi - D_\xi}{2} \tau_\xi^{L-j}, \tag{4.42}$$

where $\xi = -i\pi/2 + \eta$.

Then, any correlation function can be evaluated by means of Eqs. (4.36,4.40-4.42) in terms of determinants of only N-by-N matrices. For example, for the matrix element of the S_1^+ operator, needed for evaluation of the spectral function, one obtains [69, 70]

$$\left\langle \mathbf{v} | S_1^+ | \mathbf{u} \right\rangle = i \frac{\prod_{j=1}^{N+1} \cosh(v_j - \eta)}{\prod_{j=1}^{N} \cosh(u_j + \eta)} \frac{\sinh^{N+1}(2\eta) \det \hat{M}}{\prod_{j<i=2}^{N} \sinh(u_j - u_i) \prod_{j<i=2}^{N+1} \sinh(v_j - v_i)}, \tag{4.43}$$

where $|\mathbf{u}\rangle$ and $\langle \mathbf{v}|$ are a pair of the eigenstates of the Hamiltonian in Eq. (4.1) and the matrix elements of $\hat{M}$ are

$$M_{ab} = \frac{1}{\sinh(u_b - v_a)} \left(\prod_{j=1 \neq b}^{N} \frac{\sinh(u_b - u_j + 2\eta)}{\sinh(u_b - u_j - 2\eta)} \prod_{j=1 \neq a}^{N+1} \sinh(u_b - v_j - 2\eta) - \prod_{j=1 \neq a}^{N+1} \sinh(u_b - v_j + 2\eta) \right), \tag{4.44}$$

for $b < N + 1$, and

$$M_{ab} = \frac{1}{\cosh(v_a - \eta) \cosh(v_a + \eta)}, \tag{4.45}$$

for $b = N + 1$. The expressions of the type like above can be evaluated numerically for large systems or even analytically in some regimes, giving the full access to the correlation functions in the thermodynamic limit without any approximation in one dimension.

Chapter 5

Magnetoelasticity

Magnetoelasticity was discovered in 1842 by James Joule in the form of the magnetostriction effect in iron [71]. A sample of magnetic material changes its shape when its magnetisation changes. Phenomenologically this effect can by understood by constructing the simplest rotational invariant out of the variables involved. Magnetisation $\boldsymbol{M}$ is a vector and deformation $\hat{u}$ is a second rank tensor. Thus, the simplest scalar combination is quadratic in $\boldsymbol{M}$ and linear in $\hat{u}$, making the interaction term between the two $V = \kappa \boldsymbol{M} \cdot \hat{u} \cdot \boldsymbol{M}$, which has to be a scalar since it describes the interaction energy and where κ is a coupling constant. Since magnetisation is usually coupled to the crystalline anisotropy, the magnetostriction effect also exhibits hysteresis.

On the macroscopic level, this effect causes a loss of energy in ferromagnetic cores due to frictional heating. It is also responsible for the low-frequency humming sound that is produced by transformers. Alternating current generates a changing magnetic field, which in turn changes the shape of transformer's core periodically, making it emit acoustic waves. On the microscopic level the classical magnetostriction has to be affected by quantum effects. In the next two section we will discuss the microscopic origin of the magneto-elastic coupling and some of its observable quantities in the quantum regime that can be measured in ultrasound experiments. This chapter focuses on the one-dimension version of the effect, where the reduced dimensionality amplifies the quantum fluctuations in the strongest way possible.

5.1 Microscopic origin

Microscopically magnetostriction originates from the change of the exchange integral that is responsible for the Heisenberg interaction, see the sketch in Fig. 5.1(a), when distance between two neighbouring atoms is changed, see the sketch in Fig. 5.1(b). For small deformations, e.g. caused by a phonon, the exchange integral can be expanded in a Taylor series in small changes of the distance between the atoms with respect to its equilibrium value given by the lattice parameter b. The zeroth term in such an expansion is the usual coupling constant in the Heisenberg model and small corrections in the first, in the second, and so on orders are the spin-phonon

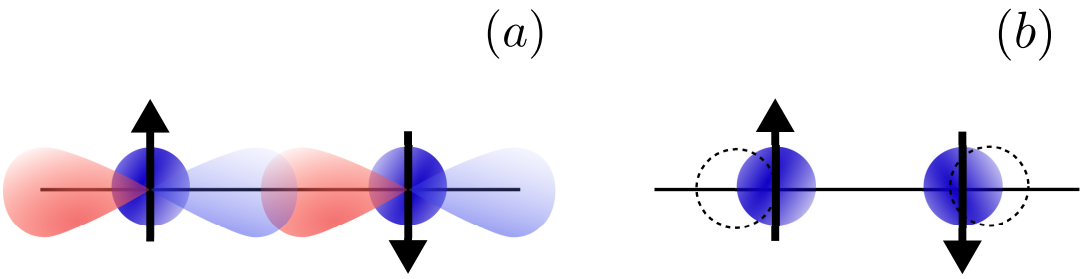

Figure 5.1: (a) A schematic overlap between a pair of orbitals of neighbouring atoms that corresponds to the exchange coupling constant between the spins on these atoms in the Heisenberg model. (b) A small deviation in the distance between the atoms from its equilibrium value that changes the exchange integral and is responsible microscopically from the magneto-elastic coupling.

couplings. In one dimension the coupling term reads

$$V = \sum_j \left(J_1 \left(x_{j+1} - x_j \right) + J_2 \left(x_{j+1} - x_j \right)^2 \right) \boldsymbol{S}_j \cdot \boldsymbol{S}_{j+1}, \tag{5.1}$$

where the coupling constants J_1 and J_2 are the derivatives of the exchange energy with respect to distance between the atoms evaluated at the lattice spacing,

$$J_n = \frac{1}{n!} \left. \frac{d^n J\left(x\right)}{dx^n} \right|_{x=b}, \tag{5.2}$$

and $x_{j+1} - x_j$ are small deviations caused by a deformation. In the quantum regime two subleading terms of the expansion are needed, unlike in the classical regime, due to peculiarities of the quantum fluctuations.

In the full quantum regime deformation field x_j also has to be quantised forming phonon modes and the total Hamiltonian consists of three parts, [72, 73]

$$H = H_m + H_{ph} + V, \tag{5.3}$$

where the Heisenberg model describing magnetism is

$$H_m = J \sum_j \boldsymbol{S}_j \cdot \boldsymbol{S}_{j+1}, \tag{5.4}$$

$J \equiv J_0$ is the exchange integral in equilibrium, $\boldsymbol{S}_j$ are the spin operators, the free phonon model describing the deformations is

$$H_{ph} = \sum_k \omega_k a_k^\dagger a_k, \tag{5.5}$$

the dispersion on the equidistant lattice is $\omega_k = 2\omega_D \left| \sin\left(k/2\right) \right|$, ω_D is Debye energy,

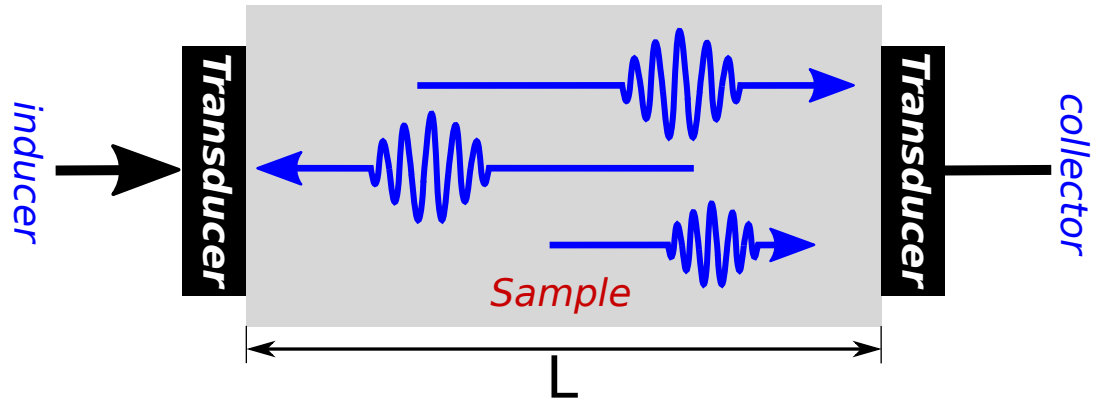

Figure 5.2: Scheme of an ultrasound experiment in an effectively one-dimensional magnetic insulator. The length of the magnetic chains is L. Inducer injects a phonon at a given time. Collector detects it recording the propagation time t and amplitude of the signal.

a_k are the bosonic operators, the position operator is

$$x_j = \sum_k \sqrt{\frac{b}{m v_0 |k| L}} \left(a_k + a_k^\dagger\right) e^{-ikj}, \tag{5.6}$$

v_0 is the sound velocity, and V is the spin-phonon coupling in Eq. (5.1).

The Heisenberg Hamiltonian H_m in Eq. (5.4) can be analysed using the nonoperative methods described in Chapters 2-4. The phonon Hamiltonian H_{ph} is already diagonal, see Eq. (5.5). And the coupling V can be treated perturbatively since the energy scale of the phonons, Debye energy ω_D, is typically very different from the energy of the magnons, exchange energy J. Thus, the whole model in Eq. (5.3) can be analysed, including its thermodynamic observables and the expectation values of relevant operators, completely on the quantum mechanical footing in one dimension.

5.2 Observables in the quantum regime

A way of probing the magnetoelastic effects in the quantum regime is provided by ultrasound in magnetic insulators. At low temperatures and at low ultrasound powers only a few phonons are excited and the magnet is close to its ground state. The spin chains can realised in anisotropic three-dimensional magnets, which are effective one-dimensional in a finite windows of temperature, e.g. $KCuF_3$ [74] or Cs_2CuCl_4 [75], in which the chains are oriented along the direction of the strongest exchange coupling.

In an ultrasound experiment, a pair of piezolements are attached on the opposite sides of a sample perpendicular to the directions of the spin chains, see the sketch of an experiment in Fig. 5.2. One piezoelement (inducer in Fig. 5.2) injects a phonon

on one side of the chain, then the phonon propagates through the sample, and is detected on the the other end by the other piezoelement (collector in Fig. 5.2). Two quantities can be measure in such a setup. One is propagation time, t, of the phonon over a fixed distance, L, that gives the phonon velocity

$$v = \frac{L}{t}. \tag{5.7}$$

The other is the phonon attenuation on the collector,

$$A = \frac{I_{collector}}{I_{inducer}}. \tag{5.8}$$

Both quantities are finite in a non-magnetic crystal: there is a finite sound velocity, $v = v_{ph}$, and there are phonon relaxation mechanisms due to their scattering off non-magnetic impurities and dislocations in a crystal, $A < 1$. However, in a magnetic crystal both quantities are magnetic-field dependent, $v(B) \neq v(B = 0)$ and $A(B) \neq A(B = 0)$. The magnetic-field sensitive parts come purely from the magnetic subsystem that is strongly affected by the magnetic field. These contributions are described microscopically by the model in Eq. (5.3). The renomalisation of sound velocity, $v(B) - v(0)$, in Eq. (5.7) is given the first magnetoelastic constant J_1 in Eq. (5.1) and attenuation of the phonon amplitude, $A(B) - A(0)$, in Eq. (5.8) by the second constant J_2 in Eq. (5.1) [40]. The one-dimensional regime in magnetic insulators is readily available in experiments on Cs_2CuCl_4 [75, 76], $CsNiCl_3$ [77], $KCuF_3$ [78], and a metal organic coordination polymer Cu(II)-2,5-bis(pyrazol-1-yl)-1,4-dihydroxybenzene [79]. Since in the experimentally relevant regimes the magnetic subsystem itself is strongly correlated, the phonons are essentially free excitations, and the coupling between them is perturbative, the ultrasound can also serve as a probe of strong correlations in one-dimensional spin systems, similarly to the neutron-scattering technique.

This chapter gives a broader physical context and provides a motivation for the microscopic theory of magneto-elasticity in one dimension that is constructed in the paper [40] reprinted in the appendix.

Chapter 6

Conclusions

The general aim of this work is advancing the microscopic understanding of the many-body physics, which is still a major open problem. At low energy the effective theory is already established on firm grounds in the form of Landau's Fermi liquid in two and three dimensions and in the form of Luttinger liquid in one dimension. However, the higher energy scales remain mainly unexplored. The only successful attempt so far emerged only recently, in the last decade, in the form of the mobile impurity model (also called the non-linear Luttinger liquid theory) in one dimension, which still describes only proximity of the spectral edges but not arbitrary many-body excitations at high energy. This result gave an inspiration for this work. The choice of the reduced dimension (one dimension) was motivated by at least somewhat simplified version of the problem, which, e.g., enables the microscopic many-body technique of Bethe ansatz, allowing to tackle the enormous complexity of the many-body systems in full in this case.

The first step was the analysis of the spectral edge mode for a variety of one-dimensional models with short-range interactions that bounds a continuum of many-body excitations. Explicit diagonalisation by means of Bethe ansatz techniques, described in Chapter 4, showed that this mode has an almost perfect parabolic dispersion in all cases [35, 36]. Based on this emergent phenomenon, the spectral edge mode can be described empirically by a free, nonrelativistic particle with effective mass identified from the low-energy theory as a free electron mass strongly renormalised by interactions via the dimensionless Luttinger parameter K (K_σ for particles with spin). However, unlike a free particle, the spectral edge mode is not protected by a symmetry, thus deviations from the quadratic dispersion may develop—the biggest discrepancy ($\lesssim 20\%$) occurs for Fermi particles with spin and a very large interaction strength. The empirical model remains robust for finite sound velocities of the collective modes at low energies $v\left(v_\sigma\right) > v_1$, where $v_1 = 2\pi/\left(mL\right)$ is the quantum of momentum.

The relevance of the Luttinger (low-energy) parameters beyond the low-energy limit implies that they can be extracted using a much wider range of experimental data using the whole energy window from the bottom of the band to the Fermi energy. However, the dispersion of the spectral edge mode itself cannot be used as

a qualitative feature to rule out interaction effects since the interactions between particles do not change the parabolic shape of the single-particle dispersion. The biggest deviations could be observed for strongly interacting spinful fermions ($K_\sigma \gtrsim 10$), e.g., electrons in semiconductors at low densities or cold Fermi atoms in a one-dimensional trap that would require a good resolution of the experiment.

This result complements the mobile impurity model, which was developed by Glazman and co-workers as a description of one-dimensional systems above the spectral edge at high energies and is summarised in Chapter 3. The parabolicity of the dispersion of the edge mode removes an arbitrary input parameter (curvature of the dispersion) that leaves only the few Luttinger parameters and the bare electron mass as a minimal set of necessary ingredients to model excitations above the spectral edge at arbitrary energies. Within such a framework, for example, exponents of the spectral function are expressed explicitly in terms of only a few Luttinger parameters. The explicit result in the case of fermions is obtained in the paper [36] and is quoted in Section 3.2

The main result of this work is identification of a hierarchy of modes as a general structure in the many-body excitations outside of the low energy regime. It was shown [37, 38] that the hierarchy, which emerges in systems of interacting fermions in one dimension at high energy, is controlled by the system length—the corresponding form factors are proportional to different powers of $\mathcal{R}^2/L^2$, where $\mathcal{R}$ is the particle-particle interaction radius and L is the length of the system, in marked contrast to the well-known fermionic quasiparticles of a Fermi liquid and hydrodynamic modes of a Luttinger liquid at low energy. The dynamic response functions have been obtained for a model of spinless fermions with short-range interactions using the exact diagonalisation methods of Bethe ansatz for the spectrum and the form factors of the system. Analysing the spectral function in detail, it has been found that the first-level (strongest) mode in long systems has a parabolic dispersion, like that of a renormalized free particle. The second-level excitations produce a singular power-law line shape for the first-level mode and different kinds of power-law behavior at the spectral edges. The threshold exponents predicted by the mobile impurity model were reproduced by the second-level excitation of the hierarchy around the spectral edges.

Using the same many-body matrix elements obtained microscopically, the local density of states (LDOS) has also been calculated, which provides a more convenient way to analyse how the hierarchical structure at high energy changes into the hydrodynamic modes of the Luttinger liquid at low energies. It has been shown, via a full Bethe-ansatz calculation, that the LDOS is suppressed at the Fermi energy in a power-law fashion in full accord with the prediction of the Tomonaga-Luttinger model. Away from the Fermi point, where the Lorentz invariance of the linear dispersion is reduced to Galilean by the parabolicity of the spectrum, the LDOS is dominated by the first (leading) level of the hierarchy. The transition from one regime to the other was demonstrated to be a smooth crossover.

This new result has already been confirmed experimentally, in tunnelling spectroscopy measurements on GaAs-AlGaAs double-quantum-well heterostructures [38,

39]. The quantum wires were formed in/out the top well by electrostatic gates and momentum-resolved tunnelling of electrons in the upper layer from/to a 2D electron gas in the lower layer probes the spectral function for spinful fermions. Control of the bias between the two wells provides the energy and magnetic field applied perpendicular to the wires provides the momentum resolution in this setup, see [28] for experimental details. A well-resolved spin-charge separation was observed at low energy with appreciable interaction strength—a distinct effect of the spinful Luttinger liquid described in Section 2.3. The ratio of charge and spin velocities is upto $v_c/v_s \approx 1.8$ confirming that the interaction energy is of the order of the kinetic energy in these experiments. At high energy, in addition to the spin and charge curves, there is only a small structure just above k_F, which amplitude decays rapidly away from the k_F point, in 10μm-long wires. This is no surprise since the amplitude of the second-level excitations is suppressed by at least four orders of magnitude with respect to the clearly observed first-level excitations, $\mathcal{R}^2/L^2 \sim 10^{-4}$. In an order of magnitude shorter wires (1μm-long) the suppression factor is two orders of magnitude weaker, $\mathcal{R}^2/L^2 \sim 10^{-2}$, and a complete second order mode is clearly observed [39]. The same experimental setup can be used to measure the spectral edge exponents in the spectral function predicted by the non-linear Luttinger liquid theory, which is described in Chapter 3.

An application of hierarchy of modes was a necessary ingredient in construction of a microscopic theory of magnetoelasticity, introduced in Chapter 5, in one dimension [40]. It was done using the diagonalisation methods of Bethe ansatz, described in Chapter 4. The matrix elements for the four-point correlation function that couples the strongly-correlated spins to phonons dynamically have been derived and it has been shown that the contribution of the static correlation function to the renormalisation of the sound velocity is parametrically larger than the dynamical correlation functions. Also it has been shown that the resonant decay of phonons in the many-body spin continuum vanishes very fast, as the fourth power of the length in long chains. However, another mechanism has been identified, hybridisation of the phonons with the magnetic excitations at high energy via the dynamical correlation function, that remains finite in the thermodynamic limit. The many-body excitations of the spin chain that are involved in this mechanism are at high energy and are away from the spectral edges. The hierarchy provides the only tool for evaluating the principal contribution to the phonon attenuation, which otherwise would not be tractable due to exponential complexity of the Fock space at high energy.

The hybridisation mechanism has already been confirmed experimentally in ultrasonic measurements on high-quality single crystals of Cs_2CuCl_4 in its one-dimensional regime [40]. The observed magnetic-field dependent part of the attenuation has the same magnetic field dependence as predicted by the hybridisation mechanism.

This work describes techniques that are used in the papers and is complementary to them. While I have tried to give a overall picture with at least a bit of detail, some topics (like the main result of the hierarchy of modes) were discussed only briefly or (like bosonic systems) were left out almost completely. For a more in-

depth discussion of these topics the reader is referred to the original research papers, which are reproduced in the appendix.

I would like to acknowledge everybody who was contributing to and helping with this work. I am grateful to Jan von Delft for introducing me to the concept of Bethe ansatz. His constructive but physically intuitive approach to this complicated many-body technique has laid out all of the necessary basics for my research in this field. The biggest appreciation is reserved for Andy Schofield for his kind hospitality at Birmingham University and for introducing me to the field of one-dimensional systems, and, which is probably even more important, for stressing the still open problems in this area of physics. I have benefited a great deal from his expertise and from his simplifying approach to even the most complicated problems that always singles out the core part of the puzzle, helping significantly to solve it and providing often at least a part of the answer. I am also grateful to Chris Ford for countless discussions of his experiments on tunnelling spectroscopy of quantum wires and for sharing the new data, which all together were a motivation for this project and in particular have led to the main result so far—the hierarchy of modes. I would like to thank Leonid Glazman, Maxim Khodas, John Chalker, Dimitri Gangardt, Maria Moreno, Yiqing Jin, Michael Lang, Bernd Wolf, and Martin Long for stimulating discussions and collaboration on this project. I am especially thankful to Peter Kopietz for inspiring discussions and for his interest in research presented here. His unceasing support and constant encouragement have made finishing this project possible.

Chapter 7

Bibliography

[1] L. D. Landau, *The Theory of a Fermi Liquid*, Sov. Phys. JETP **3**, 920 (1957).

[2] L. D. Landau, *Oscillations in a Fermi Liquid*, Sov. Phys. JETP **5**, 101 (1957).

[3] L. D. Landau, *The Properties of the Green Function for Particles in Statistics*, Sov. Phys. JETP **7**, 182 (1958).

[4] J. Bardeen, L. N. Cooper, and J. R. Schrieffer, *Theory of Superconductivity*, Phys. Rev. **108**, 1175 (1957).

[5] D. C. Mattis, *New wave-operator identity applied to the study of persistent currents in 1D*, J. Math. Phys. **15**, 609 (1974).

[6] A. Luther and I. Peschel, *Single-particle states, Kohn anomaly, and pairing fluctuations in one dimension*, Phys. Rev. B **9**, 2911 (1974).

[7] R. Heidenreich, B. Schroer, R. Seiler, and D. Uhlenbrock, *Sine-Gordon equation and one-dimensional electron-gas*, Phys. Lett. **54A**, 119 (1975).

[8] F. D. M. Haldane, *Coupling between charge and spin degrees of freedom in the one-dimensional Fermi gas with backscattering*, J. Phys. C **12**, 4791 (1979).

[9] J. von Delft and H. Schoeller, *Bosonization for beginners—refermionization for experts*, Annalen Phys. **7**, 225 (1998).

[10] M. Khodas, M. Pustilnik, A. Kamenev, and L. I. Glazman, *Dynamics of Excitations in a One-Dimensional Bose Liquid*, Phys. Rev. Lett. **99**, 110405 (2007).

[11] A. Imambekov, L. I. Glazman, *Phenomenology of One-Dimensional Quantum Liquids Beyond the Low-Energy Limit*, Phys. Rev. Lett. **102**, 126405 (2009).

[12] J. M. Luttinger, *Fermi Surface and Some Simple Equilibrium Properties of a System of Interacting Fermions*, Phys. Rev. **119**, 1153 (1960).

[13] A .A. Abrikosov, L. P. Gorkov, I. E. Dzyaloshinski, *Method of Quantum Field Theory in Statistical Physics*, Dover Publications, New York, 1975.

[14] D. S. Greywall, *Heat capacity of multilayers of He_3 adsorbed on graphite at low millikelvin temperatures*, Phys. Rev. B **41**, 1842 (1990).

[15] H. R. Glyde, B. Faak, N. H. van Dijk, H. Godfrin, K. Guckelsberger, and R. Scherm, *Effective mass, spin fluctuations, and zero sound in liquid He_3*, Phys. Rev. B **61**, 1421 (2000).

[16] P. Nozieres and J. M. Luttinger, Derivation of the Landau Theory of Fermi Liquids. I. Formal Preliminaries, Phys. Rev. 127, 1423 (1962).

[17] P. Nozieres and J. M. Luttinger, Derivation of the Landau Theory of Fermi Liquids. II. Equilibrium Properties and Transport Equation, Phys. Rev. 127, 1431 (1962).

[18] R. Shankar, *Renormalization group for interacting fermions in d>1*, Physica A **177**, 530 (1991).

[19] R. Shankar, *Renormalization-group approach to interacting fermions*, Rev. Mod. Phys. **66**, 129 (1994).

[20] Yu. A. Bychkov, L.P. Gor'kov, I.E. Dzyaloshinskii, *Possibility of Superconductivity Type Phenomena in a One-dimensional System*, Sov. Phys. JETP **23**, 489 (1966).

[21] S. Tomonaga, *Remarks on Bloch's Method of Sound Waves applied to Many-Fermion Problems*, Prog. Theor. Phys. **5**, 544 (1950).

[22] J.M. Luttinger, *An Exactly Soluble Model of a Many-Fermion System*, J. Math. Phys. **4**, 1154 (1963).

[23] T. Giamarchi, *Quantum physics in one dimension*, Clarendon press, Oxford, 2003.

[24] S. K. Satija, J. D. Axe, G. Shirane, H. Yoshizawa, and K. Hirakawa, *Neutron scattering study of spin waves in one-dimensional antiferromagnet $KCuF_3$*, Phys. Rev. B **21**, 2001 (1980).

[25] D. Jerome and H. J. Schulz, *Organic conductors and superconductors*, Adv. Phys. **31**, 299 (1982).

[26] Z. Yao, H. W. Ch. Postma, L. Balents, and C. Dekker, *Carbon nanotube intramolecular junctions*, Nature **402**, 273 (1999).

[27] O. M. Auslaender,, A. Yacoby, R. de Picciotto, K. W. Baldwin, L. N. Pfeiffer, and K. W. West, *Tunneling Spectroscopy of the Elementary Excitations in a One-Dimensional Wire*, Science **295**, 825 (2002).

[28] Y. Jompol, C. J. B. Ford, J. P. Griffiths, I. Farrer, G. A. C. Jones, D. Anderson, D. A. Ritchie, T. W. Silk, A. J. Schofield, *Probing Spin-Charge Separation in a Tomonaga-Luttinger Liquid*, Science **325**, 597 (2009).

[29] A. F. Andreev, *The hydrodynamics of two- and one-dimensional liquids*, Sov. Phys. JETP **51**, 1038 (1980).

[30] K. V. Samokhin, *Lifetime of excitations in a clean Luttinger liquid*, J. Phys. Condens. Matter **10**, L533 (1998).

[31] P. Nozieres and C. T. De Dominicis, *Singularities in the X-Ray Absorption and Emission of Metals. III. One-Body Theory Exact Solution*, Phys. Rev. **178**, 1097 (1969).

[32] M. Pustilnik, M. Khodas, A. Kamenev, and L. I. Glazman, *Dynamic Response of One-Dimensional Interacting Fermions*, Phys. Rev. Lett. **96**, 196405 (2006).

[33] M. Khodas, M. Pustilnik, A. Kamenev, and L. I. Glazman, *Fermi-Luttinger liquid: Spectral function of interacting one-dimensional fermions*, Phys. Rev. B **76**, 155402 (2007).

[34] A. Imambekov, T. L. Schmidt, and L. I. Glazman, *One-dimensional quantum liquids: Beyond the Luttinger liquid paradigm*, Rev. Mod. Phys. **84**, 1253 (2012).

[35] O. Tsyplyatyev and A. J. Schofield, *Luttinger parameters of interacting fermions in one dimension at high energies*, Phys. Rev. B **88**, 115142 (2013).

[36] O. Tsyplyatyev and A. J. Schofield, *Spectral-edge mode in interacting one-dimensional systems*, Phys. Rev. B **90**, 014309 (2014).

[37] O. Tsyplyatyev, A. J. Schofield, Y. Jin, M. Moreno, W. K. Tan, C. J. B. Ford, J. P. Griffiths, I. Farrer, G. A. C. Jones, and D. A. Ritchie, *Hierarchy of Modes in an Interacting One-Dimensional System*, Phys. Rev. Lett. **114**, 196401 (2015).

[38] O. Tsyplyatyev, A. J. Schofield, Y. Jin, M. Moreno, W. K. Tan, A. S. Anirban, C. J. B. Ford, J. P. Griffiths, I. Farrer, G. A. C. Jones, and D. A. Ritchie, *Nature of the many-body excitations in a quantum wire: Theory and experiment*, Phys. Rev. B **93**, 075147 (2016).

[39] M Moreno, C. J. B. Ford, Y. Jin, J. P. Griffiths, I. Farrer, G. A. C. Jones, D. A. Ritchie, O. Tsyplyatyev, and A. J. Schofield, *Nonlinear spectra of spinons and holons in short GaAs quantum wires*, Nat. Commun. **7**, 12784 (2016).

[40] O. Tsyplyatyev, P. Kopietz, Y. Tsui, B. Wolf, P. T. Cong, N. van Well, F. Ritter, C. Krellner, W. Aßmus, and M. Lang, *Many-body theory of magnetoelasticity in one dimension*, Phys. Rev. B **95**, 045120 (2017).

[41] M. Gaudin, *The Bethe Wavefunction*, Cambridge University Press, Cambridge, 2014.

[42] F. D. M. Haldane, *'Luttinger liquid theory' of one-dimensional quantum fluids. I. Properties of the Luttinger model and their extension to the general 1D interacting spinless Fermi gas*, J. Phys. C. **14**, 2585 (1981).

[43] I.E. Dzyaloshinskii and A.I. Larkin, *Correlation functions for a one-dimensional Fermi system with long-range interaction (Tomonaga model)*, Sov. Phys. JETP **38**, 202 (1974).

[44] J. Sòlyom, *The Fermi gas model of one-dimensional conductors*, Adv. Phys. **28**, 209 (1979).

[45] F. D. M. Haldane, *Demonstration of the "Luttinger liquid" character of Bethe-ansatz-soluble models of 1-D quantum fluids*, Phys. Lett. A **81**, 153 (1981).

[46] A. Altland and B. Simons, *Condensed Matter Field Theory*, Cambridge University Press, Cambridge, 2010.

[47] R. Heidenreich, R. Seiler, and D. A. Uhlenbrock, *The Luttinger model*, J. Stat. Phys. **22**, 27 (1980).

[48] J. W. Negele and H. Orland, *Quantum Many-Particle Systems*, Addison-Wesley Publishing Company, Redwood City, 1988.

[49] V. J. Emery, *Theory of the one-dimensional electron gas, in Highly Conducting One-Dimensional Solids*, Plenum Press, 1979.

[50] V. Meden and K. Schönhammer, *Spectral functions for the Tomonaga-Luttinger model*, Phys. Rev. B **46**, 15753 (1992).

[51] J. Voit, *Charge-spin separation and the spectral properties of Luttinger liquids*, Phys. Rev. B **47**, 6740 (1993).

[52] G. D. Mahan, *Excitons in Metals: Infinite Hole Mass*, Phys. Rev. **163**, 612 (1967).

[53] B. Roulet, J. Gavoret, and P. Noziéres, *Singularities in the X-Ray Absorption and Emission of Metals. I. First-Order Parquet Calculation*, Phys. Rev. **178**, 1072 (1969).

[54] B. Roulet, J. Gavoret, and P. Noziéres, *Singularities in the X-Ray Absorption and Emission of Metals. II. Self-Consistent Treatment of Divergences*, Phys. Rev. **178**, 1072 (1969).

[55] A. Imambekov and L. I. Glazman, *Universal theory of nonlinear Luttinger liquids*, Science **323**, 228 (2009).

[56] T. L. Schmidt, A. Imambekov, and L. I. Glazman, *The fate of 1D spin-charge separation away from Fermi points*, Phys. Rev. Lett. **104**, 116403 (2010).

[57] T. L. Schmidt, A. Imambekov, and L. I. Glazman, *Spin-charge separation in one-dimensional fermion systems beyond the Luttinger liquid theory*, Phys. Rev. B **82**, 245104 (2010).

[58] R. G. Pereira, S. R. White, and I. Affleck, *Exact Edge Singularities and Dynamical Correlations in Spin-1/2 Chains*, Phys. Rev. Lett. **100**, 027206 (2008).

[59] A. Kamenev and L. I. Glazman, *Dynamics of a one-dimensional spinor Bose liquid: A phenomenological approach*, Phys. Rev. A **80**, 011603(R) (2009).

[60] H. Bethe, *Zur Theorie der Metalle. I. Eigenwerte und Eigenfunktionen der linearen Atomkette*, Zeit. für Physik **71**, 205 (1931).

[61] V. E. Korepin, N. M. Bogoliubov, A. G. Izergin, *Quantum inverse scattering methods and correlation functions*, Cambridge University Press, Cambridge, 1993.

[62] E. H. Lieb and W. Liniger, *Exact Analysis of an Interacting Bose Gas. I. The General Solution and the Ground State*, Phys. Rev. **130**, 1605 (1963).

[63] E. H. Lieb, *Exact Analysis of an Interacting Bose Gas. II. The Excitation Spectrum*, Phys. Rev. **130**, 1616 (1963).

[64] F. H. L. Essler, H. Frahm, F. Gömann, A. Klümper, V. E. Korepin, *The One-Dimensional Hubbard Model*, Cambridge University Press, Cambridge, 2005.

[65] B. Sutherland, *Beautiful Models 70 Years of Exactly Solved Many-Body Problems*, World Scientific Publishing, Singapore, 2004.

[66] N. A. Slavnov, *Calculation of scalar products of wave functions and form factors in the framework of the alcebraic Bethe ansatz*, Theor. Math. Phys. **79**, 502 (1989).

[67] J.M. Maillet and J. Sanchez de Santos, *Drinfel'd Twists and Algebraic Bethe Ansatz*, Amer. Math. Soc. Transl. (2) **201**, 137 (2000).

[68] V. G. Drinfeld, *Constant quasiclassical solutions of the Yang-Baxter quantum equation*, Sov. Math. Dokl. **28**, 667 (1983).

[69] N. Kitanine, J.M. Maillet, V. Tetras, *Form factors of the XXZ Heisenberg spin-12 finite chain*, Nucl. Phys. B **554**, 647 (1999).

[70] N. Kitanine, J.M. Maillet, *Correlation functions of the XXZ Heisenberg spin-12 chain in a magnetic field*, Nucl. Phys. B **567**, 554 (2000).

[71] J. Joule, *On a new class of magnetic forces*, Annals of Electricity, Magnetism, and Chemistry **8**, 219 (1842).

[72] K. Tani and H. Mori, *Ultrasonic Attenuation near the Magnetic Critical Point*, Prog. Theor. Phys. 39, 876 (1968).

[73] K. Kawasaki and A. Ikushima, *Velocity of Sound in MnF_2 near the Néel Temperature*, Phys. Rev. B **1**, 3143 (1970).

[74] B. Lake, D. A. Tennant, J.-S. Caux, T. Barthel, U. Schollwöck, S. E. Nagler, and C. D. Frost, *Multispinon Continua at Zero and Finite Temperature in a Near-Ideal Heisenberg Chain*, Phys. Rev. Lett. **111**, 137205 (2013).

[75] R. Coldea, D. A. Tennant, and Z. Tylczynski, *Extended scattering continua characteristic of spin fractionalization in the two-dimensional frustrated quantum magnet Cs_2CuCl_4 observed by neutron scattering*, Phys. Rev. B **68**, 134424 (2003).

[76] 8 A. Sytcheva, O. Chiatti, J. Wosnitza, S. Zherlitsyn, A. A. Zvyagin, R. Coldea, and Z. Tylczynski, *Short-range correlations in quantum frustrated spin system*, Phys. Rev. B **80**, 224414 (2009).

[77] Y. Trudeau, M. Poirier, and A. Caillé, *Ultrasonic study of the quasi-one-dimensional spin fluctuations in $CsNiCl_3$ in the presence of a magnetic field*, Phys. Rev. B 46, 169 (1992).

[78] B. Lake, D. A. Tennant, C. D. Frost, and S. E. Nagler, *Quantum criticality and universal scaling of a quantum antiferromagnet*, Nat. Mater. **4**, 329 (2005).

[79] B. Wolf, S. Zherlitsyn, B. Lüthi, N. Harrison, U. Löw, V. Pashchenko, M. Lang, G. Margraf, H.-W. Lerner, E. Dahlmann, F. Ritter, W. Aßmus, and M. Wagner, *Acoustic and magnetic anomalies near the saturation field of the $S = 1/2$ antiferromagnetic Heisenberg chain studied on a Cu(II) coordination polymer*, Phys. Rev. B **69**, 092403 (2004).

Appendix A

Selected publications

PHYSICAL REVIEW B **88**, 115142 (2013)

Luttinger parameters of interacting fermions in one dimension at high energies

O. Tsyplyatyev and A. J. Schofield
School of Physics and Astronomy, The University of Birmingham, Birmingham, B15 2TT, United Kingdom
(Received 22 May 2013; revised manuscript received 2 July 2013; published 26 September 2013)

Interactions between electrons in one dimension are fully described at low energies by only a few parameters of the Tomonaga-Luttinger model, which is based on linearization of the spectrum. We consider a model of spinless fermions with short-range interaction via the Bethe-Ansatz technique and show that a Luttinger parameter emerges in an observable beyond the low-energy limit. A distinct feature of the spectral function, the edge that marks the lowest possible excitation energy for a given momentum, is parabolic for arbitrary momenta and the prefactor is a function of the Luttinger parameter, K.

DOI: 10.1103/PhysRevB.88.115142 PACS number(s): 71.10.Pm, 03.75.Kk, 73.21.−b

I. INTRODUCTION

The effects of interactions between fermions in one dimension are mainly understood at low energies within the scope of the Tomonaga-Luttinger model.[1] This framework is based on the linear approximation to the single-particle spectrum around the Fermi energy and provides, via the bosonization technique,[1] a generic way to calculate various correlation functions. Understanding of interacting fermions beyond the low-energy limit still presents a challenge. Studies are currently focused on dynamical response functions,[2–7] e.g., the spectral function which can be measured by momentum-resolved tunneling of electrons in semiconductors,[8,9] by angle-resolved photoemission in correlated materials[10] and by photoemission spectroscopy in cold atoms.[11] Recently significant theoretical progress was achieved in this direction by making a connection between Luttinger liquids and the Fermi edge singularity problem.[12] As a result, power-law singularities were found at the edge of the spectral function at zero temperature and their powers were related to the corresponding curvature.[13] The edge marks the smallest energy at a fixed momentum with which a particle can tunnel into the system. At low energies the edge disperses linearly with a slope which is the sound velocity of collective modes v defined by parameters from the Tomonaga-Luttinger model;[14] a small quadratic correction to the linear slope at low momenta was found in Ref. 3. In this paper we calculate the position of the edge for the spinless fermions with a short-range interaction at arbitrary energies and show that a Luttinger parameter is still relevant at large energies.

Our strategy is to consider the exact diagonalization of the model on a lattice via the Bethe-Ansatz approach. Then we analyze the spectral function in the continuum regime—a combination of the thermodynamic limit and a small occupancy of the lattice[15]—which corresponds to the continuum model with a contact interaction. In this regime we find that the position of the edge is parabolic for arbitrary momenta and the prefactor is a function of the dimensionless Luttinger parameter K [see Eq. (10)], which is defined in the low-energy domain of the Tomonaga-Luttinger model. Our result could be directly observed in experiments on spin-polarized particles such as electrons in ferromagnetic semiconductors[16] using the setups of Refs. 8 and 9 or polarized cold atoms using the setup of Ref. 11. In closely related models of spin chains,[1] the position of the edge depends on the Luttinger K in an analogous way, but for a weakly polarized chain, for example, the parabolic function of momentum becomes a cosine. With the parabolic shape found in this paper, the phenomenological nonlinear Luttinger liquid theory[13] gives a divergent power of the edge singularity.

In the continuum regime the Luttinger parameter K is bounded and the smallest K for large interaction strengths is almost degenerate with its noninteracting value $K = 1$. We use the Bethe-Ansatz approach for a finite-range interaction potential beyond nearest neighbor in the limit $V = \infty$ and show that the regime of strong interaction effects (corresponding to the minimum value of $K = 0$ in the Tomonaga-Luttinger model) can only be accessed by a microscopic model with the interaction range at least of the order of the average distance between particles.

The paper is organized as follows. Section II contains a definition of the model of spinless fermions on a lattice and the spectral function. In Sec. III we analyze the edge of the spectral function for next-neighbor interaction in the low (Sec. A) and high (Sec. B) regimes. In Sec. IV we consider a finite-range interaction in the limit of infinite interaction strength. In the Appendix we give numerical data that clarify the calculations in Secs. III and IV.

II. MODEL

Spinless fermions on a one-dimensional lattice with L sites interact via a two-body potential V_i as

$$H = -t\sum_{j=1}^{L}(c_j^\dagger c_{j+1} + c_j^\dagger c_{j-1}) + \sum_{j=1,i=1}^{L,\infty} V_i c_j^\dagger c_j c_{j+i}^\dagger c_{j+i}, \tag{1}$$

where t is a hopping amplitude and operators c_j obey Fermi commutation relations $\{c_i, c_j^\dagger\} = \delta_{ij}$.[17] Below we consider periodic boundary conditions $c_{L+1} = c_1$ to maintain the translation symmetry of the finite length chain and consider only repulsive interactions, $V_i > 0$.

The spectral function describes the tunneling probability for a particle with momentum k and energy ε, $A(k,\varepsilon) = -\mathrm{Im}G(k,\varepsilon)\,\mathrm{sgn}(\varepsilon - \mu)/\pi$, where μ is the chemical potential and $G(k,\varepsilon) = -i\sum_j \int dt e^{i(kj-\varepsilon t)}\langle T(e^{-iHt}c_j e^{iHt}c_1^\dagger)\rangle/L$ is a Fourier transform of the single-particle Green function at zero temperature. To be specific, we discuss only a particular region, $k_F < k < 3k_F$ and $\varepsilon > \mu$. The spectral function in this domain

reads[18]

$$A(k,\varepsilon) = L\sum_f |\langle f|c_1^\dagger|0\rangle|^2\delta(k-P_f)\delta(\varepsilon+E_0-E_f), \qquad (2)$$

where E_0 is the energy of the ground state $|0\rangle$, and P_f and E_f are the momenta and the eigenenergies of the eigenstates $|f\rangle$; all eigenstates are assumed normalized.

III. NEXT-NEIGHBOR INTERACTION

The model of Eq. (1) can be diagonalized using the Bethe Ansatz when the interaction potential is restricted to the nearest neighbor only, $V_i = V\delta_{i,1}$.[19] In the coordinate basis, $|\psi\rangle = \sum_{j_1<\cdots<j_n} a_{j_1\ldots j_n} c_{j_1}^\dagger \ldots c_{j_n}^\dagger|\text{vac}\rangle$, where $|\text{vac}\rangle$ is the fermionic vacuum, a superposition of plain waves, $a_{j_1\ldots j_n} = \sum_P e^{i\sum_{l=1}^n k_{P_l} j_l + i\sum_{l<m=1}^n \varphi_{P_l,P_m}}$, is an n particle eigenstate and $H|\psi\rangle = E|\psi\rangle$ with the eigenenergy

$$E = -2t\sum_{j=1}^n \cos(k_j) + 2tn\ . \qquad (3)$$

Here a constant $2tn$ was added for convenience, the phase shifts

$$e^{i2\varphi_{jm}} = -\frac{e^{i(k_j+k_m)} + 1 + \frac{V}{t}e^{ik_j}}{e^{i(k_j+k_m)} + 1 + \frac{V}{t}e^{ik_m}} \qquad (4)$$

are fixed by the two-body scattering problem, and $\sum_P$ is a sum over all permutations of n integer numbers. The periodic boundary condition quantizes all single-particle momenta simultaneously,

$$Lk_j - 2\sum_m \varphi_{jm} = 2\pi\lambda_j, \qquad (5)$$

where λ_j are integer numbers. The sum $P = \sum_j k_j$ is a conserved quantity—the total momentum of an n particle state.

The solutions of the nonlinear system of equations Eq. (5) can be classified in the limit of noninteracting particles. Under substitution of the scattering phase $2\varphi_{jm} = \pi$ for $V = 0$, Eq. (5) decouples into a set of independent quantization conditions for plain waves,

$$k_j = \frac{2\pi\lambda_j}{L}. \qquad (6)$$

The corresponding eigenstates are Slater determinants which vanish when the momenta of any two particles are equal. Thus all eigenstates are mapped onto all possible sets of n nonequal integer numbers λ_j with $-L/2 < \lambda_j \leqslant L/2$. In the absence of bound-state formation, these solutions are adiabatically continued under a smooth deformation from $V = 0$ to any finite value of V. This permits us to use the free-particle classification to label many-particle states for an arbitrary interaction strength.

The limit of infinitely strong repulsion corresponds to free fermions of a finite size. The scattering phase $\varphi_{jm} = k_j - k_m + \pi$ for $V = \infty$ makes Eq. (5) a linear system of coupled equations. In the continuum regime they decouple into a set of single-particle quantization conditions,

$$k_j = \frac{2\pi\lambda_j}{L-n}. \qquad (7)$$

Here the length of the system is reduced by the exclusion volume taken by the finite size of the particles; see also Eq. (12) for a finite-range interaction below.

The adiabatic method we are using breaks down when a bound state is formed at a finite interaction strength while sweeping from $V = 0$ to $V = \infty$. Such states occur only when some of the quasimomenta of the solutions at $V = 0$ are $|k_j| > \pi/2$ (see Appendix and Ref. 20). The bound states can be observed, for instance, in the dynamics of a spin chain following a quench.[21] In the continuum regime there is a wide range of model parameters where Eq. (7) is applicable: for momenta and energies in the spectral function smaller than $\pi/2$ and smaller than half bandwidth respectively.

The ground state is a band filled from the bottom up to the momentum $k_F = \pi(n-1)/L$ using the classification of Eq. (6). Here n is assumed odd for simplicity. Eigenstates involved in the form factors of the spectral function have a fixed number of particles $n+1$. All other eigenstates do not contribute to Eq. (2), as the number of particles is a conserved quantity.

In this paper, we are concerned with the location of the support of the spectral function (the lowest value of energy for which the spectral function is not zero) as opposed to its value, so we ignore the matrix elements in Eq. (2), assuming them to be nonzero for all f which satisfy the number constraint. Two δ functions in k and in ε map directly the total momenta and the eigenenergies of all many-body states $|f\rangle$ with $n+1$ particles into the shape of the spectral function. For a fixed value of k, the edge of the support is the smallest eigenenergy of all states $|f\rangle$, with $P_f = k$. Using the classification in Eq. (6), these states can be parametrized by a single variable ΔP [see the sketch in Fig. 2(b) and in the Appendix].

A. Low energies

At low energies the model of spinless fermions Eq. (1) is well approximated by the Tomonaga-Luttinger model with only two free parameters.[1] The first parameter is the slope of the linearized spectrum of excitations at k_F. For the states from Fig. 2(b) it is

$$v = \frac{L(E_2-E_1)}{2\pi}, \qquad (8)$$

where E_1 and E_2 are energies of the states with $\Delta P = 0$ and $\Delta P = 2\pi/L$, respectively. The second Luttinger parameter can be extracted as $K = v_F/v$,[22] where $v_F = 2t\pi(n-1)/L$ is the Fermi velocity of the noninteracting system. The numerical evaluation of K as a function of the interaction strength V is presented in Fig. 1. For small V the function is linear, $K = 1 - 2n/L \times V/t + O(V^2/t^2)$. For large V it approaches a lower bound such that $K = K(\infty) + 2n/(L-n) \times t/V + O(t^2/V^2)$, where

$$K(\infty) = \left(1 - \frac{n}{L}\right)^2 \qquad (9)$$

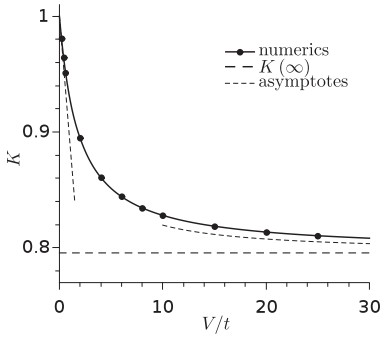

FIG. 1. The numerical evaluation of the Luttinger parameter K as a function of next-neighbor interaction strength V using Eqs. (3), (5), and (8), full ellipses; $L = 100$ and $n = 11$. We compare it with the bound on K at infinite interaction strength from Eq. (9), thick dashed line. Small and larger V asymptotes are $K = 1 - 2n/L \times V/t$ and $K = K(\infty) + 2n/(L-n) \times t/V$, thin dashed lines.

was computed using the values of quasimomenta for $V = \infty$ in Eq. (7).

The Luttinger parameter K measures the effects of interactions where for noninteracting particles $K = 1$. At $V = \infty$ the interaction potential is a hard-wall interaction with a finite interaction range, which still leaves some room for nonzero kinetic energy, thus limiting the maximum value of K.

B. High energies

The main aim of this paper is a calculation beyond low energies. In the nonlinear region the position of the edge of the spectral function is given by the momentum dependence of the states of Fig. 2(b), $\varepsilon_{\text{edge}}(k) = E_k - E_0$, where E_k corresponds to the states with $\Delta P = k_F + 2\pi/N - k$. For all values of V

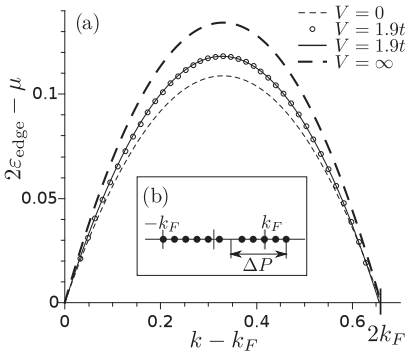

FIG. 2. (a) We show the main result of this paper, that the edge of the support of the spectral function satisfies Eq. (10). Numerical results at intermediate coupling ($V = 1.9t$) are shown as open circles and compared to the analytical result, Eq. (10), shown as a full line for $L = 400$ and $n = 39$. The asymptotes in the weak-coupling limit from Eq. (6) and the strong-coupling limit from Eq. (7) are shown as thin and thick dashed lines, respectively. (b) Sketch of the sets of quasimomenta, using classification Eq. (6), that correspond to the edge states; parameter ΔP corresponds to different momenta k.

we find it to be a parabolic function of momentum,

$$\varepsilon_{\text{edge}}(k) = \frac{mv_F^2}{K} - \frac{(k - 2mv_F)^2}{2mK}, \tag{10}$$

where $m = (2t)^{-1}$ is the bare single-electron mass and the Luttinger parameter K is determined by the slope at $k = k_F$. In the limiting cases $V = 0$ and $V = \infty$, it is calculated explicitly using the expressions for quasimomenta in Eqs. (6) and (7). The crossover for intermediate values of V is calculated using the numerical solution of the Bethe equations [Eq. (5)] and is perfectly fitted by the same parabolic formula [see Fig. 2(a)]. At $k = k_F$, Eq. (10) gives the chemical potential $\mu = mv_F^2/(2K)$, since the ground state for $n + 1$ particles is constructed by adding an extra particle to the ground state $|0\rangle$ at the lowest possible momentum above k_F, which is the state in Fig. 2(b) with $\Delta P = 0$.

The many-body states that mark the edge of the spectral function outside of the region $k_F < k < 3k_F$ are parametrized by a single variable similarly to Fig. 2(b) (see Appendix for details). In the upper half of the energy-momentum plane $\varepsilon > \mu$ the result in Eq. (10) is repeated along the momentum axis with the period $2k_F$. So $\varepsilon_{\text{edge}}(k)$ becomes $mv_F^2/K - (k - 2jmv_F)^2/(2mK) + \Delta\mu_j$ in regions $(2j-1)k_F < k < (2j+1)k_F$, with an additional shift $\Delta\mu_j$ for $|j| > 1$. The latter is given by the recurrence relation $\Delta\mu_{j+1} = \Delta\mu_j + 2|j|v_F/K$ with the initial value $\Delta\mu_1 = 0$. In the continuum regime of interest, $j \ll n$, $\Delta\mu_j$ is only a small finite size correction to μ. In the "hole region" $\varepsilon < \mu$, the position of the edge is obtained by reflection of $\varepsilon_{\text{edge}}(k)$ with respect to the line $\varepsilon = \mu$ (see Appendix).

A link between Luttinger liquids and the Fermi-edge singularity problem was very recently established as a tool to analyze interactions beyond the linear approximation in one dimension.[12] This has led to the development of a phenomenological theory of nonlinear Luttinger liquids where power-law singularities, $A(\varepsilon,k) \sim \theta[\varepsilon - \varepsilon_{\text{edge}}(k)]|\varepsilon - \varepsilon_{\text{edge}}(k)|^{-\alpha}$, were found above the edge of the support. Their exponents were related to the curvature of $\varepsilon_{\text{edge}}(k)$ for arbitrary momenta.[12] Substitution of Eq. (10) in the formula of Imambekov and Glazman from Ref. 13 yields

$$\alpha = 1 - \frac{K}{2}\left(1 - \frac{1}{K}\right)^2. \tag{11}$$

The Luttinger K of the model Eq. (1) (see Fig. 1) gives a divergent exponent smaller than 1 and larger than a limiting value calculated for $K(\infty)$ from Eq. (9). Thus the form factors in Eq. (2) are nonzero around the edge, thereby justifying our assumption about matrix elements in the spectral function.

IV. FINITE-RANGE INTERACTION

A further consequence of the non-linearity of the free particle dispersion is the bound on the Luttinger parameter K in Eq. (9). It has to be treated with care analogously to the point-splitting technique for field theoretical models,[23] in which a small interaction range must be introduced to couple a pair of fermions which cannot occupy the same point in space, and then the limit of zero range is taken. For the model on a lattice with next-neighbor coupling, the interaction

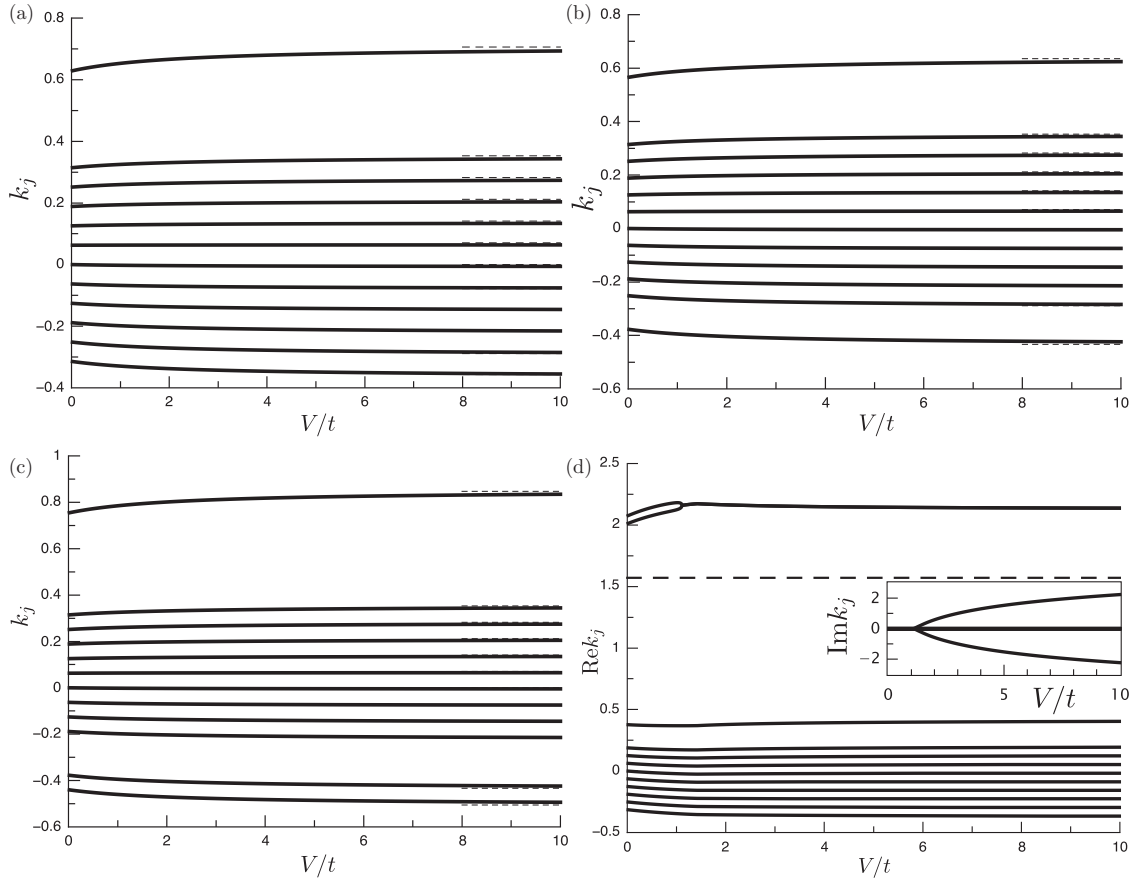

FIG. 3. The numerical solutions of Bethe equations, Eq. (5) of the main text, for k_j as a function of interaction strengths V for $n = 12$ particles and $L = 100$, full lines. The thin dashed lines at large V correspond to asymptotes from Eq. (7) of the main text. The states are classified according to Eq. (6) of the main text: (a) $\lambda_j = \{-5,-4,-3,-2,-1,0,1,2,3,4,10\}$; (b) $\lambda_j = \{-6,-4,-3,-2,-1,0,1,2,3,4,9\}$; (c) $\lambda_j = \{-7,-6,-3,-2,-1,0,1,2,3,4,12\}$; (d) $\lambda_j = \{-5,-4,-3,-2,-1,0,1,2,3,6,32,33\}$. A bound state forms out of a pair of quasimomenta with $k_j > /\pi/2$ above a finite value of V. The thick dashed line marks the value of $k = \pi/2$, and the inset is the imaginary parts of all quasimomenta k_j.

range vanishes in the continuum regime ($n \ll L$) compared to the average distance between particles; therefore $K(\infty) \to 1$, i.e., degenerate with its value for the noninteracting system $K(0) = 1$. However, the interaction range between fermions in physical systems is usually finite, e.g., the screening length for electrons in a metal or a semiconductor, making K not equal to 1. We, therefore, now consider a model with finite range.

We consider the limiting case of $V = \infty$ when the interaction range (screening length) spans a large number of lattice sites r. The Hamiltonian Eq. (1) with the potential $V_i = V\theta[i-1]\theta[r-]$, where $\theta[i]$ ($\theta[i] = 1$ for $i \geqslant 0$ and $\theta[i] = 0$ for $i < 0$) is a Heaviside step function and $V \to \infty$, can be diagonalized in the coordinate basis, $|\psi\rangle = \sum_{j_1<j_2-r\cdots<j_n-r} a_{j_1\ldots j_n} c^\dagger_{j_1}\ldots c^\dagger_{j_n}|\mathrm{vac}\rangle$, by a superposition of plain waves, $a_{j_1\ldots j_n} = \sum_P e^{i\sum_{l=1}^n k_{P_l} j_l + i\sum_{l<m=1}^n \varphi_{P_l,P_m}}$, with $2\varphi_{jm} = (k_j - k_m)r + \pi$. Application of the periodic boundary condition yields, similarly to Eq. (5),

$$k_j[L - r(n-1)] + r\sum_{m=1\neq j}^{n} k_m = 2\pi\lambda_j, \tag{12}$$

which in the continuum regime gives a set of independent quantization conditions $k_j = 2\pi\lambda_j/(L - rn)$. Finally, by repeating the same calculation used to obtain Eq. (9) we find

$$K(\infty) = \left(1 - \frac{rn}{L}\right)^2, \tag{13}$$

where the term rn/L can be interpreted as a product of screening length and particle density.

A microscopic model of spinless fermions needs to have an interaction range of the order of the average distance between particles to reach the $K = 0$ value that corresponds

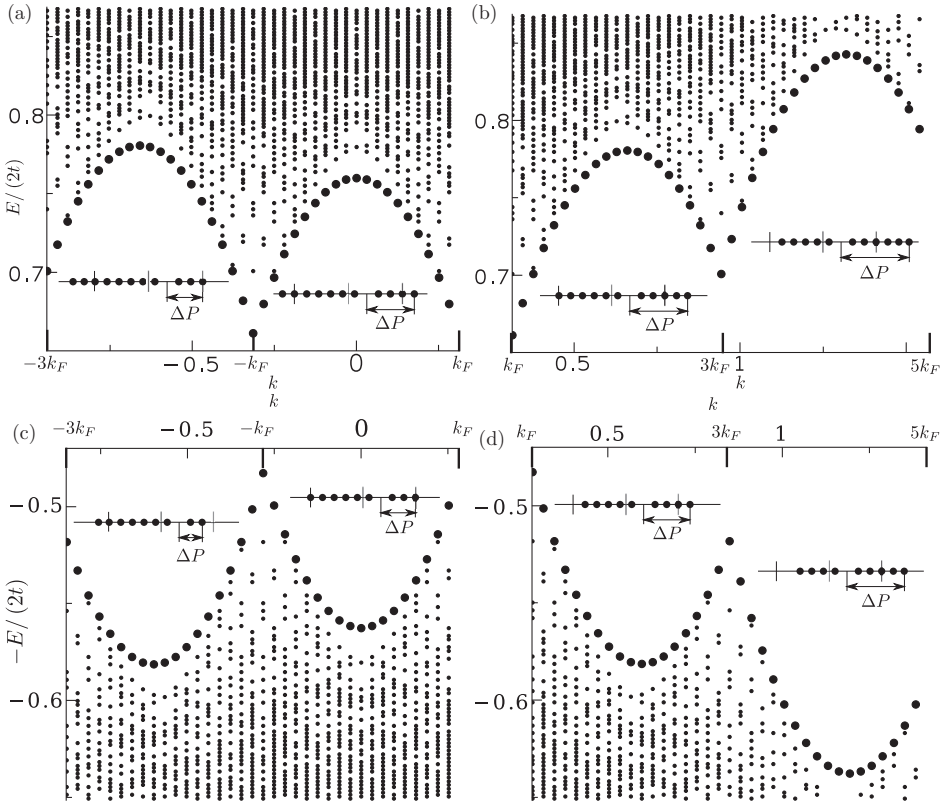

FIG. 4. Spectrum of the eigenstates, Eq. (3) of the main text, that are involved in the form factor in Eq. (2) of the main text for the ground state with $n = 19$ particles, $L = 200$, and $V \ll t$, dots. Large dots are the states at the edge. The insets are sketches of sets of quasimomenta that correspond to the edge states using the classification Eq. (6) of the main text. The positive half planes $E - E_0 > \mu$ are the states with an extra added particle: (a) momenta are from $-3k_F$ to k_F, the energies at the edge at $-3k_F$ and $-k_F$ correspond to chemical potentials μ_{-1} and μ_0; (b) momenta are from k_F to $5k_F$, the energies at the edge at k_F, $3k_F$, and $5k_F$ correspond to chemical potentials μ_1, μ_2, and μ_3. The negative half planes $E_0 - E < \mu$ are the states with one particle removed: (c) momenta are from $-3k_F$ to k_F; and (d) momenta are from k_F to $5k_F$.

to strong interaction effects in the Tomonaga-Luttinger model. Specifically, for $r = L/(2n)$, which allows some motion even when $V = \infty$, the bound is $K(\infty) = 1/4$. When r is increased further, $K(\infty)$ approaches zero.

V. CONCLUSIONS

In conclusion, we have considered the exact diagonalization of a model of spinless fermions on a lattice with next-neighbor interactions via the Bethe-Ansatz approach. By analyzing the spectral function in the continuum regime we have found that the edge of its support has a parabolic shape for arbitrary momenta and the prefactor is a function of the dimensionless Luttinger parameter K, which is defined in the low-energy domain. Additionally, we have extended our model with a finite range of interactions in order to access the strongly interacting regime (near $K = 0$) and have also found the parabolic shape for the support (for $V = \infty$), which is still characterized by K. This suggests that Luttinger parameters control physical properties at higher energies where nonlinearity cannot be ignored.

ACKNOWLEDGMENTS

We would like to thank I. V. Lerner for illuminating discussions. This work was supported by EPSRC Grant No. EP/J016888/1.

APPENDIX: NUMERICAL DATA

Here we present results of numerical calculations. Figure 1 shows some of the solutions to the Bethe-Ansatz equations, Eq. (5) of the main text, for different values of V. The states are parametrized using Eq. (6) of the main text. The states of Figs. 3(a)–3(c) have all $|k_j| < \pi/2$. The state of Fig. 3(d) contains a pair of $|k_j| > \pi/2$ that leads to formation of a bound state at a finite V. Figure 4 shows the extension of the edge beyond the region $k_F < k < 3k_F$ and $\varepsilon > \mu$. The eigenstates on the edge are marked by large dots and corresponding sets of quasimomenta are sketched in each region as insets.

[1]T. Giamarchi, *Quantum Physics in One Dimension* (Clarendon Press, Oxford, 2003).
[2]M. Pustilnik, M. Khodas, A. Kamenev, and L. I. Glazman, Phys. Rev. Lett. **96**, 196405 (2006).
[3]R. G. Pereira, J. Sirker, J.-S. Caux, R. Hagemans, J. M. Maillet, S. R. White, and I. Affleck, Phys. Rev. Lett. **96**, 257202 (2006).
[4]A. Imambekov and L. I. Glazman, Phys. Rev. Lett. **100**, 206805 (2008).
[5]J.-S. Caux and J. M. Maillet, Phys. Rev. Lett. **95**, 077201 (2005).
[6]F. H. L. Essler, Phys. Rev. B **81**, 205120 (2010).
[7]M. Khodas, M. Pustilnik, A. Kamenev, and L. I. Glazman, Phys. Rev. B **76**, 155402 (2007).
[8]O. M. Auslaender, A. Yacoby, R. de Picciotto, K. W. Baldwin, L. N. Pfeiffer, and K. W. West, Science **295**, 825 (2002).
[9]Y. Jompol, C. J. B. Ford, J. P. Griffiths, I. Farrer, G. A. C. Jones, D. Anderson, D. A. Ritchie, T. W. Silk, and A. J. Schofield, Science **325**, 597 (2009).
[10]B. J. Kim, H. Koh, E. Rotenberg, S.-J. Oh, H. Eisaki, N. Motoyama, S. Uchida, T. Tohyama, S. Maekawa, Z.-X. Shen, and C. Kim, Nat. Phys. **2**, 397 (2006).
[11]J. T. Stewart, J. P. Gaebler, and D. S. Jin, Nature (London) **454**, 744 (2008).
[12]A. Imambekov, T. L. Schmidt, and L. I. Glazman, Rev. Mod. Phys. **84**, 1253 (2012).
[13]A. Imambekov and L. I. Glazman, Phys. Rev. Lett. **102**, 126405 (2009).
[14]A. Luther and I. Peschel, Phys. Rev. B **9**, 2911 (1974).
[15]In the thermodynamic limit the length of the system L and the number of particles n are infinite but the density n/L is finite. Small occupancy of the lattice is the long-wavelength limit compared to the lattice parameter, $n \ll L$.
[16]H. Ohno, Science **281**, 951 (1998).
[17]In our notations $\hbar$ and lattice parameter are equal to one.
[18]A. A. Abrikosov, L. P. Gorkov, and I. E. Dzyaloshinski, *Methods of Quantum Field Theory in Statistical Physics* (Dover Publications, New York, 1975).
[19]V. E. Korepin, N. M. Bogoliubov, and A. G. Izergin, *Quantum Inverse Scattering Methods and Correlation Functions* (Cambridge University Press, Cambridge, UK, 1993).
[20]R. G. Pereira, S. R. White, and I. Affleck, Phys. Rev. B **79**, 165113 (2009).
[21]M. Ganahl, E. Rabel, F. H. L. Essler, and H. G. Evertz, Phys. Rev. Lett. **108**, 077206 (2012).
[22]The system becomes Galilean invariant, and the single-particle spectrum in Eq. (3) is quadratic in the continuum regime.
[23]J. von Delft and H. Schoeller, Ann. Phys. **7**, 225 (1998).

PHYSICAL REVIEW B **90**, 014309 (2014)

Spectral-edge mode in interacting one-dimensional systems

O. Tsyplyatyev and A. J. Schofield
School of Physics and Astronomy, The University of Birmingham, Birmingham B15 2TT, United Kingdom
(Received 4 March 2014; revised manuscript received 15 July 2014; published 31 July 2014)

A continuum of excitations in interacting one-dimensional systems is bounded from below by a spectral edge that marks the lowest possible excitation energy for a given momentum. We analyze short-range interactions between Fermi particles and between Bose particles (with and without spin) using Bethe-ansatz techniques and find that the dispersions of the corresponding spectral edge modes are close to a parabola in all cases. Based on this emergent phenomenon we propose an empirical model of a free, nonrelativistic particle with an effective mass identified at low energies as the bare electron mass renormalized by the dimensionless Luttinger parameter K (or K_σ for particles with spin). The relevance of the Luttinger parameters beyond the low-energy limit provides a more robust method for extracting them experimentally using a much wider range of data from the bottom of the one-dimensional band to the Fermi energy. The empirical model of the spectral edge mode complements the mobile impurity model to give a description of the excitations in proximity of the edge at arbitrary momenta in terms of only the low-energy parameters and the bare electron mass. Within such a framework, for example, exponents of the spectral function are expressed explicitly in terms of only a few Luttinger parameters.

DOI: 10.1103/PhysRevB.90.014309 PACS number(s): 71.10.Pm, 03.75.Kk, 73.21.−b

I. INTRODUCTION

The low-energy properties of interacting particles in one dimension are well described by the Tomonaga-Luttinger model [1] based on the linear approximation to the spectrum of the excitation at the Fermi energy. In this framework various correlation functions that involve a continuum of many-body excitations can be evaluated explicitly resulting in a common power-law behavior—in contrast to higher dimensions where the Fermi gas approximation with renormalized parameters (the Fermi liquid model) [2] remains robust. In the last few decades different experimental realizations of one-dimensional geometries were developed: carbon nanotubes [3], cleaved edge [4] or gated [5] one-dimensional channels in semiconductor heterostructures, and cold atomic gases in cigar-shaped optical lattices [6] where the predictions of the low-energy theory [7] have already been observed and measurements of high-energy effects are already possible.

Recently, a new theoretical understanding of the behavior at high energies was achieved by making a connection between the features of the dynamical response of the one-dimensional systems and the Fermi edge singularity in x-ray scattering in metals [8]. Application of the mobile impurity model [9] to the Tomonaga-Luttinger model gives a description of excitations at high energies incorporating dispersion of the spectral edge as an input parameter; the edge marks the smallest excitation energy at a fixed momentum. Within the resulting theory correlation functions exhibit a common power-law behavior where exponents are related to the curvature of the spectral edge and the Luttinger parameters [10–13]. However, the theory for the edge mode itself remains an open problem.

In this paper we analyze fundamental models of Fermi and Bose particles with short-range interactions (with and without spin) in one dimension using the available diagonalization methods based on Bethe ansatz. We investigate the edge mode of the spectral function—a dynamical response function that generalizes the single-particle spectrum to the many-particle systems—and find that its dispersion is close to a parabola for all cases in the thermodynamic limit [14]. It is exactly parabolic for fermions without spin and the biggest deviation ($\lesssim$20%) occurs for fermions with spin and a very large interaction potential. Based on this result we propose an empirical model of a free, nonrelativistic particle for the spectral edge mode, which describes a charge wave in the spinless case and a spin wave in the spinful case (see a graphical representation of the spectral function in Fig. 1). The effective mass m^* is identified at low energies as the bare electron mass m strongly renormalized by the dimensionless Luttinger parameter; $m^*/m = K$ and $m^*/m = K_\sigma$ in the spinless and the spinful case, respectively. The position of the edge of the spectral function in terms of this empirical model can

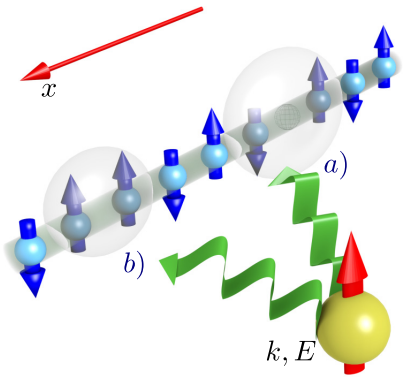

FIG. 1. (Color online) A schematic representation of a tunneling process into a one-dimensional system for a particle with fixed momentum k and energy E that is described by the spectral function. Excitations of the system are (a) density waves or [(a) and (b)] spin wave for particles with spin.

be expressed as

$$\varepsilon_{\rm edge}(k) = \mu + \frac{k_F^2}{2m^*} - \frac{(k-k_0)^2}{2m^*}, \quad (1)$$

where μ is the chemical potential, k_F is the Fermi momentum, and $k_0 = 0$ (k_F) for Fermi (Bose) particles.

The empirical model in Eq. (1) breaks down when the effective mass becomes infinite. At low energies $m^* = \infty$ is equivalent to zero sound velocity of the collective modes $v(v_\sigma)$. The characteristic threshold is given by the quantum of the momentum $v_1 = 2\pi/(mL)$ in a system of a finite size L. For slower velocities $v(v_\sigma) \lesssim v_1$ the dispersion of the spectral edge mode is not parabolalike and is not universal.

The parabolic shape of the spectral edge mode, which we obtain in microscopic calculations for different models, can be interpreted as emergence of "translational invariance." The kinetic energy of a single free particle is a parabolic function of its momentum, enforced by the translational symmetry. Finite system size discretizes the boosts for changing inertial frames of reference in quanta of $2\pi/L$. For a system consisting of N particles the minimal boost of $2\pi N/L$ corresponds to the $2k_F$ periodicity in the momentum space; note that interaction potentials are also Galilean invariant. However, the total momentum of the whole many-particle system is still quantized in the units of $2\pi/L$ that can be facilitated by giving a boost to only a fraction of the particles $j < N$. The state on the spectral edge with the momentum $k = 2\pi j/L$ corresponds to a hole left between $N - j$ particles in the rest frame and j particles which have received the minimal boost (see Sec. III for details). The effective mass of the holelike quasiparticle is strongly renormalized by interactions since a partial boost is not a Galilean invariant transformation. However, the parabolic dependence of the hole energy on momentum—which is analogous to the kinetic energy of a free particle—is common for different microscopic models thus it is an emergent phenomenon.

Excitations above the spectral edge are well described at high energies by the application of the mobile impurity model to the Tomonaga-Luttinger theory which incorporates the curvature of the spectral edge as an input parameter [15]. The result in Eq. (1) removes this arbitrary input complementing the model above. Within such a framework, for example, the edge exponents of the spectral function are expressed explicitly in terms of only a few Luttinger parameters and the bare electron mass that provides a systematic way to classify them for a wide range of microscopic parameters.

The rest of the paper is organized as follows. Section II describes the model of one-dimensional particles interacting via short-range potentials, the corresponding spectral function, and discusses their general properties. In Sec. III we evaluate momentum dependence of the spectral edge mode using the Bethe-ansatz approach for Fermi particles in the fundamental region. Section IV contains the effective field theory for excitations above the spectral edge and calculates the edge exponents of the spectral functions using the dispersion of the spectral edge mode itself obtained in Sec. III. In Sec. V we show that Bose particles have the same parabolic dispersion, with the mass renormalized by the same Luttinger parameter K of the spectral edge mode as the Fermi particles. In Sec. VI we summarize the results and discuss experimental implications.

II. MODEL

We consider particles in one dimension interacting via a contact two-body potential U as

$$H = \int_{-L/2}^{L/2} dx \left(-\frac{1}{2m} \psi_\alpha^\dagger(x) \Delta \psi_\alpha(x) - U L \rho(x)^2 \right), \quad (2)$$

where $\psi_\alpha(x)$ are the field operators of Fermi or Bose particles at point x (with a spin $\alpha = \uparrow, \downarrow$ for spinful particles), $\rho(x) = \psi_\alpha^\dagger(x)\psi_\alpha(x)$ is the particle density operator, L is the size of the system, and m is the bare mass of a single particle. Below we consider periodic boundary conditions, $\psi_\alpha(x + L) = \psi_\alpha(x)$, to maintain the translational symmetry of the finite length system, restricting ourselves to repulsive interaction only, $U > 0$, and we assume $\hbar = 1$.

The spectrum of excitations in the many-body case is given by the spectral function which describes the response of a strongly correlated system to a single-particle excitation at energy ε and momentum k, $A_\alpha(k,\varepsilon) = -\mathrm{Im}\, G_{\alpha\alpha}(k,\varepsilon)\mathrm{sgn}(\varepsilon - \mu)/\pi$, where μ is a chemical potential and $G_{\alpha\beta}(k,\varepsilon) = -i \int dx\, dt e^{i(kx-\varepsilon t)} \langle T(e^{-iHt}\psi_\alpha(x)e^{iHt}\psi_\beta(0))\rangle$ is a Fourier transform of Green function at zero temperature. To be specific, we discuss particlelike excitations, $\varepsilon > \mu$. The spectral function in this domain reads [16]

$$A_\alpha(k,\varepsilon) = \sum_f |\langle f|\psi_\alpha^\dagger(0)|0\rangle|^2 \delta(\varepsilon - E_f + E_0)\delta(k - P_f), \quad (3)$$

where E_0 is the energy of the ground state $|0\rangle$, and P_f and E_f are the momenta and the eigenenergies of the eigenstate $|f\rangle$; all eigenstates are assumed normalized.

Galilean invariance defines a fundamental region for the spectrum of excitations on the momentum axis. A minimal boost for changing an inertial frame of reference for N particles is $2\pi N/L$ which is twice the Fermi momentum $k_F = \pi N/L$. In momentum space this boost corresponds to $2k_F$ periodicity. We choose the fundamental region as $-k_F < k < k_F$ for the Fermi and as $0 < k < 2k_F$ for Bose particles.

Under a $2k_F$ translation, the form factors in Eq. (3) do not change and the energies acquire simple shifts. The interaction term in Eq. (2) is invariant under the transformation $x \to x + 2\pi tj/(mL)$, where j is the number of the translation quanta, since the latter can be absorbed into a change of the integration variable. The transformation of the momentum operator, $-i\nabla \to -i\nabla + 2\pi j/L$, in the the kinetic term results in a constant energy shift, $E \to E + 2\pi j P/(mL) + 2\pi^2 j^2 N/(mL^2)$, of the Hamiltonian but keeps its matrix structure, and therefore, eigenstates unaltered. Thus the spectral function can be extended to arbitrary momenta by simultaneous translation of the momentum and of the energy variables starting from the fundamental region.

Here, we are concerned with a distinctive feature of the spectral function—the edge that marks the lowest possible excitation energy for a given momentum. To identify its location we need to obtain only the many-body spectrum of the model due to a singularity [15] that guarantees large values of the form factors in the proximity of the spectral edge. The two δ functions in Eq. (3) directly map the total momenta P_f

and the eigenenergies E_f of all many-body states $|f\rangle$ into the points of the spectral function k and ε. We are going to identify the states that have the smallest energy for each momentum and study how the dispersion of the spectral edge mode, which they form, depends on the interaction strength.

III. FERMIONS

A. Spinless

The zero range profile of two-body interaction potential in the model in Eq. (2) has zero matrix elements for the Fermi particles without spin due to the Pauli exclusion principle. A model of interactions in this case requires a finite range of interactions which is usually introduced by the point-splitting technique [17] developed to address the problem in the low-energy limit. Here we will use a different approach of introducing a lattice with the next-neighbor interaction between particles. The lattice counterpart of the model in Eq. (2) is the Hamiltonian $H = -\sum_{j=-L/2}^{L/2}(\psi_j^\dagger\psi_{j+1} + \psi_j^\dagger\psi_{j-1})/(2m) - U\sum_{j=-L/2}^{L/2}\psi_j^\dagger\psi_j\psi_{j+1}^\dagger\psi_{j+1}$, where j is the site index on the lattice and the operators ψ_j obey the Fermi commutation relations $\{\psi_i, \psi_j^\dagger\} = \delta_{ij}$.

The model above can be diagonalized using the Bethe-ansatz approach [18]. In the coordinate basis a superposition of N plane waves, $\Psi = \sum_{P, j_1<\cdots<j_N} e^{i\sum_{l=1}^N k_{P_l} j_l + i\sum_{l<l'=1}^N \varphi_{P_l,P_{l'}}}\psi_{j_1}^\dagger\cdots\psi_{j_N}^\dagger|\text{vac}\rangle$, is an eigenstate, $H\Psi = E\Psi$, with the corresponding eigenenergy

$$E = \frac{1}{m}\sum_{j=1}^{N}[1-\cos(k_j)]. \tag{4}$$

Here $|\text{vac}\rangle$ is the vacuum state, the scattering phases are fixed by the two-body scattering problem

$$e^{i2\varphi_{ll'}} = -\frac{e^{i(k_l+k_{l'})} + 1 - 2mUe^{ik_l}}{e^{i(k_l+k_{l'})} + 1 - 2mUe^{ik_{l'}}}, \tag{5}$$

and $\sum_P$ is a sum over all permutations of N quasimomenta. The periodic boundary condition quantizes the set of N quasimomenta simultaneously,

$$Lk_j - 2\sum_{l\neq j}\varphi_{jl} = 2\pi I_j, \tag{6}$$

where I_j is a set of nonequal integer numbers. The total momentum of N particles, $P = \sum_j k_j$, is a conserved quantity.

The continuum model in Eq. (2) corresponds to the low-density (long-wavelength) limit of the lattice model. In this limit the scattering phases in Eq. (5) are linear functions of quasimomenta, $2\varphi_{ll'} = (k_l - k_{l'})/[1 + (mU)^{-1}] + \pi$, and the nonlinear system of equations in Eq. (6) becomes linear. In the thermodynamic limit we solve it using perturbation theory and obtain an independent quantization condition for each quasimomentum as solutions of the Bethe equations in the leading $1/N$ order,

$$k_j = \frac{2\pi I_j}{L - \frac{N}{1+\frac{1}{mU}}}. \tag{7}$$

Thus all N-particle eigenstates can be labeled by all possible sets of integers I_j similarly to Slater determinants for free fermions. The latter is possible as long as no bound states exist, which is the case for any value of interaction strength $U \geqslant 0$ in this limit [18].

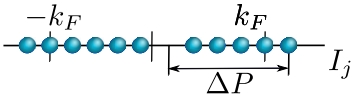

FIG. 2. (Color online) A set of quasimomenta from Eq. (7) that corresponds to the edge mode of the spectral function for Fermi particles without spin. The momentum of each many-particle state is given by $k = -k_F + \Delta P$.

The eigenstates contributing to the spectral function satisfy the number of particle constraints, i.e., fixed to be $N+1$. The lowest energy state for a fixed momentum $-k_F + \Delta P$ is given by the set of integers in Fig. 2. At low energies the system is in the universality class of Luttinger liquids. Its properties are fully determined by the linear slope of the spectrum of excitations at $\pm k_F$. Using the parametrization in Fig. 2, the first Luttinger parameter (the sound velocity of the collective modes) is a discrete derivative $v = L(E_2 - E_1)/(2\pi)$, where E_2 and E_1 are the energies of the states with $\Delta P = 2\pi/L$ and $\Delta P = 0$.

For Galilean invariant systems the product of the first and the second (dimensionless K) Luttinger parameters gives the Fermi velocity of the noninteracting system [19], $vK = v_F$ where $v_F = \pi N/(mL)$. By a straightforward calculation of the eigenenergies in Eq. (4) using Eq. (7) for a pair of states in Fig. 2 with $\Delta P = 0, 2\pi/L$ we directly obtain the second Luttinger parameter,

$$K = \left(1 - \frac{N}{L\left(1+\frac{1}{mU}\right)}\right)^2. \tag{8}$$

The dispersion of the spectral edge mode is given by the energies and the momenta of all states in Fig. 2. Starting from the solutions for quasimomenta in Eq. (7) and repeating the same calculation as before, we directly obtain the parabolic function of momentum [20] in Eq. (1), where $m^*/m = K$ from Eq. (8) [21]. This calculation also gives the chemical potential in Eq. (1) as the bare electron mass renormalized by the Luttinger parameter K, $\mu = k_F^2/(2mK)$.

B. Spinful

When Fermi particles have spin 1/2, the Pauli exclusion principle suppresses only the interaction between the particles with the same spin orientation in the model in Eq. (2). The remaining part of the density-density interaction term consists of a coupling between particles with opposite spin orientations.

This model can be diagonalized using the Bethe-ansatz approach but the Bethe hypothesis has to be applied twice [22]. In the coordinate basis, a superposition of plane waves is an eigenstate, $H\Psi = E\Psi$, of the model in Eq. (2),

$$\Psi = \int\cdots\int_{-L/2}^{L/2} dx_1\cdots dx_N \sum_{P,Q} A^{PQ} e^{i(P\mathbf{k})\cdot(Q\mathbf{x})}\psi_{Q_1}^\dagger(x_1)\cdots \times \psi_{Q_N}^\dagger(x_N)|\text{vac}\rangle, \tag{9}$$

where the operators $\psi_\alpha(x)$ obey the Fermi commutation rules $\{\psi_\alpha(x), \psi^\dagger_\beta(x')\} = \delta(x-x')\delta_{\alpha\beta}$, k_j are N quasimomenta, $\sum_{P,Q}$ is a sum over all permutations of two independent sets of N integer numbers (P and Q), and the coefficients A^{PQ} are chosen by a secondary use of the Bethe hypothesis,

$$A^{PQ} = \mathrm{sgn}(PQ) \sum_R \left(\prod_{1\leqslant l<l'\leqslant M} \frac{\lambda_{R_l} - \lambda_{R_{l'}} - imU}{\lambda_{R_l} - \lambda_{R_{l'}}} \right) \prod_{l=1}^{M} \times \frac{imU}{\lambda_{R_l} - k_{P_{z_l}} + \frac{imU}{2}} \prod_{j=1}^{z_l-1} \frac{\lambda_{R_l} - k_{P_j} - \frac{imU}{2}}{\lambda_{R_l} - k_{P_j} + \frac{imU}{2}}. \quad (10)$$

Here λ_l are spin degrees of freedom of M "up" spins with respect to the reference ferromagnetic state of N "down" spins, $\sum_R$ is a sum over all permutations of M integer numbers, and z_l is the position of the lth spin $\uparrow$ in permutation Q. The eigenenergy corresponding to the eigenstate in Eq. (9) is

$$E = \sum_{j=1}^{N} \frac{k_j^2}{2m}. \quad (11)$$

The periodic boundary condition quantizes the set of N quasimomenta k_j (charge degrees of freedom) simultaneously,

$$Lk_j - \sum_{l=1}^{M} \varphi_{jl} = 2\pi I_j, \quad (12)$$

where scattering phases $\varphi_{jl} = \log[(\lambda_l - k_j - \frac{imU}{2})/(\lambda_l - k_j + \frac{imU}{2})]/i$ depend on the quasimomenta of both kinds (k_j and λ_l), I_j is a set of N nonequal integer numbers, and M quasimomenta λ_l (spin degrees of freedom) satisfy another set of nonlinear equations,

$$\prod_{j=1}^{N} \frac{\lambda_l - k_j - \frac{imU}{2}}{\lambda_l - k_j + \frac{imU}{2}} = \prod_{l'=1\neq l}^{M} \frac{\lambda_{l'} - \lambda_m - imU}{\lambda_{l'} - \lambda_m + imU}. \quad (13)$$

The sum $P = \sum_{j=1}^{N} k_j$ is a conserved quantity—the total momentum of N particles.

The system of nonlinear equations, Eqs. (12) and (13), can be solved explicitly in the limit of infinite repulsion $U = \infty$ [23]. The quasimomenta λ_l diverge in this limit. Under the substitution of $\lambda_l = mU \tan y_l/2$, the second system of equations, Eq. (13), becomes independent of the first system of equations, Eq. (12), in leading $1/U$ order,

$$e^{iNy_l} = (-1)^{N+M-1} \prod_{l'=1\neq l}^{M} \frac{e^{i(y_l+y_{l'})} + 1 + 2e^{iy_l}}{e^{i(y_l+y_{l'})} + 1 + 2e^{iy_{l'}}}. \quad (14)$$

The above Bethe equations are identical to that of a Heisenberg antiferromagnet [18] where the number of particles N plays the role of the system size. In one dimension a spin chain is mapped into the model of interacting Fermi particles by the Jordan-Wigner transformation [18]; Eq. (14) is identical to Eqs. (5) and (6) where the interaction strength is set to $mU = -1$. Thus all solutions of Eq. (14) can be labeled by all sets of M nonequal integer numbers J_l similarly to the case of Fermi particles without spin (see Fig. 2). The system of equations for the quasimomenta k_j in Eq. (12) in the $U = \infty$ limit decouples

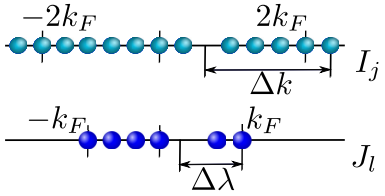

FIG. 3. (Color online) Parametrization of many-body states for fermions with spin using the $U = \infty$ limit in Eqs. (14) and (15). Chargelike excitations correspond to different sets of I_j and spinlike excitations correspond to different sets of J_j.

into a set of single-particle quantization conditions,

$$Lk_j = 2\pi I_j + \frac{1-(-1)^M}{2}\pi + \sum_{l=1}^{M} y_l. \quad (15)$$

Note that the independent magnetic subsystem, where quasimomenta y_l satisfy Eq. (14), is translationally invariant, thus $\sum_{l=1}^{M} y_l = 2\pi \sum_{l=1}^{M} J_l/N$ [as can be checked explicitly by multiplying Eq. (14) for all y_l]. Therefore, the quantization condition in Eq. (17) depends only on two sets of integer numbers, I_j and J_l.

All solutions of the original system of equations, Eqs. (12) and (13) can be labeled by all sets of $N+M$ integer numbers I_j and J_l (see Fig. 3). The values of k_j and λ_l that correspond to these integers can be obtained in two steps. First, the spin degrees of freedom y_l that correspond to a set of J_l are adiabatically continued under a smooth deformation of Eq. (6) from $U = 0$, which is the free particle limit, to $U = -1/m$, which coincides with Eq. (14). Note that the long-wavelength solution in Eq. (7) cannot be used here because the most interesting case of zero polarization for spinful fermions corresponds to half-filling of the band for the model in Eqs. (12) and (13) which is outside of the limits of applicability of the low-density regime. The values k_j that correspond to a set of I_j and J_l are obtained directly from Eq. (15). Secondly, the known values of k_j and λ_l in the $U = \infty$ limit are adiabatically continued under a smooth deformation of Eqs. (12) and (13) to arbitrary value of the interaction strength U.

The interaction effects are controlled by a single dimensionless parameter that can be defined using the $1/U$ corrections in the large U limit. Power series expansion of Eqs. (12) and (13) up to the first subleading $1/U$ order, $\lambda_l = mU \tan y_l/2 + y_l^{(1)}$ and $k_j = k_j^{(0)} + 2k_j^{(1)}/(mU)$, where y_l and $k_j^{(0)}$ are the solutions of Eqs. (14) and (15), yields

$$\sum_{j=1}^{N} \left(k_j^{(0)} - y_l^{(1)}\right) \cos^2 y_l = -2 \sum_{l'=1\neq l}^{M} \frac{y_{l'}^{(1)} - y_l^{(1)}}{(\tan y_l - \tan y_{l'})^2 + 4} \quad (16)$$

and

$$k_j^{(1)} = \frac{2}{L} \sum_{l=1}^{M} \left(k_j^{(0)} - y_l^{(1)}\right) \cos^2 y_l. \quad (17)$$

The first-order coefficients $y_l^{(1)}$ can be expressed from Eq. (16) in terms of zeroth-order coefficients $k_j^{(0)}$ and y_l. Then, in the

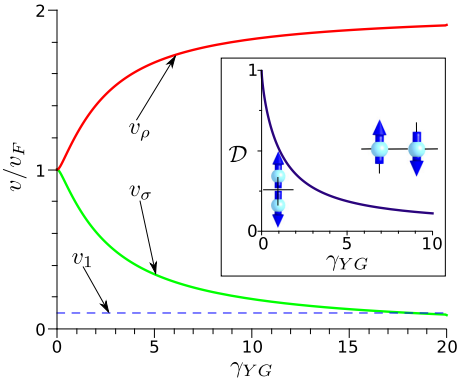

FIG. 4. (Color online) Velocities of the collective modes for fermions with spins at low energies as a function of the interaction parameters γ_{YG} from Eq. (18). The red line corresponds to the holon branch, the green line corresponds to the spinon branch, and the blue dashed line marks a quantum of momentum $v_1 = 2\pi/(mL)$; $L = 400$, $N = 40$, $\gamma_{YG} = 3.44mU$. Inset: Degree of double degeneracy [see the definition in Eq. (19)] for the ground state in Fig. 3 with $\Delta k = \Delta\lambda = 0$ as a function of the interaction parameter γ_{YG}.

thermodynamic limit, the first-order corrections to the quasimomenta k_j in Eq. (17) become $k_j^{(1)} = 2k_j^{(0)} \sum_{m=1}^{M} \cos^2 y_l/L$. This gives a condition of validity for the $1/U$ expansion of the Bethe equations, $2k_j^{(1)}/(mUk_j^{(0)})$, which is independent of both indices j and l.

We use the latter to define a single parameter,

$$\gamma_{YG} = \frac{mL}{2N} \frac{U}{\left(1 + \frac{1}{N}\sum_{l=1}^{M} \cos\, y_l\right)}, \tag{18}$$

that characterizes the degree of repulsion between fermions. When $\gamma_{YG} \gg 1$ the particles with opposite spin orientations scatter strongly off each other and when $\gamma_{YG} \ll 1$ they interact weakly with each other. For example, this is manifested in a change of degeneracy of the quasimomenta k_j that correspond to the ground state of unpolarized Fermi particles, $M = N/2$. We account for the degree of double degeneracy with respect to spin $1/2$ using

$$\mathcal{D} = 2 - \frac{L\sum_{j=1}^{N-1}(k_{j+1} - k_j)}{\pi N}. \tag{19}$$

This quantity is $\mathcal{D} = 1$ when each momentum state of free fermions is doubly occupied ($U = 0$) and is $\mathcal{D} = 0$ when each momentum state is occupied by a single particle ($U = \infty$). The crossover from one regime to another occurs at $\gamma_{YG} = 1$ where $\mathcal{D}$ crosses the value of $1/2$ (see inset in Fig. 4).

The ground state of the model in Eq. (2) has zero spin polarization when the external magnetic field is absent, $M = N/2$. To be specific we consider the ground states with even values of N and M. Excited states contributing to the spectral function satisfy the number of particles being constrained to be $N + 1$. In the $U = \infty$ limit the lowest-energy eigenstates for a fixed momentum $P = -k_F + \Delta P$ are given by a set of integers in Fig. 3 with $\Delta k = 0$ and $\Delta P = \Delta\lambda$ [24]. In the opposite limit of free fermions, the lowest-energy eigenstates for a fixed momentum $P = -k_F + \Delta P$ are doubly degenerate with respect to spin $1/2$ and are given by the set of integers in Fig. 3 for each spin orientation. The quasimomenta in both limits are smoothly connected under adiabatic deformation of Eqs. (12) and (13) from $U = \infty$ to $U = 0$ marking the edge of the spectral function in Eq. (3) for arbitrary U.

At low energies the eigenstates are strongly mixed in the spin sector due to spin-charge separation [7] implying that $A_\uparrow(k,\varepsilon) = A_\downarrow(k,\varepsilon)$. The excitations of the system are spinons and holons which are well approximated by the spinful generalization of the Tomonaga-Luttinger model with only four free parameters $v_{\rho,\sigma}$ and $K_{\rho,\sigma}$. The pair of velocities is the slopes of the linearized dispersions of the charge and spin excitations at $\pm k_F$. Using the representation of the eigenstates in Fig. 3 they are

$$v_\rho = \frac{L(E_2 - E_1)}{2\pi}, \quad v_\sigma = \frac{L(E_3 - E_1)}{2\pi}, \tag{20}$$

where E_1, E_2, and E_3 correspond to the energies of the states with ($\Delta k = 0$, $\Delta\lambda = 0$), ($\Delta k = 2\pi/L$, $\Delta\lambda = 0$), and ($\Delta k = 0$, $\Delta\lambda = 2\pi/L$), respectively [25]. The numerical evaluation of $v_{\rho,\sigma}$ as a function of the interaction parameter γ_{YG} [26] is presented in Fig. 4. For $\gamma_{YG} = 0$ both velocities coincide, $v_\rho = v_s = v_F$. For large $\gamma_{YG} \gg 1$ the holon velocity doubles, $v_\rho = 2v_F$, due to strong repulsion between particles with opposite spin orientations [27], and the spinon velocity becomes zero, $v_\sigma = 0$, since it vanishes as $\sim 1/(m^2U)$ in this limit [18]. The other pair of Luttinger parameters can be obtained directly for Galilean invariant systems using $v_{\rho,\sigma}$ and the Fermi velocity $K_{\rho,\sigma} = v_F/v_{\rho,\sigma}$ where $v_F = \pi M/L$, without the need of a second observable such as compressibility [7].

Beyond the linear regime the position of the edge of the spectral function is given by following of the low-energy spinon mode. Numerical evaluation shows that $\varepsilon_{\rm edge}(k) = E_k - E_0$, where E_k corresponds to the states in Fig. 3 with $\Delta k = 0$ and $k = -k_F + \Delta\lambda$, is close to a parabola for all values of γ_{YG} (see Fig. 5). For $\gamma_{YG} = 0$ the shape of the spectral edge mode is exactly parabolic following the dispersion of free Fermi particles. For $\gamma_H \gg 1$ deviations from a parabola are largest. We quantify them by comparing the effective mass m^*, obtained by the best fit of Eq. (1) at all energies, with the spinon velocity v_σ from Eq. (20), obtained at low energy [28]. The deviation $(v_\sigma - k_F/m^*)/v_\sigma$ decreases as the number of particles N grows but it saturates at a finite value of ~ 0.2 in the limit $N \to \infty$ [29] (see the inset in Fig. 5).

The edge of the spectral function in the complementary part of the fundamental range, $k_F < k < 3k_F$, also has a parabolic shape. The eigenstates with the smallest eigenenergies for a fixed momentum k in this range are connected with their counterparts in the $-k_F < k < k_F$ range by a shift of the spin variables $\lambda_j \to \lambda_j + 2\pi/L$. Repeating the same numerical procedure as before for $\varepsilon_{\rm edge}(k) = E_k - E_0$, where E_k corresponds to the states in Fig. 3 with $\Delta k = 0$ and $k = k_F + \Delta\lambda$, we obtain the result in Eq. (1) with $k_0 = 2k_F$. In the "hole region" $\varepsilon < \mu$, the position of the edge of the spectral function is obtained by reflection of $\varepsilon_{\rm edge}(k)$ with respect to the line $\varepsilon = \mu$.

The parabolalike behavior of the edge mode breaks down in finite-sized systems in the ultrastrong interaction regime when the spinon velocity v_σ becomes smaller than its own

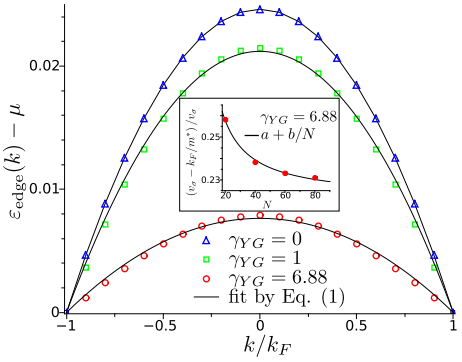

FIG. 5. (Color online) Dispersion of the spectral edge mode (extension of the spinon branch to high energies) for fermions with spins for different values of the interaction parameter $\gamma_{YG} = 0, 1, 6.88$; $L = 400$, $N = 40$. The blue triangles, green squares, and red ellipses are the numerical solutions of Eqs. (12) and (13); the solid black lines are the best parabolic fits by Eq. (1). Inset: Difference between the slope of the parabolic dispersion at E_F, which is given by the effective mass m^*, and the velocity of spin waves at low energies, which is obtained directly from Eq. (20) $[(v_\sigma - k_F/m^*)/v_\sigma]$ as a function of the number of particles N for $\gamma_{YG} = 6.88$. The solid black line is the $1/N$ fit, $a + b/N$, that gives $a = 0.22$ [29].

quantum set by the finite size of the system $v_1 = 2\pi/(mL)$ (see the dashed line in Fig. 4). Correspondingly, the threshold for entering this regime becomes $\gamma_{YG} \to \infty$ in the thermodynamic limit, as observed in Fig. 4 when $v_1 \to 0$. When $v_\sigma < v_1$, the behavior of the system is dominated by doubling of the period in the momentum space from $2k_F$ to $4k_F$, which can be seen explicitly from Eqs. (11) and (15) in the $U = \infty$ limit. The doubling in the spinful case is a direct consequence of Galilean invariance of the model in Eq. (2). However, it does not manifest itself in the thermodynamic limit for finite spinon velocities $v_\sigma > v_1$, for which the edge of the spectral function is still $2k_F$ periodic.

IV. EFFECTIVE FIELD THEORY

Eigenmodes above the spectral edge can be described by "the mobile impurity model" [15] with two different types of fields that account for all possible low-energy excitations with respect to a state on the spectral edge with a given momentum k in Figs. 2 and 3. One field is responsible for bosonic excitations around $\pm k_F$ whose behavior is well approximated by the Tomonaga-Luttinger model. Another field models the dynamics of the holelike degree of freedom, as observed in Fig. 2 for a large ΔP. For a k away from $\pm k_F$ creation of a second or removal of the existing holelike excitation is associated with a significant energy cost, thus the corresponding field describes a single Fermi particle.

The interaction between the deep hole and the excitations at $\pm k_F$ is of the density-density type since their corresponding energy bands are separated by a large barrier. Bosonization of the excitations at $\pm k_F$ leaves two unknown coupling constants between a pair of the canonically conjugated variables of the Tomonaga-Luttinger model and a fermionic field of the deep hole that can be identified by considering two different physical properties [10,30]. One is translation invariance of the hybrid system that can be represented as a motion of a fermionic excitation in a bosonic fluid with the velocity $u = \langle \nabla\theta \rangle / m$. Another is an observable that corresponds to the change of the total energy with respect to long-range variations of the density, which for the hybrid systems is given by $\delta\rho = -\langle \nabla\varphi \rangle / \pi$. Here φ and $\nabla\theta$ are the canonically conjugated variables of the Tomonaga-Luttinger model that correspond to the density and the current of the hydrodynamic modes, respectively.

For a fixed value of k, the dynamics of the free Bose-like and the free Fermi-like fields can be linearized for states close to the spectral edge. Using the dispersion in Eq. (1) for the Fermi-like field and the Luttinger parameters for the Bose-like field, the mobile impurity model reads

$$H = \int dx \Bigg[\frac{v}{2\pi} \left(K (\nabla\theta)^2 + \frac{(\nabla\varphi)^2}{K} \right) + \left(\frac{k(K-1)}{m^*} \nabla\theta + \frac{v(K+1)}{K} \nabla\varphi \right) d^\dagger d + d^\dagger \left(\frac{k^2}{2m^*} - \frac{ik\nabla}{m^*} \right) d \Bigg], \tag{21}$$

where $-k_F < k < k_F$ is the total momentum of the system—an input parameter of the model, $m^* = mK$ is the effective mass of the deep hole, v and K are the Luttinger parameters defined at $\pm k_F$, the fields θ and φ are the canonically conjugated variables $[\varphi(x), \nabla\theta(y)] = i\pi\delta(x - y)$ of the Tomonaga-Luttinger model, and the field d obeys the Fermi commutation rules $\{d(x), d^\dagger(y)\} = \delta(x - y)$.

The Hamiltonian in Eq. (21) can be diagonalized by a unitary transformation [8,10]. The rotation $e^{-iU} H e^{iU}$, where $U = \int dy [C_+(\sqrt{K}\theta + \varphi/\sqrt{K}) + C_-(\sqrt{K}\theta - \varphi/\sqrt{K})] d^\dagger d$ and $C_\pm = (2\sqrt{K})^{-1}[k(K-1) \pm k_F(K+1)]/(k \pm k_F)$, eliminates the coupling term between the fields turning Eq. (21) into a pair of free harmonic models. Then, the observables can be calculated in a straightforward way as averages over free fields only.

The spectral function in Eq. (3) can be calculated using the effective field model [8]. The original operators $\psi^\dagger(x)$ of Fermi particles of the model in Eq. (2) correspond to a composite excitation consisting of two bosons and one fermion in the field language of the model in Eq. (21) (see the state in Fig. 2). The fermionic excitation gives a dominant contribution to the spectral weight $|\langle f|\psi^\dagger(0)|0\rangle|^2$, thus at leading order in $|\varepsilon - \varepsilon_{\rm edge}(k)|$ close to the spectral edge the spectral function reads $A(k,\varepsilon) = \int dt\, dx\, e^{-i\varepsilon t} \langle d^\dagger(x,t) d(0,0) \rangle$ where $d(x,t) = e^{-iHt} d(x) e^{iHt}$ and $\langle \cdots \rangle$ is the zero temperature expectation value with respect to the model in Eq. (21). In the diagonal basis the average is evaluated over free fields by standard means. Following the steps of Ref. [10] we obtain $A(\varepsilon,k) \sim \theta[\varepsilon - \varepsilon_{\rm edge}(k)]/|\varepsilon - \varepsilon_{\rm edge}(k)|^\alpha$, where the exponent depends only on the Luttinger parameter K,

$$\alpha = 1 - \frac{K}{2} \left(1 - \frac{1}{K} \right)^2. \tag{22}$$

This result is the same for the particle and the hole parts of the spectrum. Here K is given by the analytic result in Eq. (8).

Excitations above the spectral edge for Fermi particles with spin can be described using the mobile impurity model in an analogous way [13,24]. The number of bosonic fields doubles due to the two spin orientations. Bosonization of the modes at $\pm k_F$ gives a diagonal Tomonaga-Luttinger model in the basis of spin and charge fields. Here there are four unknown coupling constants between two pairs of the canonically conjugated variables of the Tomonaga-Luttinger model and the Fermi-like field of the deep hole. One pair of constants that corresponds to the coupling to spinon modes is zero due to the symmetry with respect to the spin orientation in the original microscopic model in Eq. (2), where the external magnetic field is zero. Another pair of the constants that correspond to the coupling to holon modes can be identified by considering the same physical properties as for the Fermi particles without spin.

Using the result in Eq. (1) and the Luttinger parameters, the mobile impurity model reads

$$H = \int dx \left[\sum_{\alpha=\rho,\sigma} \frac{v_\alpha}{2\pi} \left(K_\alpha (\nabla\theta_\alpha)^2 + \frac{(\nabla\varphi_\alpha)^2}{K_\alpha} \right) + \frac{v_\sigma - \frac{k}{m^*}}{\sqrt{2}} (K_\sigma \nabla\theta_\rho + \nabla\varphi_\rho) d^\dagger d + d^\dagger \left(\frac{k^2}{2m^*} - \frac{ik\nabla}{m^*} \right) d \right], \quad (23)$$

where k is the total momentum of the system—an input parameter of the model; $m^* = mK_\sigma$ is the effective mass of the deep hole; v_ρ, K_ρ, v_σ, and K_σ are the four Luttinger parameters for the spin and the charge modes; the bosonic fields $\theta_\rho,\varphi_\rho,\theta_\sigma,\varphi_\sigma$ are canonically conjugated variables $[\varphi_\alpha(x), \nabla\theta_\beta(y)] = i\pi\delta_{\alpha\beta}\delta(x-y)$ of the Tomonaga-Luttinger model; and the field d obeys the Fermi commutation rules $\{d(x), d^\dagger(y)\} = \delta(x-y)$.

The diagonalization of the Hamiltonian in Eq. (23) can be done by a unitary transformation in a very similar fashion to the spinless case [13,24]. The rotation $e^{-iU} H e^{iU}$, where $U = \int dx [C_+(\sqrt{K_\rho}\theta + \varphi/\sqrt{K_\rho}) + C_-(\sqrt{K_\rho}\theta - \varphi/\sqrt{K_\rho})] d^\dagger d$ and $C_\pm = \mp\sqrt{K_\rho} 8^{-5/2} (k - k_F)(K_\rho^{-1} \mp K_\sigma^{-1})/(k/K_\sigma \pm k_F/K_\rho)$, removes the coupling term in the Hamiltonian in Eq. (23) allowing straightforward calculations of the observables.

The spectral function in Eq. (3) can be evaluated within the framework of the effective field model in the same way. The original Fermi operators $\psi_\alpha^\dagger(x)$ in the form factor $|\langle f|\psi_\alpha^\dagger(0)|0\rangle|^2$ correspond to composite excitation consisting of two bosons (one for spin and one for charge) and one fermion in the field language of the model in Eq. (23) (see the state in Fig. 3). The fermionic part gives the dominant contribution to the spectral weight, thus the spectral function reads $A(k,\varepsilon) = \int dt\, dx\, e^{-i\varepsilon t} \langle d^\dagger(x,t) d(0,0)\rangle$ where $d(x,t) = e^{-iHt} d(x) e^{iHt}$ and $\langle\cdots\rangle$ is the zero temperature expectation value with respect to the model in Eq. (23). In the diagonal basis the average is evaluated over free fields by standard means. Following the steps of Ref. [13] we obtain in proximity of the edge $A(\varepsilon,k) \sim \theta[\varepsilon - \varepsilon_{\text{edge}}(k)]/|\varepsilon - \varepsilon_{\text{edge}}(k)|^\alpha$ where the exponent depends only on a pair of the dimensionless Luttinger parameters and the momentum along the spectral edge,

$$\alpha = \frac{1}{2} \pm \frac{1}{2} - \frac{K_\rho}{4} \left(1 - \frac{(k-k_F)\left(\frac{k_F}{K_\rho^2} + \frac{k}{K_\sigma^2}\right)}{\left(\frac{k}{K_\sigma}\right)^2 - \left(\frac{k_F}{K_\rho}\right)^2} \right)^2 - \frac{K_\rho}{4} \left(\frac{1}{K_\rho} \pm \frac{(k-k_F)\left(\frac{k_F}{K_\rho K_\sigma} + \frac{k}{K_\rho K_\sigma}\right)}{\left(\frac{k}{K_\sigma}\right)^2 - \left(\frac{k_F}{K_\rho}\right)^2} \right)^2. \quad (24)$$

The result is different for the particle (+) and the hole (−) sectors. The values of the Luttinger parameters obtained numerically using Eq. (20) (see Fig. 4) give divergent values of $0 < \alpha < 1$ in the particle sector and cusplike positive powers $-1 < \alpha < 0$ in the hole sector.

V. BOSONS

While our primary interest lies in Fermi particles, for completeness and to test the generality of our result we consider Bose particles without spin [31]. In this case the application of the Bethe-ansatz approach is very similar to the case of Fermi particles without spin [18]. Our approach of solving a discrete model is complementary to previous approaches to this problem based around numerical solution of the continuum form of the Bethe-ansatz equations and a comparison with a mean-field-like result from the Gross-Pitaevskii equation [32].

We closely follow the original approach of Lieb and Liniger in Ref. [33]. In the coordinate basis a superposition of N plane waves, $\Psi = \int \cdots \int_{-L/2}^{L/2} dx_1 \cdots dx_N \sum_P e^{i\sum_j k_{P_j} x_j} e^{i\sum_{l<l'} \varphi_{P_l P_{l'}}} \psi^\dagger(x_1) \cdots \psi^\dagger(x_N) |\text{vac}\rangle$, is an eigenstate, $H\Psi = E\Psi$, of the model in Eq. (2) with the corresponding eigenenergy $E = \sum_{j=1}^N k_j^2/(2m)$. Here the operators $\psi(x)$ obey the Bose commutation rules $[\psi(x), \psi^\dagger(y)] = \delta(x-y)$, $\sum_P$ is a sum over all permutations of N quasimomenta k_j, and the scattering phases $2\varphi_{ll'} = \log[(k_l - k_{l'} + i2mU)/(k_l - k_{l'} - i2mU)]/i$ are fixed by the two-body scattering problem.

The periodic boundary condition quantizes a set of N quasimomenta simultaneously,

$$k_j L - \sum_{l=1\neq j}^{N} 2\varphi_{jl} = 2\pi I_j, \quad (25)$$

where I_j is a set of nonequal integer numbers. The total momentum of N particles, $P = \sum_j k_j$, is a conserved quantity.

The nonlinear system of equations, Eq. (25), can be solved explicitly in the limit of infinite repulsion. The hard-core bosons in this limit are identical to free fermions [34] which decouples Eq. (25) into a set of plane wave quantization conditions, $k_j = 2\pi I_j/L$. The corresponding eigenstates are Slater determinants whose classification is identical to that of free fermions—all many-body states correspond to all sets of N nonequal integer numbers. These values of quasimomenta k_j can be adiabatically continued under a smooth deformation of Eq. (25) by varying the interaction strength from $U = \infty$ to an arbitrary value of U.

The single parameter that controls the behavior of interacting bosons can be obtained from the Bogoliubov theory in the weak interaction regime [35]. This theory is valid when

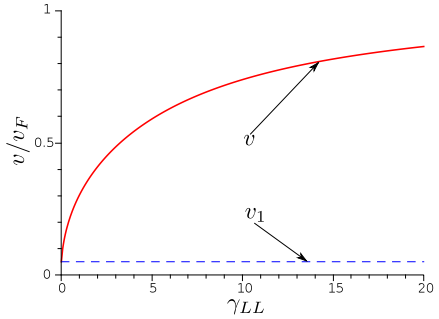

FIG. 6. (Color online) The sound velocity of the collective modes for spinless bosons v at low energies as a function of the interaction parameter γ_{LL} from Eq. (26) (red line) and the quantum of momentum $v_1 = 2\pi/(mL)$ (blue dashed line); $L = 200$, $N = 20$, and $\gamma_L = 0.2mU$.

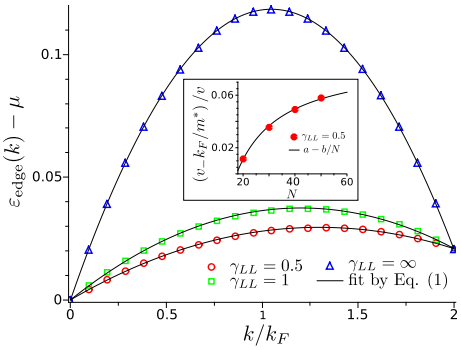

FIG. 7. (Color online) Dispersion of the spectral edge mode for spinless bosons for different values of the interaction parameter $\gamma_L = 0.5, 1, \infty$; $L = 200$, $N = 20$. The blue triangles, green squares, and red ellipses are the numerical solutions of Eq. (25), the solid black lines are the best parabolic fits by Eq. (1). Inset: Difference between the slope of the parabolic dispersion at E_F, which is given by the effective mass m^*, and the velocity of the sound modes, which is obtained by direct evaluation of the energy of the first excited state above the Fermi energy $[(v - k_F/m^*)/v]$ as a function of the number of particles N for $\gamma_{LL} = 0.5$. The solid black line is the $1/N$ fit, $a - b/N$, that gives $a = 0.09$.

the interaction length is smaller than the kinetic energy of particles, e.g., the high-density limit. The same parameter can be generalized to arbitrary interaction strengths [33],

$$\gamma_{LL} = \frac{2mUL}{N}. \tag{26}$$

When $\gamma_{LL} \ll 1$ the interacting particles are like bosons and when $\gamma_{LL} \gg 1$ the system is almost a free Fermi (Tonks-Girardeau) gas.

The eigenstates contributing to the spectral function in Eq. (3) satisfy the number of particles being constrained to be $N + 1$. The lowest energy state for a fixed momentum $-k_F + \Delta P$, where $k_F = \pi N/L$, is given by the sets of integer numbers in Fig. 2. At low energies the system is well approximated by the Tomonaga-Luttinger model with only two free parameters [7,32]. Using the parametrization in Fig. 2, the first Luttinger parameter (the sound velocity of the collective modes) is a discrete derivative $v = L(E_2 - E_1)/(2\pi)$, where E_1 and E_2 are the energies of the states in Fig. 2 with $\Delta P = 0$ and $\Delta P = 2\pi/L$. For Galilean invariant systems the second (dimensionless K) Luttinger parameter can be obtained from the relation $vK = v_F$ where $v_F = \pi N/(mL)$ [19]. Numerical evaluation of v as a function of the interaction parameters γ_{LL} is given in Fig. 6.

Beyond the linear regime the position of the edge of the spectral function is given by the momentum dependence of the states in Fig. 6, $\varepsilon_{\rm edge}(k) = E_k - E_0$ where E_k corresponds to the states with $k = \Delta P$. Numerical evaluation shows that the shape of $\varepsilon_{\rm edge}(k)$ is close to a parabola for all values of γ_{LL} (see Fig. 7). The biggest deviation from a parabola occurs when $\gamma_{LL} \ll 1$. We quantify it by comparing the effective mass m^*, obtained by the best fit of Eq. (1), with v in Fig. 6, obtained at low energies. The deviation $(v - k_F/m^*)/v$ increases as the number of particles N grows but it saturates at a finite value of ~ 0.1 in the limit $N \to \infty$ (see inset in Fig. 7).

As with Fermi particles with spin, for finite systems the parabolalike behavior of the spectral edge mode breaks down in the ultraweak interaction regime when the sound velocity of collective modes at low energies mode becomes comparable with its own quantum set by the finite size of the system $v_1 = 2\pi/(mL)$ (see the dashed line in Fig. 6). Correspondingly, the threshold for entering this regime becomes $\gamma_{LL} \to 0$ in the thermodynamic limit, as observed in Fig. 6 when $v_1 \to 0$. When $v \sim v_1$ the edge of the spectral function is linear at all energies, including the high-energy domain, with the slope that is governed by the kinetic energy of a single free Bose particle. These findings are consistent with the work in Ref. [32] where, within their methodology, the authors find a breakdown in parabolicity in the region of small γ_{LL} and a result consistent with GPE.

VI. CONCLUSIONS

In this work, we have analyzed the spectral edge mode for a variety of one-dimensional models with short-range interactions that bounds from below a continuum of many-body excitations. Explicit diagonalization by means of Bethe-ansatz techniques shows this mode to have an almost perfect parabola dispersion in all cases. Based on this emergent phenomenon, the spectral edge mode can be described empirically by a free, nonrelativistic particle with effective mass identified from the low-energy theory as a free electron mass strongly renormalized by interactions via the dimensionless Luttinger parameter K (K_σ for particles with spin). However, unlike a free particle, the spectral edge mode is not protected by a symmetry, thus deviations from the quadratic dispersion may develop—the biggest discrepancy ($\lesssim 20\%$) occurs for Fermi particles with spin and a very large interaction strength. The empirical model remains robust for finite sound velocities of the collective modes at low energies $v\,(v_\sigma) > v_1$, where $v_1 = 2\pi/(mL)$ is the quantum of momentum.

The relevance of the Luttinger (low-energy) parameters beyond the low-energy limit implies that they can be extracted

using a much wider range of experimental data using the whole energy window from the bottom of the band to the Fermi energy. However, the dispersion of the spectral edge mode itself cannot be used as a qualitative feature to rule out interaction effects since the interactions between particles do not change the parabolic shape of the single-particle dispersion. The biggest deviations could be observed for strongly interacting spinful fermions ($K_\sigma \gtrsim 10$), e.g., electrons in semiconductors at low densities or cold Fermi atoms in a 1D trap that would require a good resolution of the experiment.

The main result of this paper, Eq. (1), complements the mobile impurity model which was developed by Glazman and co-workers as a description of one-dimensional systems above the spectral edge at high energies. Our explicit expression for the dispersion of the edge mode removes an arbitrary input parameter (curvature of the dispersion) that leaves only the few Luttinger parameters and the bare electron mass as a minimal set of necessary ingredients to model excitations above the spectral edge at arbitrary energies. Within such a framework, for example, exponents of the spectral functions are expressed explicitly in terms of only a few Luttinger parameters. The results in Eqs. (22) and (24) provide a systematic way to classify the edge exponents for a wide range of microscopic parameters.

ACKNOWLEDGMENT

We thank EPSRC for the financial support through Grant No. EP/J016888/1.

[1] S. Tomonaga, Prog. Theor. Phys. **5**, 544 (1950); J. M. Luttinger, J. Math. Phys. **4**, 1154 (1963).
[2] P. Nozieres, *Theory of Interacting Fermi Systems* (Addison-Wesley, Reading, MA, 1997).
[3] M. Bockrath, D. H. Cobden, J. Lu, A. G. Rinzler, R. E. Smalley, L. Balents, and P. L. McEuen, Nature (London) **397**, 598 (1999).
[4] O. M. Auslaender, A. Yacoby, R. de Picciotto, K. W. Baldwin, L. N. Pfeiffer, and K. W. West, Science **295**, 825 (2002).
[5] Y. Jompol, C. J. B. Ford, J. P. Griffiths, I. Farrer, G. A. C. Jones, D. Anderson, D. A. Ritchie, T. W. Silk, and A. J. Schofield, Science **325**, 597 (2009).
[6] B. Paredes, A. Widera, V. Murg, O. Mandel, S. Folling, I. Cirac, G. V. Shlyapnikov, T. W. Hansch, and I. Bloch, Nature (London) **429**, 277 (2004).
[7] T. Giamarchi, *Quantum Physics in One Dimension* (Clarendon Press, Oxford, 2003); A. O. Gogolin, A. A. Nersesyan, and A. M. Tsvelik, *Bosonization and Strongly Correlated Systems* (Cambridge University Press, Cambridge, UK, 1998).
[8] M. Pustilnik, M. Khodas, A. Kamenev, and L. I. Glazman, Phys. Rev. Lett. **96**, 196405 (2006); M. Khodas, M. Pustilnik, A. Kamenev, and L. I. Glazman, Phys. Rev. B **76**, 155402 (2007).
[9] P. Nozieres and C. T. De Dominicis, Phys. Rev. **178**, 1097 (1969).
[10] Adilet Imambekov and Leonid I. Glazman, Phys. Rev. Lett. **102**, 126405 (2009).
[11] R. G. Pereira, J. Sirker, J.-S. Caux, R. Hagemans, J. M. Maillet, S. R. White, and I. Affleck, Phys. Rev. Lett. **96**, 257202 (2006).
[12] R. G. Pereira, S. R. White, and I. Affleck, Phys. Rev. Lett. **100**, 027206 (2008).
[13] T. L. Schmidt, A. Imambekov, and L. I. Glazman, Phys. Rev. Lett. **104**, 116403 (2010).
[14] In this paper we restrict ourselves to only repulse interactions. An attractive potential admits formation of bound states that can alter the properties of the system completely.
[15] A. Imambekov, T. L. Schmidt, and L. I. Glazman, Rev. Mod. Phys. **84**, 1253 (2012).
[16] A. A. Abrikosov, L. P. Gorkov, and I. E. Dzyaloshinski, *Methods of Quantum Field Theory in Statistical Physics* (Dover, New York, 1975).
[17] J. von Delft and H. Schoeller, Ann. Phys. (NY) **7**, 225 (1998).
[18] V. E. Korepin, N. M. Bogoliubov, and A. G. Izergin, *Quantum Inverse Scattering Methods and Correlation Functions* (Cambridge University Press, Cambridge, UK, 1993).
[19] F. D. M. Haldane, Phys. Lett. A **81**, 153 (1981).
[20] O. Tsyplyatyev and A. J. Schofield, Phys. Rev. B **88**, 115142 (2013).
[21] Approximation of Eq. (8) for $mU \ll 1$ reproduces the effective mass from Ref. [11].
[22] C. N. Yang, Phys. Rev. Lett. **19**, 1312 (1967); E. H. Lieb and F. Y. Wu, *ibid.* **21**, 192 (1968).
[23] M. Ogata and H. Shiba, Phys. Rev. B **41**, 2326 (1990).
[24] F. H. L. Essler, Phys. Rev. B **81**, 205120 (2010).
[25] C. F. Coll, Phys. Rev. B **9**, 2150 (1974).
[26] The definition of γ_{YG} does not change for excited states around the edge of the spectral function in the thermodynamic limit. The average energy per magnon in Eq. (18) is still set by the ground state properties which are not altered by a few excitations within the band of $\lesssim E_F$ in a large system.
[27] H. J. Schulz, Phys. Rev. Lett. **64**, 2831 (1990).
[28] This not a unique way to quantify deviations. For example, see another approach in Ref. [32].
[29] The biggest deviation of 20% quantifies the discrepancy between the best by Eq. (1) at high energy and the low-energy velocity of the collective modes obtained using Eq. (20). The fit by Eq. (1) on its own is in fact more accurate: The coefficient of determination is already $R^2 = 0.9934$ for $N = 80$ in the strong interaction regime with $\gamma_{YG} = 6.88$.
[30] A. Kamenev and L. I. Glazman, Phys. Rev. A **80**, 011603(R) (2009).
[31] Bose particles with spin could also be analyzed in a similar fashion. A comprehensive summary of this problem is given in review Ref. [15].
[32] G. E. Astrakharchik and L. P. Pitaevskii, Europhys. Lett. **102**, 30004 (2013).
[33] E. H. Lieb and W. Liniger, Phys. Rev. **130**, 1605 (1963).
[34] L. Tonks, Phys. Rev. **50**, 955 (1936); M. Girardeau, J. Math. Phys. **1**, 516 (1960).
[35] N. N. Bogoliubov, Izv. Acad. Nauk USSR **11**, 77 (1947) [J. Phys. (USSR) **11**, 23 (1947)].

Hierarchy of Modes in an Interacting One-Dimensional System

O. Tsyplyatyev and A. J. Schofield
School of Physics and Astronomy, University of Birmingham, Birmingham B15 2TT, United Kingdom

Y. Jin, M. Moreno, W. K. Tan, C. J. B. Ford, J. P. Griffiths, I. Farrer, G. A. C. Jones, and D. A. Ritchie
Cavendish Laboratory, University of Cambridge, J J Thomson Avenue, Cambridge CB3 0HE, United Kingdom
(Received 13 August 2014; published 11 May 2015)

Studying interacting fermions in one dimension at high energy, we find a hierarchy in the spectral weights of the excitations theoretically, and we observe evidence for second-level excitations experimentally. Diagonalizing a model of fermions (without spin), we show that levels of the hierarchy are separated by powers of $\mathcal{R}^2/L^2$, where $\mathcal{R}$ is a length scale related to interactions and L is the system length. The first-level (strongest) excitations form a mode with parabolic dispersion, like that of a renormalized single particle. The second-level excitations produce a singular power-law line shape to the first-level mode and multiple power laws at the spectral edge. We measure momentum-resolved tunneling of electrons (fermions with spin) from or to a wire formed within a GaAs heterostructure, which shows parabolic dispersion of the first-level mode and well-resolved spin-charge separation at low energy with appreciable interaction strength. We find structure resembling the second-level excitations, which dies away quite rapidly at high momentum.

DOI: 10.1103/PhysRevLett.114.196401 PACS numbers: 71.10.Pm, 03.75.Kk, 73.63.Nm, 73.90.+f

The challenge of understanding interacting electrons is a major open problem. Progress has so far relied on being able to assume a linear relation between energy and momentum that restricts our understanding to the low energy and low momentum excitations where this assumption is valid. This has led to the notion of a Fermi liquid [1] and, in one dimension, a Luttinger liquid [2], where those excitations are described as quasiparticles. In the case of the Luttinger liquid, the quasiparticles are quite distinct from the underlying electrons. In this Letter we have studied a model of interacting fermions where we are not constrained by linearization to low energies and find that the many-body solutions can be characterized in a hierarchical fashion by their "spectral weight"—a quantity determining how the solutions connect to physical observables. At the top of this hierarchy is an excitation that looks like a single underlying fermion but with a new dispersion. We then look for evidence of this hierarchy by undertaking experiments of momentum-conserved tunneling in 1D quantum wires of electrons. We see both the first and second levels of this hierarchy, indicating that this characterization is a robust feature of 1D interacting electrons. Despite its differences from Luttinger-liquid behavior, we are able to show how our hierarchy crosses over to the more familiar Luttinger liquid at low energies.

Our theoretical approach is the full microscopic diagonalization of a model of spinless fermions with short-range interactions and the evaluation of its spectral function via Bethe ansatz methods. We find that the spectral weights of excitations have factors with different powers of a ratio of lengths, $\mathcal{R}^2/L^2$ (which will be defined below) separating them into a hierarchy. The dispersion of the mode formed by excitations with zero power, which we call the first level, is parabolic (see Fig. 1) with a mass renormalized by the Luttinger parameter K [3]. The continuous spectrum of the second-level excitations produces a power-law line shape around the first-level mode with a singular exponent -1. Around the hole edge ($h0a$ in Fig. 1) the continuous spectrum reproduces the spectral edge singularity predicted by the very recently proposed mobile impurity model [4],

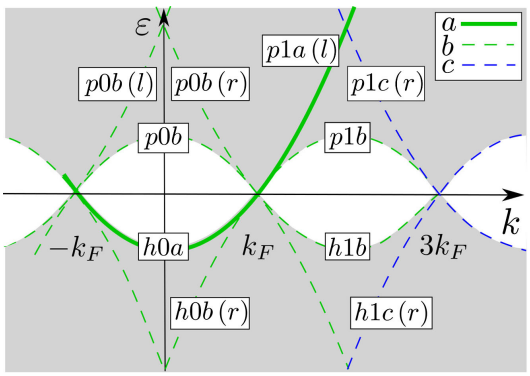

FIG. 1 (color online). The main features of spectral function for spinless fermions in the region $-k_F<k<k_F$ ($k_F<k<3k_F$) labeled by 0(1). The gray areas mark nonzero values, $p(h)$ shows the particle(hole) sector, k_F is the Fermi momentum, a, b, c, respectively, identify the level in the hierarchy in powers 0,1,2 of $\mathcal{R}^2/L^2$, and (r, l) specifies the origin in the range—modes on the edge have no such label.

but gives a different power-law behavior of the spectral function around the opposite particle edge ($p0b$ in Fig. 1).

Experimentally, we measure the momentum-resolved tunneling of electrons (fermions with spin) confined to a 1D geometry in the top layer of a GaAs-AlGaAs double-quantum-well structure from or to a 2D electron gas in the bottom layer. Probing the spectral function for spinful fermions in this setup we find the same general picture that emerges from the calculation for spinless fermions. We observe a single parabola (which particle-hole asymmetry is manifested in relaxation processes [5]) at high energy, together with well-resolved spin-charge separation (a distinct Luttinger-liquid effect) at low energy with appreciable interaction strength (ratio of charge and spin velocities $v_c/v_s \approx 1.4$) [6,7]. In addition, we can now resolve the structure just above k_F that appears to be the edge of the second-level excitations ($p1b$). However, for higher k we find no sign of the higher-level excitations, implying that their amplitude must have become at least 3 orders of magnitude weaker than for the first parabola ($h0a$). This can only be explained by the hierarchy of modes developed in the theory part of this Letter.

Spinless fermions.—We study theoretically the model of interacting Fermi particles without spin in one dimension,

$$H = \int_{-(L/2)}^{L/2} dx \left(-\frac{1}{2m} \psi^\dagger(x) \Delta \psi(x) - UL\rho(x)^2 \right), \quad (1)$$

where the field operators $\psi(x)$ satisfy the Fermi commutation relations, $\{\psi(x), \psi^\dagger(x')\} = \delta(x - x')$, $\rho(x) = \psi^\dagger(x)\psi(x)$ is the particle density operator, and m is the bare mass of a single particle. Below, we consider the periodic boundary condition $\psi(x + L) = \psi(x)$, restrict ourselves to repulsive interaction $U > 0$ only, and take $\hbar = 1$. The response of a many-body system to a single-particle excitation at momentum k and energy ε is described by a spectral function that, in terms of the eigenstates, reads as [8] $A(k, \varepsilon) = L\sum_f [|\langle f|\psi^\dagger(0)|0\rangle|^2 \delta(\varepsilon - E_f + E_0)\delta(k - P_f) + |\langle 0|\psi(0)|f\rangle|^2 \delta(\varepsilon + E_f - E_0)\delta(k + P_f)]$, where E_0 is the energy of the ground state $|0\rangle$, and P_f and E_f are the momenta and the eigenenergies of the eigenstates $|f\rangle$; all eigenstates are assumed normalized.

In the Bethe ansatz approach the model in Eq. (1) is diagonalized by N-particle states parametrized with sets of N quasimomenta k_j that satisfy the nonlinear equations $\mathcal{L}k_j - \sum_{l \neq j} \ln[-(e^{i(k_j + k_l)} + 1 - 2mUe^{ik_j})/(e^{i(k_j + k_l)} + 1 - 2mUe^{ik_l})]/i = 2\pi I_j$ [9], where I_j are sets of non-equal integers. The dimensionless length of the system $\mathcal{L} = L/\mathcal{R}$ is normalized by the short length scale $\mathcal{R}$, which is introduced using a lattice (with next-neighbor interaction) as the lattice parameter (and interaction radius) $\mathcal{R}$ that provides microscopically an ultraviolet cutoff for the theory. The latter procedure at high energy is analogous to the point-splitting technique [10] at low energy. Solving the lattice equations in the continuum regime, which corresponds to the thermodynamic ($N, \mathcal{L} \to \infty$, but $N/\mathcal{L}$ is finite) and the long wavelength ($N/\mathcal{L} \ll 1$ with $N/\mathcal{L}$ finite) limits, we obtain [11]

$$k_j = \frac{2\pi I_j}{\mathcal{L} - \frac{mUN}{mU+1}} - \frac{mU}{mU+1} \sum_{l \neq j} \frac{2\pi I_l}{(\mathcal{L} - \frac{mUN}{mU+1})^2}. \quad (2)$$

The corresponding eigenenergy and total momentum (protected by the translational invariance of the system) are $E = \sum_j k_j^2/(2m)$ and $P = \sum_j k_j$. Using the algebraic representation of the Bethe ansatz we obtain the form factor for the spectral function in the same regime as [11,17]

$$|\langle f|\psi^\dagger(0)|0\rangle|^2 = \frac{Z^{2N}}{\mathcal{L}} \frac{\prod_j (k_j^0 - P_f)^2}{\prod_{i,j}(k_j^f - k_i^0)^2} \times \prod_{i<j}(k_j^0 - k_i^0)^2 \prod_{i<j}(k_j^f - k_i^f)^2, \quad (3)$$

where $Z = mU/(mU+1)/[\mathcal{L} - NmU/(1+mU)]$ and k_j^f and k_j^0 are the quasimomenta of the eigenstate $|f\rangle$ and the ground state $|0\rangle$.

This result is singular when one or more quasimomenta of an excited state coincide with that of the ground state. The divergences occur in the first term of Eq. (2) but the second (which is smaller in $1/\mathcal{L}$) term provides a cutoff within the theory, canceling a power of $Z^2 \sim \mathcal{L}^{-2}$ per singularity; when N quasimomenta k_j^f coincide with k_j^0, Eq. (3) gives $\mathcal{L}|\langle f|\psi^\dagger(0)|0\rangle|^2 = 1$. We label the many-body excitations by the remaining powers of $\mathcal{L}^{-2}$ [18], e.g., $p0b$: $p(h)$ indicates the particle (hole) sector, 0(1) encodes the range of momenta $-k_F < k < k_F$ ($k_F < k < 3k_F$), and a, b, c reflect the terms $\mathcal{L}^{-2n}$ with $n = 0, 1, 2$. All simple modes, formed by single particlelike and holelike excitations of the ground state k_j^0, are presented in Fig. 1 and the spectral function along them is evaluated in Table I. Note that the thermodynamic limit involves both $\mathcal{L} \to \infty$ and the particle number $N \to \infty$ and the finite ratio $N/\mathcal{L}$ ensures that the spectral weight of the subleading modes, e.g., the modes $p0b$, $h1b$, and $h1b(r)$, is still apparent in the infinite system.

Excitations around the strongest a modes have an additional electron-hole pair in their quasimomenta, which introduces an extra factor of $\mathcal{L}^{-2}$,

$$|\langle f|\psi^\dagger(0)|0\rangle|^2 = \frac{Z^2}{\mathcal{L}} \frac{(k_2^f - k_1^f)^2 (k_1^0 - P_f)^2}{(k_1^f - k_1^0)^2 (k_2^f - k_1^0)^2}. \quad (4)$$

The energies of the electron-hole pairs themselves are regularly spaced around the Fermi energy with slope v_F. However, degeneracy of the many-body excitations due to the spectral linearity makes the level spacings nonequidistant. Using a version of the spectral function smoothed over energy, $\bar{A}(\varepsilon) = \int_{-\epsilon_0/2}^{\epsilon_0/2} d\epsilon A(\varepsilon + \epsilon, k)/\epsilon_0$, where ϵ_0 is a

TABLE I. Spectral weights $A(k,\varepsilon_\alpha(k))$ along the a and the b modes for $-k_F<k<k_F$ ($k_F<k<3k_F$) labeled by $x=0(1)$. Here α is the index of the mode, e.g., $\alpha=h0a$, and other terminology is the same as in Fig. 1; $\gamma=2\pi/\mathcal{L}$ and $Z=mU/(mU+1)/[\mathcal{L}-NmU/(1+mU)]$.

	$x=0$	$x=1$
pxa		1
hxa	1	
pxb	$16Z^2k_F^2k^2/(k^2-(k_F+\gamma)^2)^2$	$4Z^2\gamma^2(k-k_F+\frac{3}{2}\gamma)^2/(k-k_F+\gamma)^2(k-k_F+2\gamma)^2$
$pxb(l)$	$4Z^2(k_F+k)^2/k_F^2$	
$pxb(r)$	$4Z^2(k_F-k)^2/k_F^2$	
hxb		$4Z^2(3k_F-k-\gamma)^2(k_F+k)^2/k_F^2(k-k_F+\gamma)^2$
$hxb(l)$	$4Z^2\gamma^2/(k+k_F+2\gamma)^2$	$Z^2k_F^2k^2/((k+\gamma)^2-k_F^2)^2$
$hxb(r)$	$4Z^2\gamma^2/(k-k_F-2\gamma)^2$	

small energy scale, we obtain $\bar{A}(\varepsilon)=Z^2 2k_F(3k^2+k_F^2)/(m\gamma K)(\varepsilon_{h0a}-\varepsilon)^{-1}\theta(\varepsilon_{h0a}-\varepsilon)$ and $\bar{A}(\varepsilon)=Z^2(k+\mathrm{sgn}(\varepsilon-\varepsilon_{p1a(l)})k_F)^3/(m\gamma K)|\varepsilon-\varepsilon_{p1a(l)}|^{-1}$, where $\gamma=2\pi/\mathcal{L}$ and the dispersion of the a modes is parabolic, $\varepsilon_{h0a}(k)=\varepsilon_{p1a(l)}(k)=k^2/(2mK)$, with the mass renormalized by the Luttinger parameter K [3], around the $h0a$ and $p1a(l)$ modes. The exponent -1 coincides with the prediction of the mobile-impurity model [20], where the spectral edge is an a mode, $h0a$.

Excitations around the b modes belong to the same level of hierarchy as the modes themselves, Eq. (4), giving a more complicated shape of the spectral function. Let us focus on one mode, $p0b$. It has a new power-law behavior characterized by an exponent changing with k from $\bar{A}(\varepsilon)\sim(\varepsilon-\varepsilon_{p0b})^3$ for $k=0$ to $\bar{A}(\varepsilon)\sim\mathrm{const}-(\varepsilon-\varepsilon_{p0b})$ for $k\approx k_F$, where $\varepsilon_{p0b}(k)=k_F^2/(mK)-k^2/(2mK)$. This is essentially different from predictions of the mobile-impurity model. Here we observe that the phenomenological model in Refs. [21] is correct only for the a-mode spectral edge but higher-order edges require a different field-theoretical description. The density of states is linear, $\nu(\varepsilon)\sim(\varepsilon-\varepsilon_{p0b})$, but level statistics varies from having a regular level spacing (for k commensurate with k_F) to an irregular distribution (for incommensurate k), which is another microscopic difference between the a and b modes.

Now we use the result in Eq. (3) to calculate another observable, the local density of states. This is independent of position for the translationally invariant systems and, in term of eigenmodes, is [8,22] $\rho(\varepsilon)=\mathcal{L}\sum_f[|\langle f|\psi^\dagger(0)|0\rangle|^2\delta(\varepsilon-E_f+E_0)+|\langle 0|\psi(0)|f\rangle|^2\delta(\varepsilon+E_f-E_0)]$. The leading contribution for $\varepsilon>0$ comes from the a modes, $\rho(\varepsilon)=\theta(\varepsilon)\sqrt{2mK/\varepsilon}$, which gives the same $1/\sqrt{\varepsilon}$ functional dependence as the free-particle model—see red line in Fig. 2. Around the Fermi energy the Tomonaga-Luttinger model predicts power-law suppression of $\rho(\varepsilon)\sim|\varepsilon-\mu|^{(K+K^{-1})/2-1}$ [2] (blue region in Fig. 2) signaling that the leading-order expansion in the $\mathcal{L}|\langle f|\psi^\dagger(0)|0\rangle|^2=1$ result is insufficient. We evaluate $\rho(\varepsilon)$ numerically in this region using determinant representation of the form factors for the lattice model instead of Eq. (3) (inset in Fig. 2) [11,23]. Away from the point $\varepsilon=\mu$ the particle-hole symmetry of the Tomonaga-Luttinger model is broken by the curvature of the dispersion of the a modes. For $\varepsilon<0$ the leading contribution to $\rho(\varepsilon)$ comes from b modes. Using Eq. (4) we obtain $\rho(\varepsilon)=2Z^2k_F^2/(\gamma\mu K)[2(1-3|\varepsilon|/\mu)\sqrt{\mu}\cot^{-1}(\sqrt{|\varepsilon|/\mu})/\sqrt{|\varepsilon|}+6]\theta(-\varepsilon)$, which contains another van Hove singularity $\rho(\varepsilon)=2\pi Z^2k_F^2/(\gamma K\sqrt{\mu\varepsilon})$ at the bottom the conduction band (green line in Fig. 2).

Having established the theoretical framework for expecting a hierarchy of modes in our calculation, we now turn to experiment and the evidence from momentum-conserving tunneling of electrons. Electrons, being spin-1/2, do not directly correspond to the model above (and neither is there a method known for calculating the necessary form factors for spinful fermions). Nevertheless, the general picture that emerges for the experiment is qualitatively the same as we have established theoretically above and it provides additional support for the existence of a hierarchy.

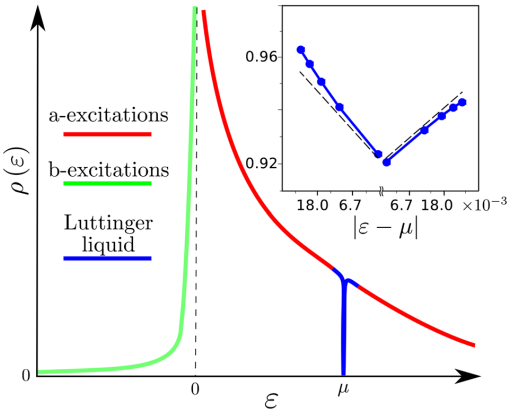

FIG. 2 (color online). The local density of states for spinless fermions: red and green lines show the contribution of a and b excitations and the blue line indicates the Luttinger-liquid regime. Inset is a log-log plot around the Fermi energy: the blue points are numerical data for $N=71$, $L=700$, $mV=6$ giving $K=0.843$, and the dashed line is $\rho(\varepsilon)=\mathrm{const}|\varepsilon-\mu|^{(K+K^{-1})/2-1}$.

Fermions with spin.— We study experimentally in a high-mobility GaAs-AlGaAs double-quantum-well structure with electron density around 2×10^{15} m^{-2} in each layer. Electrons in the top layer are confined to a 1D geometry by split gates. Our devices contain an array of ~500 highly regular wires to boost the signal from 1D to 2D tunneling. The small lithographic width of the wires, ~0.18 μm, provides a large energy spacing between the first and second 1D subbands, allowing a wide energy window for electronic excitations in the single-subband case—see device schematic in Fig. 3(f) and more details in Ref. [7].

The 2DEG in the bottom layer is separated from the wires by a $d = 14$ nm tunnel barrier (giving a spacing between the centers of the wave functions of $d = 34$ nm). It is used as a controllable injector or collector of electrons for the 1D system [24]. A sharp spectral feature in the density of states of the 2DEG produced by integration over momenta in the direction perpendicular to the wires can be shifted in energy by a dc bias between the layers, in order to probe different energies. Also, an in-plane magnetic field B applied perpendicular to the wires changes the longitudinal momentum in the tunneling between layers by $\Delta k = eBd/\hbar$, where e is the electronic charge, and so probes the momentum. Together they reveal the dispersion relation of states in each layer. In this magnetic field range the system is still within the regime of Pauli paramagnetism for the electron densities in our samples.

We have measured the tunneling conductance G between the two layers [see Fig. 3(f)] in detail in a wide range of voltage and magnetic field, corresponding to a large portion of the 1D spectral function from $-k_F$ to $3k_F$ and from -2μ to 2μ [Fig. 3(a)]. At low energy we observe spin-charge separation [7]. The slopes of the charge (C) and spin (S) branches—black dashed lines—are $v_c\approx2.03\times10^5$ and $v_s\approx1.44\times10^5$ ms^{-1}, respectively, with $v_c/v_s\approx1.4\pm0.1$ [11]. This large ratio, together with a strong zero-bias suppression of tunneling [7], confirms that our system is in the strongly interacting regime.

Unavoidable "parasitic" (p') tunneling from narrow 2D regions connecting the wires to the space constriction [7], superimpose a set of parabolic dispersions, marked by magenta and blue dotted lines in Fig. 3(a) on top of the 1D to 2D signal. Apart from them we observe a 1D parabola, marked by the solid green line in Fig. 3(a), which extends from the spin-excitation branch at low energy. The position of its minimum gives the 1D chemical potential $\mu\approx3$ meV and its crossings with the line $V_{dc} = 0$, corresponding to momenta $-k_F$ and k_F, give the 1D Fermi momentum $k_F\approx8\times10^7$ m^{-1}.

All other edges of the 1D spectral function are constructed by mirroring and translation of the hole part of the observable 1D dispersion, the dashed green and blue lines in Fig. 3. We observe a distinctive feature in the region just above the higher $V_{dc} = 0$ crossing point (k_F): the 1D peak, instead of just continuing along the noninteracting

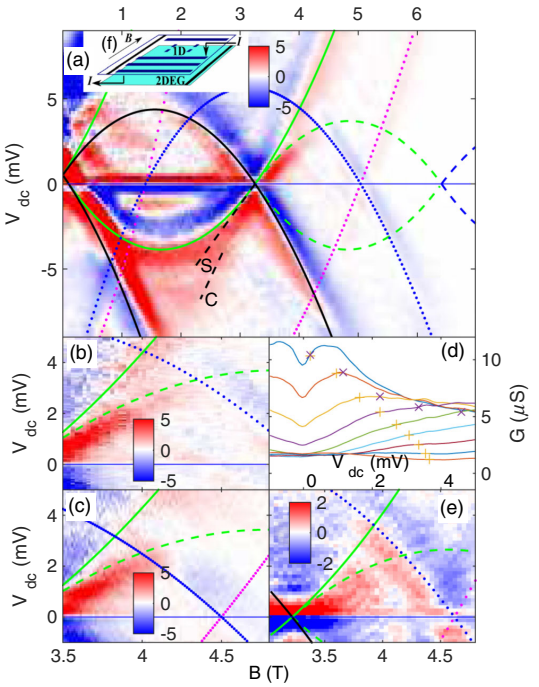

FIG. 3 (color online). Measurement of the tunneling differential conductance $G = dI/dV$ for two samples, each consisting of a set of identical wires of length $L = 10$ (a)–(d) and $L = 18$ μm (e), sketched in inset (f). (a) Intensity plot of dG/dV_{dc} to 2μ. The line is the 2D dispersion. The green solid line marks the a modes, dashed green lines the b modes, and dashed blue the c modes (as in Fig. 1); dotted magenta and blue lines are parasitic 2D dispersions. Spin (S) and charge (C) modes are indicated with black dashed lines. $T = 300$ mK. (b) Enlargement of the replica feature in (a) just above k_F. It appears as a pale band (slowly varying G) between the two green curves, after a red region (sharp rise in G). (c) The same as in (b), but with the gate voltage over most of the parasitic (p') region changed to move the p' parabolas. (d) G vs V_{dc} at various fields B from 3 to 4.8 T [from (a)]; + and × symbols on each curve indicate, respectively, the voltages corresponding to the dashed and solid [$p1b$ and $p1a(l)$] green lines in (a) and (b), showing the enhanced conductance between the two. (e) dG/dV_{dc} for a second device, at $T<100$ mK. The replica feature is similar to that shown in (b) and (c) for the other sample.

parabola, broadens, with one boundary following the parabola [$p1a(l)$] and the other bending around, analogous to the replica $p1b$. This is observed in samples with different wire designs and lengths [10 (a)–(d), and 18 μm (e)] and at temperatures from 100 up to at least 300 mK. The strength of the $p1b$ feature decreases as the B field increases away from the crossing point analogously to that for spinless fermions in Table I [25], though it then passes a p' parabola. (b) and (c) show the replica feature [26] for two different positions of the p' parabolas using a gate above most of

the p' region, showing that the replica feature is independent of the p' tunneling. G is plotted in (d) on cuts along the V_{dc} axis of (a) at various fields B from 3 to 4.8 T; between the + and × symbols on each curve is the region of enhanced conductance, characteristic of the replica $p1b$. The amplitude of the feature dies away rapidly, and beyond the p' parabolas, we have measured up to 8 T with high sensitivity, and find no measurable sign of any feature above the experimental noise threshold. This places an upper limit on the amplitude of any replica away from k_F of at least 3 orders of magnitude less than that of the a mode ($h0a$).

Making an analogy with the microscopic theory for spinless fermions above, we estimate the ratio of signals around different spectral edges using the 1D Fermi wavelength, $\lambda_F \approx 80$ nm for our samples, as the short-range scale. The amplitude of signal from the second (third)-level excitations is predicted to be smaller by a factor of more than $\lambda_F^2/L^2 = 6\times10^{-5}$ ($\lambda_F^4/L^4 = 4\times10^{-9}$), where the length of a wire is $L = 10$ μm. These values are at least an order of magnitude smaller than the noise level of our experiment. Thus, our observations are consistent with the mode hierarchy picture for fermions.

In conclusion, we have shown that a hierarchy of modes can emerge in an interacting 1D system controlled by the system length. The dominant mode for long systems has a parabolic dispersion, like that of a renormalized free particle, in contrast with distinctly nonfreeparticle-like behavior at low energy governed by the Tomonaga-Luttinger model. Experimentally, we find a clear feature resembling the second-level excitations, which dies away at high momentum.

We acknowledge financial support from the UK EPSRC through Grants No. EP/J01690X/1 and No. EP/J016888/1.

[1] P. Nozieres, *Theory of Interacting Fermi Systems* (Addison-Wesley, Reading, MA, 1997).
[2] T. Giamarchi, *Quantum Physics in One Dimension* (Clarendon Press, Oxford, 2003).
[3] O. Tsyplyatyev and A. J. Schofield, Phys. Rev. B **90**, 014309 (2014).
[4] A. Imambekov, T. L. Schmidt, and L. I. Glazman, Rev. Mod. Phys. **84**, 1253 (2012).
[5] G. Barak, H. Steinberg, L. N. Pfeiffer, K. W. West, L. Glazman, F. von Oppen, and A. Yacoby, Nat. Phys. **6**, 489 (2010).
[6] O. M. Auslaender, A. Yacoby, R. de Picciotto, K. W. Baldwin, L. N. Pfeiffer, and K. W. West, Science **295**, 825 (2002).
[7] Y. Jompol, C. J. B. Ford, J. P. Griffiths, I. Farrer, G. A. C. Jones, D. Anderson, D. A. Ritchie, T. W. Silk, and A. J. Schofield, Science **325**, 597 (2009).
[8] A. A. Abrikosov, L. P. Gorkov, and I. E. Dzyaloshinski, *Methods of Quantum Field Theory in Statistical Physics* (Dover, New York, 1975).
[9] V. E. Korepin, N. M. Bogoliubov, and A. G. Izergin, *Quantum Inverse Scattering Methods and Correlation Functions* (Cambridge University Press, Cambridge, England, 1993).
[10] J. von Delft and H. Schoeller, Ann. Phys. (N.Y.) **7**, 225 (1998).
[11] See Supplemental Material at http://link.aps.org/supplemental/10.1103/PhysRevLett.114.196401, which includes Refs. [12–16], and at the Universities of Cambridge and of Birmingham data repositories at http://www.repository.cam.ac.uk/handle/1810/247433 and http://epapers.bham.ac.uk/1956/.
[12] M. Gaudin, B. M. McCoy, and T. T. Wu, Phys. Rev. D **23**, 417 (1981); V. E. Korepin, Commun. Math. Phys. **86**, 391 (1982).
[13] N. Kitanine, J. M. Maillet, and V. Tetras, Nucl. Phys. **B554**, 647 (1999); Nucl. Phys. **B567**, 554 (2000).
[14] N. A. Slavnov, Theor. Math. Phys. **79**, 502 (1989).
[15] V. G. Drinfeld, DOKLADY AKADEMII NAUK SSSR **273**, 531 (1983) [Sov. Math. Dokl. **28**, 667 (1983)].
[16] F. Gohmann and V. E. Korepin, J. Phys. A **33**. 1199 (2000); K. Motegi and K. Sakai, Nucl. Phys. **B793**, 451 (2008).
[17] The result in Eq. (3) was verified by direct summation over spatial variables for up to $N = 3$ particles.
[18] A similar hierarchy of excitations is observed in numerical studies of spin chains at large fillings, e.g., Ref. [19], for which Eq. (3) is not applicable.
[19] J.-S. Caux and J. M. Maillet, Phys. Rev. Lett. **95**, 077201 (2005).
[20] O. Tsyplyatyev and A. J. Schofield, Phys. Rev. B **88**, 115142 (2013).
[21] M. Pustilnik, M. Khodas, A. Kamenev, and L. I. Glazman, Phys. Rev. Lett. **96**, 196405 (2006); A. Imambekov and L. I. Glazman, Phys. Rev. Lett. **102**, 126405 (2009).
[22] This is equivalent to the conventional definition, $\rho(x,\varepsilon) = -\mathrm{Im}[\int dt e^{-i\varepsilon t} G(x,x,t)]\mathrm{sgn}(\varepsilon-\mu)/\pi$, using the two point correlation function $G(x,x',t) = -i\langle T[e^{-iHt}\psi(x)e^{iHt}\psi^\dagger(x')]\rangle$ at zero temperature.
[23] The regions of validity of the Tomonaga-Luttinger model and Eq. (3) have a large overlap around $\varepsilon = \mu$ since power-law suppression of $\rho(\varepsilon)$ has a very small exponent due to only small deviations from $K = 1$ for arbitrary short-range interactions between spinless fermions.
[24] A. Altland, C. H. W. Barnes, F. W. J. Hekking, and A. J. Schofield, Phys. Rev. Lett. **83**, 1203 (1999).
[25] From Table I for spinless fermions it is natural to expect that divergence of the spectral weight of a b mode toward an a mode is a general feature, but there is no known method for performing a microscopic calculation in the spinful case.
[26] The $h0b(r)$ mode should (from Table I) be comparable to $p1b$ but it would be very difficult to resolve it due to the overlaying spin and charge lines.

PHYSICAL REVIEW B **93**, 075147 (2016)

Nature of the many-body excitations in a quantum wire: Theory and experiment

O. Tsyplyatyev,[1] A. J. Schofield,[2] Y. Jin,[3] M. Moreno,[3] W. K. Tan,[3] A. S. Anirban,[3] C. J. B. Ford,[3] J. P. Griffiths,[3] I. Farrer,[3] G. A. C. Jones,[3] and D. A. Ritchie[3]

[1]*Institut für Theoretische Physik, Universität Frankfurt, Max-von-Laue Strasse 1, 60438 Frankfurt, Germany*

[2]*School of Physics and Astronomy, University of Birmingham, Birmingham, B15 2TT, United Kingdom*

[3]*Cavendish Laboratory, University of Cambridge, J J Thomson Avenue, Cambridge, CB3 0HE, United Kingdom*

(Received 28 August 2015; revised manuscript received 18 January 2016; published 24 February 2016; corrected 9 March 2016)

The natural excitations of an interacting one-dimensional system at low energy are the hydrodynamic modes of a Luttinger liquid, protected by the Lorentz invariance of the linear dispersion. We show that beyond low energies, where the quadratic dispersion reduces the symmetry to Galilean, the main character of the many-body excitations changes into a hierarchy: calculations of dynamic correlation functions for fermions (without spin) show that the spectral weights of the excitations are proportional to powers of $\mathcal{R}^2/L^2$, where $\mathcal{R}$ is a length-scale related to interactions and L is the system length. Thus only small numbers of excitations carry the principal spectral power in representative regions on the energy-momentum planes. We have analyzed the spectral function in detail and have shown that the first-level (strongest) excitations form a mode with parabolic dispersion, like that of a renormalized single particle. The second-level excitations produce a singular power-law line shape to the first-level mode and multiple power laws at the spectral edge. We have illustrated a crossover to a Luttinger liquid at low energy by calculating the local density of states through all energy scales: from linear to nonlinear, and to above the chemical potential energies. In order to test this model, we have carried out experiments to measure the momentum-resolved tunneling of electrons (fermions with spin) from/to a wire formed within a GaAs heterostructure. We observe a well-resolved spin-charge separation at low energy with appreciable interaction strength and only a parabolic dispersion of the first-level mode at higher energies. We find a structure resembling the second-level excitations, which dies away rapidly at high momentum in line with the theoretical predictions here.

DOI: 10.1103/PhysRevB.93.075147

I. INTRODUCTION

Predicting the behavior of interacting electrons is a significant open problem. Most progress to date has been made at low energies where the linearization of the single-particle dispersion led to the construction of Fermi [1] and, in one dimension, to Luttinger-liquid theories [2] in which the natural excitations are fermionic quasiparticles and hydrodynamic modes, respectively. The only significant progress beyond the linear approximation has been achieved via the heavy impurity model, for Fermi [3–5] and Luttinger [6] liquids, showcasing threshold singularities drastically different from the low-energy behavior. In this paper, we investigate one-dimensional (1D) fermions beyond the linear approximation where the natural many-body excitations form a hierarchical structure, which we have recently discovered [7], in sharp contrast with the Fermi quasiparticles or hydrodynamic modes. We obtain the dynamical structure factor, in addition to the already known spectral function, and construct an inductive proof for calculating the form factors that are necessary for the dynamical response functions of the spinless fermion model. Experimentally, we demonstrate control over the interaction energy a 1D wire manifested as a change of the ratio of the charge and spin velocities at low-energy scales. We find a new structure resembling the second-level excitations, which dies rapidly away from the first-level mode in a manner consistent with a power law.

We analyze theoretically the dynamic response functions—that probe the many-body excitations—for spinless fermions with short-range interactions. Our approach is exact diagonalization via Bethe ansatz methods: the eigenenergies are evaluated in the coordinate representation and form factors—for the corresponding eigenstates—are derived in the algebraic representation, via Slavnov's formula [8]. On the microscopic level, the excitations arrange themselves into a hierarchy via their spectral weights—given by the form factors—with different powers of $\mathcal{R}^2/L^2$, where $\mathcal{R}$ is the

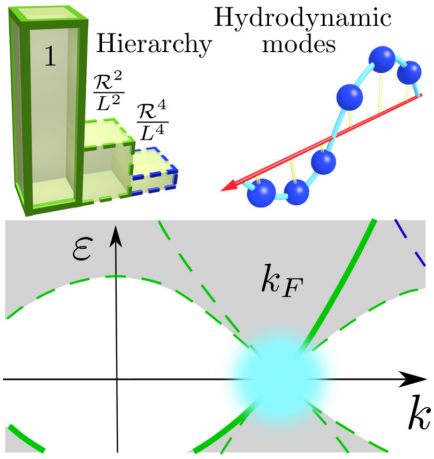

FIG. 1. Regions of the energy-momentum plane dominated by two different principal regimes of the system (bottom): hydrodynamic modes of the Luttinger liquid (top right) at low energies (marked with cyan color in the bottom panel) and the hierarchy of modes (top left) in the rest of the plane.

particle-particle interaction radius and L is the length of the system. As a result, only small numbers of states—out of an exponentially large Fock space of the many-body system—carry the principal spectral power in representative regions on the energy-momentum plane, see Fig. 1, allowing an analytical evaluation of the observables.

At small energy, this hierarchy crosses over to a hydrodynamic behavior, see Fig. 1, which we illustrate by calculating the local density of states. At low energy, it is suppressed in a power-law fashion according to the Tomonaga-Luttinger theory. Away from the Fermi point where the Lorentz invariance is reduced to Galilean by the parabolicity of the spectrum, the local density of states is dominated by the first(leading)-level excitations of the hierarchy. This produces a $1/\sqrt{\varepsilon}$ van Hove singularity, where ε is the energy measured from the bottom of the conduction band. At even higher energies, the second-level excitations produce another $1/\sqrt{|\varepsilon|}$ van Hove singularity on the other side of the band edge, in the forbidden for the noninteracting system region.

Using this framework, we study the response of the correlated system to adding/removing a particle in detail, given by the spectral function. The first-level excitations form a parabolic dispersion, like a single particle, with a mass renormalized by the Luttinger parameter K [9]. The continuous spectrum of the second-level excitations produces a power-law line shape around the first-level mode with a singular exponent -1. Around the spectral edges, the second-level excitations give a power-law behavior of the spectral function. For the hole edge, the exponent calculated microscopically reproduces the prediction of the phenomenological heavy impurity model in one dimension [6]. However, around the particle edge, the second-level excitations give a power-law of a new type.

Experimentally, momentum-resolved tunneling of electrons confined to a 1D geometry has been used to probe spin-charge separation in a Luttinger liquid [11,12,38,39]. This separation was observed to persist far beyond the energy range for which the Luttinger approximation is valid [12], showing the need for more sophisticated theories [37]. Particle-hole asymmetry has also been detected in relaxation processes [10]. In this paper, we measure momentum-resolved tunneling of electrons in the upper layer of a GaAs-AlGaAs double-quantum-well structure from/to a 2D electron gas in the lower layer. This setup probes the spectral function for spinful fermions. We observe a well-resolved spin-charge separation at low energy with appreciable interaction strength—a distinct effect of the spinful generalization of Luttinger liquid [2]. The ratio of charge and spin velocities is $v_c/v_s \approx 1.8$ [12]. At high energy, in addition to the spin and charge curves, we can also resolve the structure just above k_F that appears to be the edge of the second-level excitations. However, the amplitude decays rapidly and for higher k we find no sign of the higher-level excitations, implying that their amplitude must have become at least three orders of magnitude weaker than for the parabola formed by the first-level excitations. The picture emerging out of these experimental results can only be explained—though only qualitatively—by the hierarchy that we study for spinless fermions.

The rest of the paper is organized as follows. In Sec. II, we describe the one-dimensional model of interacting spinless fermions introducing a short-range cutoff via lattice. Section III contains a procedure of finding the many-body eigenenergy by means of the coordinate Bethe ansatz. In Sec. IV, we evaluate the form factors needed for the dynamical response functions. We give a construction of the algebraic representation of the Bethe ansatz (Sec. IV A) and evaluate the scalar product in this representation (Sec. IV B). We present a calculation of the form factors for the spectral function and the dynamical structure factor for a finite chain (Sec. IV C). We take the limit of long wavelengths deriving polynomial formulas for the form factors (Sec. IV d). Then, we analyze the obtained form factors establishing the hierarchy of excitations (Sec. IV e). Finally, we calculate the spectral function around the spectral edges (Sec. IV f). In Sec. V, we illustrate the crossover to a Luttinger liquid at low energy by evaluating the local density of states at all energy scales. Section VI describes experiments on the momentum-conserved tunnelling of electrons in semiconductor wires. Section VII is dedicated to low energies and in Sec. VIII, we analyze the measurements at high energies connecting the experiment with the theory on spinless fermions developed in this paper. The figures below are marked with spinless and spinful logos (such as those in Fig. 2 and 7, respectively) to indicate the structure of the paper visually. Appendix A contains details of the derivation of the Bethe equations in the algebraic representation. In Appendix B, we derive the expectation value of the local density operator.

II. MODEL OF SPINLESS FERMIONS

We study theoretically the model of interacting Fermi particles without spin in 1D,

$$H = \int_{-\frac{L}{2}}^{\frac{L}{2}} dx \left(-\frac{1}{2m} \psi^\dagger(x) \Delta \psi(x) + U L \rho(x)^2 \right), \qquad (1)$$

where the field operators $\psi(x)$ satisfy the Fermi commutation relations, $\{\psi(x), \psi^\dagger(x')\} = \delta(x - x')$, $\rho(x) = \psi^\dagger(x)\psi(x)$ is the particle density operator, and m is the bare mass of a single particle. Below, we consider periodic boundary conditions, $\psi(x + L) = \psi(x)$, restrict ourselves to repulsive interaction $U > 0$ only, and take $\hbar = 1$.

Nonzero matrix elements of the interaction term in Eq. (1) require a finite range of the potential profile for Fermi particles. Here, we will introduce a lattice with next-neighbor interaction whose lattice parameter and interaction radius is $\mathcal{R}$. The model in Eq. (1) becomes

$$H = \sum_{j=-\frac{\mathcal{L}}{2}}^{\frac{\mathcal{L}}{2}} \left[\frac{-1}{2m} (\psi_j^\dagger \psi_{j+1} + \psi_j^\dagger \psi_{j-1}) + U \rho_j \rho_{j+1} \right], \qquad (2)$$

where j is the site index on the lattice, the dimensionless length of the system is $\mathcal{L} = L/\mathcal{R}$, the operators obey $\{\psi_j, \psi_j^\dagger\} = \delta_{ij}$, and $\rho_j = \psi_j^\dagger \psi_j$.

The long-wavelength limit of the discrete model corresponds to the model in Eq. (1), while the interaction radius $\mathcal{R}$ provides microscopically an ultraviolet cutoff in the continuum regime. For the N-particle states of the lattice model, we additionally impose the constraint of low particle density, $N/\mathcal{L} \ll 1$, to stay within the conducting regime; a large

occupancy $N \sim \mathcal{L}$ might lead to Wigner crystal physics at sufficiently strong interactions that would localize the system. This procedure is analogous to the point splitting regularization technique [15], which is usually introduced within the framework of the Luttinger liquid mode in the linear regime.

III. SPECTRAL PROPERTIES

The model in Eq. (2) can be diagonalized via the Bethe ansatz approach, which is based on the observation that the eigenstates are superpositions of plain waves. This method is also called coordinate Bethe ansatz [13]. The eigenstates, following Ref. [13], can be parameterized with sets of N quasimomenta k_j,

$$\Psi = \sum_{\mathcal{P}, j_1<\cdots<j_N} e^{i\sum_l k_{P_l} j_l + i\sum_{l<l'} \varphi_{P_l,P_{l'}}} \psi^\dagger_{j_1} \dots \psi^\dagger_{j_N} |\mathrm{vac}\rangle. \quad (3)$$

Their corresponding eigenenergies, $H\Psi = E\Psi$, are $E = \sum_{j=1}^N (1-\cos k_j)/m$. Here, $|\mathrm{vac}\rangle$ is the vacuum state, the scattering phases are fixed by the two-body scattering problem,

$$e^{i2\varphi_{ll'}} = -\frac{e^{i(k_l+k_{l'})} + 1 + 2mUe^{ik_l}}{e^{i(k_l+k_{l'})} + 1 + 2mUe^{ik_{l'}}} \quad (4)$$

and $\sum_{\mathcal{P}}$ is a sum over all permutations of quasimomenta. The periodic boundary condition quantizes the whole set of N quasimomenta simultaneously,

$$\mathcal{L}k_j - 2\sum_{l\neq j} \varphi_{jl} = 2\pi I_j, \quad (5)$$

where I_j are sets of nonequal integer numbers.

Generally, the system of equations in Eq. (5) has to be solved numerically to obtain the full spectral structure of the observables. However, in the long-wavelength regime, the solutions can be evaluated explicitly.

In this limit, the scattering phases in Eq. (4) are linear functions of quasimomenta, $2\varphi_{ll'} = (k_l - k_{l'})/(1+(mU)^{-1}) + \pi$, which makes the nonlinear system of Bethe ansatz equations in Eq. (5) a linear system [9]. Then, solving the linear system for $\mathcal{L} \gg 1$ via the matrix perturbation theory up to the first subleading order in $1/\mathcal{L}$, we obtain

$$k_j = \frac{2\pi I_j}{\mathcal{L} - \frac{mUN}{mU+1}} - \frac{mU}{mU+1}\sum_{l\neq j} \frac{2\pi I_l}{\left(\mathcal{L} - \frac{mUN}{mU+1}\right)^2}. \quad (6)$$

Note that this calculation is valid for any interaction strength at low densities. The corresponding eigenenergy and total momentum (protected by the translational invariance of the system) are

$$E = \sum_j \frac{k_j^2}{2m} \quad (7)$$

and $P = \sum_j k_j$.

The spectrum of the many-body states is governed by the first term in Eq. (6). Reduction of the quantization length in the denominator of the first term in Eq. (6) is an exclusion volume taken by the sum of interaction radii of all particles. Thus all N-particle eigenstates at an arbitrary interaction strength are given straightforwardly by the same sets of integer numbers I_j as the free fermions' states, e.g., the ground state corresponds to $I_j = -N/2, \dots, N/2$.

For example, this result can be used to calculate the low-energy excitations explicitly that define the input parameters of the Luttinger-liquid model, the velocity of the sound wave v and of the Luttinger parameter K. The first pair of the particle-like excitations, when an extra electron is added just above the Fermi energy, have $I_{N+1} = N/2+1$ and $I_{N+1} = N/2+2$. The difference in their energies and momenta are $E_2 - E_1 = (2\pi)^2 N/[2m(\mathcal{L} - \frac{mUN}{mU+1})^2]$ and $P_2 - P_1 = 2\pi/\mathcal{L}$. Evaluating the discrete derivative, which gives the slope of the dispersion around the Fermi energy, as $v = (E_2 - E_1)/(P_2 - P_1)$ we obtain

$$v = \frac{v_\mathrm{F}}{\left(1 - \frac{NmU}{\mathcal{L}(1+mU)}\right)^2} \quad \text{and} \quad K = \left(1 - \frac{NmU}{\mathcal{L}(1+mU)}\right)^2, \quad (8)$$

where $v_\mathrm{F} = \pi N/(mL)$ is the Fermi velocity and the relation $vK = v_\mathrm{F}$ between the Luttinger parameters for Galilean invariant systems [14] was used.

IV. MATRIX ELEMENTS

Now we turn to the calculation of matrix elements. However, first we need to select operators that correspond to specific observables. Our interest lies in the dynamical response functions that correspond to adding/removing a single particle to/from a correlated system and to creating an electron-hole pair excitation out of the ground state of a correlated system. For example, the first type of dynamics can be realized in experiments using semiconductor nanostructures [11,12] where an electrical current, generated by electrons tunneling into/from the nanostructure with their momentum and energy under control, probe the system.

The response of the many-body system to a single-particle excitation at momentum k and energy ε is described by spectral function [16] $A(k,\varepsilon) = -\mathrm{Im}[\int dxdt e^{i(kx-\varepsilon t)} G(x,0,t)]\mathrm{sgn}(\varepsilon-\mu)/\pi$. Here, μ is the chemical potential and $G(x,x',t) = -i\langle T(e^{-iHt}\psi(x)e^{iHt}\psi^\dagger(x'))\rangle$ is the Green function at zero temperature. In terms of the eigenstates, the spectral function reads

$$A(k,\varepsilon) = L\sum_f |\langle f|\psi^\dagger(0)|0\rangle|^2 \delta(\varepsilon - E_f + E_0)\delta(k - P_f) + L\sum_f |\langle 0|\psi(0)|f\rangle|^2 \delta(\varepsilon + E_f - E_0)\delta(k + P_f), \quad (9)$$

where E_0 is the energy of the ground state $|0\rangle$, and P_f and E_f are the momenta and the eigenenergies of the eigenstates $|f\rangle$; all eigenstates are assumed normalized.

The creation of an electron-hole pair out of the correlated state at zero temperature at momentum k and energy ε is described by a dynamical structure factor [16] $S(k,\varepsilon) = \int dxdt e^{i(kx-\varepsilon t)}\langle\rho(x,t)\rho(0,0)\rangle$, where $\rho(x,t) = e^{-iHt}\rho(0)e^{iHt}$ is the density operator evolving under the Hamiltonian to time t and the average $\langle\dots\rangle$ is taken over the ground state. In terms

of the eigenstates, the dynamical structure factor reads

$$S(k,\varepsilon) = L\sum_f |\langle f|\rho(0)|0\rangle|^2\delta(\varepsilon - E_f)\delta(k - P_f). \quad (10)$$

Thus we will be analyzing the expectation values of the local operators $\psi(0)$ and $\rho(0)$. To proceed with this calculation, we will borrow the result from Refs. [17,18] for Heisenberg chains. Our strategy is to perform the full calculation for the discrete model in Eq. (2) obtaining the matrix elements of ψ_j and ρ_j as determinants. Then we will take the long-wavelength limit to evaluate the form factors for the continuum model explicitly, which will be the main technical result in the theoretical part of this paper. Below, we will construct the algebraic form of Bethe ansatz, use the Slavnov's formula [8] to express the scalar product and the normalization factors in this representation, and finally calculate the matrix elements of the local operators.

A. Algebraic Bethe ansatz

The wave functions of the N-particle eigenstates are factorized in the algebraic representation, which allows the general calculation of various scalar products between them. Here, we will follow the construction in Ref. [13] for XXZ spins chains changing basis from 1/2-spins to spinless fermions.

The so-called R matrix acts on a tensor product $V_1 \otimes V_2$ space and depends on an auxiliary parameter u, where V_1 and V_2 are element-element subspaces, each of which consists of two states $|0\rangle_j$ and $|1\rangle_j$. It is a solution of Yang-Baxter equation $R_{12}(u_1-u_2)R_{13}(u_1)R_{23}(u_2) = R_{23}(u_2)R_{13}(u_1)R_{12}(u_1-u_2)$. For the lattice model in Eq. (2), the R matrix reads

$$\begin{aligned} R_{12} = {} & 1 - (1-b(u))(c_1^\dagger c_1 + c_2^\dagger c_2) \\ & - 2b(u)c_1^\dagger c_1 c_2^\dagger c_2 + c(u)(c_1^\dagger c_2 + c_2^\dagger c_1), \end{aligned} \quad (11)$$

where

$$b(u) = \frac{\sinh(u)}{\sinh(u+2\eta)}, \quad c(u) = \frac{\sinh(2\eta)}{\sinh(u+2\eta)}. \quad (12)$$

Here, η is the interaction parameter, and the tensor product space is defined using a fermionic basis $|0\rangle_j$ and $|1\rangle_j$ with corresponding fermionic operators $\{c_i, c_j^\dagger\} = \delta_{ij}$ that act in these bases as $c_j^\dagger|0\rangle_j = |1\rangle_j$. The latter will account for the anticommuting nature of the lattice fermions on different sites in contrast to the commutation relation of the spin operators of a spin chain model [22,23]. All further calculations are identical to spin chains where the anticommutation relations of the Fermi particles are, however, automatically fulfilled. This approach is more convenient than direct mapping of the results for spin chains using Jordan-Wigner transformation [19].

A two-states subspace of the R matrix can be identified with the two-states fermionic subspace of the lattice site j of the model in Eq. (2). Then, the quantum version of the Lax operator (the so called L matrix) can be defined as $L_j = R_{\xi j}$. In the auxiliary subspace ξ its matrix and operator forms are

$$\begin{aligned} L_j &= \begin{pmatrix} \frac{\cosh(u-\eta(2\rho_j-1))}{\cosh(u-\eta)} & -i\frac{\sinh 2\eta c_j^-}{\cosh(u-\eta)} \\ -i\frac{\sinh 2\eta c_j^\dagger}{\cosh(u-\eta)} & -\frac{\cosh(u+\eta(2\rho_j-1))}{\cosh(u-\eta)} \end{pmatrix} \\ &= A^j(1-c_\xi^\dagger c_\xi) + c_\xi^\dagger C^j + B^j c_\xi + D^j c_\xi^\dagger c_\xi. \end{aligned} \quad (13)$$

Here, the top left element of the matrix is a transition between $|0\rangle_\xi$ and $\langle 0|_\xi$ states of the auxiliary subspace, c_j and ρ_j are the fermionic operators of the lattice model in Eq. (2), and A^j, B^j, C^j, D^j label the matrix elements of L_j. The prefactor in front of L_j was chosen such that for $u = i\pi/2 - \eta$ it becomes a permutation matrix and for $\eta = 0$ the L operator is diagonal.

By construction, the L operator satisfies the algebra generated by the Yang-Baxter equation,

$$R(u-v)\big(L_j(u)\otimes L_j(v)\big) = \big(L_j(v)\otimes L_j(u)\big)R(u-v). \quad (14)$$

The entries give commutation relations between the matrix elements of L matrix. Here, we write down three of them that will be used later,

$$\big\{B_u^j, C_v^j\big\} = \frac{c(u-v)}{b(u-v)}\big(D_v^j A_u^j - D_u^j A_v^j\big), \quad (15)$$

$$A_u^j C_v^j = \frac{1}{b(v-u)}C_v^j A_u^j - \frac{c(v-u)}{b(v-u)}C_u^j A_v^j, \quad (16)$$

$$D_u^j C_v^j = -\frac{1}{b(u-v)}C_v^j D_u^j + \frac{c(u-v)}{b(u-v)}C_u^j D_v^j. \quad (17)$$

These relations can be also be checked explicitly by direct use of the definition in Eq. (13) and the Fermi commutation relations.

The transition matrix $T(u)$ for a chain with $\mathcal{L}$ sites—the so-called monodromy matrix—can be defined similarly to the classical problem as

$$T(u) = \sum_{j=1}^{\mathcal{L}} L_j(u). \quad (18)$$

If all single-site L matrices satisfy Eq. (14) then the T matrix also satisfies the same Yang-Baxter equation, e.g., see proof in Ref. [13]. Therefore the matrix elements of $T = A(1-c_\xi^\dagger c_\xi) + c_\xi^\dagger C + Bc_\xi + Dc_\xi^\dagger c_\xi$ in the 2×2 auxiliary space ξ obey the same commutation relations in Eqs. (15)–(17). The transfer matrix for the whole chain,

$$\tau = \mathrm{str}T = A(u) - D(u), \quad (19)$$

is the super trace of T matrix due to the fermionic definition of the auxiliary space [22,23]. The latter gives a family of commuting matrices $[\tau(u),\tau(v)] = 0$, which contain all conserved quantities of the problem including the Hamiltonian.

The vacuum state $|0\rangle$—in the Fock space of the model in Eq. (2)—is an eigenstate of the transfer matrix τ. The corresponding eigenvalue, $\tau(u)|0\rangle = (a(u) - d(u))|0\rangle$, is the difference of the eigenvalues of the A and D operators which can be obtained directly by use of the definitions in Eqs. (13) and (18). Noting that for $\mathcal{L} = 2$ Eq. (18) gives $A(u)|0\rangle = a_1(u)a_2(u)|0\rangle$ and $D(0)|0\rangle = d_1(u)d_2(u)|0\rangle$, where $a_1(u) = a_2(u) = \cosh(u+\eta)/\cosh(u-\eta)$ and $d_1(u) = d_2(u) = 1$,

and generalizing this observation for arbitrary $\mathcal{L}$ one obtains

$$a(u) = \frac{\cosh(u+\eta)^{\mathcal{L}}}{\cosh(u-\eta)^{\mathcal{L}}}, \quad \text{and} \quad d(u) = 1. \tag{20}$$

A general state of N particles'—Bethe state–is constructed by applying the operator $C(u)$ N times with different values of the auxiliary variable u_j,

$$\Psi = \prod_{j=1}^{N} C(u_j)|0\rangle, \tag{21}$$

where a set of N values u_j corresponds to N quasimomenta k_j in coordinate representation of Bethe states in Eq. (3). The state in Eq. (21) with an arbitrary set of u_j is not an eigenstate of the transfer matrix τ. For instance, it can be seen by commuting the operators A and D from left to right through all operators $C(u_j)$ that generates many different states according to the commutation relations in Eqs. (16) and (17). However, the contribution of all of the states that are nondegenerate with Ψ can made to be zero by choosing particular sets of u_j that satisfy the following set of equations

$$\frac{a(u_j)}{d(u_j)} = (-1)^{N-1} \prod_{l=1\neq j}^{N} \frac{b(u_l - u_j)}{b(u_j - u_l)} \tag{22}$$

(see Appendix A for details).

Under the substitution of the vacuum eigenvalues $a(u_j)$ and $d(u_j)$ of A and D operators from Eq. (20) and $b(u_l - u_j)$—which define the commutation relations Eqs. (16) and (17)—from Eq. (12) this so-called eigenvalue equation above becomes

$$\frac{\cosh(u_j-\eta)^{\mathcal{L}}}{\cosh(u_j+\eta)^{\mathcal{L}}} = (-1)^{N-1} \prod_{l=1\neq j}^{N} \frac{\sinh(u_j - u_l - 2\eta)}{\sinh(u_j - u_l + 2\eta)}. \tag{23}$$

Thus all the sets of u_j that satisfy the above equation give eigenstates of the transfer matrix in the representation of Eq. (21) with the corresponding eigenvalues $\tau(u)\Psi = \mathcal{T}(u)\Psi$, where

$$\mathcal{T}(u) = a(u)\prod_{j=1}^{N} \frac{1}{b(u_j - u)} - (-1)^N d(u) \prod_{j=1}^{N} \frac{1}{b(u - u_j)}. \tag{24}$$

This eigenvalue equation in the algebraic framework is the direct analog of the Bethe ansatz equation (5) in the coordinate representation. Direct mapping between the two is done by the substitution of

$$e^{ik_j} = \frac{\cosh(u_j - \eta)}{\cosh(u_j + \eta)}, \quad mU = -\cosh 2\eta, \tag{25}$$

in Eq. (5) and by taking its exponential.

The original lattice Hamiltonian can be obtained from the transfer matrix $\tau(u)$ that contains all of the conserved quantities of the problem. The logarithmic derivatives of $\tau(u)$ give the global conservation laws by means of the so-called trace identities, see Ref. [13]. The linear coefficient in the Taylor series around the point $u = \frac{i\pi}{2} - \eta$ is proportional to the Hamiltonian itself. After restoring the correct prefactor, the expression reads

$$H = -\frac{\sinh\eta}{2m}\partial_u \ln\tau(u)|_{u=\frac{i\pi}{2}-\eta}. \tag{26}$$

Substitution of the interaction parameter η from Eq. (25) in terms of the particle-particle interaction constant U into the right-hand side of the above relation recovers the lattice model in Eq. (2).

B. Scalar product

The basic quantity on which the calculations of the expectation values will be based on is the scalar product of two wave functions. A general way of evaluating it is based on the commutation relations in Eqs. (15)–(17) and the vacuum expectation values of the A and D operators. The result of such a calculation simplifies greatly if one of the Bethe states is an eigenstate of the transfer matrix $\tau(u)$, as was first shown by Slavnov [8]. Then, the same result was rederived in Refs. [17,18] using the so-called factorizing F matrix [20], which is a representation of a Drinfeld twist [21]. The latter will not be used in this section but it will be needed later in calculations of the matrix elements of the local operators.

Let $|\mathbf{u}\rangle = \prod_{j=1}^{N} C(u_j)|0\rangle$ be an eigenstate of the transfer matrix so that N parameters u_j satisfy the Bethe equation in Eq. (23); and let $\langle\mathbf{v}| = \langle 0|\prod_{j=1}^{N} B(v_j)$ be another Bethe state parametrized by a set of N arbitrary values v_j. The scalar product of these two states $\langle\mathbf{v}|\mathbf{u}\rangle$ can be evaluated by commuting each operator $B(v_j)$ through the product of $C(u_j)$ operators using the commutation relation in Eq. (15), which generates the A and D operators with all possible values of u_j and v_j. They, in turn, have also to be commuted to the right through the remaining products of the $C(u_j)$ operators. Finally, products of the A and D operators, which act upon the vacuum state, just give products of their vacuum eigenvalues $a(u_j), d(u_j)$ and $a(v_j), d(v_j)$ according to Eq. (20). The resulting sums of products can be written, using the relation between u_js in Eq. (23), in a compact form as a determinant of an $N \times N$ matrix [8]:

$$\langle\mathbf{v}|\mathbf{u}\rangle = \frac{\prod_{i,j=1}^{N}\sinh(v_j - u_i)}{\prod_{j<i}\sinh(v_j - v_i)\prod_{j<i}\sinh(u_j - u_i)} \det\hat{S}, \tag{27}$$

where the matrix elements are $S_{ab} = \partial_{u_a}\mathcal{T}(v_b)$. Under a substitution of the eigenvalues of the transfer matrix from Eq. (24), these matrix elements read in explicit form as

$$S_{ab} = -\frac{\cosh^L(v_b+\eta)}{\cosh^L(v_b-\eta)}\frac{\sinh(2\eta)}{\sinh^2(u_a - v_b)}\prod_{j=1\neq a}^{N}\frac{\sinh(u_j - v_b + 2\eta)}{\sinh(u_j - v_b)} - (-1)^N \frac{\sinh(2\eta)}{\sinh^2(v_b - u_a)}\prod_{j=1\neq a}^{N}\frac{\sinh(v_b - u_j + 2\eta)}{\sinh(v_b - u_j)}. \tag{28}$$

For $N = 1$, the result in Eqs. (27) and (28) follows directly from Eq. (15). For arbitrary N, the proof is more complicated: it employs the residue formula [8] (the function $\langle\mathbf{v}|\mathbf{u}\rangle$ has first order poles when $v_i \to u_j$) and the recurrent relation for the scalar product of $N+1$ particles in terms of the scalar product of N particles, see also details in Ref. [13].

The normalization factor of Bethe states can be obtained from Eq. (27) by taking the limit $\mathbf{v} \to \mathbf{u}$. The first-order singularities, $(v_b - u_b)^{-1}$, in the off-diagonal matrix elements (28) are canceled by zeros in the numerator in Eq. (27). The diagonal $a = b$ matrix elements contain second-order singularities $(v_b - u_b)^{-2}$ for $\mathbf{v} \to \mathbf{u}$. However, the numerator also becomes zero when $\mathbf{v} \to \mathbf{u}$ in the leading order. Its expansion up to the first subleading order cancels the second-order singularity of the denominator giving a finite expression for the matrix elements in the limit. The normalization factor is found to be

$$\langle \mathbf{u}|\mathbf{u}\rangle = \sinh^N(2\eta) \prod_{i\neq j=1}^{N} \frac{\sinh(u_j - u_i + 2\eta)}{\sinh(u_j - u_i)} \det \hat{Q}, \tag{29}$$

where the matrix elements are

$$Q_{ab} = \begin{cases} -\mathcal{L}\frac{\sinh 2\eta}{\cosh(u_a+\eta)\cosh(u_a-\eta)} - \sum_{j\neq a} \frac{\sinh 4\eta}{\sinh(u_a-u_j-2\eta)\sinh(u_a-u_j+2\eta)}, & a = b, \\ \frac{\sinh 4\eta}{\sinh(u_b-u_a+2\eta)\sinh(u_b-u_a-2\eta)}, & a \neq b. \end{cases} \tag{30}$$

The last formula was originally derived by Gaudin using quantum-mechanical identities in the coordinate representation of Bethe ansatz [24]. Mapping of the resulting expression in Ref. [24] to the algebraic representation by means of Eq. (25) gives directly the result in Eqs. (27) and (28) with a different prefactors due to different normalization factors in the definitions of the states in Eq. (3) and of the states in Eq. (21). We will use the algebraic form in Eq. (21) for the calculation of the local matrix elements below.

C. Expectation values of local operators

Operators of the algebraic Bethe ansatz in Eqs. (13) and (18) are nonlocal in the basis of the original fermionic operators of the lattice model in Eq. (2). Thus the first nontrivial problem in calculating the matrix elements of the local operators $\psi_j^\dagger$ and ρ_1 in the algebraic representation of Bethe states in Eq. (21) is expressing the operators of our interest in terms of the nonlocal A, B, C, and D operators from Eqs. (13) and (18). Alternatively, these Bethe operators can be expressed in terms of the local operators of the lattice model. The latter approach is much more complicated since the product of matrices in Eq. (18) is a large sum (exponential in the number of sites in the chain) restricting severely the ability to do explicit calculations using the fermionic representation in practice.

An alternative way was found by constructing the F-matrix representation of a Drinfeld twist [20]. In the F basis, the monodromy matrix in Eq. (18) becomes quasilocal, i.e., its diagonal elements A and D become direct products of diagonal matrices on each site over all sites of the chain and the off-diagonal B and C are single sums over such direct products. Direct calculations become much easier in this basis. Specifically, analysis of A, B, C, and D operators leads to a simple result for representing the ψ_j operator in terms of algebraic Bethe ansatz operators, which then is shown to be basis independent [17,18],

$$\psi_j^\dagger = \tau^{j-1}\left(\frac{i\pi}{2} - \eta\right) C\left(\frac{i\pi}{2} - \eta\right) \tau^{\mathcal{L}-j}\left(\frac{i\pi}{2} - \eta\right). \tag{31}$$

Here, $\tau(u) = A(u) - D(u)$ is the supertrace of the monodromy matrix and $C(u)$ is its matrix element.

The transfer matrices in the right-hand side of the above equation give only a phase prefactor in the expectation values with respect to the Bethe states in Eq. (21). Let $|\mathbf{u}\rangle$ be an eigenstate of the transfer matrix with N particles, let $|\mathbf{v}\rangle$ be an eigenstate with $N+1$ particles, and let us consider the case of $j = 1$. Acting with the $\tau^{\mathcal{L}-1}(i\pi/2 - \eta)$ operator on the eigenstates $|\mathbf{u}\rangle$ gives the eigenvalue $\prod_{j=1}^{N} \cosh^{\mathcal{L}-1}(u_j - \eta)/\cosh^{\mathcal{L}-1}(u_j + \eta)$ according to Eq. (24). Then, using the mapping to the coordinate representation in Eq. (25) and the Bethe equation in the form of Eq. (5), this eigenvalue can be expressed as $\exp[i P_u(\mathcal{L} - 1)]$, where P_u is the total momentum of the state u_j, a quantum number. Similar phase factors for $j \neq 1$ are evaluated in an analogous way and each of them cancels out under modulus square in the form factor in Eq. (9) making the local form factors independent of j in full accord with the translational invariance of the system and the observable in Eq. (9). Thus we will only calculate the value of $\langle \mathbf{v}|\psi_1^\dagger|\mathbf{u}\rangle$.

Since $C(\frac{i\pi}{2} - \eta)\prod_{j=1}^{N} C(u_j)|0\rangle$ is also a Bethe state $|\frac{i\pi}{2} - \eta, u_j\rangle$, though it is not an eigenstate, the expectation value can be calculated using the result for the scalar product $\langle \mathbf{v}|\psi_j^\dagger|\mathbf{u}\rangle = \langle \mathbf{v}|\frac{i\pi}{2} - \eta, u_j\rangle$. Substituting $\frac{i\pi}{2} - \eta, u_j$ in Eqs. (27) and (28) explicitly, one obtains

$$\langle \mathbf{v}|\psi_1^\dagger|\mathbf{u}\rangle = (-1)^{N+1} i \frac{\prod_{j=1}^{N+1}\cosh(v_j - \eta)}{\prod_{j=1}^{N}\cosh(u_j + \eta)} \times \frac{\sinh^{N+1}(2\eta)\det \hat{M}}{\prod_{j<i=2}^{N}\sinh(u_j - u_i)\prod_{j<i=2}^{N+1}\sinh(v_j - v_i)}, \tag{32}$$

where the matrix elements are

$$M_{ab} = \frac{(-1)^{N-1}}{\sinh(u_b - v_a)}\left(\prod_{j=1\neq b}^{N} \frac{\sinh(u_b - u_j + 2\eta)}{\sinh(u_b - u_j - 2\eta)} \prod_{j=1\neq a}^{N+1} \sinh(u_b - v_j - 2\eta) + \prod_{j=1\neq a}^{N+1} \sinh(u_b - v_j + 2\eta)\right), \tag{33}$$

for $b < N+1$, and

$$M_{ab} = \frac{1}{\cosh(v_a - \eta)\cosh(v_a + \eta)}, \tag{34}$$

for $b = N+1$. Here, the Bethe equation, Eq. (23), was used to express $a(v_j)/d(v_j)$ in the matrix elements, and some factors in the matrix elements and the overall prefactor cancel out. This result can be checked by a numerical evaluation of the sums over the spacial variables using the coordinate representation in Eq. (3) for a small number of particles $N = 1,2,3$, which we have done.

The determinant results in Eqs. (29), (27), and (32) can be checked by a numerical evaluation of the sums over the spacial variables using the coordinate representation in Eq. (3). However, the latter summation over many coordinates has factorial complexity, which already limits numerical calculations to a few particles on chains of a few dozen sites. The results of the algebraic Bethe ansatz calculations have a power-law complexity that allows general studies, at least numerically, of systems with hundreds of particles on arbitrary long chains without making any approximations, e.g., the studies of correlation functions in one-dimensional systems in Refs. [25–30].

D. The long-wavelength limit

We now turn to the evaluation of the long-wavelength limit for matrix elements in the determinant form with the aim of calculating the determinants explicitly. The resulting expressions will then be used to study physical observables.

Such an analysis is more convenient in the coordinate representation. For small k_j the nonlinear mapping in Eq. (25) becomes linear, similarly to Bethe equation in Eq. (5) in this limit. Then, a simple inversion of the linear function gives

$$u_j = \frac{i}{2}\sqrt{\frac{mU+1}{mU-1}}k_j \quad \text{and} \quad \eta = -\frac{1}{2}\text{acosh}(mU). \tag{35}$$

Note that $|u_j|$ and k_j are simultaneously much smaller than one, while the interaction strength U can be of an arbitrary magnitude.

We start from the expansion of the normalisation factor in Eq. (29) up to the leading nonvanishing order in the quasimomenta. We first substitute Eq. (35) in the matrix elements in Eq. (30), then expand them up to the leading nonvanishing order in $k_j \ll 1$, and obtain the diagonal matrix elements as follows:

$$Q_{aa} = 2\mathcal{L}\sqrt{\frac{mU-1}{mU+1}} - \frac{2(N-1)mU}{\sqrt{m^2U^2-1}} \tag{36}$$

and

$$Q_{ab} = \frac{2mU}{\sqrt{m^2U^2-1}}, \tag{37}$$

for $a \neq b$. The off-diagonal matrix elements are small compared to the diagonal entries as $Q_{ab}/Q_{aa} \sim 1/\mathcal{L}$ so the leading contribution to the determinant is accumulated on the diagonal. Also expanding the prefactor of Eq. (29) in small k_j we obtain the following expression for the normalisation in the long-wavelength limit:

$$\langle \mathbf{k}|\mathbf{k}\rangle = \frac{2^{N^2}(-1)^N(1-mU)^{N^2}\left(\mathcal{L} - \frac{mUN}{mU+1}\right)^N}{i^{N(N-1)}\prod_{i\neq j}(k_j - k_i)}, \tag{38}$$

where k_j are quasimomenta in the coordinate representation of Bethe ansatz.

Our primary interest lies in the spectral function that contains the local matrix element of $\psi_j^\dagger$ operators so here we will focus on the determinant result in Eq. (32). Similarly to the calculation of the normalization factor, we substitute Eq. (35) into Eq. (33), which, however, becomes zero in the zeroth order in k_j. Expanding it up to linear order in k_j we obtain

$$M_{ab} = 2mU(m^2U^2-1)^{\frac{N-1}{2}}\frac{\sum_{j=1}^N k_j^u - \sum_{j=1\neq a}^{N+1} k_j^v}{k_b^u - k_a^v} \tag{39}$$

for $b < N+1$, where $\Delta P = \sum_j k_j^u - \sum_j k_j^v$ is the difference of two conserved quantities, the momenta of two states $\mathbf{k}^u$ and $\mathbf{k}^v$. The matrix elements in Eq. (34) are already nonzero in the zeroth order in k_j giving

$$M_{ab} = \frac{2}{mU+1}, \tag{40}$$

for $b = N+1$. Also expanding the prefactor in Eq. (32) and rearranging the expressions by taking a common factor out of the matrix elements we obtain

$$\left\langle \mathbf{k}^v|\psi^\dagger(0)|\mathbf{k}^u\right\rangle = (-1)^{N+1}i^{N^2}2^{N^2+N+\frac{1}{2}} \times 1 \times \frac{(mU-1)^{N^2+\frac{1}{2}}m^N U^N \mathcal{D}}{\prod_{j<i}^N\left(k_j^u - k_i^u\right)\prod_{j<i}^{N+1}\left(k_j^v - k_i^v\right)}, \tag{41}$$

where the entries of the matrix under the determinant, $\mathcal{D} = \det\hat{\mathcal{M}}$, for $b < N+1$ are

$$\mathcal{M}_{ab} = \frac{\Delta P + k_a^v}{k_b^u - k_a^v} \quad \text{and} \quad \mathcal{M}_{a,N+1} = 1. \tag{42}$$

All matrix elements are of the same order so the determinant in Eq. (41) is a sum of a large number of terms unlike the normalisation factor in Eq. (38). Doing the summation we find an explicit expression in the form of a fraction of two polynomials in quasimomenta of the initial and the final states,

$$\mathcal{D} = (-1)^{N+1}\frac{\prod_j\left(\Delta P + k_j^u\right)}{\prod_{i,j}\left(k_j^v - k_i^u\right)}\prod_{j<i}^N\left(k_j^u - k_i^u\right)\prod_{j<i}^{N+1}\left(k_j^v - k_i^v\right). \tag{43}$$

For $N = 1$, the result above is evaluated straightforwardly as a determinant of a 2×2 matrix with the matrix elements in Eq. (42). For arbitrary N we prove it by induction. Using the Laplace development on the $N+1$ row, the determinant

for $N+1$ particles can be expressed as a sum of minors given, in turn, by determinants for N particles, $\mathcal{D}_{N+1} = \sum_{a=1}^{N+2}(-1)^{N+1+a}\mathcal{M}_{a,N+1}\mathrm{minor}_{a,N+1}$, which—let us assume for purposes of the inductive method—are given by Eq. (43):

$$\mathrm{minor}_{a,N+1} = (-1)^{N+1}\frac{\prod_{j=1}^{N}\left(\Delta P + k_j^u\right)}{\prod_{i=1,j=1\neq a}^{N,N+2}\left(k_j^v - k_i^u\right)}\prod_{j<i}^{N}\left(k_j^u - k_i^u\right)\prod_{j<i\neq a}^{N+2}\left(k_j^v - k_i^v\right). \tag{44}$$

Here, $\mathcal{M}_{a,N+1}$ are given by the matrix elements in Eq. (42), N quasimomenta k_j^u are labeled by $j = 1,\ldots,N$, and $N+1$ quasimomenta k_j^v are labeled by $j = 1,\ldots,N+2$ with ath elements excluded. After taking a common factor in front of the sum, the determinant for $N+1$ particles becomes

$$\begin{aligned}\mathcal{D}_{N+1} = (-1)^{N+2}&\frac{\prod_{j=1}^{N+1}\left(\Delta P + k_j^u\right)\prod_{j<i}^{N+1}\left(k_j^u - k_i^u\right)\prod_{j<i}^{N+2}\left(k_j^v - k_i^v\right)}{\prod_{i,j}\left(k_j^v - k_i^u\right)}\\ &\times\frac{1}{\Delta P + k_{N+1}^u}\sum_{a=1}^{N+2}\frac{\left(\Delta P + k_a^v\right)\prod_{j=1\neq a}^{N+2}\left(k_j^v - k_{N+1}^u\right)\prod_{j=1}^{N}\left(k_j^u - k_a^v\right)}{\prod_{j=1}^{N}\left(k_j^u - k_{N+1}^u\right)\prod_{j=1\neq a}^{N+2}\left(k_j^v - k_a^v\right)}.\end{aligned} \tag{45}$$

The sum in the above expression gives, by direct calculation, $\sum_{a=1}^{N+2}\cdots = \Delta P + k_{N+1}^u$, which makes the whole second line unity. The determinant is equal to the first line of Eq. (45), which is also equal to the result in Eq. (43) for $N+1$ particles. Thus we obtained the same result for $N+1$ particles starting from Eq. (43) for N particles. Hence it is proved by induction.

Finally, the form factor in Eq. (9) is the modulus squared of Eq. (41). Normalizing the initial and the final state wave functions using Eq. (38) as $|\langle f|\psi^\dagger(0)|0\rangle|^2 = |\langle\mathbf{k}^f|\psi^\dagger(0)|\mathbf{k}^0\rangle|^2\langle\mathbf{k}^f|\mathbf{k}^f\rangle^{-1}\langle\mathbf{k}^0|\mathbf{k}^0\rangle^{-1}$, we obtain

$$\begin{aligned}|\langle f|\psi^\dagger(0)|0\rangle|^2 = &\frac{Z^{2N}}{\mathcal{L}}\frac{\prod_j^N\left(k_j^0 - P_f\right)^2}{\prod_{i,j}^{N,N+1}\left(k_j^f - k_i^0\right)^2}\\ &\times\prod_{i<j}^{N}\left(k_j^0 - k_i^0\right)^2\prod_{i<j}^{N+1}\left(k_j^f - k_i^f\right)^2,\end{aligned} \tag{46}$$

where $Z = mU/(mU+1)/(\mathcal{L} - NmU/(1+mU))$, k_j^f and k_j^0 are the quasimomenta of the eigenstate $|f\rangle$ and the ground state $|0\rangle$, respectively, and $P_0 = 0$ for the ground state.

The calculation of $\langle f|\rho(0)|0\rangle$ is done in a similar way by expressing the local density operator ρ_1, within the framework of the lattice model, in terms of the algebraic Bethe ansatz operators A, B, C, D and, then, by using the Slavnov formula. Details are given in Appendix B. In the long-wavelength limit, we obtain

$$\begin{aligned}|\langle f|\rho(0)|0\rangle|^2 = &\frac{Z^{2N-2}}{\mathcal{L}^2}\frac{P_f^{2N}}{\prod_{i,j}^{N,N}\left(k_j^f - k_i^0\right)^2}\\ &\times\prod_{i<j}^{N}\left(k_j^0 - k_i^0\right)^2\prod_{i<j}^{N}\left(k_j^f - k_i^f\right)^2,\end{aligned} \tag{47}$$

where the final states $|f\rangle$ have the same number of excitations N as the ground state $|0\rangle$, unlike in Eq. (46), and $P_0 = 0$ for the ground state as in Eq. (46).

These form factors in Eqs. (46) and (47) together with the solution of Bethe equations in Eq. (6) is the main technical result in the theory part of our work. We will analyze its physical consequences in the next two sections. The similarity between these two expressions means that the hierarchy of modes we will identify below is a general feature of one and two body operators.

E. Hierarchy of modes

The results in Eqs. (46) and (47) have one or more singularities when one or more quasimomenta of an excited state coincide with a quasimomentum of the ground state, $k_j^f = k_j^0$. Both results have a multiplicand $Z^{2N} \sim \mathcal{L}^{-2N}$ that becomes virtually zero in the thermodynamic limit, in which $\mathcal{L}\to\infty$. Thus the product of these two opposite factors produces an uncertainty in the limiting behavior (of the $0\times\infty$ type) that has to be resolved. Since we are specifically interested in a transport experiment in this paper, in which the spectral function is measured, we will mainly focus on solving the uncertainty problem for the result in Eq. (46).

The maximum number of singularities is N in the extreme case, when the quasimomenta k_j^f of an excited state coincide with all of the N quasimomenta of the ground state k_j^0 given in Fig. 2(gs). The excited states of this kind are given in Fig. 2(a). The divergences in the denominator of Eq. (46) occur only in the leading order—the first term in Eq. (6)—but the subleading order—the second term in Eq. (6)—already provides a self-consistent cutoff within the theory. The interaction shift of the quasimomenta at subleading order does not cancel for the extra added particle in the excited state, making the factors in the denominator of Eq. (46)

$$k_j^f - k_j^0 = \frac{mU}{mU+1}\frac{k_{N+1}^f - k_j^0}{\mathcal{L} - \frac{mUN}{mU+1}}, \tag{48}$$

where in the right-hand side (r.h.s.), only the first term from Eq. (6) is relevant for k_{N+1}^f and k_j^0. The numerator for the states in Fig. 2(a) becomes

$$k_j^0 - P_f = k_j^0 - k_{N+1}^f. \tag{49}$$

Substitution of Eqs. (48) and (49) in Eq. (46) for one particle, say for $j = N$, cancels one factor $Z^2 \sim \mathcal{L}^{-2}$ and the other part of the product for $i\neq j$ in the denominator of the first line of Eq. (46) cancels partially the products in the second line of Eq. (46). The expression for the remaining $N-1$ particles is the same as Eq. (46) but the numbers of terms in the products

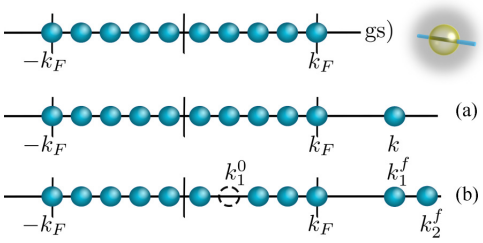

FIG. 2. Configurations of quasimomenta that solve the Bethe equations in Eqs. (5) and (4) for the spinless fermions model in Eq. (2): (gs) the ground state, (a) excitations that form the a level of the hierarchy, and (b) excitations that form the b level of the hierarchy.

are reduced by one, $N \to N-1$, giving

$$|\langle f|\psi^\dagger(0)|0\rangle|^2 = \frac{Z^{2N-2}}{\mathcal{L}} \frac{\prod_j^{N-1}\left(k_j^0 - P_f\right)^2}{\prod_{i,j}^{N-1,N}\left(k_j^f - k_i^0\right)^2} \times \prod_{i<j}^{N-1}\left(k_j^0 - k_i^0\right)^2 \prod_{i<j}^{N}\left(k_j^f - k_i^f\right)^2. \quad (50)$$

Repeating the procedure $N-1$ times, we cancel the remaining Z^{2N-2} factor completely (with the rest of other terms) and obtain

$$\mathcal{L}|\langle f|\psi^\dagger(0)|0\rangle|^2 = 1. \quad (51)$$

Corrections to this result originate from higher subleading orders in the solutions to Bethe equations in Eq. (6) and are of the order of $O(\mathcal{L}^{-1})$. This becomes much smaller than one at the leading order of Eq. (51) in the thermodynamic limit.

Substitution of Eq. (51) in Eq. (9) gives the value of the spectral function $A(k,\varepsilon(k)) = 1$. The energies and the momenta of the excitations in Fig. 2(a) form a single line on the spectral plane, like a single particle with dispersion $\varepsilon(k) = k^2/(2m^*)$, where the effective mass is renormalized by the Luttinger parameter K, $m^* = mK$ [47]. Note that, since we still resolve individual levels here, the delta functions in the definition of the spectral function in Eq. (9) become discrete Kronecker deltas. Thus $A(k,\varepsilon)$ at each discrete point k,ε describes the probability of adding (removing) a particle, which is non-negative and is bound by one from above, instead of the probability density as in the continuum case. Dimensional analysis makes this distinction clear immediately.

The excitations that have one singularity less ($N-1$ in total) can be visualized systematically as an extra electron-hole pair created in addition to adding an extra particle, see Fig. 2(b). Staring from Eq. (46) and using the same procedure as before Eq. (50) but $N-1$ instead of N times, we obtain

$$|\langle f|\psi^\dagger(0)|0\rangle|^2 = \frac{Z^2}{\mathcal{L}} \frac{\left(k_2^f - k_1^f\right)^2\left(k_1^0 - P_f\right)^2}{\left(k_1^f - k_1^0\right)^2\left(k_2^f - k_1^0\right)^2}, \quad (52)$$

where k_1^f, k_2^f, and k_1^0 are positions of two particles and one hole in Fig. 2(b). Substitution of Eq. (52) in Eq. (9) gives values of the spectral function $A(k,\varepsilon) \sim \mathcal{L}^{-2}$ that are smaller than the values for the excitations in Fig. 2(a) [in Eq. (9)] by a factor of $\mathcal{L}^{-2}$. For two singularities less ($N-2$ in total), we find $A(k,\varepsilon) \sim \mathcal{L}^{-4}$ and so on.

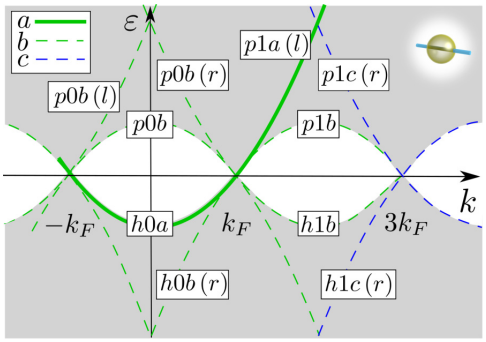

FIG. 3. The spectral function for interacting spinless fermions in the region $-k_F < k < k_F$ ($k_F < k < 3k_F$) labeled by 0(1). The grey areas mark nonzero values. The green and the blue lines are modes of the hierarchy labeled as follows: $p(h)$ shows the particle (hole) sector, k_F is the Fermi momentum, a, b, c, respectively, identify the level in the hierarchy in powers 0, 1, 2 of $\mathcal{R}^2/L^2$, and (r,l) specifies the origin in the range—modes on the edge have no such label.

This emerging structure separates the plethora of many-body excitations into a hierarchy according to the remaining powers of $\mathcal{L}^{-2}$ in their respective form factors. We label the levels of the hierarchy as a, b, c reflecting the factors $\mathcal{L}^{-2n}$ with $n = 0, 1, 2$. While the leading a excitations form a discrete single-particle-like dispersion, see $h0a$ and $p1a(l)$ lines in Fig. 3, the spectral properties of the subleading excitations are described by a more complicated continuum of states on the energy-momentum plane. We will explore the b excitations below.

All simple modes, formed by single-particle and holelike excitations of the type in Fig. 2(b), in the range $-k_F < k < 3k_F$ are presented in Fig. 3. We use the following naming scheme: $p(h)$ indicates the particle (hole) sector, 0(1) encodes the range of momenta $-k_F < k < k_F (k_F < k < 3k_F)$, a, b, c reflect the terms $\mathcal{L}^{-2n}$ with $n = 0, 1, 2$. The suffix (r) or (r) marks a particlelike mode, e.g., the states with in Fig. 2(b) with $k_1^f = -k_F - \gamma$, $k_1^0 = k_F$, and $k_F > P_f = -2k_F + k_2^f > -k_F$ forms the mode $p0b(l)$. Holelike modes have no suffixes, e.g., the states in Fig. 2(b) with $k_1^f = -k_F - \gamma$, $k_2^f = k_F + \gamma$, and $-k_F < P_f = -k_1^0 < k_F$ form the mode $p0b$. Simple modes formed by excitations of lower levels of the hierarchy are obtained by translation of the b modes constructed in this paragraph by integer numbers of $\pm 2k_F$. A couple of simple modes formed by c excitations are presented on Fig. 3. They have the same naming scheme as the b modes.

Now we evaluate values of the spectral function along all simple b modes in the range $-k_F < k < 3k_F$. Let us start from the $p0b$ mode, see Fig. 3. Along this mode, the spectral function is a bijective function of k, $A(k,\varepsilon_{p0b}(k))$ where $\varepsilon_{p0b}(k) = k_F^2/(mK) - k^2/(2mK)$. The states that form it belong to b excitations in Fig. 2(b) with $k_1^f = -k_F - \gamma, k_2^f = k_F + \gamma$, and $k = P_f = -k_1^0$. Substituting this parametrization

TABLE I. Spectral weights along the a and the b modes for $-k_F < k < k_F$ ($k_F < k < 3k_F$) labeled by $x = 0(1)$. Terminology is the same as in Fig. 3; $\gamma = 2\pi/\mathcal{L}$ and $Z = mU/(mU+1)/(\mathcal{L} - NmU/(1+mU))$.

	$x=0$	$x=1$
pxa		1
hxa	1	
pxb	$\frac{16Z^2k_F^2k^2}{(k^2-(k_F+\gamma)^2)^2}$	$\frac{4Z^2\gamma^2(k-k_F+\frac{3}{2}\gamma)^2}{(k-k_F+\gamma)^2(k-k_F+2\gamma)^2}$
$pxb(l)$	$\frac{4Z^2(k_F+k)^2}{k_F^2}$	
$pxb(r)$	$\frac{4Z^2(k_F-k)^2}{k_F^2}$	
hxb		$\frac{4Z^2(3k_F-k-\gamma)^2(k_F+k)^2}{k_F^2(k-k_F+\gamma)^2}$
$hxb(l)$	$\frac{4Z^2\gamma^2}{(k+k_F+2\gamma)^2}$	$\frac{Z^2k_F^2k^2}{((k+\gamma)^2-k_F^2)^2}$
$hxb(r)$	$\frac{4Z^2\gamma^2}{(k-k_F-2\gamma)^2}$	

in Eq. (52), we obtain

$$A(k,\varepsilon_{p0b}(k)) = \frac{16Z^2k_F^2k^2}{(k^2-(k_F+\gamma)^2)^2}. \tag{53}$$

The spectral function along all other b modes in Fig. 3 is calculated in the very same way and the results (together with a modes) are summarized in Table I.

The amplitude of the subleading b excitations does not vanish in the thermodynamic limit, though it is proportional to $1/\mathcal{L}$. The limit involves both $\mathcal{L} \to \infty$ and the particle number $N \to \infty$ but keeps the density $N/\mathcal{L}$ finite. The spectral weights of the subleading modes $p0b$, $h1b$, and $h1b(r)$ from Table I are proportional to the density squared for some values for k, e.g., the modes $p0b$ at $k = k_F$ gives

$$A(k_F,\varepsilon_{p0b}(k_F)) = \left(\frac{mU}{1+mU}\right)^2 \frac{N^2}{\left(\mathcal{L} - \frac{NmU}{1+mU}\right)^2}, \tag{54}$$

see Table I for other modes, and are apparent in the infinite system.

Assessing further the continuum of b excitations we consider the spectral function and how it evolves as one moves away slightly from the of the strongest a mode. Just a single step of a single quantum of energy away from the a mode requires the addition of an electron-hole pair on top of the configuration of quasimomenta in Fig. 2(a). This immediately moves such states one step down the hierarchy to b excitations. Let us consider the spectral function as a function of energy only making a cut along a line of constant k. The energies of the electron-hole pairs themselves are regularly spaced around the Fermi energy with slope v_F. However, the degeneracy of the many-body excitations due to the spectral linearity makes the level spacings nonequidistant. We smooth this irregularity using an averaging of the spectral function over energy,

$$\overline{A}(k,\varepsilon) = \int_{-\frac{\epsilon_0}{2}}^{\frac{\epsilon_0}{2}} \frac{d\epsilon}{\epsilon_0} A(k,\varepsilon+\epsilon), \tag{55}$$

where ϵ_0 is a small energy scale.

Then, using the parametrization of b excitations in Fig. 2(b) in the vicinity of the principal parabola, we linearize the energies of the extra electron-hole pairs around the Fermi energy and of the particle around its original position. We then substitute the resulting expressions for $k_{1,2}^f$ and k_1^0 in terms of the energy E from Eq. (7) in Eq. (52), similar to our procedure of obtaining Eq. (53). Finally, we use the averaging rule in Eq. (55) and obtain

$$\overline{A}(k,\varepsilon) = \frac{Z^2 2k_F\left(3k^2+k_F^2\right)\theta(\varepsilon_{h0a}(k)-\varepsilon)}{m\gamma K(\varepsilon_{h0a}(k)-\varepsilon)} \quad \text{for } -k_F < k < k_F, \tag{56}$$

$$\overline{A}(k,\varepsilon) = \frac{Z^2[k+\mathrm{sgn}(\varepsilon-\varepsilon_{p1a(l)}(k))k_F]^3}{m\gamma K|\varepsilon-\varepsilon_{p1a(l)}(k)|} \quad \text{for } k_F < k < 3k_F, \tag{57}$$

where $\gamma = 2\pi/\mathcal{L}$ and $\varepsilon_{h0a}(k) = \varepsilon_{p1a(l)}(k) = k^2/(2mK)$ is the parabolic dispersion of the a mode.

The result in Eqs. (56) and (57) can be interpreted as the line shape of the a mode. However, it has an unusual form—namely that of a divergent power law. The divergence at the parabola is cut off by the lattice spacing recovering $\overline{A}(k,\varepsilon_{h0a,p1a}(k)) = 1$ from Eq. (51). In Eq. (57), the line shape is asymmetric due to different prefactors $(k \pm k_F)^3$ above and below the line. In Eq. (56), the higher energy part $[\varepsilon > \varepsilon_{h0a}(k)]$ is absent due to the absence of the excitation in this region, forbidden by the kinematic constraint.

Not every simple mode marks a distinct feature. The states at least on one side, above or below the mode in energy, have to belong to a different level of the hierarchy than the mode itself, which results in a divergence or in a jump of the spectral function in the continuum of excitations. Otherwise, the spectral function is continuous across all of the modes that belong to the same level of the hierarchy as the excitations around them. The a modes are distinct since excitations around them belong to a different b level. All modes on the spectral edges, $p0b$, $p1b$, $h1b$, and so on, are distinct since on one side there are no excitations (due to the kinematic constraint) and on the other side there is a finite density of states resulting in a jump of the spectral function.

An example of an observable subleading mode in the continuum is $h0b(r)$. On the higher-energy side of this mode, the excitations are described by the same type of states in Fig. 2(b) but on the lower-energy side creation of an additional electron-hole pair in the quasimomenta results in states that have two noncancelled singularities in Eq. (46), which lowers their corresponding level of the hierarchy to c from b. This, in turn, results in an observable feature in the spectral function

at the position of the $h0b(r)$ mode. On the other hand, the $p0b(r)$ and $h1b(l)$ modes in continuum are not detectable since excitations on both sides around them belong to the same b level of the hierarchy. Observability of all other modes can be easily assessed in the same way by considering their corresponding states in the form of Figs. 2(a) and 2(b) and excitations around the modes.

The structure of the matrix element in Eq. (47) is quite similar to the matrix element in Eq. (46). Thus the dynamical structure factor exhibits the same hierarchy of excitations (and modes formed by them) as the spectral function analysed in detail in this section. The strongest excitations correspond to only a single electron-hole pair, the first subleading level corresponds to two electron-hole pairs, and so on.

Also, a similar hierarchy of excitations was observed in numerical studies of spin chains, e.g., Refs. [25–27,31–33]. There, it was found that only a small number of electron-hole pairs are sufficient to saturate the sum rules for the dynamics response functions. For example, integration of Eq. (9) over the energy and momentum,

$$\int d\varepsilon dk A(k,\varepsilon) = \mathcal{L} - N, \tag{58}$$

gives the number of empty sites. If a sum over only a small number of electron-hole pairs in the intermediate state f in Eq. (9) is sufficient to fulfill this rule in Eq. (58) then a few electron-hole pairs already account for a major part of all of the spectral density and the states with more electron-hole pair have vanishing spectral weights, as in the hierarchy of modes established in this work. Our analytic work demonstrates how this can arise in a Bethe ansatz solution, though the numerical studies of spin chains were done at large fillings ($\mathcal{L} \sim N$), for which our result in Eq. (46) is not directly applicable.

F. Spectral edge modes

In this section, we consider another important role played by the continuum of eigenstates, namely how they form the spectral function close to the spectral edges. These edges separate regions where there are excitations from regions where there are none, see borders between white and grey regions in Fig. 3. The recently proposed model of a mobile impurity [34–37] gives a field-theoretical description of the dynamic response functions around the spectral edges predicting a general (divergent) power-law behavior $A(k,\varepsilon) \sim |\varepsilon - \varepsilon_{\text{edge}}(k)|^{-\alpha}$, see Refs. [28,34–37,40–46]. For spinless fermions, the exponent of the spectral function is given by [47]

$$\alpha = 1 - \frac{K}{2}\left(1 - \frac{1}{K^2}\right) \tag{59}$$

for both the particle ($p0b$) and hole edges ($h0a$), where Eq. (8) gives the Luttinger parameter K in terms of the microscopic parameter of the model in Eq. (1). Here, we will compare the field-theoretical result in Eq. (59) with the microscopic calculation in Eqs. (6) and (46). We find agreement in many cases, but interestingly we also find some cases where the mobile impurity results are not consistent with the analytic solution, suggesting this field-theoretical approach is not the complete story.

The hole edge is an a mode, $h0a$, whereas the continuum around it is dominated by b excitations. The spectral function formed by these b excitations has already been calculated in Eq. (56) giving the power-law behavior with the exponent $\alpha = 1$. Note that for spinless fermions the Luttinger parameter K has only small deviations from 1 for arbitrary magnitude of the short-range interactions, see Eq. (8). This makes the result in Eq. (59) close to $\alpha = 1$ for all values of U; comparison of small deviations (which are U-dependent) require a better accuracy in evaluating Eq. (56). Thus the result of the microscopic calculation coincides with the prediction of the mobile-impurity model in Eq. (59) for the hole edge.

The particle edge is a b mode, $p0b$, and the excitations around it belong to the same b level of the hierarchy as the mode itself. Parameterizing the b excitations in this region of the continuum as in Fig. 2(b) and using the averaging procedure in Eq. (55) we obtain, repeating the same steps as before, Eqs. (56) and (57),

$$\overline{A}(\varepsilon) \sim (\varepsilon - \varepsilon_{p0b})^3 \tag{60}$$

for $k \approx 0$ to

$$\overline{A}(\varepsilon) \sim \text{const} - (\varepsilon - \varepsilon_{p0b}) \tag{61}$$

for $k \approx k_{\text{F}}$, where $\varepsilon_{p0b}(k) = k_{\text{F}}^2/(mK) - k^2/(2mK)$. This is a new power-law behavior characterized by an exponent α changing essentially with k from $\alpha = -3$ for $k = 0$ to $\alpha = -1$ for $k \approx \pm k_{\text{F}}$ and is *different* from the predictions of the mobile-impurity model in Eq. (59). Here, we observe that the phenomenological model in Refs. [34–36] is correct only for the a-mode spectral edge but higher-order edges would require a different field-theoretical description.

On a more detailed level, the difference between the particle and the hole edges manifests itself in different statistics of level spacings around the edges. An evaluation of the density of states, $\nu(k,\varepsilon) = \sum_f \delta(\varepsilon - E_f)\delta(k - P_f)$, is performed using E_f from Eq. (7) for a fixed momentum k. For b excitations in Fig. 2(b), we obtain the same results,

$$\nu(k,\varepsilon) \sim |\varepsilon - \varepsilon_{p0b(h0a)}(k)|, \tag{62}$$

in the vicinity of both the particle $p0b$ and the hole $h0a$ edges. However, the statistics of the level spacings

$$\mathcal{P}(s,k) = \sum_f \delta(s - (E_{f+1} - E_f))\delta(k - P_f), \tag{63}$$

where E_f are assumed sorted by their values, is different in the two regions. For the hole edge, the energy levels are spaced regularly and are governed by the slope of dispersion at the Fermi energy $\approx v$. This gives a bimodal $\mathcal{P}(s,k)$ with a sharp peak at $s = 0$ (due to many-body degeneracy of almost linear spectrum at E_{F}) and at $s \approx v\gamma$. For the particle edge, the statistics of the level spacings varies from having a regular level spacing [for k commensurate with k_{F} in Fig. 4(a)] to an irregular distribution [for incommensurate k in Fig. 4(b)].

The change in the characteristics of the underlying statistics is another microscopic difference between the particle (b-mode) and the hole (a-mode) edges that signals a difference in underlying physics for the particles and for the holes spectral edges beyond the low-energy region.

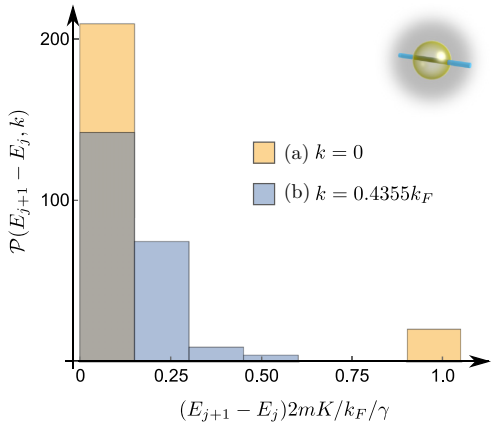

FIG. 4. Distributions of level spacings in the vicinity $(\max(E_f-\varepsilon_{p0b}(k))/\varepsilon_F = 1/100)$ of the particle mode $p0b$ accumulated along energy axis for the values of momenta (a) $k=0$ and (b) $k=0.4355k_F$; $N=2\times10^3$ and $L=2\times10^5$.

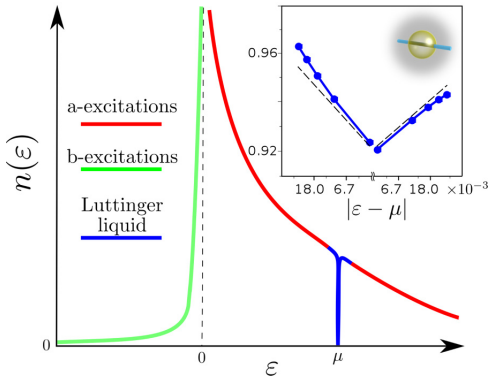

FIG. 5. The local density of states for interacting spinless fermions: the red and the green lines show the contribution of a and b excitations and the blue line indicates the Luttinger-liquid regime. Inset is a log-log plot around the Fermi energy: the points are numerical data for $N=71$, $L=700$, $mV=6$ giving $K=0.843$, and the dashed line is $n(\varepsilon)=\text{const}|\varepsilon-\mu|^{(K+K^{-1})/2-1}$.

V. LOCAL DENSITY OF STATES

Now we turn to another macroscopic observable, the local density of states (LDOS), which describes the probability of tunneling a particle in or out of the wire at a given position in space and at a given energy. Since the model in Eq. (1) is translationally invariant, the LDOS depends only on a single variable—energy, making it a more convenient quantity to study qualitatively how the physical properties change from low to high energies. In this section, we will show how the power-law result of the Tomonaga-Luttinger model [2] at low-energy crosses over into the hierarchy of mode-dominated behavior at high energy.

The probability of local tunneling at energy ε and at position x is described by [16] $n(x,\varepsilon) = -\text{Im}[\int dt e^{-i\varepsilon t}G(x,x,t)]\text{sgn}(\varepsilon-\mu)/\pi$, where μ is the chemical potential and $G(x,x',t) = -i\langle T(e^{-iHt}\psi(x)e^{iHt}\psi^\dagger(x'))\rangle$ is the two-point correlation function at zero temperature. In terms of eigenmodes, it reads

$$n(\varepsilon) = \mathcal{L}\sum_f [|\langle f|\psi^\dagger(0)|0\rangle|^2\delta(\varepsilon - E_f + E_0) + |\langle 0|\psi(0)|f\rangle|^2\delta(\varepsilon + E_f - E_0)], \quad (64)$$

where the coordinate dependence drops out explicitly, the eigenenergy E_f has already been calculated in Eq. (7) and the matrix elements $|\langle 0|\psi(0)|f\rangle|^2$ are given in Eq. (46). Note that the definition in Eq. (64) is connected to the definition of the spectral function in Eq. (9) via

$$n(\varepsilon) = \int dk A(k,\varepsilon). \quad (65)$$

The leading contribution for $\varepsilon > 0$ comes from a excitations. Substituting the matrix element for the a excitations from Eq. (51), we sum over the single-particle-like excitations [with $\varepsilon = k^2/(2mK)$] that form the mode and obtain

$$n(\varepsilon) = \sqrt{\frac{2mK}{\varepsilon}}\theta(\varepsilon). \quad (66)$$

This result gives the same $1/\sqrt{\varepsilon}$ functional dependence—see red line in Fig. 5—and the same $1/\sqrt{\varepsilon}$ van Hove singularity at the bottom of the band $\varepsilon = 0$ as the free-particle model.

For $\varepsilon < 0$, the leading contribution to $n(\varepsilon)$ comes from b excitations. Instead of performing a summation in Eq. (64) over every b excitation in this region, we use an intermediate result in Eq. (56) where the matrix elements of b excitations in Eq. (52) are already smoothed over many eigenstates and the relation in Eq. (65). Evaluating the integral over k in Eq. (65), after the substitution of Eq. (52) into it, for $\varepsilon < 0$ we obtain

$$n(\varepsilon) = \frac{2Z^2k_F^2}{\gamma\mu K}\theta(-\varepsilon) \times\left[2\left(1-\frac{3|\varepsilon|}{\mu}\right)\sqrt{\frac{\mu}{|\varepsilon|}}\cot^{-1}\left(\sqrt{\frac{|\varepsilon|}{\mu}}\right)+6\right]. \quad (67)$$

There is a finite probability to find a particle below the bottom of the conduction band—green line in Fig. 5—which is allowed only due to interactions between many particles. The factor Z is proportional to the interaction strength V—see Eq. (46)—making $n(\varepsilon) = 0$ for $\varepsilon < 0$ in the free particle limit of $V = 0$. At the bottom of the band below the $\varepsilon = 0$ point in Fig. 5, the result in Eq. (67) contains another Van Hove singularity,

$$\rho(\varepsilon) = \frac{2\pi Z^2k_F^2}{\gamma K\sqrt{\mu|\varepsilon|}}, \quad (68)$$

which also disappears when $V = 0$. The appearance of the identical exponent as in Eq. (66) exponent $1/\sqrt{|\varepsilon|}$ seems coincidental.

Around the Fermi energy (the point $\varepsilon = \mu$ in Fig. 5), the Tomonaga-Luttinger model predicts a power-law suppression

of LDOS,

$$n(\varepsilon) \sim |\varepsilon - \mu|^{(K+K^{-1})/2-1}, \tag{69}$$

e.g., see the book in Ref. [2]. However, the result for the a-mode in Eq. (66) is finite at this point, $n(\mu) = \sqrt{2mK/\mu}$. In order to resolve the apparent discrepancy, we evaluate $n(\varepsilon)$ numerically around the Fermi energy using the determinant representation of the form factors in Eqs. (32) and (33) instead of Eq. (46), which accounts for all orders in $1/\mathcal{L}$, and indeed find a suppression of LDOS around $\varepsilon = \mu$, see blue line in the inset in Fig. 5. This signals that the leading-order expansion in the $\mathcal{L}|\langle f|\psi^\dagger(0)|0\rangle|^2 = 1$ result is insufficient at low energies. Very close to the Fermi point (the linear region of the single-particle dispersion) all $1/\mathcal{L}$ orders of the Bethe ansatz calculation are needed to reproduce the result of the Tomonaga-Luttinger model, see dashed lines in the inset in Fig. 5. However, away from the linear region, the particle-hole symmetry of the Tomonaga-Luttinger model is broken by the finite curvature of the dispersion and only the leading $1/\mathcal{L}$ order in Eq. (46) is sufficient to account for the main contribution there.

The general picture emerging in Fig. 5 is a power-law crossover between different energy scales. At low energies (blue region in Fig. 5) Eq. (46) breaks down and the collective modes of the Tomonaga-Luttinger model are a better description of the system. At high energies (the red and the green regions in Fig. 5), the hierarchy of modes, which directly follows from Eqs. (46) and (6), becomes the dominant physical picture. For spinless fermions, the extent of the crossover region is large due to only small deviations from $K = 1$ for arbitrary short-range interactions. For very small exponents $[(K + K^{-1})/2 - 1] \ll 1$, the power-law in Eq. (69) deviates significantly from 1 only in an extremely narrow region around $\varepsilon = \mu$ having a large window of energies where it overlaps with the a-mode result in Eq. (66).

VI. EXPERIMENTS ON SPINFUL FERMIONS

So far, in this paper, we have established the theoretical framework for expecting a hierarchy of modes in a interacting system at high energy. Now we turn to a measurement of tunneling of electrons in a one-dimensional (1D) nanostructure, which gives experimental evidence for the existence of the hierarchy. Electrons have spin 1/2, which does not correspond directly to the model of spinless fermions in Eq. (1), and there is currently no known method for calculating the necessary form factors for spinful fermions. However, the general picture that emerges from the experiment is qualitatively the same as our result in the theory part of this paper.

The design of our device [12] is based on a high-mobility GaAs–AlGaAs double-quantum-well structure (blue and yellow layers in Fig. 6), with electron densities around 3 and 2×10^{15} m^{-2} in the upper and lower layers, respectively, before application of gate voltages. Electrons in the upper layer are confined to a 1D geometry ("wires") in the x direction by applying a negative voltage to split "finger" gates on the surface (gold layer in Fig. 6).

Electrons underneath the gates are completely depleted, but electrons below the gap between gates are squeezed into a narrow 1D wire. The extremely regular wires are arranged

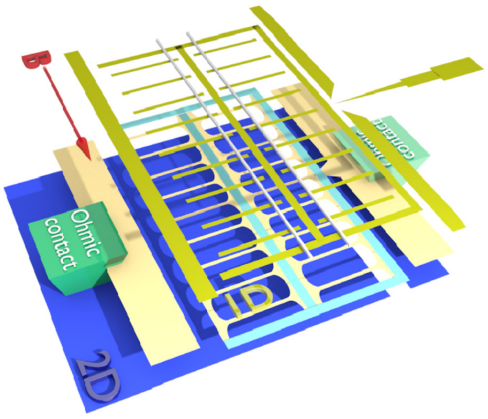

FIG. 6. Schematic of the device made out of a double-well heterostructure. The dark blue and cream layers are the lower and upper quantum wells, respectively. The lower layer hosts the two-dimensional electron gas (2DEG). The wires are defined in the upper layer by gating. The gold top layer represents metallic gates deposited on the surface of the semiconductor heterostructure. The array of parallel "finger" gates defines the 1D wires in the upper well. The white lines represent air bridges joining the finger gates together. Current is injected from the ohmic contact on the right solely into the upper well through the constriction at top right in the diagram. The constriction is formed and pinched off by a split pair of gates, and charge is induced again in the upper well in the constriction by a gate in the center of the channel. The current then flows into the 1D wires via the narrow, nominally 2D, regions shown in light blue. Tunneling to the 2DEG below is possible, and this gives a small "parasitic" current in parallel with the tunnel current from the 1D wires. To tune this tunneling off resonance in the regions of interest by changing the density, a "p" gate is placed above the "p"' regions and a voltage V_P is applied. Current is prevented from flowing from the upper well into the left-hand ohmic contact by a barrier gate shown on the left, which only depletes the upper well. The red arrow shows the direction of the externally applied magnetic field B, which is in the plane of the wells and perpendicular to the wires.

in an array containing ∼600 of them to boost the signal. The small lithographic width of the wires, ∼0.18 μm, provides a large energy spacing between the first and second 1D subbands defined by spatial modes perpendicular to the wires (∼3−5 meV, probably somewhat smaller than for overgrown wires [11]). This allows a wide energy window for electronic excitations in the single 1D subband that covers a range of a few chemical potentials of the 1D system. The lower 2DEG (blue in Fig. 6) is separated from the wires by a $d = 14$ nm tunnel barrier. The wafer is doped with Si symmetrically in the AlGaAs barriers above and below the pair of wells. The doping is separated from the wells by spacer layers. The spacing between the centres of the two quantum wells is nominally $d = 32$ nm but we find a value of $d = 35$ nm fits the data better, and this can be explained by the fact that the centres of the wave functions will be slightly further apart owing to the opposite electric fields in each well.

The 2DEG in the lower (dark blue) layer is used as a controllable injector or collector of electrons for the 1D

system [48,49]. The current I tunneling in the z direction between the layers is proportional to the convolution of the 1D and 2D spectral functions (a pair of peaks at $k_x = \pm k_F$ broadened in k_y by the 1D confinement, and a circle, respectively). An in-plane magnetic field B applied in the y direction, perpendicular to the wires (show with a red arrow in Fig. 6), produces a Lorentz force that changes the longitudinal momentum k_x acquired while tunneling between layers by $\Delta k = eBd/\hbar$, where e is the electronic charge. Thus B shifts the spectral functions in k_x relative to each other, and so probes the momentum. One spectral function can also be shifted relative to the other in energy by applying a voltage V between the layers, in order to probe the 1D and 2D dispersion relations at different energies. The conductance $G = dI/dV$ has a peak when the sharp features in the spectral functions have a significant overlap. At $V = 0$, this occurs when Δk is equal to the sum or difference of the Fermi wave numbers k_F and k_2 of the 1D and 2D systems, respectively, so there are two peaks for $B > 0$, at $B_\pm = \frac{\hbar}{ed}|k_2 \pm k_F|$. By sweeping B and V, one can map out the dispersion relation of states in each layer. The range of magnetic fields that we apply to the system is still within the regime of Pauli paramagnetism for the electron densities in our samples.

VII. LOW ENERGY

The results from two samples are presented, each consisting of a set of identical wires of length $L = 10\,\mu$m (sample A) and $L = 18\,\mu$m (sample B). First, we measure the tunneling conductance $G = dI/dB$ in a small range of voltages and magnetic fields around $V = 0$ and $B = B_+ = 3.15$ T that corresponds to a region on the momentum-energy plane around the Fermi point ($\varepsilon = \mu, k = k_F$), see Fig. 7. Below the Fermi energy, we observe splitting of the single-particle line into two lines with different dispersions—spin (S) and charge (C) separation [11,12]—giving two different slopes v_s and v_c (black dashed lines in Fig. 7). We assume that v_s is the same as for noninteracting electrons and so take it to be the gradient

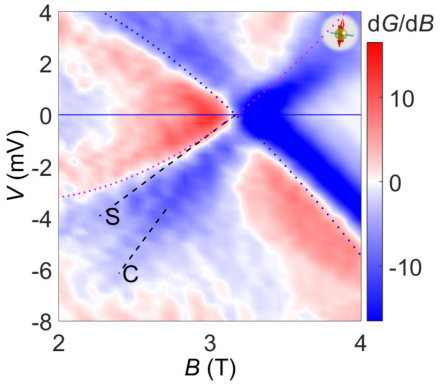

FIG. 7. Intensity plot of dG/dB at low energies around the Fermi point k_F. Spin (S) and charge (C) dispersions are indicated by dashed lines. The dotted lines indicate the parabolae expected in the noninteracting model. The finger-gate voltage $V_F = -0.70$ V and the temperature $T \sim 300$ mK (sample A).

of the parabola at $V = 0$. We estimate v_c from the positions of steepest gradient and hence obtain $v_s \approx 1.2 \times 10^5$ ms^{-1} and $v_c \approx 2.3 \times 10^5$ ms^{-1} at the finger-gate voltage $V_F = -0.70$ V.

Theoretically, the low-energy physics of the interacting 1D electrons is described well by a spinful generalization of the Luttinger-liquid model [2]. Its excitations are collective hydrodynamiclike modes that are split into charge-only and spin-only excitations. For any finite strength of the interactions between fermions, the two types of modes have linear dispersions with different slopes v_c and v_s. In the absence of interactions, the difference between the two velocities vanishes in accordance with the free-electron model, in which the spin degree of freedom does not affect the spectrum but results only in the double degeneracy of the fermionic states. Thus the ratio of v_c/v_s serves as a good measure of the interaction strength. Since the Coulomb interaction between electrons is repulsive, the charge branch always has a steeper slope $v_c \geqslant v_s$ (see Ref. [2]). Thus the ratio varies from 1 for free to ∞ for infinitely repelling particles. In our experiment, we measure the tunneling of electrons and observe two peaks that we attribute to the charge and the spin dispersions. The pair of velocities above gives a large $v_c/v_s \approx 1.8 \pm 0.1$ (for $V_F = -0.70$ V), confirming that our system is in the strongly interacting regime.

VIII. HIGH ENERGY

Now we extend the ranges of the voltage and magnetic field measuring the tunneling conductance G across the double quantum well in Fig. 6 accessing a large portion of the 1D spectral function from below $-k_F$ to $3k_F$ and from -2μ to 2μ, see Fig. 8. There is an unavoidable "parasitic" ("p") tunneling from narrow 2D regions (light blue strips in Fig. 6) that connect the wires to the injector constriction. This superimposes a set of parabolic 2D-2D dispersions on top of the 1D-2D signal, which are marked by magenta and blue dotted lines in Fig. 8.

Apart from the parasitic and the 2D dispersion signals, we observe only a single 1D parabola away from $B = 0$, marked by the solid green line in Fig. 8. It extends from the spin-excitation branch at low energy and the position of its minimum multiplied by the electronic charge e gives the 1D chemical potential $\mu \approx 4$ meV. The B_- and B_+ crossings with the line $V = 0$, corresponding to momenta $-k_F$ and k_F, give the 1D Fermi momentum $k_F \approx 8 \times 10^7$ m^{-1}. All other edges of the 1D spectral function are constructed by mirroring and translation of the hole part of the observable 1D dispersion, dashed green and blue lines in Fig. 8.

For positive voltages in the region just above the higher $V = 0$ crossing point (B_+, which corresponds to k_F), we observe a distinctive feature: the 1D peak broadens, instead of just continuing along the noninteracting parabola, with one boundary following the parabola [$p1a(l)$] and the other bending around, analogous to the replica $p1b$. This is visible in the conductance, but is most easily seen in the differentials, particularly dG/dV (left column of Fig. 8). The broadening is observed at temperatures from 100 mK up to at least 1.5 K, and in samples with different wire designs (with or without air bridges) and lengths: in Fig. 9, dG/dV is shown in detail for the broadened "replica" region for the 10-μm wires already presented (a)–(d), and for another sample with wires 18-μm long [(e) and (f)]. G is plotted in Figs. 9(b) and 9(d) and f

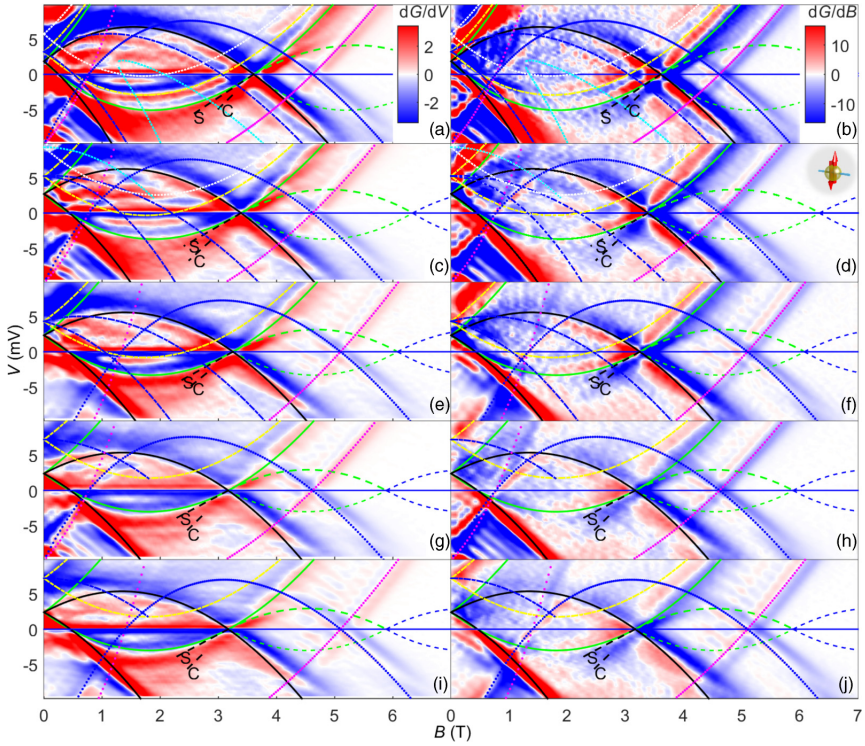

FIG. 8. Intensity plots of dG/dV (left column, in μS/mV) and dG/dB (right column, in μS/T) from below $-k_F$ to above $3k_F$ and from $\sim -2\mu$ to $\sim\mu$, for various finger-gate voltages: -0.60 [(a) and (b)], -0.65 [(c) and (d)], -0.68 [(e) and (f)], and -0.70 V [(g)–(j)]. The solid black lines map out the dispersion of the lower (2D) layer. The green solid line marks a modes, thick and thin dashed green lines, $p1b$ and $h1b$ modes, respectively, and dashed blue, higher-k modes (as in Fig. 3). Dot-dashed yellow (blue) and dotted white (cyan) lines show second and third 1D subbands (2D dispersion measured by those subbands), respectively (though the third is empty, electrons can tunnel into it from the 2D layer and hence there are sometimes signs of its effects for $V > 0$, especially near $B = 0$). Dotted magenta and blue lines are "parasitic" 2D dispersions of the two layers. The voltage on the gate over this region $V_P = 0$ V except for [(e) and (f)] ($V_P = 0.2$ V) and [(i) and (j)] ($V_P = 0.3$ V), which shifts the parabolae to the right without changing the signal from the 1D wires. The lines have all been adjusted to take account of the capacitive coupling between the layers. Spin (S) and charge (C) modes are indicated with black dashed lines. $T \sim 300$ mK. See Table II for the densities and the ratio v_c/v_s for each gate voltage.

on cuts along the V axis of the corresponding plots in the left column at various fields B from B_+ to 4.8 T—between the "+" and "×" symbols on each curve is a region of enhanced conductance characteristic of the replica $p1b$.

Filling of the second 1D subband changes significantly the screening radius for the Coulomb interaction potential in the first 1D subband. This is manifested by a change of the ratio v_c/v_s when the occupation of the second subband is changed by varying voltage of the finger gates V_F in Figs. 8(a), 8(c), 8(e), and 8(g), see Table II. The ratio v_c/v_s is a measure of interaction energy. Thus the finger gates give a degree of experimental control over the interactions within our design of the 1D system. We use the maximum change of the ratio v_c/v_s for different finger gate voltages to estimate the relative change of the interaction strength as $(\max(v_c/v_s) - \min(v_c/v_s))/\min(v_c/v_s)$ obtaining a change of about 20%.

It also has to be noted that the "replica" is visible even when a second subband is present in the 1D wires, see Figs. 8(a)–8(f). In (a) and (b), it appears to go 25%–30% higher in voltage than expected for a precise copy of the usual 1D parabola (even allowing for capacitive correction) due to a contribution of the second subband, which we do not analyze in detail here.

At even higher magnetic fields, the $p1b$ line passes a "p" parabola. Figures 9(a) and 9(c) [and the corresponding cuts (b) and (d)] show the replica feature for two different positions of

TABLE II. Densities of the 2D layer (n_{2D}) and of the 1D wires (n_{1D}), the 1D Fermi wave vector k_F (all to about ±1%), and the ratio of the charge and the spin velocities at low energies (to about ±5%), extracted from the gradients of the S and C lines in Fig. 8, for different finger-gate voltages V_F.

V_F (V)	n_{2D} (10^{15} m^{-2})	n_{1D} (10^7 m^{-1})	k_F (10^7 m^{-1})	v_c/v_s
−0.60	1.67	5.68	8.9	1.5
−0.65	1.65	4.99	7.8	1.6
−0.68	1.52	4.79	7.5	1.5
−0.70	1.48	4.60	7.2	1.8

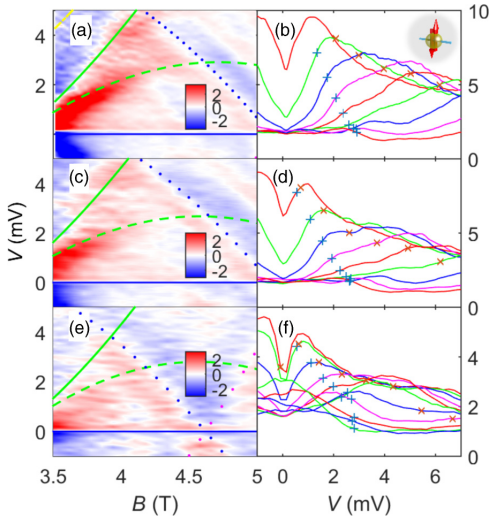

FIG. 9. (Left) Intensity plots of dG/dV (in μS/mV), for various finger-gate voltages and samples: [(a) and (b)] $V_F = -0.68$ V, $V_P = 0.2$ V, from Fig. 8(e), sample A, which had 10 μm-long wires ($T \sim 300$ mK); [(c) and (d)] $V_F = -0.70$ V, $V_P = 0.3$ V, from Fig. 8(i), sample A; [(e) and (f)] a similar single-subband result from sample B (18 μm-long wires, $T < 100$ mK). The replica feature just above k_F appears as a pale triangle (slowly varying G) between the two green curves, after a red region (sharp rise in G). The replica feature for sample B is somewhat weaker than that for sample A, in line with the wire-length dependence predicted in this paper. Right column: G vs V at various fields B from 3 to 4.8 T for the data in the matching plots in the left column; "+" and "×" symbols on each curve indicate, respectively, the voltages corresponding to the dashed and solid [$p1b$ and $p1a(l)$] green lines in the left column (and in Fig. 8), showing the enhanced conductance between the two.

the "p" parabolae using a gate above most of the "p" region, showing that the replica feature is independent of the "p" tunneling. The amplitude of the feature dies away rapidly, and beyond the "p" parabolae, we have measured up to 8 T with high sensitivity, but find no sign of any feature that can be distinguished from the decaying tails of the other features.

In the range of fields where the $p1b$ feature is observed its strength decreases as the B field increases away from the crossing point analogously to the power law for spinless fermions in Table I. On general grounds, it is natural to expect that divergence of the spectral weight of a b mode toward an a mode is a general feature, but there is no known method for performing a microscopic calculation in the spinful case. A similar feature should mark the $h0b(r)$ mode (see Fig. 3 and Table I) for negative voltages and for the magnetic field just below the crossing point k_F, but it would be very difficult to resolve due to the overlaying spin and charge lines.

Making an analogy with the microscopic theory for spinless fermions in the first part of this paper, we estimate the ratio of signals around different spectral edges using the 1D Fermi wavelength, $\lambda_F \approx 130$ nm for our samples, as the short-range scale $\mathcal{R}$. The signal from the principal parabola, see Fig. 8(b), gives the amplitude of the a mode as $G_a \approx 5\,\mu$S. Then the amplitude of the signal from the second (third)-level excitations is predicted to be smaller by a factor of more than $\lambda_F^2/L^2 \sim 2 \times 10^{-4}$ ($\lambda_F^4/L^4 = 3 \times 10^{-8}$), where the length of a wire is $L = 10\,\mu$m. These values $G_a\lambda_F^2/L^2 \sim 10^{-3}\,\mu$S ($G_a\lambda_F^4/L^4 \sim 10^{-7}\,\mu$S) are at least two orders of magnitude smaller than the background and noise levels of our experiment $G_{\rm noise} \sim 10^{-2}\,\mu$S, which places an upper limit on the amplitude of any replica away from k_F. Thus our observations are consistent with the mode hierarchy picture for fermions.

In an effort to quantify the decay of the replica feature, we have fitted the gradual background fall in conductance and the noninteracting 1D and 2D peaks (solid green and blue lines in Figs. 7–9) with a Gaussian and/or Lorentzian functions of B, at each value of $V > 0$. The fitting parameters are then fitted to smooth functions in order to represent the general behavior of the peaks as a function of V. This idealized landscape is then subtracted from the data, see Fig. 10(a), and the "replica"

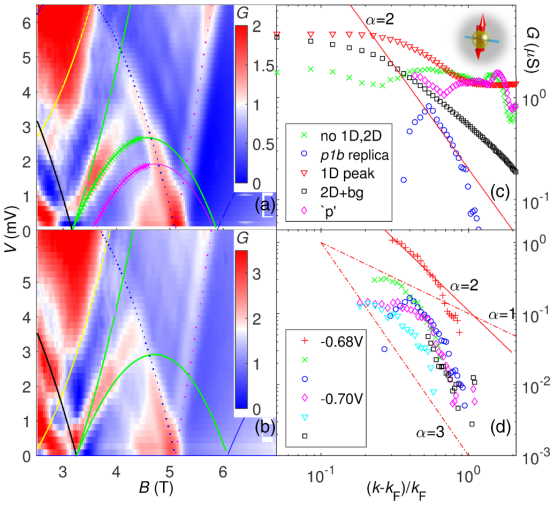

FIG. 10. (a) and (b) The conductance for $V_F = -0.70$ and $-0.68\,V$, respectively, for sample A, after subtraction of an idealized landscape made up of fits or estimates of the noninteracting 1D-2D and "p" parabolae (see text). The $p1b$ replica is seen clearly as the red region of enhanced conductance. (c) The conductance along the $p1b$ replica parabola, for the data in (a) (green crosses). The conductance on $p1b$ has a large contribution from the "p" region [the line in (a) marked with blue dots, which is blurred to the left by multiple copies at slightly different positions]. In order to correct for this contribution, the conductance along a matching parabola shifted along the dotted "p" line in (a) (shown as a dashed magenta line there), is subtracted from the $p1b$ data. This yields the points marked with blue circles, which appears to be nonzero because of the enhancement at $p1b$. The amplitude decays rapidly. There are many uncertainties in the fitting of the other peaks, but the replica appears clearly and the decay of the conductance is consistent with an inverse-square power law $G \propto (k - k_F)^{-\alpha}$ (labelled $\alpha = 2$), which is the behavior predicted by the theory for $k > k_F + \gamma$ where $\gamma \ll k_F$ (see Table I). (d) The $p1b$ conductance enhancement as shown with circles in (b). Three different methods of fitting the background and the 1D and 2D peaks are compared for each of two gate voltages as shown. The curves are offset vertically for clarity. The lines marked with values of α are guides to the eye. The data are all consistent with $\alpha = 2 \pm 1$.

is then fairly easily observed in the remaining conductance. A copy of a nearby region along the "p" curve is then subtracted too, as an approximation to the rather diffuse signal arising from the main "p" peak and smaller versions of it at slightly different densities. This also reduces errors in the peak and background fitting used in (a). We then plot the conductance along the expected parabola [dashed line in (a)] as a function of $(k-k_F)/k_F = (B-B_+)/((B_+-B_-)/2)$. These data are shown as circles in (c), where all the other contributions to the conductance along the same parabola are shown. Here, $B_+ = 3.17$ T and $k_F = 7.2\times10^7$ m^{-1}. It is very hard to be sure that this procedure is reliable due to significant error bars imposed by contributions from the various other peaks, but it is clear that the replica feature dies away rapidly as a function of $k-k_F$, and it is consistent with the $1/(k-k_F)^2$ law predicted for $p1b$ in Table I for $k-k_F \gg \gamma$. Though the overall prefactor is unknown theoretically in the spinful case, this singular power law may overcome the reduction factor $\mathcal{R}^2/L^2$ close to k_F.

IX. CONCLUSIONS

In this work, we have shown that a hierarchy of modes emerges in systems of interacting fermions in one dimension at high energy controlled by the system length, in marked contrast to the well-known fermionic quasiparticles of a Fermi liquid and hydrodynamic modes of a Luttinger liquid at low energy. We have obtained theoretically the dynamic response functions for a model of spinless fermions with short-range interactions using the exact diagonalisation methods of the Bethe ansatz for the spectrum and the form factors of the system. Analysing the spectral function in detail, we have found that the first-level (strongest) mode in long systems has a parabolic dispersion, like that of a renormalized free particle. The second-level excitations produce a singular power-law line shape for the first-level mode and different kinds of power-law behavior at the spectral edges. Evaluating the form factor necessary for the dynamical structure factor we have shown that it has the same general form as the form factor of the spectral function, manifesting the same hierarchy of modes.

Using the same many-body matrix elements obtained microscopically, we have also calculated the local density of states. It provides a more convenient way to analyze how the hierarchy at high energy changes into the hydrodynamic modes of the Luttinger liquid at low energies. We have shown, via a full Bethe-ansatz calculation, that the LDOS is suppressed at the Fermi energy in a power-law fashion in full accord with the prediction of the Tomonaga-Luttinger model. Away from the Fermi point, where the Lorentz invariance of the linear dispersion is reduced to Galilean by the parabolicity of the spectrum, the LDOS is dominated by the first (leading) level of the hierarchy. We have demonstrated that the transition from one regime to another is a smooth crossover.

We measure momentum-resolved tunneling conductance in one-dimensional wires formed in the GaAs/AlGaAs double-well heterostructure by an array of finger gates. In this setup, we probe the spectral function of unpolarized electrons (spinful fermions) and find a pronounced spin-charge separation at low energy with a ratio of the spin and the charge velocities up to 1.8, which confirms that our system is in the strongly interacting regime. By varying the gate voltage that controls the width of our 1D wires, we demonstrate control of the interaction strength of about 20%; the deeper confining potential of the wires populates higher 1D subbands as well which in turn screens stronger Coulomb interactions in the principal 1D band reducing the interaction strength. In 10 μm-long wires, we find a clear feature resembling the second-level excitations, which dies away rapidly at high momentum. A qualitative fit shows that the feature decays in a fashion that is consistent with the power-law prediction in this paper for spinless electrons. Thus we have shown that the hierarchy is apparently a generic phenomenon at least for one- and two-point correlation functions of fermions without spin, and for a transport experiment for fermions with spin.

Data associated with this work are available from [50].

ACKNOWLEDGMENTS

We acknowledge financial support from the UK EPSRC through Grants No. EP/J01690X/1 and No. EP/J016888/1 and from the DFG through SFB/TRR 49. This research was supported in part by the National Science Foundation under Grant No. NSF PHY11-25915.

APPENDIX A: EIGENVALUE EQUATION IN THE ALGEBRAIC FRAMEWORK

The eigenvalue of the transfer matrix $\tau(u)$ in Eq. (19) can be evaluated using the commutation relations in Eqs. (16) and (17). Let Ψ be a Bethe state in the algebraic representation of Eq. (21). The results of acting with $A(u)$ and $D(u)$ operators on the state Ψ are obtained by commuting these operators from left to right though the product of $C(u_j)$ in Eq. (21) and then by using their vacuum eigenvalues in Eq. (20).

Let us consider the case of $N=2$ and the operator $A(u)$ first. Commuting once by means of Eq. (16) gives

$$A(u)C(u_2)C(u_1)|0\rangle = \left(\frac{1}{b(u_2-u)}C(u_2)A(u) - \frac{c(u_2-u)}{b(u_2-u)}C(u)A(u_2)\right)C(u_1)|0\rangle. \tag{A1}$$

Applying Eq. (16) the second time gives

$$\begin{aligned} A(u)C(u_2)C(u_1)|0\rangle = &\left(\frac{1}{b(u_2-u)}\frac{1}{b(u_1-u)}C(u_2)C(u_1)a(u) - \frac{c(u_1-u)}{b(u_1-u)}\frac{1}{b(u_2-u)}C(u_2)C(u)a(u_1)\right)|0\rangle \\ &+\left(-\frac{1}{b(u_1-u_2)}\frac{c(u_2-u)}{b(u_2-u)}C(u)C(u_1)a(u_2) + \frac{c(u_1-u_2)}{b(u_1-u_2)}\frac{c(u_2-u)}{b(u_2-u)}C(u)C(u_2)a(u_1)\right)|0\rangle, \end{aligned} \tag{A2}$$

where the vacuum eigenvalue of $A(u)$, $A(u)|0\rangle = a(u)|0\rangle$, was substituted explicitly. The second terms in the first and the second lines of the above equation have the same operator form but different scalar factors. Summation of the two scalar factor, using the explicit form of $b(u)$ and $c(u)$ from Eq. (12), yields

$$\frac{a(u_1)}{b(u_2-u)}\left[\frac{c(u_1-u_2)}{b(u_1-u_2)}c(u_2-u)-\frac{c(u_1-u)}{b(u_1-u)}\right]=-\frac{a(u_1)}{b(u_2-u_1)}\frac{c(u_1-u)}{b(u_1-u)}. \tag{A3}$$

Thus the four terms can be rewritten as only three terms,

$$A(u)C(u_2)C(u_1)|0\rangle=\left(a(u)\prod_{j=1}^{2}\frac{C(u_j)}{b(u_j-u)}-\sum_{j=1}^{2}a(u_j)\frac{c(u_j-u)}{b(u_j-u)}C(u)\prod_{l=1\neq j}^{2}\frac{C(u_l)}{b(u_l-u_j)}\right)|0\rangle. \tag{A4}$$

Extension of the same procedure for $N>2$ gives

$$A(u)\prod_{j=1}^{N}C(u_j)|0\rangle=\left(a(u)\prod_{j=1}^{N}\frac{1}{b(u_j-u)}C(u_j)-\sum_{j=1}^{N}a(u_j)\frac{c(u_j-u)}{b(u_j-u)}C(u)\prod_{l=1\neq j}^{N}\frac{1}{b(u_l-u_j)}C(u_l)\right)|0\rangle \tag{A5}$$

Commuting of the operator $D(u)$ is done in the same way using Eq. (17) and yields

$$D(u)\prod_{j=1}^{N}C(u_j)|0\rangle=\left(d(u)\prod_{j=1}^{N}\frac{-1}{b(u-u_j)}C(u_j)+\sum_{j=1}^{N}d(u_j)\frac{c(u-u_j)}{b(u-u_j)}C(u)\prod_{l=1\neq j}^{N}\frac{-1}{b(u_j-u_l)}C(u_l)\right)|0\rangle. \tag{A6}$$

Thus a Bethe state in Eq. (21) parametrized by an arbitrary set of u_j is not an eigenstate of the transfer matrix since acting of the operator $\tau(u)$ on such a state does not only result in multiplying by a scalar but also generates many different states: the second terms in Eqs. (A5) and (A6). However, the coefficients in front of each of these extra states can be made zero by a specific choice of u_j,

$$a(u_j)\prod_{l=1\neq j}^{N}\frac{1}{b(u_l-u_j)}-d(u_j)\prod_{l=1\neq j}^{N}\frac{-1}{b(u_j-u_l)}=0. \tag{A7}$$

When a set of u_j satisfies the system of equations above, the corresponding Bethe state is an eigenstate of the transfer matrix, $\tau(u)\Psi=\mathcal{T}(u)\Psi$, with the eigenvalue $\mathcal{T}$ given by the first terms in Eqs. (A5) and (A6),

$$\mathcal{T}(u)=a(u)\prod_{j=1}^{N}\frac{1}{b(u_j-u)}-d(u)\prod_{j=1}^{N}\frac{-1}{b(u-u_j)}. \tag{A8}$$

Equation (A7) is the set of Bethe equations in the algebraic representation, Eq. (22) of the main part of the text, and Eq. (A8) gives the eigenvalue of the transfer matrix, Eq. (24) of the main part of the text.

APPENDIX B: CALCULATION OF AVERAGES OF THE LOCAL DENSITY OPERATOR $\rho(0)$

The calculation of the average of the local density operator $\rho(0)$ is done in the same way as for the field operator $\psi^\dagger(0)$ in Sec. IV C. We start from the lattice model in Eq. (2) and the corresponding construction of the algebraic Bethe ansatz in Sec. IV A.

The local density operator can be represented in terms of A and D operators as [17,18]

$$\rho_1=-D\left(\frac{i\pi}{2}-\eta\right)\tau\left(\frac{i\pi}{2}-\eta\right)^{\mathcal{L}-1}. \tag{B1}$$

The action of the second factor in the above expression on an eigenstate $|\mathbf{u}\rangle$ just gives a phase factor—see an explanation after Eq. (31)—that we will ignore since we are interested in the modulus squared of this form factor. Then commuting the operator D of the first factor in the equation above through all C operators of the eigenstate $|\mathbf{u}\rangle$—in the form in Eq. (21)—gives the result in Eq. (A6).

The scalar product of Eq. (A6), where the auxiliary parameter u is set to $i\pi/2-\eta$, with another eigenstate $\langle\mathbf{v}|$ gives

$$\langle\mathbf{v}|\rho_1|\mathbf{u}\rangle=(-1)^N\prod_{j=1}^{N}\frac{\cosh\left(u_j-\eta\right)}{\cosh\left(u_j+\eta\right)}\langle\mathbf{u}|\mathbf{v}\rangle+i(-1)^N\sum_{b=1}^{N}\frac{\sinh 2\eta}{\cosh\left(u_b+\eta\right)}\prod_{l=1\neq b}^{N}\frac{\sinh\left(u_b-u_l+2\eta\right)}{\sinh\left(u_b-u_l\right)}\left\langle u_{b-1},\frac{i\pi}{2}-\eta,u_{b+1}|\mathbf{v}\right\rangle, \tag{B2}$$

where $\langle u_{b-1},\frac{i\pi}{2}-\eta,u_{b+1}|$ is a Bethe state which is constructed from the eigenstate $\mathbf{u}$ by replacing bth quasimomenta with $i\pi/2-\eta$. Note that the properties $\langle\mathbf{v}|\mathbf{u}\rangle=\langle\mathbf{u}|\mathbf{v}\rangle$, where u_j satisfy the Bethe equations and v_j is an arbitrary set of quasimomenta [17,18], was used.

The scalar product in the first line in Eq. (B2) is given by Eqs. (27) and (28) where $\mathbf{u}$ and $\mathbf{v}$ are swapped. Substitution of $\mathbf{u} = u_{b-1}, \frac{i\pi}{2} - \eta, u_{b+1}$ in the same expressions for the scalar products in the second line of Eq. (B2) yields

$$\left\langle u_{b-1}, \frac{i\pi}{2} - \eta, u_{b+1} | \mathbf{v} \right\rangle = -i \frac{\sinh^N(2\eta) \prod_{j=1}^N \cosh(v_j - \eta) \det \hat{T}^{(b)}}{\prod_{j<i} \sinh(v_j - v_i) \prod_{j<i\neq b} \sinh(u_j - u_i)(-1)^{b-1} \prod_{j=1\neq b}^N \cosh(u_j + \eta)}, \tag{B3}$$

where all matrix elements of $\hat{T}^{(b)}$ are

$$T^{(b)}_{ab'} = \prod_{l=1\neq b'}^N \frac{\sinh(u_{b'} - u_l + 2\eta)}{\sinh(u_{b'} - u_l - 2\eta)} \frac{1}{\sinh(u_{b'} - v_a)} \prod_{j=1\neq a}^N \sinh(u_{b'} - v_j - 2\eta) - \frac{1}{\sinh(u_{b'} - v_a)} \prod_{j=1\neq a}^N \sinh(u_{b'} - v_j + 2\eta) \tag{B4}$$

for $b' \neq b$

$$\hat{T}^{(b)}_{ab'} = \frac{1}{\cosh(v_a + \eta) \cosh(v_a - \eta)} \tag{B5}$$

for $b' = b$.

After pulling a common factor out of the brackets in Eq. (B2) and absorbing the b-dependent prefactors in front of the determinants in the second line of Eq. (B2) into the bth columns of the matrices under the determinants, the form factor in Eq. (B2) reads as

$$\langle \mathbf{v}|\rho_1|\mathbf{u}\rangle = \prod_{j=1}^N \frac{\cosh(u_j - \eta)}{\cosh(u_j + \eta)} \frac{\sinh^N(2\eta)}{\prod_{j<i} \sinh(v_j - v_i) \prod_{j<i} \sinh(u_j - u_i)} \left[\det \hat{T} + \sum_{b=1}^N \det \hat{\tilde{T}}^{(b)} \right]. \tag{B6}$$

Here the matrix elements of $\hat{\tilde{T}}^{(b)}$, which are obtain by multiplying by the corresponding scalars, are

$$\tilde{T}^{(b)}_{ab'} = \prod_{l=1\neq b'}^N \frac{\sinh(u_{b'} - u_l + 2\eta)}{\sinh(u_{b'} - u_l - 2\eta)} \frac{1}{\sinh(u_{b'} - v_a)} \prod_{j=1\neq a}^N \sinh(u_{b'} - v_j - 2\eta) - \frac{1}{\sinh(u_{b'} - v_a)} \prod_{j=1\neq a}^N \sinh(u_{b'} - v_j + 2\eta) \tag{B7}$$

for $b' \neq b$

$$\tilde{T}^{(b)}_{ab'} = (-1)^N \prod_{l=1\neq b'}^N \sinh(u_{b'} - u_l + 2\eta) \prod_{j=1}^N \frac{\cosh(v_j - \eta)}{\cosh(u_j - \eta)} \frac{\sinh(2\eta)}{\cosh(v_a + \eta) \cosh(v_a - \eta)} \tag{B8}$$

for $b' = b$. Note that $\tilde{T}^{(b)}_{ab'} = T_{ab'}$ for $b' \neq b$.

Finally, the summation over b in Eq. (B6) can be evaluated using a general matrix identity: $\det \hat{T} + \sum_{b=1}^N \det \hat{\tilde{T}}^{(b)} = \det(\hat{T} + \hat{B})$, where $\hat{\tilde{T}}^{(b)}$ is obtained from the matrix $\hat{T}$ by substituting bth column from matrix $\hat{B}$. After constructing the matrix $\hat{B}$ out matrix elements $\tilde{T}^{(b)}_{ab}$ from Eq. (B8) and performing the summation over b in Eq. (B6), the form factor reads

$$\langle \mathbf{v}|\rho_1|\mathbf{u}\rangle = \prod_{j=1}^N \frac{\cosh(u_j - \eta)}{\cosh(u_j + \eta)} \frac{\sinh^N(2\eta)}{\prod_{j<i} \sinh(v_j - v_i) \prod_{j<i} \sinh(u_j - u_i)} \det \hat{K}, \tag{B9}$$

where the matrix elements of $\hat{K}$ are

$$\begin{aligned} K_{ab} = & \prod_{l=1\neq b}^N \frac{\sinh(u_b - u_l + 2\eta)}{\sinh(u_b - u_l - 2\eta)} \frac{1}{\sinh(u_b - v_a)} \prod_{j=1\neq a}^N \sinh(u_b - v_j - 2\eta) - \frac{1}{\sinh(u_b - v_a)} \prod_{j=1\neq a}^N \sinh(u_b - v_j + 2\eta) \\ & + (-1)^N \prod_{l=1\neq b}^N \sinh(u_b - u_l + 2\eta) \prod_{j=1}^N \frac{\cosh(v_j - \eta)}{\cosh(u_j - \eta)} \frac{\sinh(2\eta)}{\cosh(v_a + \eta) \cosh(v_a - \eta)}. \end{aligned} \tag{B10}$$

Now, we evaluate the long-wavelength limit for the result above. Applying the inversion mapping from the algebraic to the coordinate representation from Eq. (35) to the matrix elements in Eq. (B10) and expanding the result up to the leading order $k^u_j, k^v_j \ll 1$, we obtain

$$K_{ab} = (-1)^{N-1} 2mU((mU)^2 - 1)^{\frac{N-2}{2}} \frac{\sum_{j=1}^N k^v_j - \sum_{j=1}^N k^u_j - k^v_a + k^u_a}{k^u_b - k^v_a} + 2(mU + 1)((mU)^2 - 1)^{\frac{N-2}{2}}. \tag{B11}$$

Repeating the same procedure for the prefactor in Eq. (B9) and pulling a common scalar factor out of the matrix elements under the determinant, we obtain

$$\langle \mathbf{v}|\rho(0)|\mathbf{u}\rangle = (-1)^{N^2} 2^N \frac{(mU)^N}{(mU+1)^N} (mU-1)^{N^2} \det \hat{\mathcal{K}}, \tag{B12}$$

where the matrix elements of $\hat{\mathcal{K}}$ are

$$\mathcal{K}_{ab} = \frac{k_a^u - k_a^v - \Delta P}{k_b^u - k_a^v} + (-1)^{N-1} \frac{mU+1}{mU}, \tag{B13}$$

and $\Delta P = \sum_{j=1}^N k_j^u - \sum_{j=1}^N k_j^v$.

Evaluating the determinant, we obtain

$$\det \mathcal{K} = \frac{mU+1}{mU} \frac{(\Delta P)^N \prod_{i<j} \left(k_i^u - k_j^u\right) \prod_{i<j} \left(k_i^v - k_j^v\right)}{\prod_{i,j} \left(k_i^u - k_j^v\right)}. \tag{B14}$$

This formula can be proved by induction analogously to the proof of Eq. (43).

The form factor appearing in the dynamical structure factor in Eq. (10) is a modulus squared of Eq. (B12). Normalizing the initial and the finial states using Eq. (38) as $|\langle f|\rho(0)|0\rangle|^2 = |\langle \mathbf{k}^f|\rho(0)|\mathbf{k}^0\rangle|^2 \langle \mathbf{k}^f|\mathbf{k}^f\rangle^{-1} \langle \mathbf{k}^0|\mathbf{k}^0\rangle^{-1}$, we obtain

$$|\langle f|\rho(0)|0\rangle|^2 = \frac{(mU)^{2N-2}}{(mU+1)^{2N-2}} \frac{P_f^{2N} \prod_{i<j}^N \left(k_i^0 - k_j^0\right)^2 \prod_{i<j}^N \left(k_i^f - k_j^f\right)^2}{\left(\mathcal{L} - \frac{NmU}{1+mU}\right)^{2N} \prod_{i,j=1}^N \left(k_i^0 - k_j^f\right)^2}, \tag{B15}$$

where $P_0 = 0$ for the ground state. Equation (B15) is Eq. (47) in the main part of the text with $Z = mU/(mU+1)/(\mathcal{L} - NmU/(1+mU))$.

Note that when the final state becomes the ground state, $\mathbf{k}^f = \mathbf{k}^0$, Eq. (B15) is divergent. In this case, the matrix element is evaluated using only translational symmetry and the definition of the number of particles operator as

$$|\langle f|\rho(0)|0\rangle|^2 = \frac{N^2}{\mathcal{L}^2}, \tag{B16}$$

which also follows directly from Eqs. (B9) and (B10), by taking the limit $\mathbf{v} \to \mathbf{u}$.

[1] P. Nozières, *Theory of Interacting Fermi Systems* (Addison-Wesley, New York, 1997).

[2] T. Giamarchi, *Quantum Physics in One Dimension* (Clarendon press, Oxford, 2003).

[3] B. Roulet, J. Gavoret, and P. Nozières, Phys. Rev. **178**, 1072 (1969).

[4] P. Nozières, J. Gavoret, and B. Roulet, Phys. Rev. **178**, 1084 (1969).

[5] P. Nozières and C. T. de Dominicis, Phys. Rev. **178**, 1097 (1969).

[6] A. Imambekov, T. L. Schmidt, and L. I. Glazman, Rev. Mod. Phys. **84**, 1253 (2012).

[7] O. Tsyplyatyev, A. J. Schofield, Y. Jin, M. Moreno, W. K. Tan, C. J. B. Ford, J. P. Griffiths, I. Farrer, G. A. C. Jones, and D. A. Ritchie, Phys. Rev. Lett. **114**, 196401 (2015).

[8] N. A. Slavnov, Theor. Math. Phys. **79**, 502 (1989).

[9] O. Tsyplyatyev and A. J. Schofield, Phys. Rev. B **90**, 014309 (2014).

[10] G. Barak, H. Steinberg, L. N. Pfeiffer, K. W. West, L. Glazman, F. von Oppen, and A. Yacoby, Nat. Phys. **6**, 489 (2010).

[11] O. M. Auslaender, A. Yacoby, R. de Picciotto, K. W. Baldwin, L. N. Pfeiffer, and K. W. West, Science **295**, 825 (2002).

[12] Y. Jompol, C. J. B. Ford, J. P. Griffiths, I. Farrer, G. A. C. Jones, D. Anderson, D. A. Ritchie, T. W. Silk, and A. J. Schofield, Science **325**, 597 (2009).

[13] V. E. Korepin, N. M. Bogoliubov, and A. G. Izergin, *Quantum Inverse Scattering Methods and Correlation Functions* (Cambridge University Press, Cambridge, 1993).

[14] F. D. M. Haldane, Phys. Lett. A **81**, 153 (1981).

[15] J. von Delft and H. Schoeller, Ann. Phys. **7**, 225 (1998).

[16] A. A. Abrikosov, L. P. Gorkov, and I. E. Dzyaloshinski, *Methods of Quantum Field Theory in Statistical Physics* (Dover, New York, 1975).

[17] N. Kitanine, J. M. Maillet, and V. Tetras, Nucl. Phys. B **554**, 647 (1999).

[18] N. Kitanine and J. M. Maillet, Nucl. Phys. B **567**, 554 (2000).

[19] P. Jordan and E. Wigner, Zeitschrift fur Physik **47**, 631 (1928).

[20] J. M. Maillet and J. Sanchez de Santos, Amer. Math. Soc. Trause. **201**(2), 137 (2000), arXiv:q-alg/9612012.

[21] V. G. Drinfeld, Doklady Akademii Nauk SSSR **273**, 531 (1983) [Sov. Math. Dokl. **28**, 667 (1983)].

[22] F. Gohmann and V. E. Korepin, J. Phys. A **33**, 1199 (2000).

[23] K. Motegi and K. Sakai, Nucl. Phys. B **793**, 451 (2008).

[24] M. Gaudin, B. M. McCoy, and T. T. Wu, Phys. Rev. D **23**, 417 (1981).

[25] J.-S. Caux and J. M. Maillet, Phys. Rev. Lett. **95**, 077201 (2005).

[26] J.-S. Caux, R. Hagemans, and J. M. Maillet, J. Stat. Mech. (2005) P09003.

[27] J.-S. Caux, P. Calabrese, and N. Slavnov, J. Stat. Mech. (2007) P01008.

[28] R. G. Pereira, J. Sirker, J.-S. Caux, R. Hagemans, J. M. Maillet, S. R. White, and I. Affleck, Phys. Rev. Lett. **96**, 257202 (2006).
[29] R. G. Pereira, S. R. White, and I. Affleck, Phys. Rev. B **79**, 165113 (2009).
[30] J. Links, H.-Q. Zhou, R. H. McKenzie, and M. D. Gould, J. Phys. A **36**, R63 (2003).
[31] D. Biegel, M. Karbach, and G. Muller, Europhys. Lett. **59**, 882 (2002).
[32] D. Biegel, M. Karbach, and G. Muller, J. Phys. A **36**, 5361 (2003).
[33] J. Sato, M. Shiroishi, and M. Takahashi, J. Phys. Soc. Jpn. **73**, 3008 (2004).
[34] M. Pustilnik, M. Khodas, A. Kamenev, and L. I. Glazman, Phys. Rev. Lett. **96**, 196405 (2006),
[35] M. Khodas, M. Pustilnik, A. Kamenev, and L. I. Glazman, Phys. Rev. B **76**, 155402 (2007).
[36] A. Imambekov and L. I. Glazman, Phys. Rev. Lett. **102**, 126405 (2009).
[37] A. Imambekov and L. I. Glazman, Science **323**, 228 (2009).
[38] O. M. Auslaender, H. Steinberg, A. Yacoby, Y. Tserkovnyak, B. I. Halperin, K. W. Baldwin, L. N. Pfeiffer, and K. W. West, Science **308**, 88 (2005).
[39] Y. Tserkovnyak, B. I. Halperin, O. M. Auslaender, and A. Yacoby, Phys. Rev. B **68**, 125312 (2003).
[40] M. Khodas, M. Pustilnik, A. Kamenev, and L. I. Glazman, Phys. Rev. Lett. **99**, 110405 (2007).
[41] R. G. Pereira, J. Sirker, J.-S. Caux, R. Hagemans, J. M. Maillet, S. R. White, and I. Affleck, J. Stat. Mech. (2007) P08022.
[42] A. Imambekov and L. I. Glazman, Phys. Rev. Lett. **100**, 206805 (2008).
[43] A. Kamenev and L. I. Glazman, Phys. Rev. A **80**, 011603 (2009).
[44] T. L. Schmidt, A. Imambekov, and L. I. Glazman, Phys. Rev. Lett. **104**, 116403 (2010).
[45] T. L. Schmidt, A. Imambekov, and L. I. Glazman, Phys. Rev. B **82**, 245104 (2010).
[46] F. H. L. Essler, Phys. Rev. B **81**, 205120 (2010).
[47] O. Tsyplyatyev and A. J. Schofield, Phys. Rev. B **88**, 115142 (2013).
[48] A. Altland, C. H. W. Barnes, F. W. J. Hekking, and A. J. Schofield, Phys. Rev. Lett. **83**, 1203 (1999).
[49] B. Kardynal, C. H. W. Barnes, E. H. Linfield, D. A. Ritchie, K. M. Brown, G. A. C. Jones, and M. Pepper, Phys. Rev. Lett. **76**, 3802 (1996).
[50] https://www.repository.cam.ac.uk/handle/1810/254193.

nature COMMUNICATIONS

ARTICLE

Received 18 Nov 2015 | Accepted 2 Aug 2016 | Published 15 Sep 2016

DOI: 10.1038/ncomms12784 OPEN

Nonlinear spectra of spinons and holons in short GaAs quantum wires

M. Moreno[1], C.J.B. Ford[1], Y. Jin[1], J.P. Griffiths[1], I. Farrer[1,†], G.A.C. Jones[1], D.A. Ritchie[1], O. Tsyplyatyev[2,†] & A.J. Schofield[2]

One-dimensional electronic fluids are peculiar conducting systems, where the fundamental role of interactions leads to exotic, emergent phenomena, such as spin-charge (spinon-holon) separation. The distinct low-energy properties of these 1D metals are successfully described within the theory of linear Luttinger liquids, but the challenging task of describing their high-energy nonlinear properties has long remained elusive. Recently, novel theoretical approaches accounting for nonlinearity have been developed, yet the rich phenomenology that they predict remains barely explored experimentally. Here, we probe the nonlinear spectral characteristics of short GaAs quantum wires by tunnelling spectroscopy, using an advanced device consisting of 6000 wires. We find evidence for the existence of an inverted (spinon) shadow band in the main region of the particle sector, one of the central predictions of the new nonlinear theories. A (holon) band with reduced effective mass is clearly visible in the particle sector at high energies.

[1] Cavendish Laboratory, University of Cambridge, JJ Thomson Avenue, Cambridge CB3 0HE, UK. [2] School of Physics and Astronomy, University of Birmingham, Edgbaston, Birmingham B15 2TT, UK. † Present addresses: Department of Electronic & Electrical Engineering, University of Sheffield, Mappin Street, Sheffield S1 3JD, UK (I.F.); Institut für Theoretische Physik, Universität Frankfurt, Max-von-Laue Strasse 1, 60438 Frankfurt, Germany (O.T.). Correspondence and requests for materials should be addressed to M.M. (email: mmoreno.spain@gmail.com).

The electronic properties of one-dimensional (1D) electron systems are fundamentally different from those of their two-dimensional (2D) and three-dimensional (3D) counterparts, owing to the prominent role of interactions under 1D confinement[1–9]. Fermi-liquid theory, applicable to normal 2D and 3D electron systems, breaks down spectacularly in the 1D case, which is better described by the theory of Tomonaga–Luttinger liquids[10,11]. While elementary excitations of Fermi liquids behave as quasi-free fermions, those of interacting electrons in 1D systems are collective bosonic modes. Out of equilibrium, electrons confined to 1D lose their individual identity, separating into two collective excitation types (quantized waves of density): spin modes (spinons) that carry spin without charge, and charge modes (holons) that carry charge without spin[2,12]. Spinons and holons travel at different velocities, resulting in so-called spin-charge separation, revealed in photoemission and tunnelling experiments[12–15]. The spectral function $A(\hbar\mathbf{k}, \hbar\omega)$, describing the probability for an electron with momentum $\hbar\mathbf{k}$ and energy $\hbar\omega>0$ ($\hbar\omega<0$) to tunnel into (out of) the system, theoretically displays narrow Lorentzian singularities for normal 3D and 2D systems, whereas it displays wide asymmetric power-law singularities for 1D systems[12,16,17].

The theory of Tomonaga–Luttinger liquids, based on a linearization of the dispersion relation around the right ($+k_F^{1D}$) and left ($-k_F^{1D}$) Fermi points[10,11], has been successfully used for a long time to describe 1D electron systems in the limit of low energies but, in order to understand their behaviour at higher energies, that is, away from the Fermi points, the curvature of the dispersion relation has to be taken into account. Recently, a new nonlinear theory of 1D quantum fluids beyond the low-energy limit has been developed[18–28]. The new theory represents a giant advance towards full understanding of the behaviour of 1D electron systems, but many of its specific predictions remain barely explored experimentally.

Here, we report on the spectra of elementary excitations in short GaAs quantum wires, probed by momentum- and energy-resolved tunnelling spectroscopy, focusing on the nonlinear high-energy regime. We use a 1D–2D vertical tunnelling device with a large number of wires in parallel, to boost the wire signal and so maximize the chances to observe weak features of the wire spectral function. Our tunnelling conductance maps reveal, for the first time, the existence of an inverted (spinon) shadow band in the main region of the particle sector, symmetrically replicating the dispersion of the main spinon hole band, as anticipated by the nonlinear theory. They also reveal a (holon) band with reduced effective mass in the particle sector at high energies. Holons appear to be long-lived in the particle sector, but short-lived in the hole sector.

Results

Vertical tunnelling device. Our device (Fig. 1) consists of a double GaAs quantum-well structure separated by a thin AlGaAs barrier, and various surface gates, among them an array of 1 μm-long wire gates (WG) interconnected with air bridges (Fig. 2). We apply a negative voltage V_{wg} to the wire gates, which is strong enough to pinch off (fully deplete) the upper-well (UW) regions under the wire gates, but not strong enough to pinch off the lower-well (LW) regions under the wire gates. Hence, in the lower well, electrons can move under the wire gates, but in the upper well they cannot. Electrons in the upper well are laterally confined to a network of narrow parallel channels (W regions in Fig. 1c) so-called wires, and perpendicular wide trenches (La, Lb, Lc and Ld regions in Fig. 1c, jointly denoted L) so-called leads. In the UW-wire regions, electrons are strongly confined to a narrow width, thus becoming 1D. In contrast, in the UW-lead regions, no dimension is very narrow, and so electrons remain 2D. In the lower well, electrons are not laterally confined, and so their dimensionality is 2D. The quantum wells are separately contacted using a surface-gate depletion technique (see Methods section for details). A fixed ac voltage $V_{ac}=50\,\mu V$ and a variable dc-bias V_{dc} are applied between them. The bias is applied to the lower well, while the upper well is grounded. The current I, injected through one of the quantum wells, is forced to tunnel through the barrier that separates them, before leaving the device through the other quantum well. The differential tunnelling conductance $G=dI/dV_{ac}$, in a variable in-plane magnetic field B perpendicular to the wires, is measured at $\sim$57 mK lattice temperature (higher electron temperature) in a dilution refrigerator, using standard lock-in techniques. The W and L regions of the device contribute distinct signals in $G(B, V_{dc})$ maps. The W signal has 1D–2D nature, that is, it corresponds to tunnelling between the UW 1D wires and the LW 2D electron gas. The L signal has 2D–2D nature, that is, it corresponds to tunnelling between the UW 2D leads and the LW 2D electron gas.

Control of electron density in the wires. The electron density in the UW wires can be controlled by tuning the wire–gate voltage V_{wg}. This is shown in Figs 3 and 4. Figure 3 maps dG/dV_{wg} for conditions close to equilibrium ($V_{dc}\approx 0$). The map reveals the 1D wire subbands participating in 1D–2D tunnelling. The single-subband regime is achieved with V_{wg} in the range $-0.78\,V \lesssim V_{wg} \lesssim -0.69\,V$. For $V_{wg}> -0.69\,V$, more than one wire subband participates in 1D–2D tunnelling and, for $V_{wg}< -0.78\,V$, the wires are completely depleted of carriers. Figure 3 shows the magnetic-field values B_W^-, B_W^+, $-B_L^-$ and B_L^+, at which tunnelling resonances cross the $V_{dc}=0$ axis in $G(B, V_{dc})$ maps (for example Fig. 5), as a function of the wire–gate voltage. There are two sets of crossing values. One, $\pm B_W^{\pm}$, corresponds to tunnelling in the W regions of the device, and another, $\pm B_L^{\pm}$, to tunnelling in the L regions. Note that $B_W^{\pm}$ denote the values corresponding to the first UW wire subband. The crossing values are related to the Fermi-wavevector components along the wire direction as follows:

$$B_W^{\pm} = \hbar\left(k_F^{LW,W} \pm k_F^{1D}\right)/(ed) \quad (1)$$

$$B_L^{\pm} = \hbar\left(k_F^{LW,L} \pm k_F^{UW,L}\right)/(ed). \quad (2)$$

Here, $\hbar k_F^{1D}$ ($\hbar k_F^{LW,W}$) is the Fermi-wavevector component in the W regions of the upper well (lower well), $\hbar k_F^{UW,L}$ ($\hbar k_F^{LW,L}$) is the Fermi-wavevector component in the L regions of the upper well (lower well), d is the distance between the centres of the UW and LW wavefunctions, and $-e$ is the electron charge. It happens that $k_F^{1D}<k_F^{LW,W}\approx k_F^{LW,L}<k_F^{UW,L}$, and so $B_W^->0$ and $B_L^-<0$. The Fermi wavenumber k_F^{1D} (k_F^{2D}) in a 1D (2D) system is related to its equilibrium 1D (2D) electron density n_{1D} (n_{2D}) as follows:

$$n_{1D} = 2k_F^{1D}/\pi \quad (3)$$

$$n_{2D} = (k_F^{2D})^2/(2\pi). \quad (4)$$

Hence, the equilibrium electron densities in the upper and lower wells, for the wire (W) and lead (L) regions of the device, can be estimated from the values of $B_W^{\pm}$ and $B_L^{\pm}$ in Fig. 3. These are shown in Fig. 4. The wire gates efficiently tune electron density in the wire (W) regions of the upper well (Fig. 4a), but have little influence on densities in the lower well and in the lead (L) regions of the upper well (Fig. 4b). Note that the LW density in the W regions is only slightly smaller than that in the L regions (Fig. 4b), and notably higher than the UW density in the W regions (Fig. 4a).

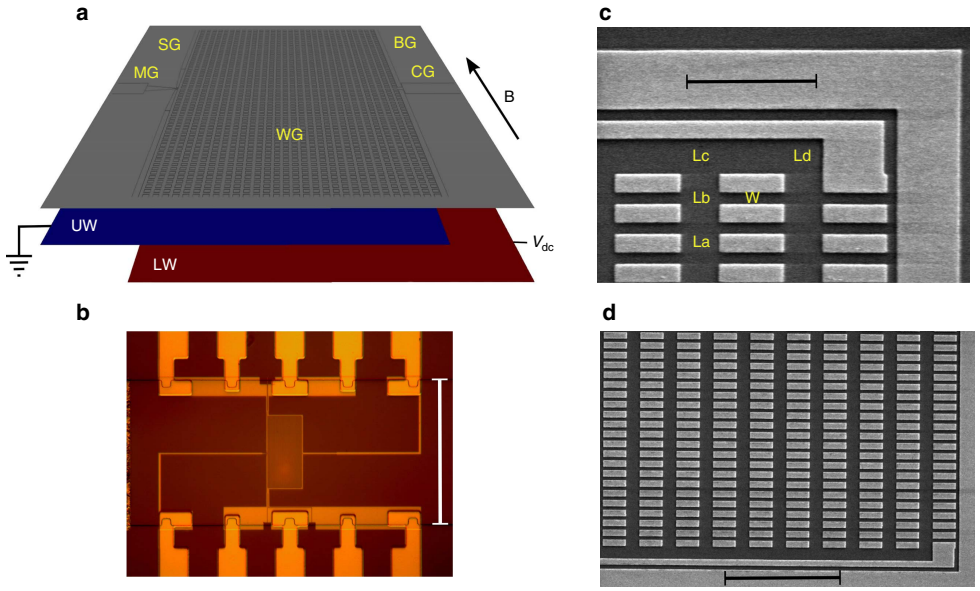

Figure 1 | Tunnelling device. (**a**) Schematic of the tunnelling device. It consists of a double quantum-well structure and various surface gates: split (SG), mid-line (MG), bar (BG) and cut-off (CG) gates—used to define the experimental area and to set-up tunnelling conditions—and a 30×200 array of parallel 1 μm-long air-bridged wire gates—used to define the quantum wires in the upper well. A dc-bias V_{dc} is applied to the lower well (LW), while the upper well (UW) is grounded. An in-plane magnetic field B is applied perpendicular to the long side of the wire gates. (**b**) Optical micrograph of the surface gates, fabricated on a Hall bar 200 μm-wide (white scale bar). (**c**,**d**) Scanning electron microscopy (SEM) micrographs of the upper-right (**c**) and lower-right (**d**) corners of the experimental area (device surface) before bridge fabrication. In **c** the black scale bar is 2 μm-long, and in **d** it is 5 μm-long. Dark grey corresponds to (oxidized) semiconductor areas, and bright grey to metallic gates. Electron fluids lie in the (buried) upper and lower wells. In the lower well, electrons are not laterally confined; they can move under the wire gates. In the upper well, electrons cannot move under the wire gates; they are confined to a network of narrow wires (W regions in **c**) and wide leads (La, Lb, Lc and Ld regions in **c**, jointly denoted L). UW electrons have 1D character in W regions, and 2D character in L regions. LW electrons have 2D character.

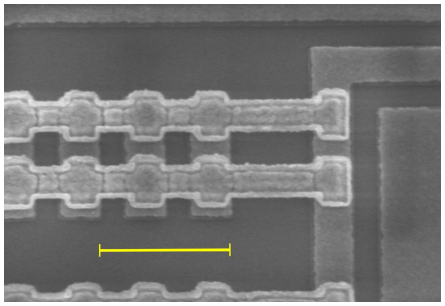

Figure 2 | Air bridges. Scanning electron microscopy (SEM) micrograph of a device's surface region, showing air-bridge interconnections between wire gates. Dark grey corresponds to (oxidized) semiconductor areas, and bright grey to metallic gates. The yellow scale bar is 1 μm-long.

Regime of a single 1D wire subband filled. The rate of electron tunnelling between the upper and lower wells depends on the overlap between the respective spectral functions, which can be varied by tuning the magnetic field and the dc-bias. The magnetic field B and the dc-bias V_{dc} shift the UW and LW spectral functions relative to each other, in the momentum and energy directions, by $\hbar\Delta k = eBd$ and $\hbar\Delta\omega = eV_{dc}$, respectively. Hence, by mapping out the tunnelling conductance $G(B, V_{dc})$, the spectral characteristics of the UW wires, UW leads and lower well are probed. Figure 5 shows a map corresponding to the single-subband regime ($V_{wg} = -0.69$ V). It displays quasi-parabolic resonances, corresponding to tunnelling from ground states of the source (spectrometer) to excited states of the drain (probe) occurring with conservation of energy and momentum, that is, the tunnelling condition

$$\varepsilon_{UW}(k-\Delta k) = \varepsilon_{LW}(k) - eV_{dc} \qquad (5)$$

is satisfied, with either $|k| = k_F^{LW}$ or $|k-\Delta k| = k_F^{UW}$, where k_F^{LW} (k_F^{UW}) is the Fermi wavenumber of the lower well (upper well) in the wire or lead regions of the device. Here, $\varepsilon_{UW}(k)$ and $\varepsilon_{LW}(k)$ are the dispersions of the elementary excitations in the upper and lower wells, respectively, in the wire or lead regions. The map reflects tunnelling events occurring between ground states of the upper well and excited states of the lower well, and between ground states of the lower well and excited states of the upper well. The wire (W) and lead (L) regions of the device contribute distinct signals. The solid (dashed) green lines in Fig. 5 mark resonances corresponding to tunnelling in W (L) regions, from UW ground states $\varepsilon_{UW}(\pm k_F^{UW})$ to LW states; they reveal the LW dispersion in W (L) regions of the device. The dash-dotted green lines mark resonances corresponding to tunnelling in L regions from LW ground states $\varepsilon_{LW}(\pm k_F^{LW,L})$ to UW states; they reveal the UW-lead dispersion. Most importantly here, the resonances marked by the black and white arrows correspond to tunnelling in W regions, from LW ground states $\varepsilon_{LW}(\pm k_F^{LW,W})$ to UW-wire states. They reveal 1D UW-wire dispersions: a holon band in the particle sector (h+), and a spinon band in the hole sector (s−), as elucidated below. Remarkably, an extra wire band (s+), symmetric of s−, is also observed in the wires' particle sector.

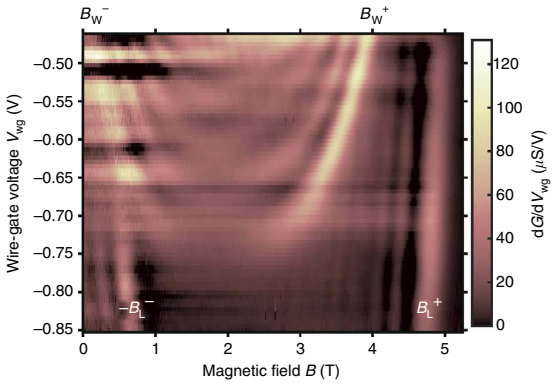

Figure 3 | 1D wire subbands participating in 1D–2D tunnelling. The derivative of the tunnelling conductance G, with respect to the wire-gate voltage V_{wg}, is plotted as a function of V_{wg} and in-plane magnetic field B perpendicular to the wires, for conditions close to equilibrium ($V_{dc} \approx 0$). Each quasi-parabolic resonance corresponds to one of the 1D wire subbands. The centres of the tunnelling resonances approximately correspond to the inflection points in the colour contrast, in going upwards from bright to dark. The magnetic field values B_W^-, B_W^+, $-B_L^-$ and B_L^+, at which tunnelling resonances cross the $V_{dc} = 0$ axis in $G(B, V_{dc})$ maps, are indicated. B_W^- and B_W^+ correspond to tunnelling in W (wire) regions of the device. $-B_L^-$ and B_L^+ correspond to tunnelling in L (lead) regions.

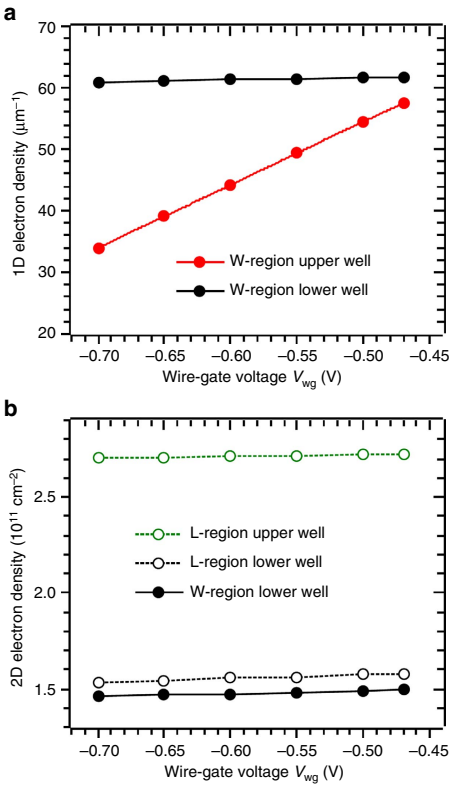

Figure 4 | Equilibrium electron densities in the upper and lower wells. (**a**) 1D and (**b**) 2D electron densities in the upper (red and green lines and symbols) and lower (black lines and symbols) wells, for the wire (W, solid lines and symbols) and lead (L, dashed lines and open symbols) regions of the device, as a function of the wire-gate voltage V_{wg}, estimated from the measured magnetic field values $B_{\bar{W}}$, B_W^+, $-B_L^-$ and B_L^+. Note that electrons are not laterally confined in the lower well, and so the W-region lower-well density that has physical meaning is the 2D-like one, shown in **b**. A 1D-like W-region lower-well density is shown in **a** just for comparison with the 1D-like density corresponding to the upper-well wires.

Note that the particle and hole sectors for the upper well are inverted relative to those for the lower well. The width of 1D bands in Fig. 5 is to a large extent associated to intrinsic physical effects. The width parallel to the magnetic-field axis correlates to momentum uncertainty, which (according to the Heisenberg's principle) is inversely proportional to the wire length. Wire shortness is thus a cause of resonance broadening. 1D bands are also broad parallelly to the dc-bias axis, because of the power-law (slow-decaying) shape of 1D singularities. Tunnelling maps are symmetric with respect to the sign of the magnetic field. Note, however, that the map in Fig. 5 is not symmetric with respect to the sign of the dc-bias. The dispersions of the s$-$ and s$+$ bands are symmetric, but this is just a local symmetry. The map does not exhibit general symmetry with respect to V_{dc}. This indicates that potentials are different in the upper and lower layers. Note that resonances in the map of Fig. 5 do not cross the $V_{dc} = 0$ axis at $B = 0$. That is, $B_{W,L}^- \neq 0$. This indicates that equilibrium electron densities, and Fermi wavenumbers, are different in the upper and lower layers.

Regime of three 1D wire subbands filled. Maps corresponding to the regime of three 1D subbands filled ($V_{wg} = -0.55$ V) are shown in Fig. 6. To better discriminate the location of resonances, the derivatives dG/dV_{dc} and dG/dB are plotted. Mapping of dG/dB (dG/dV_{dc}) emphasizes conductance modulations as a function of momentum (excitation energy). In Fig. 6, tunnelling resonances correspond to peaks of enhanced conductance, across which colour contrast changes quite abruptly. These peaks define quasi-parabolic lines on the maps (see the guide-to-the-eye lines drawn). Note that valleys, with colour contrast sequence opposite to that of peaks, do not correspond to resonances, but to regions of low conductance. The resonances marked by the green lines in Fig. 6a,b have the same meanings as in Fig. 5. Most importantly here, the black lines mark 1D UW-wire bands. The dashed-black line drawn in Fig. 6a,b for $V_{dc} > 0$ (lower half of the plots) marks the (first) spinon hole subband (s$-$), best discriminated in Fig. 6a,c as a line with red/blue contrast. Remarkably, a band with symmetric (inverted) dispersion is seen in the particle sector (dashed-black line for $V_{dc} < 0$, upper half of the plots), as in the single-subband regime (s$+$). The inverted band is best discriminated in Fig. 6b,d as a line with red/white contrast. The (first) holon subband (h$+$, marked by the solid-black line) appears well discriminated in the particle sector ($V_{dc} < 0$) at high energies, but hardly discernible in the hole sector ($V_{dc} > 0$). In addition, Fig. 6b,d reveals quasi-horizontal features. Similar states are seen in the regime of fully depleted wires. The quasi-horizontal features seen in Fig. 6b,d possibly are superpositions of contributions from (i) the bottoms of the second and third UW wire subbands, and from (ii) localized states[29–31] likely formed at intersection and/or bending points of the UW leads (Lb, Lc and/or Ld regions in Fig. 1c). Momentum-conserving resonances in Figs 5 and 6 (green and black lines) are seen not to be perfectly symmetric in their right and left sides, as opposed to the symmetric dispersions to which they correspond. The small asymmetry is known to be caused by capacitance effects[32], for which we account on the basis of a simple model previously used[15] (see Methods section for details).

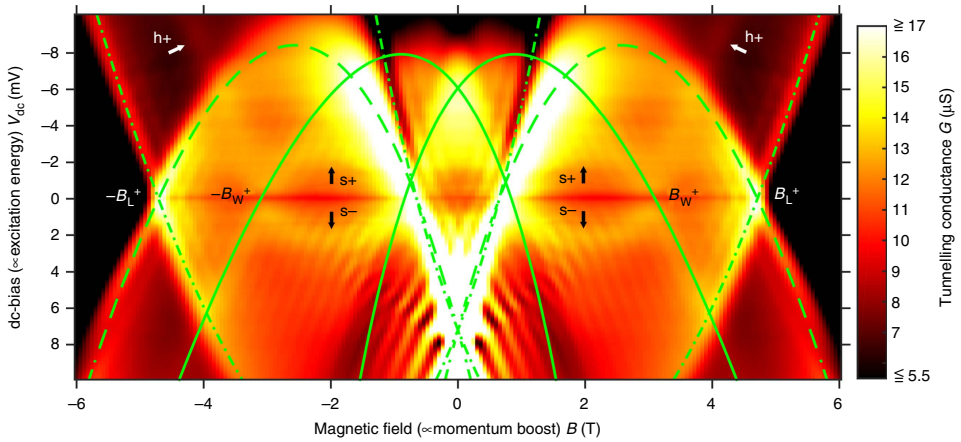

Figure 5 | Regime of a single 1D wire subband filled. The tunnelling conductance G is plotted as a function of the dc-bias V_{dc} and in-plane magnetic field B perpendicular to the wires, for the regime of a single 1D subband filled, achieved by setting the wire-gate voltage to $V_{wg} = -0.69$ V. The electron density in the wires is $n_{1D} \cong 35\,\mu m^{-1}$. The solid (dashed) green lines mark resonances corresponding to tunnelling between upper-well wire W (lead L) ground states and lower-well states; they reveal the dispersion of the elementary excitations in the 2D lower well, in the wire (lead) regions of the device. The dash-dotted green lines mark resonances corresponding to tunnelling between LW ground states and UW lead states; they reveal the dispersion of the elementary excitations in the 2D UW leads. The resonances marked by the black and white arrows correspond to tunnelling from LW ground states to UW wire states; they reveal dispersions of elementary excitations in the 1D UW wires: a holon band in the particle sector (h+), and spinon bands in the hole (s−) and particle (s+) sectors. The labels $\pm B_{W,L}^{+}$ indicate specific magnetic field values at which W and L tunnelling resonances cross the $V_{dc} = 0$ axis.

Conductance oscillations. When tunnelling occurs through a barrier of finite (short) length l in the in-plane direction perpendicular to the magnetic field, momentum is not strictly conserved in tunnelling and, as a consequence, the tunnelling conductance exhibits oscillations[32–35]. The maps in Figs 5 and 6 exhibit oscillations of this kind (diagonal short-period conductance oscillations), associated to tunnelling in (central or peripheral) La regions of the device (see Fig. 1c). In these regions, the UW states are laterally confined under the action of the wire gates, in the in-plane direction perpendicular to the magnetic field. For square confinement, the magnetic-field period ΔB of tunnelling conductance oscillations has been shown[34,35] to be $\Delta B \approx \phi_0/(ld)$, where $\phi_0 = 2\pi\hbar/e$ is the quantum of flux. For soft confinement, the period of the oscillations has been shown[34,35] to be $\Delta B \approx \phi_0/(\Delta x\, d)$, where Δx is the distance between the classical turning points. In our device, La regions are nominally 0.6 μm-wide, corresponding to the gap between the wire gates. In the maps of Figs 5 and 6, the oscillation period is $\Delta B \approx 0.26$ T, which corresponds to a confinement width $\Delta x \approx 0.5$ μm. This is just a bit smaller than the gap between the wire gates, consistent with the small lateral depleting effect that the gates produce.

Band assignment. Within the linear theory of Luttinger liquids, the spectral function of repulsive spinful 1D fermions has power-law singularities at linear spinon and holon mass shells $\varepsilon_{s,c}^{LL}(k) = v_{s,c}^{F}\left(\pm k - k_F^{1D}\right)$ and at the inverted holon mass shell $-\varepsilon_c^{LL}(k) = -v_c^{F}\left(\pm k - k_F^{1D}\right)$ near the right (+) and left (−) Fermi points[22,23]. Spinons and holons travel at different velocities v_s^F and v_c^F, respectively ($v_s^F < v_c^F$). Within the nonlinear theory[22–24], the excitation with lowest possible energy for a given momentum (edge of support) is predicted to coincide, in the main $|k| < k_F^{1D}$ region of the hole sector ($\omega < 0$), with the spinon mass-shell $\varepsilon_s(k)$. In the main region of the particle sector ($\omega > 0$), the edge is predicted to coincide with the inverted spinon mass shell $-\varepsilon_s(k)$. For arbitrary k in the regions $(2j-1)k_F^{1D} < k < (2j+1)k_F^{1D}$ defined by integer j, the edge is predicted to coincide with periodic $2jk_F^{1D}$-shifts of the functions $\pm\varepsilon_s(k)$, see Fig. 1a in ref. 22. Holon singularities may exist at the holon mass shell $\varepsilon_c(k)$, as well as at $2jk_F^{1D}$-shifted holon lines. The leading nonlinear correction to the holon dispersion near the Fermi points is quadratic[23,24]:

$$\varepsilon_c(k) \approx v_c^F\hbar\left(\pm k - k_F^{1D}\right) + \frac{\hbar^2}{2m_c^*}\left(\pm k - k_F^{1D}\right)^2 = \frac{\hbar^2}{2m_c^*}\left[k^2 - \left(k_F^{1D}\right)^2\right], \quad (6)$$

whereas that to the spinon dispersion is cubic:

$$\varepsilon_s(k) \approx v_s^F\hbar\left(\pm k - k_F^{1D}\right) - \xi\left(\pm k - k_F^{1D}\right)^3. \quad (7)$$

Here, $m_c^* = \hbar k_F^{1D}/v_c^F$ is the holon effective mass, and ξ is a positive parameter. Note that the nonlinear corrections have opposite sign for holons and for spinons in the particle sector ($|k| > k_F^{1D}$), and same sign in the hole sector ($|k| < k_F^{1D}$). The precise shapes of the spinon and holon dispersions, away from the Fermi points, are generally unknown theoretically.

According to the nonlinear theory[22,23], states at the edge of support are spinon states (not holon states); spinon excitations are protected from decay, but holon excitations are subjected to decay. Hence, the resonance labelled s− in Fig. 5 (as well as that marked by the dashed-black line in the lower half of Fig. 6a,b) should correspond to the main spinon band. Consistent with the nonlinear theory, the symmetric inverted replica seen in the particle sector (s+ in Fig. 5, and the upper-half dashed-black-line resonance in Fig. 6a,b) appears to be its shadow (spinon) band. On the other hand, given its positive curvature (upwards bending), the resonance labelled h+ in Fig. 5 (as well as that marked by the solid-black line in the upper half of Fig. 6a,b) should correspond to a holon band. It cannot correspond to a spinon band, because the dispersion of spinons has opposite curvature in this sector (see Fig. 1a in ref. 22).

Spinon and holon effective masses. To extract quantitative information, we simulate the experimental holon dispersion

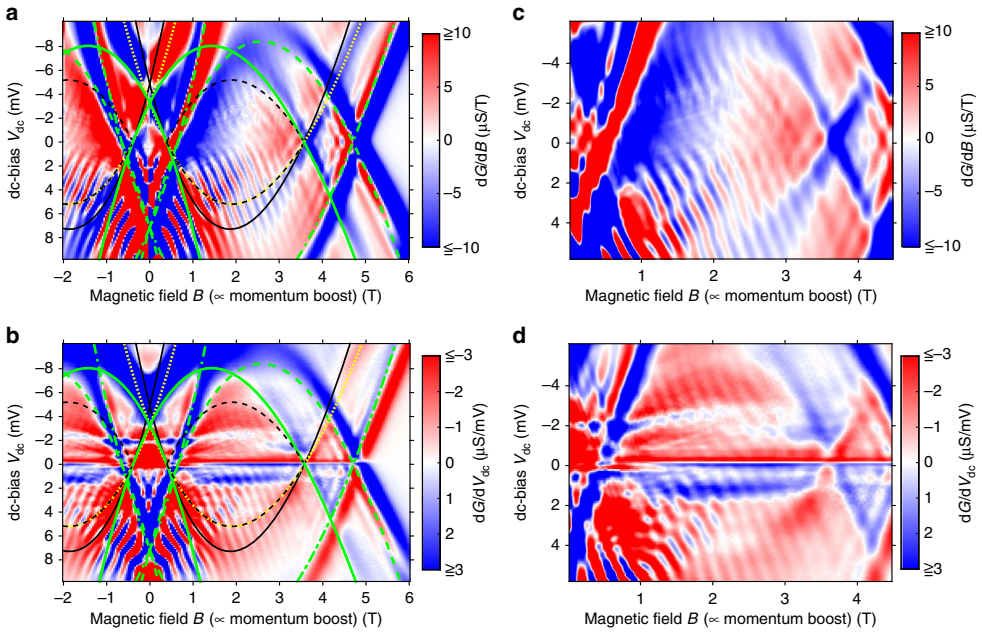

Figure 6 | Regime of three 1D wire subbands filled. The derivatives of the tunnelling conductance G, with respect to either B or V_{dc}, are plotted as a function of the dc-bias V_{dc} and in-plane magnetic field B perpendicular to the wires, for the regime of three 1D wire subbands filled, achieved by setting the wire-gate voltage to $V_{wg} = -0.55$ V. The electron density in the wires is $n_{1D} \cong 49\,\mu m^{-1}$. The resonances marked by the solid and dashed green lines reveal the dispersion of the elementary excitations in the 2D lower well, in the W (wire) and L (lead) regions of the device, respectively. The resonances marked by the dash-dotted green lines reveal the dispersion in the 2D upper-well leads. The resonances marked by the black lines reveal (first subband) dispersions for elementary excitations in the 1D upper-well wires, for spinons (dashed lines) and for holons (solid lines). (**a**,**b**) Wide dG/dB and dG/dV_{dc} maps. (**c**,**d**) High-resolution dG/dB and dG/dV_{dc} maps, zooming in on the magnetic-field region $B_W^- \leq B \leq B_W^+$, corresponding to the main wavenumber region $|k| \leq k_F^{1D}$ for the 1D upper-well wires.

(h+, solid-black lines) with a quadratic functional form (equation (6)). It has been shown[26] that the spinon dispersion in the nonlinear regime is approximately parabolic. Therefore, we simulate the spinon dispersion (s−, dashed-black lines) in the hole sector (lower half of the plots) of the main $|k| < k_F^{1D}$ region ($B_W^- < B < B_W^+$) with a quadratic functional form, analogous to that of holons, but with a different effective mass $m_s^* = \hbar k_F^{1D}/v_s^F$:

$$\varepsilon_s(k) \approx v_s^F \hbar \left(\pm k - k_F^{1D}\right) + \frac{\hbar^2}{2m_s^*}\left(\pm k - k_F^{1D}\right)^2 = \frac{\hbar^2}{2m_s^*}\left[k^2 - \left(k_F^{1D}\right)^2\right]. \quad (8)$$

We express the holon and spinon effective masses as $m_{c,s}^* = \tilde{K}_{c,s} m_{2D}^*$, where $\tilde{K}_{c,s}$ are phenomenological parameters, accounting for renormalization of the effective mass due to 1D confinement[26], and m_{2D}^* is the effective mass of the noninteracting electron-like quasiparticles in the parent UW Fermi liquid. Note that a change in the nature of the elementary excitations occurs upon imposing lateral 1D confinement, but not upon 2D confinement. $\tilde{K}_{c,s}$ thus account for mass renormalization in going from a 2D Fermi liquid to a 1D Luttinger liquid. The spinon dispersion is found to be characterized by an effective mass similar to that of noninteracting quasiparticles in the UW-lead and LW Fermi liquids, that is, $m_s^* = m_{2D}^*$, corresponding to $\tilde{K}_s = 1$. (See Methods section for details of simulations of the LW and UW-lead dispersions.) Note that the spinon momentum is bounded[23], and so the spinon quasi-parabolas (lower-half dashed-black lines in Fig. 6) do not continue beyond $B_W^- < B < B_W^+$ ($|k| < k_F^{1D}$), but theoretically replicate through shifts and inversions (see Fig. 1a in ref. 22). In contrast, the holon momentum is not bounded[23], and so the holon quasi-parabolas (solid-black lines in Fig. 6) theoretically extend from the particle sector $\omega > 0$ ($V_{dc} < 0$) into the hole sector $\omega < 0$ ($V_{dc} > 0$) without changing the sign of their curvature (see Fig. 1a in ref. 22). Fitting of the holon dispersion is carried out in the particle sector (upper half of the plots), where it is well discriminated. The holon dispersion is found to be characterized by an effective mass notably smaller than that of noninteracting quasiparticles in the UW-lead and LW Fermi liquids. The mass renormalization parameter is found to be $\tilde{K}_c = 0.65$ ($\tilde{K}_c = 0.75$) in the regime of one (three) subband(s) filled. This is consistent with the expected effect of repulsive interactions, for which the theoretical Luttinger-liquid parameter K_c is in the range $0 < K_c < 1$. The higher value of $\tilde{K}_c$ in the regime of three subbands filled is understood considering that the second and third subbands somewhat screen interactions in the first subband. Nevertheless, observation of the inverted spinon shadow band (s+), when more than one subband is filled (Fig. 6), indicates that the first 1D subband remains highly correlated even in the presence of screening by higher subbands. We emphasize that the wire bands seen in the hole sector (s− in Fig. 5, lower-half dashed-black lines in Fig. 6a,b) and in the particle sector (h+ in Fig. 5, upper-half solid-black lines in Fig. 6a,b) cannot be adequately described with a single parabola. A continuation of the lower-half dashed-black lines—dotted yellow lines in Fig. 6a,b—is clearly unsatisfactory in fitting the

resonance observed in the particle sector at high energies (upper half of the plots, $V_{dc} \ll 0$). The spinon (s−, lower-half dashed-black-line) and holon (h+, upper-half solid-black-line) bands are characterized by notably different effective masses.

Discussion

We finally comment on the physical meaning of the observed 1D bands in the context of the new nonlinear theory[22–24]. The injection of a spin-up (spin-down) electron into a wire leads to the creation (annihilation) of a spinon and the creation of a holon. If the energy of the incoming electron is $\hbar\omega = \varepsilon_s(k)$, the final state will contain a spinon carrying the whole-energy $\hbar\omega$, and a holon carrying no energy. Similarly, if the energy of the incoming electron is $\hbar\omega = \varepsilon_c(k)$, the final state will contain a holon with energy $\hbar\omega$, and a spinon with no energy. Spinon excitations are protected from decay by energy and momentum conservation laws. Therefore, the (spinon) edge singularity is predicted to be robust. Holon excitations are subjected to decay to some (not accurately known) extent, and so it is theoretically unclear whether holon singularities should be observable away from the Fermi points[23,24]. Here, the holon band appears experimentally well discriminated in the particle sector, but hardly discernible in the hole sector. That is, holon particles appear long-lived, but holon holes short-lived. Phenomenological theoretical expressions yield the j- and k-dependent exponents of the power-law singularities at the spinon and holon mass shells[22–24]. The spinon exponents in the particle sector are similar to those in the hole sector, except for different selection rules $m_{\pm}$. Hence, the (main region) spinon singularity is theoretically predicted to be a divergent one in the hole sector (thus easy to observe), and a convergent one in the particle sector (thus difficult to observe). This would explain why observation of the spinon shadow band in the particle sector of the main region, reported here, has been previously elusive. Our results indicate that this shadow band does exist, supporting the predictions of the new nonlinear theories[22–24]. They show that the shadow band has appreciable weight for short wires ($\sim$1 μm long), wire length appearing as a relevant parameter modulating the spectral weight of shadow bands for electronic (spinful) systems. Theoretical studies[27,28] indicate that the spectral weight of shadow bands for spinless systems increases strongly with decreasing wire length. Here, the experimental observation of the inverted spinon shadow band (s+) appears to be facilitated by (i) the wire shortness, (ii) the array design of our device that boosts the wire signal and (iii) the homogeneity of the lithography.

Methods

Experimental device. The vertical structure of the device, grown by molecular-beam epitaxy, comprises two 18 nm-wide GaAs quantum wells, a 14 nm-wide tunnel barrier in between, and spacer and Si-doped $Al_{0.33}Ga_{0.67}As$ layers at both sides. The structure terminates with a 10 nm-wide GaAs cap layer. The tunnel barrier is a $10 \times [(0.833\ nm)Al_{0.33}Ga_{0.67}As/(0.556\ nm)GaAs]$ superlattice. The lower (upper) spacer is 40 nm (20 nm) wide and the Si-doped layers (10^{18} donors cm^{-3}) are 40 nm wide. The electrical (surface) structure of the device was fabricated on a 200 μm-wide Hall bar (Fig. 1b). Electron-beam lithography was used to pattern surface gates, that is, split (SG), mid-line (MG), bar (BG) and cut-off (CG) gates (Fig. 1a)—used to define the experimental area and to set-up tunnelling conditions—and a 30×200 array of air-bridged wire gates (Fig. 1d and Fig. 2)—used to define the quantum wires in the upper well. The wire gates are 1 μm-long and 0.3 μm-wide. They are separated by 0.19 μm-wide gaps (W wire regions) in the transverse direction and by 0.6 μm-wide gaps (L lead regions) in the longitudinal direction (Fig. 1c). The device dimensions were chosen carefully to achieve minimal modulation of the LW carrier density by the negative wire–gate voltage.

Tunnelling set-up. The two quantum wells are separately contacted with AuGeNi Ohmic contacts by using a surface-gate depletion technique. At one side of the device (Fig. 1a), gate SG is negatively biased to pinch off both the upper and lower layers, while gate MG is positively biased to open a narrow conducting channel in the upper layer only. At the other side of the device, gates BG and CG are negatively biased to pinch off just the upper layer. Hence, the current injected through one of the Ohmic contacts is forced to tunnel between the upper and lower layers, before flowing out through the other Ohmic contact.

Modelling of the LW and UW-lead dispersions. The electron density in the lower well (UW leads) is $n_{LW} = 1.5 \times 10^{11}\ cm^{-2}$ ($n_{UW,L} = 2.7 \times 10^{11}\ cm^{-2}$), obtained from the crossing magnetic-field values $B_L^{\pm}$. For these densities, 2D electron systems are known to be Fermi liquids with effective mass renormalized by interactions[36,37]. We thus simulate the LW and UW-lead dispersions with the parabolic functional form

$$\varepsilon_{2D}(k) = \frac{\hbar^2}{2m^*_{2D}}\left[k^2 - \left(k_F^{2D}\right)^2\right], \tag{9}$$

characteristic of Fermi-liquid quasiparticles, where m^*_{2D} is the effective mass in the lower well or in the UW leads. Replacing the corresponding dispersions in equation (5), one obtains functions of the type

$$V_{dc}(B) = \pm\frac{ed^2}{2m^*_{2D}}B^2 + c_1 B + c_0 \tag{10}$$

that we use to simulate the tunnelling resonances corresponding to the LW (+) and UW-lead (−) dispersions. By setting $d = 32$ nm (nominal value), the LW and UW-lead dispersions are found to be well described by an effective mass $m^*_{2D} = 0.050m_0 = 0.75m_b$, somewhat smaller than the band mass of GaAs ($m_b = 0.067m_0$), where m_0 is the electron rest mass. This is consistent with previous measurements and theoretical predictions for quantum wells with similar densities[38–42]. If the bands were substantially bent across the quantum wells, the wavefunctions would be somewhat displaced relative to flat-band conditions, and the distance d (between the centres of the UW and LW wavefunctions) would somewhat differ from the distance between the centres of the quantum wells (32 nm). Equally good fits are obtained if we impose the effective mass to be equal to the band mass ($m^*_{2D} = m_b$) and allow for variation of d. The best fit is then achieved for $d = 37$ nm. We cannot determine the individual contributions of m^*_{2D} and d to the curvature of tunnelling resonances. Nevertheless, we note that the mass $m^*_{2D} = 0.050m_0$ is in very good agreement with the careful measurements carried out by Hayne *et al.*[38,39].

Modelling of capacitance effects. Tunnel transport between the upper and lower layers of the device, across its dielectric barrier, is affected by capacitance effects, which cause a small deformation of the observed dispersions. The finite capacitance of the device (C/A per unit area, C/L per unit length) leads to a small increase/reduction of the electron density $\pm\delta n_{2D/1D}$ at each side of the barrier ($e\delta n_{2D} = V_{dc}C/A$ for 2D systems, and $e\delta n_{1D} = V_{dc}C/L$ for 1D systems), and consequently to changes of the Fermi wavenumbers of the source and drain systems ($\pm\delta k_F^{2D} = \pm\pi\delta n_{2D}/k_F^{2D}$ for 2D systems, and $\pm\delta k_F^{1D} = \pm\pi\delta n_{1D}/2$ for 1D systems). To account for capacitance effects[15] in simulations of the measured resonances, we replace the Fermi wavenumbers, corresponding to zero capacitance, by modified ones

$$k_F^{2D\prime} = k_F^{2D} \pm \delta k_F^{2D} = k_F^{2D} \pm \frac{\pi V_{dc} C}{e k_F^{2D} A} \tag{11}$$

for 2D systems, and

$$k_F^{1D\prime} = k_F^{1D} \pm \delta k_F^{1D} = k_F^{1D} \pm \frac{\pi V_{dc} C}{2e L} \tag{12}$$

for 1D systems, in the expressions describing tunnelling conditions (equation (5)). Hence, dispersions $V_{dc}(B)$ initially symmetric become somewhat asymmetric. Satisfactory fits are achieved with capacitance values $C/A \approx 0.004\ F\,m^{-2}$, $C/L \approx 0.1\ nF\,m^{-1}$.

Data availability. Data associated with this work are available at the University of Cambridge data repository (http://dx.doi.org/10.17863/CAM.797; see ref. 43).

References

1. Voit, J. One-dimensional Fermi liquids. *Rep. Prog. Phys.* **58,** 977–1116 (1995).
2. Giamarchi, T. *Quantum Physics in One Dimension* (Oxford University Press, 2004).
3. Deshpande, V. V., Bockrath, M., Glazman, L. I. & Yacoby, A. Electron liquids and solids in one dimension. *Nature* **464,** 209–216 (2010).
4. Barak, G. *et al.* Interacting electrons in one dimension beyond the Luttinger-liquid limit. *Nat. Phys.* **6,** 489–493 (2010).
5. Blumenstein, C. *et al.* Atomically controlled quantum chains hosting a Tomonaga-Luttinger liquid. *Nat. Phys.* **7,** 776–780 (2011).
6. Wakeham, N. *et al.* Gross violation of the Wiedemann-Franz law in a quasi-one-dimensional conductor. *Nat. Commun.* **2,** 396 (2011).
7. Laroche, D., Gervais, G., Lilly, M. P. & Reno, J. L. Positive and negative Coulomb drag in vertically integrated one-dimensional quantum wires. *Nat. Nanotechnol.* **6,** 793–797 (2011).

8. Laroche, D., Gervais, G., Lilly, M. P. & Reno, J. L. 1D-1D Coulomb drag signature of a Luttinger liquid. *Science* **343,** 631–634 (2014).
9. Kamata, H., Kumada, N., Hashisaka, M., Muraki, K. & Fujisawa, T. Fractionalized wave packets from an artificial Tomonaga–Luttinger liquid. *Nat. Nanotechnol.* **9,** 177–181 (2014).
10. Haldane, F. D. M. 'Luttinger liquid theory' of one-dimensional quantum fluids. I. Properties of the Luttinger model and their extension to the general 1D interacting spinless Fermi gas. *J. Phys. C: Solid State Phys.* **14,** 2585–2609 (1981).
11. Haldane, F. D. M. Effective harmonic-fluid approach to low-energy properties of one-dimensional quantum fluids. *Phys. Rev. Lett.* **47,** 1840–1843 (1981).
12. Voit, J. Charge-spin separation and the spectral properties of Luttinger liquids. *Phys. Rev. B* **47,** 6740–6743 (1993).
13. Auslaender, O. M. *et al.* Spin-charge separation and localization in one dimension. *Science* **308,** 88–92 (2005).
14. Kim, B. J. *et al.* Distinct spinon and holon dispersions in photoemission spectral functions from one-dimensional $SrCuO_2$. *Nat. Phys.* **2,** 397–401 (2006).
15. Jompol, Y. *et al.* Probing spin-charge separation in a Tomonaga-Luttinger liquid. *Science* **325,** 597–601 (2009).
16. Meden, V. & Schönhammer, K. Spectral functions for the Tomonaga-Luttinger model. *Phys. Rev. B* **46,** 15753–15760 (1992).
17. Gogolin, A. O., Nersesyan, A. A. & Tsvelik, A. M. *Bosonization and Strongly Correlated Systems* (Cambridge University Press, 2004).
18. Pustilnik, M., Khodas, M., Kamenev, A. & Glazman, L. I. Dynamic response of one-dimensional interacting fermions. *Phys. Rev. Lett.* **96,** 196405 (2006).
19. Imambekov, A. & Glazman, L. I. Universal theory of nonlinear Luttinger liquids. *Science* **323,** 228–231 (2009).
20. Imambekov, A. & Glazman, L. I. Phenomenology of one-dimensional quantum liquids beyond the low-energy limit. *Phys. Rev. Lett.* **102,** 126405 (2009).
21. Pereira, R. G. & Sela, E. Spin-charge coupling in quantum wires at zero magnetic field. *Phys. Rev. B* **82,** 115324 (2010).
22. Schmidt, T. L., Imambekov, A. & Glazman, L. I. Fate of 1D spin-charge separation away from Fermi points. *Phys. Rev. Lett.* **104,** 116403 (2010).
23. Schmidt, T. L., Imambekov, A. & Glazman, L. I. Spin-charge separation in one-dimensional fermion systems beyond Luttinger liquid theory. *Phys. Rev. B* **82,** 245104 (2010).
24. Imambekov, A., Schmidt, T. L. & Glazman, L. I. One-dimensional quantum liquids: beyond the Luttinger liquid paradigm. *Rev. Mod. Phys.* **84,** 1253 (2012).
25. Tsyplyatyev, O. & Schofield, A. J. Luttinger parameters of interacting fermions in one dimension at high energies. *Phys. Rev. B* **88,** 115142 (2013).
26. Tsyplyatyev, O. & Schofield, A. J. Spectral-edge mode in interacting one-dimensional systems. *Phys. Rev. B* **90,** 014309 (2014).
27. Tsyplyatyev, O. *et al.* Hierarchy of modes in an interacting one-dimensional system. *Phys. Rev. Lett.* **114,** 196401 (2015).
28. Tsyplyatyev, O. *et al.* Nature of the many-body excitations in a quantum wire: theory and experiment. *Phys. Rev. B* **93,** 075147 (2016).
29. Schult, R. L., Ravenhall, D. G. & Wyld, H. W. Quantum bound states in a classically unbound system of crossed wires. *Phys. Rev. B* **39,** 5476–5479 (1989).
30. Ji, Z.-L. & Berggren, K.-F. Quantum bound states in narrow ballistic channels with intersections. *Phys. Rev. B* **45,** 6652–6658 (1992).
31. Chen, Y. P., Xie, Y. E. & Yan, X. H. The evolution of bound states in quantum wires under potential modulation. *Physica B* **373,** 253–257 (2006).
32. Boese, D., Governale, M., Rosch, A. & Zülicke, U. Mesoscopic effects in tunneling between parallel quantum wires. *Phys. Rev. B* **64,** 085315 (2001).
33. Governale, M., Grifoni, M. & Schön, G. Tunneling spectroscopy calculations of a Luttinger wire. *Phys. Rev. B* **62,** 15996–16000 (2000).
34. Tserkovnyak, Y., Halperin, B. I., Auslaender, O. M. & Yacoby, A. Finite-size effects in tunneling between parallel quantum wires. *Phys. Rev. Lett.* **89,** 136805 (2002).
35. Tserkovnyak, Y., Halperin, B. I., Auslaender, O. M. & Yacoby, A. Interference and zero-bias anomaly in tunneling between Luttinger-liquid wires. *Phys. Rev. B* **68,** 125312 (2003).
36. Zhang, Y. & Das Sarma, S. Density-dependent spin susceptibility and effective mass in interacting quasi-two-dimensional electron systems. *Phys. Rev. B* **72,** 075308 (2005).
37. Ando, T., Fowler, A. B. & Stern, F. Electronic properties of two-dimensional systems. *Rev. Mod. Phys.* **54,** 437–672 (1982).
38. Hayne, M., Usher, A., Harris, J. J. & Foxon, C. T. Exchange enhancement of the Landau-level separation for two-dimensional electrons in $GaAs/Ga_xAl_{1-x}As$ heterojunctions. *Phys. Rev. B* **46,** 9515–9519 (1992).
39. Coleridge, P. T., Hayne, M., Zawadzki, P. & Sachrajda, A. S. Effective masses in high-mobility 2D electron gas structures. *Surf. Sci.* **361–362,** 560–563 (1996).
40. Tan, Y.-W. *et al.* Measurements of the density-dependent many-body electron mass in two dimensional GaAs/AlGaAs heterostructures. *Phys. Rev. Lett.* **94,** 016405 (2005).
41. Hatke, A. T. *et al.* Evidence for effective mass reduction in GaAs/AlGaAs quantum wells. *Phys. Rev. B* **87,** 161307(R) (2013).
42. Kwon, Y., Ceperley, D. M. & Martin, R. M. Quantum Monte Carlo calculation of the Fermi-liquid parameters in the two-dimensional electron gas. *Phys. Rev. B* **50,** 1684–1694 (1994).
43. Moreno, M. *et al. Research data supporting 'Nonlinear spectra of spinons and holons in short GaAs quantum wires' [dataset]* (University of Cambridge data repository, 2016).

Acknowledgements

This work was supported by the UK EPSRC [Grant Nos. EP/J01690X/1 and EP/J016888/1]. M.M. thanks J. Waldie for her assistance with device fabrication and transport measurements, and P. See for his advice on device fabrication.

Author contributions

Project planning: C.J.B.F. and A.J.S.; MBE growth: I.F. and D.A.R.; optical and electron-beam lithography: M.M. and J.P.G., with assistance from Y.J. and G.A.C.J.; transport measurements: M.M., C.J.B.F. and Y.J.; analysis of results and theoretical interpretation: M.M., C.J.B.F., O.T. and A.J.S.; manuscript preparation: M.M. with contributions from C.J.B.F.

Additional information

Competing financial interests: The authors declare no competing financial interests.

Reprints and permission information is available online at http://npg.nature.com/reprintsandpermissions/

How to cite this article: Moreno, M. *et al.* Nonlinear spectra of spinons and holons in short GaAs quantum wires. *Nat. Commun.* 7:12784 doi: 10.1038/ncomms12784 (2016).

PHYSICAL REVIEW B **95**, 045120 (2017)

Many-body theory of magnetoelasticity in one dimension

O. Tsyplyatyev and P. Kopietz
Institut für Theoretische Physik, Goethe-Universität Frankfurt, Max-von-Laue Strasse 1, 60438 Frankfurt am Main, Germany

Y. Tsui, B. Wolf, P. T. Cong,[*] N. van Well,[†] F. Ritter, C. Krellner, W. Aßmus, and M. Lang
Physikalisches Institut, Goethe-Universität Frankfurt, Max-von-Laue-Strasse 1, 60438 Frankfurt am Main, Germany
(Received 13 August 2016; revised manuscript received 23 December 2016; published 17 January 2017)

We construct a many-body theory of magnetoelasticity in one dimension and show that the dynamical correlation functions of the quantum magnet, connecting the spins with phonons, involve all energy scales. Accounting for all magnetic states nonperturbatively via the exact diagonalization techniques of Bethe ansatz, we find that the renormalization of the phonon velocity is a nonmonotonous function of the external magnetic field and identify a new mechanism for attenuation of phonons—via hybridization with the continuum of excitations at high energy. We conduct ultrasonic measurements on a high-quality single crystal of the frustrated spin-1/2 Heisenberg antiferromagnet Cs_2CuCl_4 in its nearly one-dimensional regime and confirm the theoretical predictions, demonstrating that ultrasound can be used as a powerful probe of strong correlations in one dimension.

DOI: 10.1103/PhysRevB.95.045120

I. INTRODUCTION

Magnetic insulators present a good example of interacting quantum systems where phonons can serve as an intrinsic probe of the strongly-correlated spins [1]. The first microscopic theory of magnetoelasticity was developed at finite temperatures [2,3], where the static and the dynamic correlation functions of the spins were shown to couple to phonons with the same strength in the perturbative regime. At low temperature, assuming existence of a spin-liquid regime in two- and three-dimensional Heisenberg antiferromagnets, phonons were shown to measure the mass and lifetime of the spin-liquid quasiparticles [4,5]. In one dimension (1D)—where interacting magnons form a spin-Luttinger liquid at low energy—the theory remains largely unexplored. At the same time such 1D systems are readily accessible in experiments on Cs_2CuCl_4 [6,7], $CsNiCl_3$ [8], $KCuF_3$ [9], and a metal organic coordination polymer Cu(II)-2,5-bis(pyrazol-1-yl)-1,4-dihydroxybenzene [10].

In this paper we construct a microscopic theory of magnetoelasticity in 1D using the diagonalization methods of Bethe ansatz [11]. We derive the matrix elements for the four-point correlation function that couples the strongly-correlated spins to phonons dynamically and show that Luttinger liquid at low energy contributes comparably with the high-energy excitations that we are able to account for due to the hierarchy of modes [12–14]. The contribution of the static correlation function to the renormalization of the sound velocity is parametrically larger than the dynamical correlation functions. The resonant decay of phonons in the many-body spin continuum vanishes very fast, as the fourth power of the length in large systems. However we identify another mechanism, hybridization with the excitations at high energy via the dynamical correlation function, that remains finite in the thermodynamic limit. This work advances the many-body diagonalization tools in 1D [15–19] in to the field of magnetoelasticity, which is beginning to receive attention also in spintronics [20–23].

To test our theory we conduct ultrasonic measurements on a high-quality single crystal of Cs_2CuCl_4 in its nearly 1D regime, i.e., at temperatures of 0.7–2.1 K and magnetic fields up to 9 T [24,25]. The observed dependencies of the sound velocity and attenuation of the sound wave on the magnetic field agree well with all theoretical predictions. We find that the magnetic-field dependent part of the attenuation is governed by the hybridization mechanism. Our results demonstrate that ultrasonic investigations, besides neutron-scattering experiments [6,9,26], can be used as a powerful probe of correlation functions of the many-body system in 1D in magnetic insulators, just as tunneling spectroscopy in semiconductor heterostructures [27,28].

The paper is organized as follows. Section II contains the definition of the magnetostrictive interactions between the Heisenberg model and the phonon models in one dimension and the diagonalization of the isolated Heisenberg model by means of Bethe ansatz. In Sec. III we study renormalization of sound velocity by evaluating microscopically the dynamical correlation function of the spins that couples to the phonons (Sec. III A) and by analyzing it using the hierarchy of interacting modes (Sec. III B). In Sec. IV we consider different mechanisms of attenuation of phonons. In Sec. V we conduct an ultrasound experiment on Cs_2CuCl_4 in its nearly one-dimensional regime and confirm the theoretical predictions. In Appendix A we derive the quantization equation for the pi-pairs' solutions of Bethe equations in the XY limit. In Appendix B we quote the normalization factor of the Bethe states together with the algebraic Bethe ansatz method. In Appendix C we derive the matrix element of the spin operator needed for the magnetostrictive interaction.

II. MODEL

Theoretically, we consider phonons interacting with 1/2 spins on a 1D lattice of length L via a magnetostrictive

[*]Present address: Dresden High Magnetic Field Laboratory, Helmholtz-Zentrum Dresden-Rossendorf, D-01314 Dresden, Germany.

[†]Present address: Laboratory for Neutron Scattering and Imaging, Paul Scherrer Institute, 5232 Villigen, Switzerland.

interaction as [2,3]

$$H = H_m + H_{\rm ph} + V, \tag{1}$$

where

$$H_m = \sum_{j=1}^{L} \left(J\mathbf{S}_j \cdot \mathbf{S}_{j+1} + BS_j^z \right), \quad H_{\rm ph} = \sum_k \omega_k a_k^\dagger a_k, \tag{2}$$

$$V = \sum_{j=1}^{L} [J_1(x_{j+1} - x_j) + J_2(x_{j+1} - x_j)^2] \mathbf{S}_j \cdot \mathbf{S}_{j+1} \tag{3}$$

are the Heisenberg model of spins, the free phonon model, and the interaction between them, respectively, $\mathbf{S}_j$ are the spin-1/2 operators, J is the exchange interaction between spins when the atoms are in equilibrium, and B is the external magnetic field in energy units. Here a_k are Bose operators of the phonons, $\omega_k = 2\omega_D |\sin(k/2)|$ is the phonon dispersion, ω_D is Debye energy, $x_j = \sum_k \sqrt{\frac{\hbar b}{m v_0 |k| L}} (a_k + a_{-k}^\dagger) e^{-ikj}$ is the position operator of an atom with the mass m at lattice site j, and v_0 is the sound velocity. Phononic excitations modulate the exchange integrals resulting in a set of magnetostrictive constants $J_n = \partial_x^n J(x)|_{x=b}/n!$ that quantify the magnetoelastic interaction, where b is the lattice parameter. We assume the periodic boundary condition: $\mathbf{S}_{j+L} = \mathbf{S}_j$ and $x_{j+L} = x_j$.

The spin Hamiltonian in Eq. (2) is diagonalized by N-magnon states parameterized with a set of N quasimomenta $\mathbf{q} = (q_1 \dots q_N)$ that satisfy the nonlinear Bethe equations [11]

$$q_j L - \sum_{l \neq j} \varphi_{jl} = 2\pi I_j, \tag{4}$$

where the two-body scattering phases are

$$e^{i\varphi_{ij}} = -\frac{e^{i(q_i+q_j)} + 1 - 2\Delta e^{iq_i}}{e^{i(q_i+q_j)} + 1 - 2\Delta e^{iq_j}}, \tag{5}$$

$\Delta = 1$, and I_j is a set of nonequal integers. Solutions of Bethe equations can be found via numerical deformation from the XY point $\Delta = 0$ (where $\varphi_{ij} = \pi$ gives the solutions $q_j = 2\pi I_j/L$) to the Heisenberg point $\Delta = 1$ [29]. However, Bethe equations remain nonlinear, $\alpha L - \Phi(\alpha, \mathbf{q}) = 2\pi I_j$, for some solutions that contain at least a pair of quasimomenta satisfying the condition $q_i + q_j = \pm\pi$ in the $\Delta = 0$ limit—see derivation in Appendix A. Here $q_i = \pm\pi - \alpha$, $q_j = \alpha$, the scattering phase

$$e^{i\Phi(\alpha,\mathbf{q})} = -\frac{i\frac{2\lambda}{L}\sum_{j=1}^{N-2r} \frac{1-\sin q_j \sin\alpha}{\sin q_j - \sin\alpha} + e^{i\alpha}}{i\frac{2\lambda}{L}\sum_{j=1}^{N-2r} \frac{1-\sin q_j \sin\alpha}{\sin q_j - \sin\alpha} - e^{-i\alpha}} \tag{6}$$

depends on another quasimomenta, n is the number of such pi-pairs, and $\lambda = 1$. Solutions for α can be obtained again via deformation from the $\lambda = 0$ to the $\lambda = 1$ point. The eigenenergy of H_m corresponding to the state $\mathbf{q}$ is

$$\varepsilon = \sum_{j=1}^{N} (J\cos q_j - J + B) + \left(\frac{J}{2} - B\right)\frac{L}{2} \tag{7}$$

and the total momentum—preserved by the translational invariance—is $Q = \sum_{j=1}^{N} q_j$.

We consider renormalization of phonons by spins via the magnetostrictive interaction V perturbatively. The perturbation series for the eigenenergy of H is

$$E(k) = \varepsilon_0 + \omega_k + \langle k|V|k\rangle + \sum_{\{\mathbf{k},\mathbf{q}\}} \frac{|\langle \mathbf{k},\mathbf{q}|V|k\rangle|^2}{\varepsilon_0 + \omega_k - \varepsilon_{\mathbf{q}} - \omega_{\mathbf{k}}}, \tag{8}$$

where ε_0 is the ground state energy of H_m, $\omega_{\mathbf{k}}$ is an eigenenergy of $H_{\rm ph}$ parameterized by M momenta $\mathbf{k} = (k_1, \cdots, k_M)$. The unperturbed state $|k\rangle = |k\rangle_{\rm ph}|0\rangle_m$ is a direct product of a single phonon $|k\rangle_{\rm ph}$ and the spin ground state $|0\rangle_m$ and $|\mathbf{k},\mathbf{q}\rangle = |\mathbf{k}\rangle_{\rm ph}|\mathbf{q}\rangle_m$ are the intermediate states.

III. RENORMALIZATION OF SOUND VELOCITY

Change of the sound velocity is given by a derivative of $E(k)$ as

$$\delta v = \delta v_1 + \delta v_2, \tag{9}$$

where evaluation of the phononic matrix elements leaves the spin correlation functions split into the static and the dynamic parts,

$$\delta v_1 = \frac{J_2 b^2 \hbar}{2 m v_0} \langle 0|\mathbf{S}_1 \cdot \mathbf{S}_2|0\rangle_m, \tag{10}$$

$$\delta v_2 = \frac{J_1^2 b^2 \hbar}{m v_0} \sum_{\{\mathbf{q}\}:Q=p} \frac{L|\langle \mathbf{q}|\mathbf{S}_1 \cdot \mathbf{S}_2|0\rangle_m|^2 (\varepsilon_0 - \varepsilon_{\mathbf{q}})}{(\varepsilon_0 - \varepsilon_{\mathbf{q}})^2 - (\omega_D p)^2}. \tag{11}$$

Here $\hbar p/b = 2\pi\hbar/(bL)$ is the quantum of the momentum and the sum over all of the many-magnon states, $\{\mathbf{q}\}$, and is restricted by momentum conservation to the states with $Q = p$. The static correlation function in δv_1 is immediately obtained from ε_0 using the translational invariance

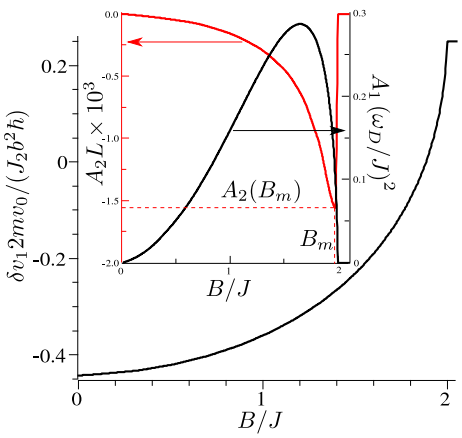

FIG. 1. The static spin correlation function from Eq. (10) as a function of the magnetic field B, calculated using Bethe ansatz. Inset is the dynamic correlation function from Eq. (11) calculated using the matrix element in Eq. (13): The black line is the Luttinger liquid contribution in Eq. (20), and the red line is the high-energy contribution in Eq. (21).

as [30]

$$\langle 0|\mathbf{S}_1\cdot\mathbf{S}_2|0\rangle_m=\frac{\varepsilon_0-B\left(N-\frac{L}{2}\right)}{JL}. \tag{12}$$

Its dependence on the magnetic field, changing from the ferromagnetic value of 0.25 at high fields to the antiferromagnetic $\simeq -0.44$ in zero field, is shown in Fig. 1.

A. Dynamical correlation function of spins

The dynamical part in δv_2 is a fourth-order correlation function. We evaluate the needed matrix element using the algebraic Bethe ansatz [31] and obtain it as a sum over determinants of $N\times N$ matrices, see Appendix C for details,

$$\begin{aligned}\langle \mathbf{q}|\mathbf{S}_1\cdot\mathbf{S}_2|0\rangle=(\sqrt{\langle 0|0\rangle\langle \mathbf{q}|\mathbf{q}\rangle})^{-1}\Bigg\{&\frac{\prod_i \mathrm{ch}(v_j+\eta)}{\prod_{i<j}\mathrm{sh}(v_i-v_j)}\sum_y(-1)^y\frac{\prod_{i,j;j\neq y}\mathrm{sh}(u_j-v_i)}{\prod_j \mathrm{ch}^2(u_j-\eta)}\prod_{l;l\neq y}\frac{\mathrm{sh}(u_l-u_y+2\eta)}{\mathrm{sh}(u_l-u_y)}\\&\times\left[\det\hat{K}^{(y)}-\left(1-\frac{2\,\mathrm{sh}(2\eta)\mathrm{sh}\eta\,\mathrm{sh}u_y\prod_{j;j\neq y}\mathrm{ch}(u_j+\eta)}{\prod_{i<j\neq y}\mathrm{sh}(u_i-u_j)}\right)\det\hat{G}^{(y)}\right]\\&-\frac{\prod_j\mathrm{ch}(u_j+\eta)\prod_j\mathrm{ch}(v_j+\eta)}{\prod_j\mathrm{ch}^2(u_j-\eta)\prod_{i<j}\mathrm{sh}(v_i-v_j)}\det\hat{K}\Bigg\},\end{aligned} \tag{13}$$

where the matrix elements are

$$K_{ab}=T_{ab}+\frac{(-1)^b\mathrm{sh}^3(2\eta)\mathrm{sh}u_b\prod_{l;l\neq b}\mathrm{sh}(u_l-u_b+2\eta)}{\prod_{i<j\neq b}\mathrm{sh}(u_i-u_j)\prod_{l;l\neq b}\mathrm{sh}(u_l-u_b)}\frac{\mathrm{sh}\eta\prod_{j,i;i\neq b}\mathrm{sh}(u_i-v_j)\left[\frac{\mathrm{sh}u_b}{\mathrm{ch}\eta}+\sum_l\frac{\mathrm{sh}(2\eta)\mathrm{ch}(u_b+\eta)}{\mathrm{ch}(v_l-\eta)\mathrm{ch}(v_l+\eta)}\right]}{\mathrm{ch}(u_b+\eta)\mathrm{ch}(u_b+\eta)\mathrm{ch}(v_a-\eta)\mathrm{ch}(v_a+\eta)}, \tag{14}$$

$$\begin{aligned}K^{(y)}_{ab}=T_{ab}+&\frac{(-1)^b\mathrm{sh}^3(2\eta)\mathrm{sgn}(y-b)\mathrm{ch}(u_y-\eta)}{\mathrm{ch}(v_a-\eta)\mathrm{ch}(v_a+\eta)\prod_i\mathrm{sh}(u_b-v_i)}\frac{\mathrm{ch}(u_b+\eta)\prod_{l;l\neq y,b}\mathrm{sh}(u_l-u_b+2\eta)}{\prod_{i<j\neq y,b}\mathrm{sh}(u_i-u_j)\prod_{l;l\neq y,b}\mathrm{sh}(u_l-u_b)}\\&\times\left[\frac{\mathrm{ch}(u_b-\eta)}{\mathrm{ch}(u_b+\eta)}-\frac{\mathrm{sh}(u_y-u_b+2\eta)}{\mathrm{sh}(u_y-u_b-2\eta)}+\frac{\mathrm{sh}2\eta\mathrm{ch}(u_b-2\eta)\mathrm{sh}u_y}{\mathrm{ch}(u_y-\eta)\mathrm{ch}(u_b+\eta)}\right],\end{aligned} \tag{15}$$

when $b\neq y$ and

$$K^{(y)}_{ay}=\frac{\mathrm{sh}(2\eta)\mathrm{sh}(2v_a)}{\mathrm{ch}^2(v_a-\eta)\mathrm{ch}^2(v_a+\eta)}, \tag{16}$$

$G^{(y)}_{ab}=T_{ab}$ when $b\neq y$ and $G^{(y)}_{ay}=K^{(y)}_{ay}$,

$$T_{ab}=\frac{\mathrm{ch}^L(v_b-\eta)}{\mathrm{ch}^L(v_b+\eta)}\frac{\mathrm{sh}(2\eta)}{\mathrm{sh}^2(v_b-u_a)}\prod_{j;j\neq a}\frac{\mathrm{sh}(v_b-u_j+2\eta)}{\mathrm{sh}(v_b-u_j)}-\frac{\mathrm{sh}(2\eta)}{\mathrm{sh}^2(u_a-v_b)}\prod_{j;j\neq a}\frac{\mathrm{sh}(u_j-v_b+2\eta)}{\mathrm{sh}(u_j-v_b)}. \tag{17}$$

The normalization factors of Bethe states [32,33] $\langle 0|0\rangle$ and $\langle \mathbf{q}|\mathbf{q}\rangle$ are quoted in Appendix B in terms of a determinant of an $N\times N$ matrix. Here $\eta=(\mathrm{acosh}1)/2$,

$$u_j=\ln\left(\frac{\sqrt{1-e^{iq_j^0-2\eta}}}{\sqrt{1-e^{-iq_j^0-2\eta}}}\right)-i\frac{q_j^0}{2} \tag{18}$$

are the quasimomenta of the ground state $\mathbf{q}^0$ in Orbach parametrization, and v_j is obtained from u_j by $q_j^0\to q_j$ where $\mathbf{q}$ are the excited states [11].

B. Hierarchy of modes

The excitations in the sum over $\mathbf{q}$ in Eq. (11) have the same number of quasimomenta as the ground state at a given magnetic field. They are constructed by removing a quasimomentum from the ground state distribution and promoting it to an empty position, see sketch in Fig. 2. We will label these excitations as $\psi\psi^*$ pairs.

The whole dynamical correlation function in Eq. (11) exhibits a hierarchy of modes governed by their spectral strength [12–14]. The excitations split into groups according to $n=1,2,3,\ldots$ $\psi\psi^*$ pairs that have progressively smaller amplitudes of their matrix elements, $|\langle \mathbf{q}|\mathbf{S}_1\cdot\mathbf{S}_2|0\rangle|^2\sim 1/L^{2n}$. We keep the first three levels of the hierarchy,

$$\delta v_2=\frac{J_1^2b^2\hbar}{mv_0J}(A_1+A_2+A_3). \tag{19}$$

The first level consists of only one pair with the minimally possible momentum $Q=p$,

$$A_1(B)=\frac{v_mJL^2|\langle p|\mathbf{S}_1\cdot\mathbf{S}_2|0\rangle_m|^2}{2\pi\omega_D^2}, \tag{20}$$

where $v_m=(\varepsilon_p-\varepsilon_0)/p$ is the renormalized velocity of Luttinger liquid and we have used smallness of the exchange energy compared with Debye energy $J/\omega_D\sim 10^{-3}$ for general material parameters [34]. The only matrix element in Eq. (20) can be obtained using the bosonic modes of Luttinger liquid [35], where the dispersion is almost linear. We, however,

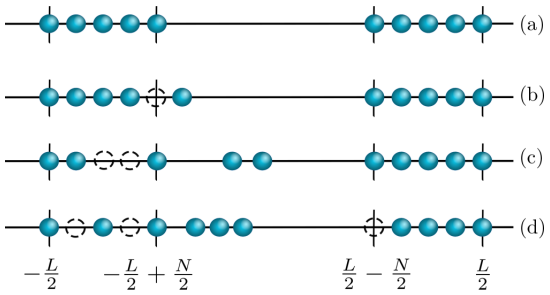

FIG. 2. Configurations of nonequal integer numbers I_j that correspond to the solutions of the Bethe equations for the model H_m: (a) the ground state, (b) one $\psi\psi^*$-pair excitation, (c) two $\psi\psi^*$-pair excitations, (d) three $\psi\psi^*$-pair excitations. These eigenstates include complex solutions at $\Delta = 1$, which are obtained via numerical deformation of Bethe equations from the $\Delta = 0$ to the $\Delta = 1$ point.

use a more general Bethe ansatz approach here. Solutions of Bethe equations give v_m directly that, together with the matrix element in Eq. (13), gives the magnetic field dependence of $A_1(B)$ shown in the inset (right axis) in Fig. 1.

There are polynomially many states in the second and in the third levels of the hierarchy,

$$A_{2(3)}(B) = \sum_{\{\mathbf{q}\}:Q=p} \frac{L|\langle \mathbf{q}|\mathbf{S}_1 \cdot \mathbf{S}_2|0\rangle_m|^2}{\varepsilon_{\mathbf{q}} - \varepsilon_0}, \qquad (21)$$

where the summand in Eq. (11) was expanded in a Taylor series in $\omega_D p/(\varepsilon_0 - \varepsilon_{\boldsymbol{q}}) \ll 1$ since the sum over $\mathbf{q}$ accumulates dominantly at high energy. Contribution of the low-energy excitations (for which $(\varepsilon_0 - \varepsilon_{\boldsymbol{q}})/\omega_D p \ll 1$) has an additional small factor J^2/ω_D^2, like in Eq. (20). At intermediate energies, $(\varepsilon_0 - \varepsilon_{\boldsymbol{q}}) \simeq \omega_D p$, the perturbation theory for $E(k)$ becomes inapplicable since these magnetic excitations are in resonance with the acoustic phonon. However, the width of the anti-crossing [36] $\lesssim J_1\sqrt{\hbar b\omega_D^2/(mJ^3L^5)}$ is much smaller than the many-magnon level spacing J/L that is still in the Luttinger liquid regime. The nonperturbative contribution of these levels is of the order of the anticrossing width and vanishes in large systems.

We obtain the magnetic field dependence of A_2 numerically as a sum over the two $\psi\psi^*$ pairs in Eq. (21), see inset in Fig. 1. At high fields A_2 is small since there are only a few excitations, the strength of which is small as $1/L^4$ at the second level of the hierarchy, and at small fields A_2 is again small since the majority of the excitations belongs to the class of pi-pairs close to the half filling of the magnetic band, which makes their amplitudes even weaker than $1/L^4$ due to Eq. (6). At the intermediate fields the $1/L^4$ smallness is partially compensated by a large number of the excitations, whose majority does not have pi-pairs yet. The position of the maximum of $|A_2(B)|$ is identified from numerics at $B_m = 2J - 9\pi^2 J/(2L^2)$. The value of the function at this point is $A_2(B_m) = -0.0016/L$ for large systems, see scaling of $A_2(B_m)$ in Fig. 3, which is small in a different parameter compared with A_1.

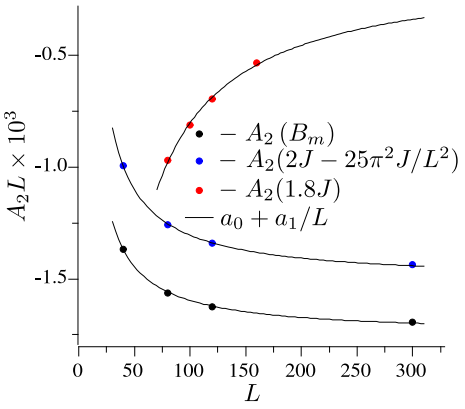

FIG. 3. Scaling of A_2L defined in Eq. (21) with the system length at three values of the magnetic field $B = B_m, 2J - 25\pi^2 J/L^2, 1.8J$. The fitting of finite size corrections, $A_2L = a_0 + a_1/L$, gives $(a_0,a_1) \times 10^2 = (-0.17, 1.51), (-0.15, 2.04), (-0.01, -6.95)$ for the three magnetic fields, respectively.

For typical values of material parameters, A_1 and A_2 are of the same order, e.g., $1/L \sim 10^{-6}$ and $(\omega_D/J)^2 \sim 10^{-6}$ for ultrasonic measurements in a magnetic insulator [1]. The three $\psi\psi^*$-pairs contribution A_3 is smaller than A_2 due to an additional $1/L^2$ in accord with the hierarchy of modes [12–14] for the whole range of magnetic fields, see Fig. 4.

IV. ATTENUATION OF PHONONS

Next let us analyze decay of the phonons into the spin excitations. The excitation spectrum of Heisenberg model in Eq. (2) is continuous which always has some states in resonance with the single phonon energy $\omega_D p$ providing a channel for the direct relaxation, unlike the previous phenomenological approaches [37,38]. The rate of such a

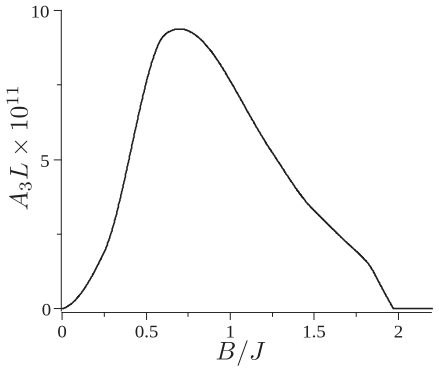

FIG. 4. Contribution of the third level of the hierarchy of modes to δv_2 defined in Eq. (21); $L = 40$. It is small compared with A_2 in the inset of Fig. 1 for the whole range of magnetic fields.

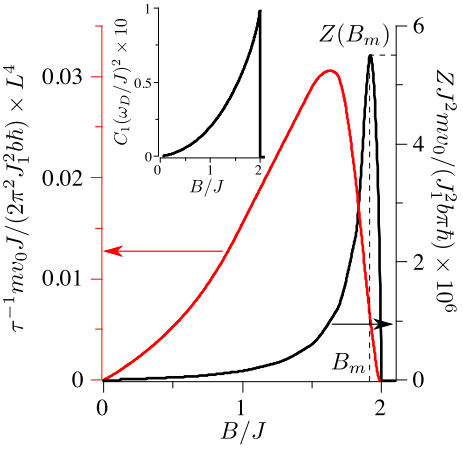

FIG. 5. Two mechanisms of the sound attenuation: the red line is the relaxation rate τ^{-1} calculated using the Fermi golden rule in Eq. (22), while the black line is the degree of hybridization Z of a sound phonon with the magnetic excitations dominated by high energies in Eq. (24). Inset is the low energy contribution to Eq. (24).

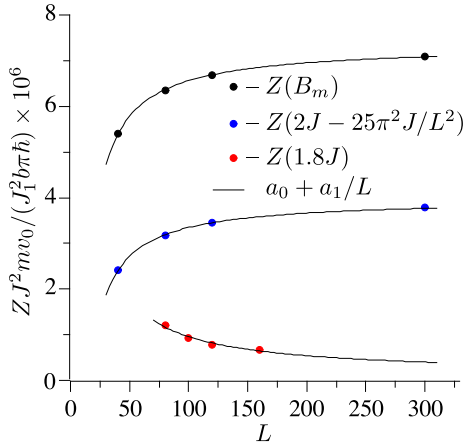

FIG. 6. Scaling of Z defined in Eq. (24) with the system length at three values of the magnetic field $B=B_m, 2J-25\pi^2J/L^2, 1.8J$. The fitting of finite size corrections, $ZJ^2mv_0/(J_1^2b\pi\hbar^2)=a_0+a_1/L$, gives $(a_0,a_1)\times 10^5=(0.73,-7.8)$, $(0.40,-6.3)$, $(0.012,8.4)$ for the three magnetic fields, respectively.

process is given by the Fermi golden rule,

$$\tau^{-1}=\frac{2\pi^2J_1^2b}{mv_0}\sum_{\{\mathbf{q}\};Q=p}|\langle\mathbf{q}|\mathbf{S}_1\cdot\mathbf{S}_2|0\rangle_m|^2\delta(\Delta E), \tag{22}$$

where $\Delta E=\varepsilon_{\mathbf{q}}-\varepsilon_0-\omega_p$ and the contribution of the J_2 term in Eq. (3) is zero due to $\delta(\Delta E)$. The principal value of the sum in Eq. (22) is accumulated by the second level of the hierarchy, which we evaluate numerically—see the magnetic field dependence of τ^{-1} in Fig. 5. Its maximum value has the same small prefactor $1/L^4$ as the matrix element in Eq. (13) making the direct relaxation extremely slow in large systems.

However, the amplitude of the free phonons can also be reduced via hybridization with the magnetic excitations, similarly to the δv_2 renormalization of their velocity. The first order in perturbation theory for the wave function,

$$|\Psi_k\rangle=|k\rangle+\sum_{\{\mathbf{k},\mathbf{q}\}}\frac{\langle\mathbf{k},\mathbf{q}|V|k\rangle}{\varepsilon_0+\omega_k-\varepsilon_{\mathbf{q}}-\omega_{\mathbf{k}}}|\mathbf{k}\rangle_{\rm ph}|\mathbf{q}\rangle_m, \tag{23}$$

gives suppression at low momenta, $Z=1-|\langle p|\Psi_p\rangle|^2$, as

$$Z=\frac{J_1^2b\pi\hbar^2}{mv_0}\sum_{\{\mathbf{q}\};Q=p}\frac{|\langle\mathbf{q}|\mathbf{S}_1\cdot\mathbf{S}_2|0\rangle_m|^2}{(\varepsilon_0-\varepsilon_{\mathbf{q}}-\omega_D p)^2}, \tag{24}$$

which we analyze using the hierarchy of modes:

$$Z=\frac{J_1^2b\pi\hbar^2}{J^2mv_0}(C_1+C_2+C_3), \tag{25}$$

where

$$C_1=\frac{(J/\omega_D)^2L^2|\langle p|\mathbf{S}_1\cdot\mathbf{S}_2|0\rangle_m|^2}{(2\pi)^2} \tag{26}$$

and

$$C_{2(3)}=\sum_{\{\mathbf{q}\};Q=p}\frac{|\langle\mathbf{q}|\mathbf{S}_1\cdot\mathbf{S}_2|0\rangle_m|^2}{(\varepsilon_0-\varepsilon_{\mathbf{q}})^2}, \tag{27}$$

like in the analysis of Eq. (11) before. The first level contribution C_1 is small in J^2/ω_D^2 like A_1, see inset in Fig. 5. But C_2, shown in Fig. 5, remains finite in the thermodynamic limit (see scaling in Fig. 6) unlike A_2 above, and C_3 is small in $1/L^2$ compared with C_2, see Fig. 7. This hybridization mechanism can be distinguished from other nonmagnetic channels of relaxation via its magnetic field dependence and from the exponential decay into the resonant magnetic states described by Eq. (22) since it is constant in the temporal and spatial domains.

V. ULTRASOUND EXPERIMENT ON Cs_2CuCl_4

Finally, we discuss our experimental results. High-quality single crystals of several mm size of the frustrated spin-1/2 antiferromagnet Cs_2CuCl_4 were grown from an aqueous solution by an evaporation technique [39]. A pair of

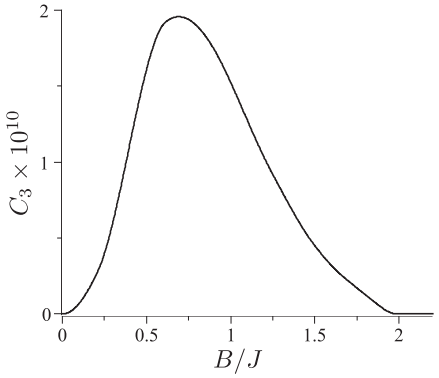

FIG. 7. Contribution of the third level of the hierarchy of modes to Z defined in Eq. (27); $L=40$. It is small compared with C_2 in Fig. 5 for the whole range of magnetic fields.

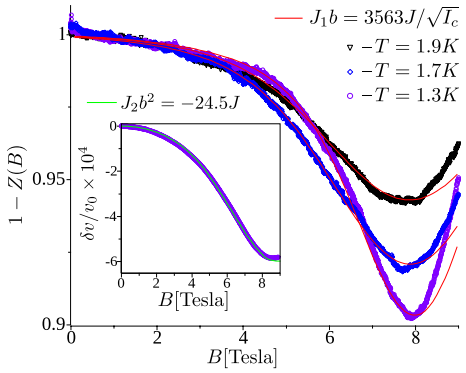

FIG. 8. Experimental results (open triangles, diamonds, and circles) of the renormalized amplitude $1 - Z$ of the longitudinal ultrasound wave propagating along the [010] axis of Cs_2CuCl_4 at $T = (1.900 \pm 0.005)$ K, $T = (1.700 \pm 0.005)$ K, and $T = (1.300 \pm 0.005)$ K. The red lines represent the results of Eq. (24) with $J_1b = 3563J/\sqrt{I_c}$. The inset shows data (open circles) of the corresponding normalized sound velocity at $T = (1.300 \pm 0.005)$ K. The green line shows the result of Eq. (10) using $J_2b^2 = -24.5J$. Additional data are presented in Fig. 9.

piezoelectric polymer-foil transducers was glued to opposite parallel surfaces perpendicular to the [010] direction for the generation and the detection of the ultrasound waves. These longitudinal waves propagate along the [010] direction that corresponds to the elastic mode c_{22}. Changes of the sound velocity δv and the renormalized amplitude of the sound wave $1 - Z$ were measured as functions of magnetic field at constant temperatures, using the experimental set up described in detail in Ref. [40].

In Fig. 8 we compare the experimental data for the sound velocity with the theoretical results expressed in Eqs. (10) and (11). By fitting the static correlation function given by Eq. (10), we extract $J_2b^2 = -24.5J$, with the magnetic coupling constant $J = 0.375$ meV taken from Ref. [6]—see inset in Fig. 8. We find no signatures of the dynamical correlation functions represented by Eq. (11)—which are parametrically small—down to the noise level of our experiment. This defines an upper bound to the other microscopic constant $J_1b \leqslant 1.25 \times 10^4 J$.

Analyzing the attenuation of the amplitude of the sound wave Z, we find that its functional dependence on the magnetic field is in good agreement with the dynamic hybridization mechanism represented by Eq. (24)—see Fig. 8 and additional data in Fig. 9. By fitting its amplitude, we extract the other microscopic parameter as $J_1b = 3563J/\sqrt{I_c}$, where I_c is the

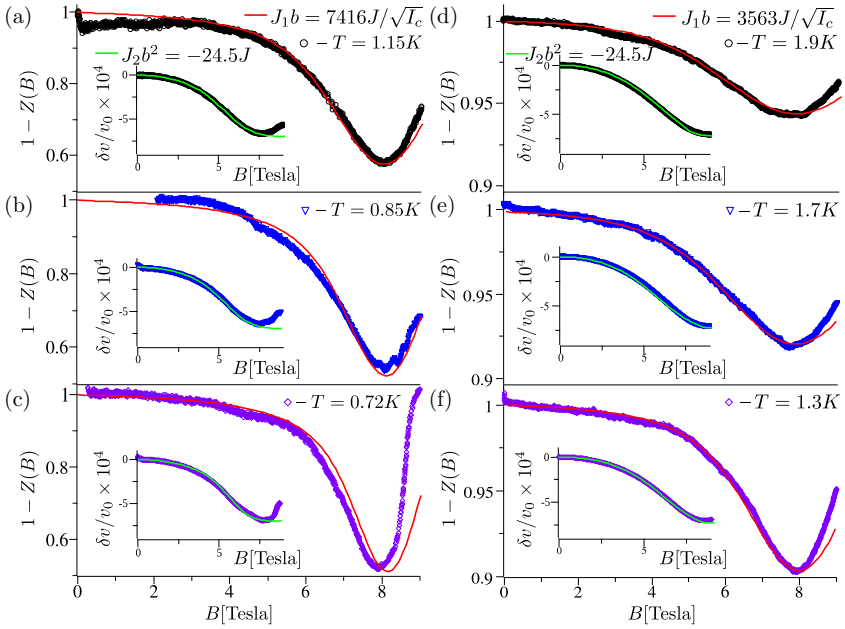

FIG. 9. Experimental results (open circles, triangles, and diamonds) of the renormalized amplitude $1 - Z$ of the longitudinal ultrasound wave propagating along the [010] axis of Cs_2CuCl_4 at the temperatures of (a) $T = (1.150 \pm 0.005)$ K, (b) $T = (0.850 \pm 0.005)$ K, (c) $T = (0.720 \pm 0.005)$ K, (d) $T = (1.900 \pm 0.005)$ K, (e) $T = (1.700 \pm 0.005)$ K, and (f) $T = (1.300 \pm 0.005)$ K. The red lines represent the results of Eq. (24) with $J_1b = 7416J/\sqrt{I_c}$ for (a)–(c) and with $J_1b = 3563/\sqrt{I_c}$ for (d)–(f). The data in (d)–(f) were taken in a different cryostat system using upgraded electronics and a better quality sample compared with the data in (a)–(c) leading to a decrease of the nonmagnetic losses by a factor of $I_c(a,b,c)/I_c(d,e,f) \approx 4.3$. The insets show data of the corresponding normalized sound velocities at the same temperatures. The green lines show the result of Eq. (10) using $J_2b^2 = -24.5J$. The results of our ultrasound experiments are still relatively close to the 1D regime at the temperature of $T = (0.720 \pm 0.005)$ K, at which the system is already in a transitional state between the 1D and a 2D regime.

degree of nonmagnetic losses. A quantitative determination of these losses is not possible since they consist of various extrinsic (e.g., coupling and diffraction losses, nonparallel alignment of the sample, etc.) and intrinsic attenuation mechanisms like direct scattering at defects or dislocation damping [41]. However, even for $I_c = 1$ this value of $J_1 b$ is consistent with the bound from the measurement of the sound velocity.

The values of the microscopic constants are significantly different from the values measured along the a axis in Ref. [42] manifesting an anisotropy of Cs_2CuCl_4. Our very good fit of the magnetic field dependencies by the purely one-dimensional theory in Figs. 8 and 9 gives a further argument that the interchain interactions in Cs_2CuCl_4 in the finite temperature regime are negligible despite only a moderate degree of the exchange anisotropy of $\sim$3 in the a-b plane [43].

VI. CONCLUSIONS

In conclusion, constructing a microscopic theory of magnetoelasticity in 1D we have shown that the necessary correlation functions involve the many-body excitations at all energy scales and have identified a new mechanism of sound attenuation. Our theoretical predictions agree with our ultrasound experiments in the 1D regime of Cs_2CuCl_4.

ACKNOWLEDGMENT

We acknowledge financial support by the DFG through the SFB/TRR 49.

APPENDIX A: DERIVATION OF THE QUANTIZATION EQUATION FOR PI-PAIRS

The XXZ model is a generalization of Heisenberg model that introduces the interaction strength between magnons $J\Delta$ as a model parameter, which breaks the rotational symmetry of the spin-spin interaction term $\mathbf{S}_j \cdot \mathbf{S}_{j+1}$. In one dimension the model reads

$$H_m = \sum_{j=1}^{L} \left(J \frac{S_j^- S_{j+1}^+ + S_j^+ S_{j+1}^-}{2} + J\Delta S_j^z S_{j+1}^z + B S_j^z \right), \tag{A1}$$

where $S_j^{\pm} = S_j^x \pm i S_j^y$. For $\Delta = 1$ this model becomes the model in Eq. (2). The N-magnon eigenstates of this Hamiltonian can be found by solving a set of Bethe equations,

$$q_j L - \sum_{l \neq j} \varphi_{jl} = 2\pi I_j, \tag{A2}$$

for N quasimomenta q_j, where the two-magnon scattering phases are given by

$$e^{i\varphi_{ij}} = -\frac{e^{i(q_i+q_j)} + 1 - 2\Delta e^{iq_i}}{e^{i(q_i+q_j)} + 1 - 2\Delta e^{iq_j}} \tag{A3}$$

and I_j is a set of N nonequal integer numbers.

In the free magnon limit $\Delta = 0$ the two-body phase shifts φ_{ij} become independent of quasimomenta and equal to the shifts of free fermions or hard-core bosons, $\varphi_{ij} = \pi$ that is immediately obtained by taking the $\Delta \to 0$ limit of Eq. (A3) giving $\exp(i\varphi_{ij}) = -1$. This result restores the plain wave quantization condition for each magnon independently, $q_j = 2\pi(I_j + 1/2)/L$ [44], from the system of nonlinear Bethe equations in Eq. (A2). Alternatively, the free magnon result can be obtained by setting $\Delta = 0$ in the Hamiltonian in Eq. (A1) and then by diagonalizing the resulting XY model directly [45].

However, the noninteracting limit becomes ambiguous when at least one pair of quasimomenta in an N magnon state satisfies the condition $q_i + q_j = 2\pi(I_i + I_j + 1)/L = \pm\pi$ at $\Delta = 0$. In evaluating the $\Delta = 0$ limit of Eq. (A3), the leading order of $e^{i(q_i+q_j)} + 1$ is zero in the Taylor series around the $\Delta = 0$ point, both in the numerator and in the denominator. Thus, higher order coefficients have to be calculated, $e^{i(q_i+q_j)} + 1 = c_1\Delta + c_2\Delta^2 + \ldots$, that requires, in general, solving the whole set of N Bethe equation in Eq. (A2) in a nonlinear fashion, i.e., $c_1, c_2, \ldots$ depend on all q_l—not just q_i and q_j—since Δ is still finite, which requires solving all N Bethe equations for all q_l simultaneously in taking the limit. This issue was noted in Refs. [46,47] but was never resolved. Here we start from a finite but small Δ, for which all scattering phase are well behaved, and then take the limit $\Delta \to 0$ systematically.

Let us consider a N-magnon solution of Bethe equations that contains $2r$ quasimomenta that satisfy the $q_{2j} + q_{2j+1} = \pm\pi$ condition (we will call these pairs of quasimomenta pi-pairs below) and $N - 2r$ quasimomenta that do not have a pi-pair. For a finite but small $\Delta \ll 1$ the quasimomenta of a pi-pair can be parameterized as

$$q_{2j} = \pm\pi - \alpha_j + \frac{\delta_j}{2}, \quad j \leqslant r, \tag{A4}$$

$$q_{2j+1} = \alpha_j + \frac{\delta_j}{2}, \tag{A5}$$

where α_j is an unknown parameter of the jth pi-pair that has a nonzero value, since Bethe equations for this pair cannot be solved due to the unknown (at the moment) phase shift $\varphi_{2j,2j+1}$ at $\Delta = 0$, and δ_j is a parameter that vanishes at $\Delta = 0$. On the other hand, the remaining quasimomenta $j > 2r$ can be found immediately for $\Delta = 0$ since all of their scattering phases in Eq. (A3) for these quasimomenta are well behaved, $\varphi_{ij} = \pi$. Thus at a finite $\Delta \ll 1$ we can write

$$q_j = \frac{2\pi\left(I_j + \frac{1}{2}\right)}{L} + \epsilon_j, \quad j > 2r, \tag{A6}$$

where ϵ_j are small corrections due to a finite Δ that depend on all other quasimomenta and vanish for $\Delta = 0$. Conservation of the total momentum of N magnons, $\sum_{j=1}^{N} q_j = 2\pi \sum_{j=1}^{N} I_j/L$ including the pi-pairs, is independent of the interactions and imposes an additional constraint on δ_j and ϵ_j,

$$\sum_{j=2r+1}^{N} \epsilon_j = -\sum_{j=1}^{r} \delta_j. \tag{A7}$$

It is obtained as a sum of all equations in Eq. (A2) after substitution of Eqs. (A4)–(A6).

Since α_j cannot be obtained directly from its own Bethe equation due to the undefined scattering phase within the corresponding pi-pair, we are going to obtain an equation for α_j from the other $j > 2r$ Bethe equations that do not have this issue. We start from expanding φ_{ji} for $j > 2r$

magnons—which are defined at the point $\Delta = 0$—up to the linear order in small Δ. Taking into account that ϵ_j is proportional to Δ and δ_j is linear (or a higher order) in Δ we obtain the following expansion of φ_{ji} between the jth magnon and a pi-pair and the jth magnon and another j'th magnons, which do not have a pi-pair, respectively,

$$\varphi_{j,2i} = \pi - 2\Delta \frac{\sin\frac{q_j-\alpha_i}{2}}{\cos\frac{q_j+\alpha_i}{2}}, \tag{A8}$$

$$\varphi_{j,2i+1} = \pi - 2\Delta \frac{\cos\frac{q_j+\alpha_i}{2}}{\sin\frac{q_j-\alpha_i}{2}}, \tag{A9}$$

$$\varphi_{jj'} = \pi - 2\Delta \frac{\sin\frac{q_j-q_{j'}}{2}}{\cos\frac{q_j+q_{j'}}{2}}. \tag{A10}$$

Then we substitute these expansions in Eq. (A2) and sum all of them with $j > 2r$ obtaining a relation between δ_i and α_i that parameterizes the quasimomenta for $j \leqslant 2r$,

$$-L\sum_{i=1}^{r}\delta_i + 4\Delta\sum_{i=1}^{r}\sum_{j=2n+1}^{N}\frac{1-\sin q_j \sin\alpha_i}{\sin q_j - \sin\alpha_i} = 0, \tag{A11}$$

where the sum over j is taken over the remaining quasimomenta that do not have a pi-pair, given by Eq. (A6) with $\epsilon_j = 0$. Here we used Eq. (A7) to express ϵ_j through δ_j and canceled all $\varphi_{jj'}$ terms for both $j, j' > 2r$ due to the $\varphi_{jj'} = -\varphi_{j'j}$ symmetry of Eq. (A10)—note that the scattering phases are defined up to an arbitrary period 2π times an integer.

The equation in Eq. (A11) is a sum of r terms and each term depends only on two unknown variables δ_i and α_i. Thus Eq. (A11) splits into r independent equations and solving them separately we find

$$\delta_i = \frac{4}{L}\sum_{j=2r+1}^{N}\frac{1-\sin q_j \sin\alpha_i}{\sin q_j - \sin\alpha_i}\Delta. \tag{A12}$$

This result shows that the linear term in the Taylor expansion for δ_i in Δ does not vanish. However it depends on the still unknown parameter α_i. In order to find it, we take the $\Delta \to 0$ limit of Eq. (A3) for the two quasimomenta within the ith pi-pair and obtain

$$e^{i\varphi_{2i,2i+1}} = \frac{i\frac{2}{L}\sum_{j=2r+1}^{N}\frac{1-\sin q_j\sin\alpha_i}{\sin q_j-\sin\alpha_i} - e^{-i\alpha_i}}{i\frac{2}{L}\sum_{j=2r+1}^{N}\frac{1-\sin q_j\sin\alpha_i}{\sin q_j-\sin\alpha_i} + e^{i\alpha_i}}, \tag{A13}$$

where

$$e^{i(q_{2i}+q_{2i+1})} + 1 = \frac{4}{L}\sum_{j=2r+1}^{N}\frac{1-\sin q_j\sin\alpha_i}{\sin q_j-\sin\alpha_i}\Delta \tag{A14}$$

was expanded up to the linear order in Δ, substituted in Eq. (A3), and Δ was canceled from the whole expression altogether. Substituting Eq. (A13) into each of the $2i$th (or $2i+1$st) Bethe equation in Eq. (A2) in the exponential form we obtain an equation for each α_i independently in the $\Delta = 0$ limit,

$$-e^{iL\alpha_i}\frac{i\frac{2}{L}\sum_{j=2r+1}^{N}\frac{1-\sin q_j\sin\alpha_i}{\sin q_j-\sin\alpha_i} - e^{-i\alpha_i}}{i\frac{2}{L}\sum_{j=2r+1}^{N}\frac{1-\sin q_j\sin\alpha_i}{\sin q_j-\sin\alpha_i} + e^{i\alpha_i}} = 1. \tag{A15}$$

This result does not coincide with the free wave quantization condition $\exp(i\alpha_i L) = -1$, being a nonlinear equation for α_i. Its solutions can be found by introducing an extra deformation parameter λ,

$$-e^{iL\alpha}\frac{i\frac{2\lambda}{L}\sum_{j=2r+1}^{N}\frac{1-\sin q_j\sin\alpha}{\sin q_j-\sin\alpha} - e^{-i\alpha}}{i\frac{2\lambda}{L}\sum_{j=2r+1}^{N}\frac{1-\sin q_j\sin\alpha}{\sin q_j-\sin\alpha} + e^{i\alpha}} = 1, \tag{A16}$$

where the subscript was omitted, $\alpha_i \to \alpha$, since the equation is the same for all indices i. The solutions can be classified in the limit $\lambda = 0$, like the Bethe equations, where Eq. (A16) is solved by $\alpha = 2\pi(I_j + 1/2)/(L-2)$. Then a smooth deformation of the equation from $\lambda = 0$ to $\lambda = 1$ gives all solutions of of the nonlinear Eq. (A15). The quantization equation of pi-pairs in the $\Delta = 0$ limit before Eq. (6) is Eq. (A16) in the logarithmic form.

The two-magnon solutions of Bethe equations that we identified as pi-pairs in Eq. (A16) at $\Delta = 0$ can account for the missing complex solutions, which instead remain real, of the XXX model at $\Delta = 1$ found in Ref. [48]. For $N = 2$ the parameter δ in Eq. (A12) remains zero for any Δ making the scattering phase $\varphi_{12} = -2\alpha$ and Eq. (A2) independent of Δ as well, in this case. Thus this two-magnon solution remains real at $\Delta = 1$ and has to be removed from the class of complex conjugated quasimomenta. We also note that pi-pairs are still solutions of Bethe equations at any finite Δ in full accord with the arguments of Ref. [49]. It is only the limit $\Delta \to 0$ of these solutions that does not recover the single particle quantization rule $q_j = 2\pi(I_j + 1/2)/L$.

APPENDIX B: NORMALIZATION FACTORS OF BETHE STATES

The eigenstates of the XXZ model in Eq. (A1) are the Bethe states

$$|\Psi\rangle = \sum_{\mathcal{P}, j_1<\cdots<j_N} e^{i\sum_l q_{\mathcal{P}_l} j_l + i\sum_{l<l'}\varphi_{\mathcal{P}_l,\mathcal{P}_{l'}}/2} S^+_{j_1}\ldots S^+_{j_N}|\Downarrow\rangle, \tag{B1}$$

where $\mathcal{P}$ is a permutation of N quasimomenta q_j and $|\Downarrow\rangle$ is the ferromagnetic ground state. In this so-called coordinate representation the many-body states $|\Psi\rangle$ are not factorizable making calculations of scalar products and expectation values in this representation almost intractable. However, a calculation of the form factors needed in Eq. (13) becomes manageable using the algebraic form of Bethe ansatz [31], in which Bethe states are factorized in terms of operators with given commutation relations.

Following Ref. [31] we write down the many-body wave functions using operators that satisfy a Yang-Baxter algebra as

$$|\mathbf{u}\rangle = \prod_{j=1}^{N} C(u_j)|\Downarrow\rangle, \tag{B2}$$

where u_j are N auxiliary parameters and $C(u)$ is one of the four matrix elements of the transition matrix

$$T(u) = \begin{pmatrix} A(u) & B(u) \\ C(u) & D(u) \end{pmatrix}, \tag{B3}$$

which is defined in an auxiliary 2×2 space. This T-matrix satisfies the Yang-Baxter equation

$$R(u-v)(T(u)\otimes T(v)) = (T(v)\otimes T(u))R(u-v). \quad \text{(B4)}$$

Here we use the following R-matrix that corresponds to the spin Hamiltonian in Eq. (A1),

$$R(u) = \begin{pmatrix} 1 & & & \\ & b(u) & c(u) & \\ & c(u) & b(u) & \\ & & & 1 \end{pmatrix}, \quad \text{(B5)}$$

where $b(u) = \sinh(u)/\sinh(u+2\eta)$ and $c(u) = \sinh(2\eta)/\sinh(u+2\eta)$.

The entries of Eq. (B4) give commutation relations between the matrix elements of T. Here we write down four of them that will be used later,

$$[B_u, C_v] = \frac{c(u-v)}{b(u-v)}(A_u D_v - A_v D_u), \quad \text{(B6)}$$

$$A_u C_v = \frac{1}{b(u-v)} C_v A_u - \frac{c(u-v)}{b(u-v)} C_u A_v, \quad \text{(B7)}$$

$$D_u C_v = \frac{1}{b(v-u)} C_v D_u - \frac{c(v-u)}{b(v-u)} C_u D_v, \quad \text{(B8)}$$

$$[A_u, D_v] = \frac{c(u-v)}{b(u-v)}(C_v B_u - C_u B_v). \quad \text{(B9)}$$

We have introduced the subscript u and v as a shorthand of the argument, e.g. $A_u \equiv A(u)$, above.

The transfer matrix $\tau(u) = \mathrm{Tr}T(u) = A(u) + D(u)$ contains all of the conserved quantities of the model in Eq. (A1) including the Hamiltonian. Thus if $|\mathbf{u}\rangle$ is a eigenstate of $\tau(u)$ then it is an eigenstate of the Hamiltonian. The eigenvalue equation, $\tau(u)|\mathbf{u}\rangle = \mathcal{T}_u|\mathbf{u}\rangle$ where $\mathcal{T}_u$ is a scalar quantity—the corresponding eigenvalue, can be solved using the commutation relations in Eqs. (B6)–(B9). The results of acting with the A_u and D_u operators on the state $|\mathbf{u}\rangle$ in Eq. (B2) are obtained by commuting them from left to right through the product of $C(u_j)$ operators,

$$A_u \prod_{j=1}^{N} C(u_j)|0\rangle = a_u \prod_{j=1}^{N} \frac{1}{b_{uj}} C(u_j)|0\rangle - \sum_{j=1}^{N} a_j \frac{c_{uj}}{b_{uj}} C(u) \times \prod_{l=1\neq j}^{N} \frac{1}{b_{jl}} C(u_l)|\Downarrow\rangle, \quad \text{(B10)}$$

$$D_u \prod_{j=1}^{N} C(u_j)|0\rangle = d_u \prod_{j=1}^{N} \frac{1}{b_{ju}} C(u_j)|0\rangle + \sum_{j=1}^{N} d_j \frac{c_{uj}}{b_{uj}} C(u) \times \prod_{l=1\neq j}^{N} \frac{1}{b_{lj}} C(u_l)|\Downarrow\rangle, \quad \text{(B11)}$$

where the vacuum eigenvalues of the operators, $A_u|\Downarrow\rangle = a_u|\Downarrow\rangle$ and $D_u|\Downarrow\rangle = d_u|\Downarrow\rangle$, are

$$a_u = \frac{\cosh^L(u-\eta)}{\cosh^L(u+\eta)} \quad \text{and} \quad d_u = 1. \quad \text{(B12)}$$

Since the right hand side of Eqs. (B10) and (B11) contains terms that are not proportional to the original state multiplied by a scalar, an arbitrary Bethe state is not an eigenstate of the transfer matrix τ for an arbitrary set of the auxiliary parameters u_j. However, the second terms in Eqs. (B10) and (B11) can be made zero by selecting specific sets of u_j that are solutions of the following set of nonlinear equations,

$$\frac{a_j}{d_j} = \prod_{l=1\neq j}^{N} \frac{b_{jl}}{b_{lj}}, \quad \text{(B13)}$$

where we have used the shorthand with the subscripts, i.e. $a_j \equiv a(u_j)$ and $b_{jl} \equiv b(u_j - u_l)$. Substitution of the expressions for a_j and d_j from Eq. (B12) and for b_{jl} from Eq. (B5) gives the following Bethe equation and the eigenvalue of the transfer matrix τ,

$$\frac{\cosh(u_j-\eta)^L}{\cosh(u_j+\eta)^L} = \prod_{l=1\neq j}^{N} \frac{\sinh(u_j-u_l-2\eta)}{\sinh(u_j-u_l+2\eta)}, \quad \text{(B14)}$$

$$\mathcal{T}_u = a_u \prod_{j=1}^{N} \frac{1}{b_{uj}} + d_u \prod_{j=1}^{N} \frac{1}{b_{ju}}. \quad \text{(B15)}$$

The Bethe ansatz equations—in the coordinate representation—are obtained under substitution of

$$u_j = \ln\left[\sqrt{\frac{1-e^{iq_j-2\eta}}{1-e^{-iq_j-2\eta}}}\right] - \frac{iq_j}{2} \quad \text{(B16)}$$

and

$$\eta = \frac{\mathrm{acosh}\Delta}{2} \quad \text{(B17)}$$

into Eq. (B14).

The scalar product between two Bethe states $\langle\mathbf{v}|$ and $|\mathbf{u}\rangle$ can be calculated using the commutation relations in Eqs. (B6)–(B9). The multiplication of the bra and ket states in the form of Eq. (B2) is evaluated by commuting each operator $B(v_j)$ from left to right through the product of $C(u_j)$ operators and then by using the vacuum eigenvalues of the generated A and D operators from Eq. (B12). When u_j is a solution of Eq. (B14) and v_j is an arbitrary set of auxiliary parameters the result can be written in a compact form as a determinant of an $N \times N$ matrix—the so-called Slavnov's formula [50],

$$\langle\mathbf{v}|\mathbf{u}\rangle = \frac{\prod_{i,j=1}^{N}\sinh(v_j-u_i)}{\prod_{j<i}\sinh(v_j-v_i)\prod_{j<i}\sinh(u_j-u_i)} \det \hat{T}, \quad \text{(B18)}$$

where matrix elements are $T_{ab} = \partial_{u_a}\mathcal{T}(v_b)$. Under substitution of $\mathcal{T}(u)$ from Eq. (B5) these matrix elements read

$$T_{ab} = \frac{\cosh^L(v_b-\eta)}{\cosh^L(v_b+\eta)} \frac{\sinh(2\eta)}{\sinh^2(v_b-u_a)} \prod_{j=1\neq a}^{N} \frac{\sinh(v_b-u_j+2\eta)}{\sinh(v_b-u_j)} - \frac{\sinh(2\eta)}{\sinh^2(u_a-v_b)} \prod_{j=1\neq a}^{N} \frac{\sinh(u_j-v_b+2\eta)}{\sinh(u_j-v_b)}. \quad \text{(B19)}$$

The normalization factor of Bethe states in Eq. (B2) can be evaluated by taking the $\mathbf{v} \to \mathbf{u}$ limit of Eq. (B18) [32,33],

$$\langle \mathbf{u}|\mathbf{u}\rangle = \sinh^N(2\eta) \prod_{i\neq j=1}^{N} \frac{\sinh(u_j - u_i + 2\eta)}{\sinh(u_j - u_i)} \det \hat{M}, \tag{B20}$$

where the matrix elements are

$$M_{ab} = \begin{cases} -L\frac{\sinh 2\eta}{\cosh(u_a+\eta)\cosh(u_a-\eta)} - \sum_{j\neq a} \frac{\sinh 4\eta}{\sinh(u_a-u_j-2\eta)\sinh(u_a-u_j+2\eta)}, & a = b, \\ \frac{\sinh 4\eta}{\sinh(u_b-u_a+2\eta)\sinh(u_b-u_a-2\eta)}, & a \neq b. \end{cases} \tag{B21}$$

APPENDIX C: DERIVATION OF THE DYNAMICAL MATRIX ELEMENT FOR SPINS

In this section we will calculate the matrix element $\langle \mathbf{q}|\mathbf{S}_1 \cdot \mathbf{S}_2|0\rangle$—with respect to Bethe states of the spin Hamiltonian—that is needed for evaluating Eq. (11). We start by splitting the matrix element of the scalar product $\mathbf{S}_1 \cdot \mathbf{S}_2$ into three parts,

$$\langle \mathbf{q}|\mathbf{S}_1 \cdot \mathbf{S}_2|0\rangle_m = G_{+-} + G_{-+} + G_{zz}, \tag{C1}$$

where

$$G_{+-} = \tfrac{1}{2}\langle \mathbf{v}|S_1^+ S_2^-|\mathbf{u}\rangle, \tag{C2}$$

$$G_{-+} = \tfrac{1}{2}\langle \mathbf{v}|S_1^- S_2^+|\mathbf{u}\rangle, \tag{C3}$$

$$G_{zz} = \langle \mathbf{v}|S_1^z S_2^z|\mathbf{u}\rangle, \tag{C4}$$

u_j are the quasimomenta of the ground state $|0\rangle$, and v_j are the quasimomenta of an excited state $|\mathbf{q}\rangle$ with the same number of particles.

The local spin operators of the model in Eq. (A1) can be expressed in terms of the algebraic Bethe ansatz operators from Eq. (B3) as [15,16,51]

$$S_1^+ = C_\xi \tau_\xi^{L-1}, \quad S_2^+ = \tau_\xi C_\xi \tau_\xi^{L-2}, \tag{C5}$$

$$S_1^- = B_\xi \tau_\xi^{L-1}, \quad S_2^- = \tau_\xi B_\xi \tau_\xi^{L-2}, \tag{C6}$$

$$S_1^z = S_2^z \frac{A_\xi - D_\xi}{2}\tau_\xi^{L-1}, \quad S_2^z = \tau_\xi \frac{A_\xi - D_\xi}{2}\tau_\xi^{L-2}, \tag{C7}$$

where $\xi = -i\pi/2 + \eta$.

Firstly, we evaluate the $+-$ correlation function. Under the substitution of Eqs. ((C5), (C6)) in to Eq. (C2) it reads

$$G_{+-} = \tfrac{1}{2}\langle \mathbf{v}|C_\xi B_\xi|\mathbf{u}\rangle. \tag{C8}$$

Commuting of the B_ξ operator from left to right through a product of $C(u_j)$ operators by means of the commutation relations in Eqs. ((B6)–(B9)) gives

$$B_\xi \prod_{j=1}^{N} C_{u_j}|\Downarrow\rangle = \sum_{x=1}^{N+1} a_x c_{x\xi} \prod_{i=1\neq x}^{N+1} \frac{1}{b_{xi}} \sum_{y=1\neq x}^{N+1} c_{\xi y} \prod_{j=1\neq x,y}^{N+1} \frac{1}{b_{jy}} \prod_{j=1\neq x,y}^{N+1} C_{u_j}|\Downarrow\rangle, \tag{C9}$$

where $u_{N+1} \equiv \xi$. Multiplying the above expression by C_ξ and evaluating the scalar product with the final state $\langle \mathbf{v}|$ we obtain

$$\begin{aligned} G_{+-} = {} & \frac{1}{2}\sum_{x=1}^{N} a_x \frac{c_{x\xi}}{b_{x\xi}} \prod_{i=1\neq x}^{N} \frac{1}{b_{xi}} \sum_{y=1\neq x}^{N} \frac{c_{\xi y}}{b_{\xi y}} \prod_{j=1\neq x,y}^{N} \frac{1}{b_{jy}} \langle u_{x-1},\xi,u_{x+1},u_{y-1},\xi,u_{y+1}|\mathbf{v}\rangle \\ & + \frac{1}{2}\sum_{x=1}^{N} a_x \frac{c_{x\xi}}{b_{x\xi}} \prod_{i=1\neq x}^{N} \frac{1}{b_{xi}} \prod_{j=1\neq x}^{N} \frac{1}{b_{j\xi}} \langle u_{x-1},\xi,u_{x+1}|\mathbf{v}\rangle. \end{aligned} \tag{C10}$$

Here the property $\langle \mathbf{v}|\mathbf{u}\rangle = \langle \mathbf{u}|\mathbf{v}\rangle$ where v_j satisfy the Bethe equations and u_j is an arbitrary set of auxiliary parameters [15,16] was used.

The remaining scalar product can be evaluated using the Slavnov's formula (B18). By substituting $\xi = -i\pi/2 + \eta$ into $\langle u_{x-1},\xi,u_{x+1}|\mathbf{v}\rangle$ in the second line of Eq. (C10) explicitly we obtain

$$\langle u_{x+1},\xi,u_{x-1}|\mathbf{v}\rangle = \frac{i(-1)^x \prod_j^N \cosh(v_j+\eta)\prod_{j,i\neq x}^N \sinh(u_i - v_j)\det \hat{T}^{(x)}}{\prod_{j\neq x}^N \cosh(u_j-\eta)\prod_{i<j}\sinh(v_i-v_j)\prod_{i<j\neq x}\sinh(u_i-u_j)}, \tag{C11}$$

where the matrix elements are

$$T_{ab}^{(x)} = T_{ab}, \quad b \neq x, \tag{C12}$$

$$T_{ax}^{(x)} = \frac{\sinh(2\eta)}{\cosh(v_a-\eta)\cosh(v_a+\eta)}, \quad b = x, \tag{C13}$$

and T_{ab} are given in Eq. (B19).

Substitution of the two identical $u_j = u_{j'} = \xi$ into the scalar product $\langle u_{x-1},\xi,u_{x+1},u_{y-1},\xi,u_{y+1}|\mathbf{v}\rangle$ in the first line in Eq. (C10) makes the prefactor in Eq. (B18) divergent, i.e. the prefactor has a pole of the first order as a function of $(u_{j'} - u_j)$. Simultaneously, the determinant in Eq. (B18) becomes zero under the same substitution $u_j = u_{j'} = \xi$ since two lines of the matrix in Eq. (B19) becomes identical. Thus, we will derive the explicit expression for the whole scalar product by substituting $u_j = \xi$ first, then, by taking the limit $u_{j'} = \bar{\xi} \to \xi$. Expanding the matrix elements in Eq. (B19) in a Taylor series in $(\bar{\xi} - \xi)$ and using general matrix identities we obtain

$$\begin{vmatrix} \cdots \\ \mathbf{A}^T \\ \cdots \\ \mathbf{A}^T + (\beta\mathbf{A}^T + \mathbf{X}^T)(\bar{\xi} - \xi) \\ \cdots \end{vmatrix} = (\bar{\xi} - \xi) \begin{vmatrix} \cdots \\ \mathbf{A}^T \\ \cdots \\ \mathbf{X}^T \\ \cdots \end{vmatrix}, \tag{C14}$$

where

$$A_a = \frac{\sinh(2\eta)}{\cosh(v_a - \eta)\cosh(v_a + \eta)} \prod_j^N \frac{\cosh(v_j + \eta)}{\cosh(v_j - \eta)} \tag{C15}$$

is the jth row of Eq. (B19) under the substitution $u_j = \xi$,

$$X_a = \frac{\sinh 2\eta \sinh 2v_a}{\cosh^2(v_a - \eta)\cosh^2(v_a + \eta)} \prod_j^N \frac{\cosh(v_j + \eta)}{\cosh(v_j - \eta)}, \tag{C16}$$

is the linear coefficient in the Taylor expansion of the j'th row of Eq. (B19) around the point $u_{j'} = \xi$, which is not collinear with A_a in the vector space, and β is the part of the linear coefficient that is collinear with A_a.

Cancellation of the $\bar{\xi} - \xi$ from the denominator in Eq. (C14) with the $1/(\bar{\xi} - \xi)$ from the prefactor in Eq. (B18) makes the whole scalar product finite. Contributions of the orders higher than one (in the expansion of the determinant) vanish in the limit $\bar{\xi} \to \xi$ and we obtain

$$\langle u_{x-1},\xi,u_{x+1},u_{y-1},\xi,u_{y+1}|\mathbf{v}\rangle = (-1)^{x+y} \frac{\prod_j \cosh^2(v_j + \eta)}{\prod_{j\neq x,y}\cosh^2(u_j - \eta)} \frac{\prod_{j,j';j'\neq x,y}\sinh(u_{j'} - v_j)\det \hat{T}^{(xy)}}{\prod_{j<j'}\sinh(v_i - v_j)\prod_{j<j'\neq x,y}\sinh(u_i - u_j)}, \tag{C17}$$

where the matrix elements are

$$T_{ab}^{(xy)} = \begin{cases} T_{ab}, & b \neq x,y, \\ T_{ab}^{(b)}, & b = \min(x,y), \\ \frac{\sinh 2\eta \sinh 2v_a}{\cosh^2(v_a-\eta)\cosh^2(v_a+\eta)}, & b = \max(x,y). \end{cases} \tag{C18}$$

Secondly, we turn to evaluating the $-+$ correlation function. Under the substitution of Eqs. (C5) and (C6) into Eq. (C3) it reads

$$G_{-+} = \tfrac{1}{2}\langle \mathbf{v}|B_\xi C_\xi|\mathbf{u}\rangle. \tag{C19}$$

When B_ξ is commuted through the product of C_{u_j} operators using the general result in Eq. (C9), the first step of commuting B_ξ with C_ξ introduces a divergent denominator through the commutation relation in Eq. (B6). However, the operator factor in the numerator of Eq. (B6) becomes zero at the same time making the whole expression finite. Since the divergence occurs at the first step of commuting B_ξ through a product of $N+1$ operators $C(u_j)$, taking the limit after using Eq. (C9), as it is done in Ref. [16], creates an extra and significant computation problems: the original divergence spreads through many terms under the sum in Eq. (C9) and cancelling them explicitly is a complicated problem.

Here we will do it in a different way by canceling this intermediate divergence from the beginning in Eq. (C19). Expanding the numerator and the denominator of the commutation relation in Eq. (B6) up to the linear order in $\bar{\xi} - \xi$, where $u \to \bar{\xi}$ and $v \to \xi$ auxiliary parameters were relabeled, we cancel the $\bar{\xi} - \xi$ with $1/(\bar{\xi} - \xi)$. Then, substituting the result of this procedure in Eq. (C19) we obtain

$$G_{-+} = \frac{1}{2}\langle \mathbf{v}|C_\xi B_\xi|\mathbf{u}\rangle + \frac{\sinh 2\eta}{2} \lim_{\bar{\xi}\to\xi} \partial_{\bar{\xi}}(\langle \mathbf{v}|A_{\bar{\xi}} D_\xi|\mathbf{u}\rangle - \langle \mathbf{v}|A_\xi D_{\bar{\xi}}|\mathbf{u}\rangle), \tag{C20}$$

where $\langle \mathbf{v}|C_\xi B_\xi|\mathbf{u}\rangle$ has already been calculated in Eq. (C10).

The remaining two correlation functions under the derivative in Eq. (C20) can be calculated by successive use of the general result of commuting A_u and D_v operators through a product of $C(u_j)$ operators in Eqs. (B10) and (B11). The scalar product of $\langle \mathbf{v}|$ with the result of the commutation procedure gives

$$\begin{aligned} \langle \mathbf{v}|A_{\bar{\xi}} D_\xi|\mathbf{u}\rangle = {} & a_{\bar{\xi}} \prod_{l=1}^N \frac{1}{b_{l\bar{\xi}}} \prod_{j=1}^N \frac{1}{b_{\bar{\xi}j}} \delta_{\mathbf{u},\mathbf{v}} - \prod_{l=1}^N \frac{1}{b_{l\bar{\xi}}} \sum_{j=1}^N a_j \frac{c_{\bar{\xi}j}}{b_{\bar{\xi}j}} \prod_{l=1\neq j}^N \frac{1}{b_{jl}} \langle u_{j-1},\bar{\xi},u_{j+1}|\mathbf{v}\rangle \\ & + \sum_{j=1}^N \frac{c_{\xi j}}{b_{\xi j}} \prod_{l=1\neq j}^N \frac{1}{b_{lj}} a_\xi \frac{1}{b_{\xi\xi}} \prod_{l=1\neq j}^N \frac{1}{b_{\xi l}} \langle u_{j-1},\xi,u_{j+1}|\mathbf{v}\rangle - \sum_{j=1}^N \frac{c_{\xi j}}{b_{\xi j}} \prod_{l=1\neq j}^N \frac{1}{b_{lj}} \sum_{j'=1\neq j}^N a_{j'} \frac{c_{\bar{\xi}j'}}{b_{\bar{\xi}j'}} \frac{1}{b_{j'\xi}} \\ & \times \prod_{l=1\neq j,j'}^N \frac{1}{b_{j'l}} \langle u_{j-1},\xi,u_{j+1},u_{j'-1},\bar{\xi}u_{j'+1}|\mathbf{v}\rangle - \sum_{j=1}^N \frac{c_{\xi j}}{b_{\xi j}} \prod_{l=1\neq j}^N \frac{1}{b_{lj}} a_\xi \frac{c_{\xi\xi}}{b_{\xi\xi}} \prod_{l=1\neq j}^N \frac{1}{b_{\xi l}} \langle u_{j-1},\bar{\xi},u_{j+1}|\mathbf{v}\rangle, \end{aligned} \tag{C21}$$

$$\langle \mathbf{v}|A_\xi D_\xi|\mathbf{u}\rangle = a_\xi \prod_{l=1}^{N}\frac{1}{b_{l\xi}}\prod_{j=1}^{N}\frac{1}{b_{\bar\xi j}}\delta_{\mathbf{u},\mathbf{v}} - \prod_{l=1}^{N}\frac{1}{b_{l\xi}}\sum_{j=1}^{N}a_j\frac{c_{\xi j}}{b_{\bar\xi j}}\prod_{l=1\neq j}^{N}\frac{1}{b_{jl}}\langle u_{j-1},\bar\xi,u_{j+1}|\mathbf{v}\rangle$$
$$+\sum_{j=1}^{N}\frac{c_{\xi j}}{b_{\xi j}}\prod_{l=1\neq j}^{N}\frac{1}{b_{lj}}a_\xi\frac{1}{b_{\bar\xi\xi}}\prod_{l=1\neq j}^{N}\frac{1}{b_{\bar\xi l}}\langle u_{j-1},\xi,u_{j+1}|\mathbf{v}\rangle$$
$$-\sum_{j=1}^{N}\frac{c_{\xi j}}{b_{\xi j}}\prod_{l=1\neq j}^{N}\frac{1}{b_{lj}}\sum_{j'=1\neq j}^{N}a_{j'}\frac{c_{\xi j'}}{b_{\bar\xi j'}}\frac{1}{b_{j'\xi}}\prod_{l=1\neq j,j'}^{N}\frac{1}{b_{j'l}}\langle u_{j-1},\xi,u_{j+1},u_{j'-1},\bar\xi u_{j'+1}|\mathbf{v}\rangle \tag{C22}$$

for both terms in the second line of Eq. (C20), respectively. Then, after taking the derivative of Eqs. (C21) and (C22), with respect to $\bar\xi$ and the limit $\bar\xi\to\xi$, we substitute the results in to Eq. (C20) and obtain

$$G_{-+} = G_{+-} + \frac{\sinh 2\eta}{2}\Bigg[\prod_{l=1}^{N}\frac{1}{b_{l\xi}}\sum_{j=1}^{N}\sum_{l=1}^{N}[\tanh(u_l+\eta)-\tanh(v_l-\eta)]a_j\frac{c_{j\xi}}{b_{j\xi}}\prod_{l=1\neq j}^{N}\frac{1}{b_{jl}}\langle u_{j-1},\xi,u_{j+1}|\mathbf{v}\rangle$$
$$+\sum_{j=1}^{N}\frac{c_{j\xi}}{b_{j\xi}}\prod_{l=1\neq j}^{N}\frac{1}{b_{lj}}\sum_{j'=1\neq j}^{N}a_{j'}\frac{c_{\xi j'}}{b_{\xi j'}}(\tanh(u_{j'}+\eta)-\tanh(u_j-\eta))\frac{1}{b_{j'\xi}}\prod_{l=1\neq j,j'}^{N}\frac{1}{b_{j'l}}\langle u_{j-1},\xi,u_{j+1},u_{j'-1},\xi u_{j'+1}|\mathbf{v}\rangle$$
$$+\prod_{l=1}^{N}\frac{1}{b_{l\xi}}\sum_{j=1}^{N}a_j\frac{c_{j\xi}}{b_{j\xi}}\prod_{l=1\neq j}^{N}\frac{1}{b_{jl}}\langle u_{j-1},\xi,u_{j+1}|\mathbf{v}\rangle'\Bigg], \tag{C23}$$

where the derivative of $\langle u_{j-1},\bar\xi,u_{j+1}|\mathbf{v}\rangle$ with respect to $\bar\xi$ results in an additional determinant,

$$\langle u_{x-1},\xi,u_{x+1}|\mathbf{v}\rangle' = \frac{i(-1)^j\prod_{j'}^{N}\cosh(v_{j'}+\eta)\prod_{j',i\neq x}^{N}\sinh(u_i-v_{j'})\det\hat T^{'(x)}}{\prod_{j'\neq x}^{N}\cosh(u_{j'}-\eta)\prod_{i<j'}\sinh(v_i-v_{j'})\prod_{i<j'\neq x}\sinh(u_i-u_{j'})}, \tag{C24}$$

where the matrix elements are

$$T_{ax}^{'(x)} = \frac{2\sinh 2\eta\tanh(v_a-\eta)}{\cosh(v_a-\eta)\cosh(v_a+\eta)} - \frac{\sinh^2 2\eta}{\cosh(v_a-\eta)\cosh(v_a+\eta)}\sum_{j=1\neq a}^{N}\frac{1}{\cosh(v_j-\eta)\cosh(v_j+\eta)} \tag{C25}$$

for $b=x$ and the remaining entries for $b\neq x$ are $T_{ab}^{'(x)}\equiv T_{ab}$ from Eq. (B19).

Thirdly, we evaluate the zz correlation function. Under the substitution of Eq. (C7) in Eq. (C4) it reads

$$G_{zz} = \tfrac{1}{4}\langle\mathbf{v}|(A_\xi - D_\xi)(A_\xi - D_\xi)|\mathbf{u}\rangle. \tag{C26}$$

Before proceeding with the commutation procedure as in the two previous cases we rewrite the above expression in a form more convenient for such a calculation using the definition of the transfer matrix, $A_\xi - D_\xi = 2A_\xi - \tau_\xi$, and its eigenvalue $\tau_\xi|\mathbf{u}\rangle = \mathcal{T}_\xi|\mathbf{u}\rangle$,

$$G_{zz} = \tfrac{1}{2}\langle\mathbf{v}|A_\xi^2 - \mathcal{T}_\xi A_\xi - D_\xi A_\xi|\mathbf{u}\rangle, \tag{C27}$$

where $\mathcal{T}_\xi = \prod_j b_{j\xi}^{-1}$ is given by Eq. (B15) and we have assumed that $\langle\mathbf{v}|$ and $|\mathbf{u}\rangle$ are a pair of orthogonal eigenstates, i.e., $\langle\mathbf{v}|\mathbf{u}\rangle = 0$.

The correlation function of A_ξ and A_ξ^2 can be calculated using Eq. (B10) once and twice, respectively. The scalar products of $\langle\mathbf{v}|$ with the results of the commutation procedures are

$$\langle\mathbf{v}|A_\xi|\mathbf{u}\rangle = -\sum_{x=1}^{N}a_j\frac{c_{\xi x}}{b_{\xi x}}\prod_{l=1\neq j}^{N}\frac{1}{b_{xl}}\langle u_{x+1},\xi,u_{x-1}|\mathbf{v}\rangle, \tag{C28}$$

$$\langle\mathbf{v}|A_\xi^2|\mathbf{u}\rangle = 4\sum_{x=1}^{N}a_x\frac{c_{\xi x}}{b_{\xi x}}\prod_{l;l\neq x}^{N}\frac{1}{b_{xl}}\sum_{y;y\neq x}^{N}a_y\frac{c_{\xi y}}{b_{\xi y}}\prod_{l;l\neq x,y}^{N}\frac{1}{b_{xl}}\frac{1}{b_{y\xi}}\langle u_{x-1},\xi,u_{x+1},u_{y-1},\xi,u_{y+1}|\mathbf{v}\rangle, \tag{C29}$$

where the scalar products on the right hand sides are already given in Eqs. (C11) and (C17) in explicit form.

Evaluation of the remaining $D_\xi A_\xi$ correlation function involves the same problem of taking the limit $v\to u=\xi$ in commutation relation Eq. (B9), as in the calculation of the $-+$ correlation function. Here we resolve it in the same way as we have already done in evaluating Eq. (C19). Expanding the numerator and the denominator of Eq. (B9) in $v-u\to 0$ we

rewrite the $D_\xi A_\xi$ correlation function as

$$\langle \mathbf{v}|D_\xi A_\xi|\mathbf{u}\rangle = \langle \mathbf{v}|\mathcal{T}_\xi A_\xi - A_\xi^2|\mathbf{u}\rangle - \sinh 2\eta \lim_{\bar{\xi}\to\xi} \partial_{\bar{\xi}} \langle \mathbf{v}|C_{\bar{\xi}} B_{\bar{\xi}} - C_{\bar{\xi}} B_{\bar{\xi}}|\mathbf{u}\rangle. \tag{C30}$$

We use the general result in Eq. (C9) and write the $C_\xi B_{\bar{\xi}}$ and $C_{\bar{\xi}} B_\xi$ correlation functions under the derivative as

$$\begin{aligned}\langle \mathbf{v}|C_{\bar{\xi}} B_\xi|\mathbf{u}\rangle &= \sum_{x=1}^N a_x \frac{c_{x\bar{\xi}}}{b_{x\bar{\xi}}} \prod_{i=1\neq x}^N \frac{1}{b_{xi}} \sum_{y=1\neq x}^N d_y \frac{c_{\bar{\xi}y}}{b_{\bar{\xi}y}} \prod_{j=1\neq x,y}^N \frac{1}{b_{jy}} \langle u_{x-1},\bar{\xi},u_{x+1},u_{y-1},\xi,u_{y+1}|\mathbf{v}\rangle \\ &+ \sum_{x=1}^N a_x \frac{c_{x\bar{\xi}}}{b_{x\bar{\xi}}} \prod_{i=1\neq x}^N \frac{1}{b_{xi}} \prod_{j=1\neq x}^N \frac{1}{b_{j\bar{\xi}}} \langle u_{x-1},\bar{\xi},u_{x+1}|\mathbf{v}\rangle, \end{aligned} \tag{C31}$$

$$\begin{aligned}\langle \mathbf{v}|C_{\bar{\xi}} B_\xi|\mathbf{u}\rangle &= \sum_{x=1}^N a_x \frac{c_{x\xi}}{b_{x\xi}} \prod_{i=1\neq x}^N \frac{1}{b_{xi}} \sum_{y=1\neq x}^N d_y \frac{c_{\xi y}}{b_{\xi y}} \prod_{j=1\neq x,y}^N \frac{1}{b_{jy}} \langle u_{x-1},\xi,u_{x+1},u_{y-1},\bar{\xi},u_{y+1}|\mathbf{v}\rangle \\ &+ \sum_{x=1}^N a_x \frac{c_{x\xi}}{b_{x\xi}} \prod_{i=1\neq x}^N \frac{1}{b_{xi}} \prod_{j=1\neq x}^N \frac{1}{b_{j\xi}} \langle u_{x-1},\xi,u_{x+1}|\mathbf{v}\rangle. \end{aligned} \tag{C32}$$

Then, taking the derivative over $\bar{\xi}$, the limit $\bar{\xi}\to\xi$, and substituting the pair of the expressions above in Eqs. (C27) and (C30), together with the expressions in Eqs. (C28) and (C29), we obtain

$$\begin{aligned} G_{zz} &= \prod_j^N \frac{1}{b_{j\xi}} \sum_{j=1}^N a_j \frac{c_{\xi j}}{b_{\xi j}} \prod_{l=1\neq j}^N \frac{1}{b_{jl}} \langle u_{j+1},\xi,u_{j-1}|\mathbf{v}\rangle + \sum_{j=1}^N a_j \frac{c_{\xi j}}{b_{\xi j}} \prod_{l=1\neq j}^N \frac{1}{b_{jl}} \sum_{j'=1\neq j}^N a_{j'} \frac{c_{\xi j'}}{b_{\xi j'}} \prod_{l=1\neq j,j'}^N \frac{1}{b_{j'l}} \\ &\times \frac{1}{b_{j'\xi}} \langle u_{j-1},\xi,u_{j+1},u_{j'-1},\xi,u_{j'+1}|\mathbf{v}\rangle + \frac{\sinh 2\eta}{2} \Bigg[\sum_{x=1}^N a_x \frac{c_{x\xi}}{b_{x\xi}} \prod_{i=1\neq x}^N \frac{1}{b_{xi}} \sum_{y=1\neq x}^N \frac{c_{\xi y}}{b_{\xi y}} \\ &\times (\tanh(u_x-\eta)+\tanh(u_y-\eta)) \prod_{j=1\neq x,y}^N \frac{1}{b_{jy}} \langle u_{x-1},\xi,u_{x+1},u_{y-1},\xi,u_{y+1}|\mathbf{v}\rangle \\ &+ \sum_{x=1}^N a_x \frac{c_{x\xi}}{b_{x\xi}} \prod_{i=1\neq x}^N \frac{1}{b_{xi}} \prod_{j=1\neq x}^N \frac{1}{b_{j\xi}} \Bigg[\tanh(u_x-\eta)+\tanh(v_x-\eta) \\ &+ \sum_{j'=1\neq x}^N [\tanh(v_{j'}-\eta)-\tanh(u_{j'}+\eta)] \Bigg] \langle u_{x-1},\xi,u_{x+1}|\mathbf{v}\rangle - \sum_{x=1}^N a_x \frac{c_{x\xi}}{b_{x\xi}} \prod_{i=1\neq x}^N \frac{1}{b_{xi}} \prod_{j=1\neq x}^N \frac{1}{b_{j\xi}} \langle u_{x-1},\xi,u_{x+1}|\mathbf{v}\rangle' \Bigg], \end{aligned} \tag{C33}$$

where all scalar products are already given in explicit form above.

Finally, we substitute Eqs. (C10), (C23), and (C33) in Eq. (C1), rewrite the result in a more compact form by collecting similar terms, and use a general matrix identity $\det\hat{T} + \sum_{x=1}^N \det\hat{T}^{(x)} = \det(\hat{T}+\hat{X})$, where the matrix $T^{(b)}$ is obtained by substitution of the xth column from the matrix $\hat{X}$ and rank of $\hat{X}$ is equal to one. After constructing the corresponding matrices $\hat{X}$ for a single sum over x and for a sum over only one variable in the double sum over x,y we obtain

$$\begin{aligned}\langle \mathbf{q}|\mathbf{S}_1\cdot\mathbf{S}_2|0\rangle &= \frac{\prod_j^N \cosh(v_j+\eta)}{\prod_{i<j}\sinh(v_i-v_j)} \sum_{x=1}^N (-1)^x \frac{\prod_{i,j;j\neq x}^N \sinh(u_j-v_i)}{\prod_j^N \cosh^2(u_j-\eta)} \prod_{l=1\neq x}^N \frac{\sinh(u_l-u_x+2\eta)}{\sinh(u_l-u_x)} \\ &\times \left[\det\hat{K}^{(x)} - \left(1 - \frac{\sinh(2\eta)\sinh\eta\sinh u_x \prod_{j;j\neq x}^N \cosh(u_j+\eta)}{\prod_{i<j\neq x}\sinh(u_i-u_j)}\right) \det\hat{G}^{(x)} \right] \\ &- \frac{\prod_j \cosh(u_j+\eta)\prod_j\cosh(v_j+\eta)}{\prod_j\cosh^2(u_j-\eta)\prod_{i<j}\sinh(v_i-v_j)} \det\hat{K}, \end{aligned} \tag{C34}$$

where the matrix elements are

$$K_{ab} = T_{ab} + (-1)^b \frac{\sinh^3(2\eta)\sinh\eta\sinh u_b}{\cosh(u_b+\eta)} \frac{\prod_{j,i\neq b}^{N}\sinh(u_i-v_j)}{\prod_{i<j\neq b}\sinh(u_i-u_j)} \prod_{l=1\neq b}^{N} \frac{\sinh(u_l-u_b+2\eta)}{\sinh(u_l-u_b)}$$
$$\times \frac{\frac{\sinh u_b}{\cosh(u_b+\eta)\cosh\eta} + \sum_{l=1}^{N}[\tanh(v_l+\eta)-\tanh(u_l+\eta)]}{\cosh(v_a-\eta)\cosh(v_a+\eta)}, \tag{C35}$$

$$T_{ab} = \frac{\cosh^L(v_b-\eta)}{\cosh^L(v_b+\eta)} \frac{\sinh(2\eta)}{\sinh^2(v_b-u_a)} \prod_{j=1\neq a}^{N} \frac{\sinh(v_b-u_j+2\eta)}{\sinh(v_b-u_j)} - \frac{\sinh(2\eta)}{\sinh^2(u_a-v_b)} \prod_{j=1\neq a}^{N} \frac{\sinh(u_j-v_b+2\eta)}{\sinh(u_j-v_b)}, \tag{C36}$$

$$K^{(x)}_{ab} = T_{ab} + \frac{(-1)^b\sinh^3(2\eta)\mathrm{sgn}(x-b)}{\cosh(v_a-\eta)\cosh(v_a+\eta)} \prod_{l=1\neq x,b}^{N} \frac{\sinh(u_l-u_b+2\eta)}{\sinh(u_l-u_b)} \frac{\cosh(u_b+\eta)\cosh(u_x-\eta)}{\prod_i^N\sinh(u_b-v_i)\prod_{i<j\neq x,b}\sinh(u_i-u_j)}$$
$$\times \left(\frac{\cosh(u_b-\eta)}{\cosh(u_b+\eta)} - \frac{\sinh(u_x-u_b+2\eta)}{\sinh(u_x-u_b-2\eta)} + \frac{\sinh 2\eta\cosh(u_b-2\eta)\sinh u_x}{\cosh(u_x-\eta)\cosh(u_b+\eta)} \right), \tag{C37}$$

when $b \neq x$,

$$K^{(x)}_{ax} = \frac{\sinh(2\eta)\sinh(2v_a)}{\cosh^2(v_a-\eta)\cosh^2(v_a+\eta)} \tag{C38}$$

when $b = x$, $G^{(x)}_{ab} = T_{ab}$ when $b \neq x$, and $G^{(x)}_{ax} = K^{(x)}_{ax}$ when $b = x$. The result in Eq. (C34) was checked numerically for $N = 2,3$ using the direct summation over the spacial coordinates. Equations (C34)–(C37) are Eqs. (13)–(16).

[1] B. Lüthi, *Physical Acoustics in the Solid State* (Springer, Berlin, 2005).
[2] K. Tani and H. Mori, Prog. Theor. Phys. **39**, 876 (1968).
[3] K. Kawasaki and A. Ikushima, Phys. Rev. B **1**, 3143 (1970).
[4] Y. Zhou and P. A. Lee, Phys. Rev. Lett. **106**, 056402 (2011).
[5] M. Serbyn and P. A. Lee, Phys. Rev. B **87**, 174424 (2013).
[6] R. Coldea, D. A. Tennant, and Z. Tylczynski, Phys. Rev. B **68**, 134424 (2003).
[7] A. Sytcheva, O. Chiatti, J. Wosnitza, S. Zherlitsyn, A. A. Zvyagin, R. Coldea, and Z. Tylczynski, Phys. Rev. B **80**, 224414 (2009).
[8] Y. Trudeau, M. Poirier, and A. Caille, Phys. Rev. B **46**, 169 (1992).
[9] B. Lake, D. A. Tennant, C. D. Frost, and S. E. Nagler, Nat. Mater. **4**, 329 (2005).
[10] B. Wolf, S. Zherlitsyn, B. Luthi, N. Harrison, U. Low, V. Pashchenko, M. Lang, G. Margraf, H. W. Lerner, E. Dahlmann, F. Ritter, W. Assmus, and M. Wagner, Phys. Rev. B **69**, 092403 (2004).
[11] M. Gaudin, *The Bethe Wavefunction* (Cambridge University Press, Cambridge, 2014).
[12] O. Tsyplyatyev, A. J. Schofield, Y. Jin, M. Moreno, W. K. Tan, C. J. B. Ford, J. P. Griffiths, I. Farrer, G. A. C. Jones, and D. A. Ritchie, Phys. Rev. Lett. **114**, 196401 (2015).
[13] O. Tsyplyatyev, A. J. Schofield, Y. Jin, M. Moreno, W. K. Tan, A. S. Anirban, C. J. B. Ford, J. P. Griffiths, I. Farrer, G. A. C. Jones, and D. A. Ritchie, Phys. Rev. B **93**, 075147 (2016).
[14] M. Moreno, C. J. B. Ford, Y. Jin, J. P. Griffiths, I. Farrer, G. A. C. Jones, D. A. Ritchie, O. Tsyplyatyev, and A. J. Schofield, Nat. Commun. **7**, 12784 (2016).
[15] N. Kitanine, J. M. Maillet, and V. Tetras, Nucl. Phys. B **554**, 647 (1999).
[16] N. Kitanine and J. M. Maillet, Nucl. Phys. B **567**, 554 (2000).
[17] J.-S. Caux and J. M. Maillet, Phys. Rev. Lett. **95**, 077201 (2005).
[18] J.-S. Caux, P. Calabrese, and N. Slavnov, J. Stat. Mech. (2007) P01008.
[19] B. Lake, D. A. Tennant, J. S. Caux, T. Barthel, U. Schollwock, S. E. Nagler, and C. D. Frost, Phys. Rev. Lett. **111**, 137205 (2013).
[20] A. Kamra and G. E. W. Bauer, Solid State Commun. **198**, 35 (2014).
[21] A. Kamra, H. Keshtgar, P. Yan, and G. E. W. Bauer, Phys. Rev. B **91**, 104409 (2015).
[22] A. Ruckriegel, P. Kopietz, D. A. Bozhko, A. A. Serga, and B. Hillebrands, Phys. Rev. B **89**, 184413 (2014).
[23] A. Ruckriegel and P. Kopietz, Phys. Rev. Lett. **115**, 157203 (2015).
[24] R. Coldea, D. A. Tennant, R. A. Cowley, D. F. McMorrow, B. Dorner, and Z. Tylczynski, Phys. Rev. Lett. **79**, 151 (1997).
[25] M. Kohno, O. A. Starykh, and L. Balents, Nat. Phys. **3**, 790 (2007).
[26] M. T. Hutchings, G. Shirane, R. J. Birgeneau, and S. L. Holt, Phys. Rev. B **5**, 1999 (1972).
[27] O. M. Auslaender, A. Yacoby, R. de Picciotto, K. W. Baldwin, L. N. Pfeiffer, and K. W. West, Science **295**, 825 (2002).
[28] Y. Jompol, C. J. B. Ford, J. P. Griffiths, I. Farrer, G. A. C. Jones, D. Anderson, D. A. Ritchie, T. W. Silk, and A. J. Schofield, Science **325**, 597 (2009).
[29] Complex quasimomenta (string solutions) at the $\Delta = 1$ point emerge under the numerical deformation, starting from the real quasimomenta at the $\Delta = 0$ point.
[30] R. Orbach, Phys. Rev. **112**, 309 (1958).
[31] V. E. Korepin, N. M. Bogoliubov, and A. G. Izergin, *Quantum Inverse Scattering Methods and Correlation Functions* (Cambridge University Press, Cambridge, 1993).
[32] M. Gaudin, B. M. McCoy, and T. T. Wu, Phys. Rev. D **23**, 417 (1981).

[33] V. E. Korepin, Commun. Math. Phys. **86**, 391 (1982).
[34] C. Kittel, *Introduction to Solid State Physics* (Wiley, New York, 1996).
[35] T. Giamarchi, *Quantum Physics in One Dimension* (Clarendon Press, Oxford, 2003).
[36] The width of the anticrossing is estimated as a matrix element of the magnetostrictive interaction in Eq. (3), $J_1\sqrt{\hbar b/(m\omega_D)}/L^4$ (where the spin matrix element belongs to the second level of the hierarchy $\sim 1/L^4$) times the superradiant enhancement factor $(\omega_D L/J)^{3/2}$ since the number of the almost degenerate levels is $\sim(\omega_D L/J)^3$.
[37] A. Kreisel, P. Kopietz, P. T. Cong, B. Wolf, and M. Lang, Phys. Rev. B **84**, 024414 (2011).
[38] S. Streib, P. Kopietz, P. T. Cong, B. Wolf, M. Lang, N. van Well, F. Ritter, and W. Aßmus, Phys. Rev. B **91**, 041108(R) (2015).
[39] N. Krüger, S. Belz, F. Schossau, A. A. Haghighirad, P. T. Cong, B. Wolf, S. Gottlieb-Schoenmeyer, F. Ritter, and W. Aßmus, Cryst. Growth Design **10**, 4456 (2010).
[40] B. Lüthi, G. Bruls, P. Thalmeier, B. Wolf, D. Finsterbusch, and I. Kouroudis, J. Low Temp. Phys. **95**, 257 (1994).
[41] R. Truell, C. Elbaum, and B. B. Chick, *Ultrasonic Methods in Solid State Physics* (Academic Press, New York, 1969).
[42] P. T. Cong, L. Postulka, B. Wolf, N. van Well, F. Ritter, W. Aßmus, C. Krellner, and M. Lang, J. Appl. Phys. **120**, 142113 (2016).
[43] L. Balents, Nature (London) **464**, 199 (2010).
[44] In this paper we assume that N is even obtaining $q_j = 2\pi(I_j + 1/2)/L$ in the $\Delta \to 0$ limit. For odd Ns the $\Delta \to 0$ limit of Eqs. (1.2) and (1.3) gives $q_j = 2\pi I_j/L$ that is a parity effect. We do not consider it here.
[45] E. H. Lieb, T. D. Schultz, and D. C. Mattis, Ann. Phys. (NY) **16**, 407 (1961).
[46] J. D. Noh, D.-S. Lee, and D. Kim, Physica A **287**, 167 (2000).
[47] K. Fabricius and B. M. McCoy, J. Stat. Phys. **103**, 647 (2001).
[48] F. H. L. Essler, V. E. Korepin, and K. Schoutens, J. Phys. A **25**, 4115 (1992).
[49] R. J. Baxter, J. Stat. Phys. **108**, 1 (2002).
[50] N. A. Slavnov, Theor. Math. Phys. **79**, 502 (1989).
[51] J. M. Maillet and J. Sanchez de Santos, Amer. Math. Soc. Transl. **201(2)**, 137 (2000).